universität wien

DISSERTATION / DOCTORAL THESIS

Titel der Dissertation /Title of the Doctoral Thesis

„Neuronal dynamics governing behavior in *Caenorhabditis elegans*“

verfasst von / submitted by

Harris Kaplan

angestrebter akademischer Grad / in partial fulfilment of the requirements for the degree of

Doctor of Philosophy (PhD)

Wien, 2019 / Vienna 2019

Studienkennzahl lt. Studienblatt / degree programme code as it appears on the student record sheet:	A 794 685 490
Dissertationsgebiet lt. Studienblatt / field of study as it appears on the student record sheet:	Molecular Biology
Betreut von / Supervisor:	Univ.-Prof. Dr. Manuel Zimmer

Table of Contents

1. Acknowledgements

A thesis can have only one author, but in reality is always the product of many peoples' time, effort, energy, thoughtfulness, and care. I have had the good fortune to have several absolutely essential contributions over these years, both personally and scientifically.

Manuel, your example and your guidance has shown me what it means to be a scientist. I can only hope to one day approach your level of critical and detailed thinking, breadth and depth of knowledge, creativity, and constant push to tackle big questions in a rigorous manner. As a mentor, your patience, trust, and insistence on high quality work has enabled me to grow as a scientist way beyond what I had anticipated. Any future success I might have will be in many ways a result of what I've learned from you over these years.

Oriana, thanks for producing both awesome data and endless laughs, constantly, for the entire second half of my PhD, and for being a clear-headed sounding board for my ideas (and complaints!). I'll be extremely lucky if I ever again get to work so closely with someone as smart and talented as you are. Tina, I owe you so much: first, you taught me many of the techniques I still use today, and how to do them extremely carefully; next, your care, dedication, and ambition led to whole-brain imaging, which ended up being in many ways the foundation of my PhD. I learned so much from you, and had a ton of fun doing it. Saul, I'm so glad you joined when you did, and only wish you'd stayed longer. You were an endless source of ideas, insight, and explanations, as well as good times.

Susanne and Ingrid, along with Tina, thanks for being extremely welcoming from the moment I interviewed, which made me feel surprisingly comfortable with the idea of moving across the ocean. I can't imagine having made it through those first few years in the lab without your help and your company. Annika, having you in the lab was so much fun, and your effortless generosity and dedication were contagious. I'm aspiring to your example all the time.

Thanks to all other Zimmer lab members, current – Rich, Daniel, Julia, Kerem, Mara, Ulises, Lukas, Matthew, Marc, Niklas, and Anton – and former – Tomas K, Tomas E, Charlie, Fanny, Dagi, Lisa, and Michi. From all of you, I learned a ton scientifically and personally, and had a lot of fun doing it. Thanks to Luisa and her lab, for being extremely helpful and generous sharing knowledge and tools; thanks to Ines, Chris, Manuela, Sabine, Pawel, and all other IMP/IMBA support/staff members for making my move and my science super smooth over the years; and thanks to my committee members Wulf and Gasper for providing critical feedback on my work along the way. And a big thanks to Justin for introducing me to the joy of doing science and for giving me invaluable advice on choosing my PhD position, without which I wouldn't have gone to Vienna.

Dave, you've taught me so much. For example, never flat aces pre-flop against calling stations. But really, I simply could not have navigated this PhD without your informal mentorship. Your all-around approach to doing science has had a profound impact on me, and I will be reaping the profits from that for, hopefully, decades to come. I have to thank many other friends, especially Ramin, Neha, Thomas, and IhnSeon, for supporting me emotionally and enriching my life tremendously, so that when things in the lab were not great, things outside the lab were.

This thesis is dedicated to two people who unfortunately did not live to see its completion. I recognized Mattias's curiosity and playfulness immediately when we met during our PhD interviews; after just that short week, even before I moved to Vienna, I felt I had a great friend there, in him. In many ways, this thesis would not be possible without my Aunt Bea: beyond rescuing me from sleep-away camp, she set me up in my first research position, which has ultimately led me to this thesis. I know that, if she were here, no one else would be happier for me, and I miss her love and support dearly.

My family – especially Leah, Bob, Howie, Jane, and of course Max, Mom and Dad - is a bottomless source of pure positivity, love, and support, which makes difficult things like PhD theses possible. Thanks so much for withstanding these years apart.

2. Summary

2.1 Zusammenfassung

Tierverhalten ist eines der faszinierendsten und geheimnisvollsten Themen der Biologie. Die Erzeugung von Verhalten wird weithin als eine primäre Funktion des Nervensystems angesehen, dennoch bleibt unklar, wie das Gehirn die Bewegungen in ein angemessenes, organisiertes Verhalten koordiniert. In dieser Arbeit beschäftige ich mich damit, indem ich die unterschiedliche Hirndynamik beschreibe, die dem Verhaltensrepertoire des Fadenwurm Caenorhabditis elegans (C. elegans) zugrunde liegt. Ich habe die neuronale Aktivität während des Verhaltens mit genetisch kodierten Kalziumindikatoren aufgezeichnet, die in bestimmten neuronalen Klassen von Interesse exprimiert wurden; die Kombination dieser Ergebnisse mit Daten aus hirnweiten Aufzeichnungen der neuronalen Aktivität bei immobilisierten Tieren ergab zwei Hauptprinzipien des Nervensystems des Wurms. Erstens wird die grundlegende Handlungssequenz des Wurms durch eine niedrigdimensionale neuronale Populationsdynamik bestimmt. Dieser Befund, der aufgrund der numerischen Einfachheit des Wurmgehirns unvorhergesehen war, etablierte den Wurm als potenzielles Modellsystem für die neuronale Populationsdynamik, wie sie beispielsweise bei Insekten und Säugetieren das Verhalten beeinflussen soll. Zweitens habe ich die oben genannten Techniken mit quantitativer Verhaltensanalyse und gezielter Manipulation spezifischer neuronaler Klassen kombiniert, um zu untersuchen, wie das Gehirn das Verhalten über mehrere Zeiträume hinweg koordiniert. Meine Ergebnisse stützen eine jahrzehntelange Hypothese in der Ethologie: dass das Verhalten auf verschiedenen Zeitskalen hierarchisch organisiert ist. Diese strenge, nicht überlappende, Top-Down-Organisation wird durch verschachtelte neuronale Dynamik erreicht, im Gegensatz zu einer hierarchischen Schaltungsarchitektur. Diese Arbeit zeigt, dass verschachtelte neuronale Dynamik ein wiederholtes dynamisches Motiv des C. elegans Nervensystems ist.

Ähnliche Wechselwirkungen neuronaler Aktivität im Mehrzeitbereich wurden bei einer Vielzahl anderer Tiere, einschließlich Säugetiere, beschrieben, aber ihre funktionellen Folgen werden weiterhin diskutiert. Insgesamt bietet diese Arbeit eine detaillierte Darstellung der neuronalen Dynamik, die dem Verhalten von C. elegans zugrunde liegt, mit potenzieller Relevanz für die Funktion des Nervensystems im gesamten Tierreich.

2.2 Abstract

Animal behavior is one of the most fascinating and mysterious topics in biology. The generation of behavior is widely regarded as a primary function of the nervous system, yet it remains unclear how the brain coordinates movements into appropriate, organized behavior. In this thesis, I address this by describing the diverse brain dynamics underlying the behavioral repertoire of the nematode *Caenorhabditis elegans* (*C. elegans*). I recorded neuronal activity during behavior using genetically encoded calcium indicators expressed in specific neuronal classes of interest; combining these results with data from brain-wide neuronal activity recordings in immobilized animals revealed two major principles of the worm's nervous system. First, the worm's basic action sequence is driven by low-dimensional neuronal population dynamics. This finding, which was unanticipated due to the numerical simplicity of the worm brain, established the worm as a potential model system for neuronal population dynamics, such as those thought to drive behavior in insects and mammals. Second, I combined the aforementioned techniques with quantitative behavior analysis and targeted manipulation of specific neuronal classes to examine how the brain coordinates behavior across multiple timescales. My findings supported a decades-old hypothesis in ethology: that behaviors on different timescales are organized hierarchically. This strict, non-overlapping, top-down organization is achieved via nested neuronal dynamics, in contrast to a hierarchical circuit architecture. This work demonstrates that nested neuronal dynamics are a repeated dynamical

motif of the *C. elegans* nervous system. Similar multi-timescale neuronal activity interactions have been described in a variety of other animals, including mammals, yet their functional consequences remain debated. Altogether, this work provides a detailed account of the neuronal dynamics underlying behavior in *C. elegans*, with potential relevance to nervous system function across the animal kingdom.

3. Introduction

3.1 How does the brain generate organized behavior?

A fundamental feature of animal behavior is that it is highly organized. Indeed, such organization is so crucial that it is often taken for granted. Human language is one instructive example: even before we learn formal grammatical structure in school, we absorb and implement its rules with ease. Beyond spoken language, the space of possible body movement combinations is incredibly large, yet human movement trajectories typically occupies only a small subset of that space (Franklin and Wolpert, 2011). Similar results have recently been found for mouse body language, during exploratory behavior (Wiltschko et al., 2015). Indeed, some form of organized exploratory behavior, involving specific types of locomotory and active sensing maneuvers, has been described for a wide variety of animals (Hills et al., 2015; Yang et al., 2016). This suggests that the nervous system is able to produce complex, organized motor outputs in a "spontaneous" manner, i.e. without the instruction of a simultaneously time-varying sensory input to guide its execution (Lashley, 1951). The organization of behavior therefore appears to be at least partly internal, the product of neuronal dynamics that are coordinated such that behavioral output is organized as well. These observations lead to two major questions: (1) what are the organizing rules of behavior? and (2) how are these organizing rules implemented by neuronal dynamics? One hope is that by investigating the second question, e.g. via neuronal activity recordings, we may learn about the brain's representation of behavior sufficiently enough to provide insight into the first question, regarding the organizing rules themselves (Brown and de Bivort, 2018). In this thesis, I will address these questions, focusing on two types of organized behavior: (1) an action sequence on a single timescale and (2) a behavioral hierarchy across timescales.

3.2 Behavioral organization: action sequence

One of the oldest observations in ethology is that individual actions typically occur in serial sequences, with specific ordering (Lashley, 1951; Tinbergen, 1951). Konrad Lorenz, one of the founders of modern ethology, elaborated on earlier observations of stereotypic action sequences by detailing the "fixed action pattern" (Moltz, 1961). These sequences are initiated by a particularly salient stimulus, known as the "sign" or "releasing" stimulus, which triggers the first action in the sequence. Once the first action is initiated, the sequence of actions that follows is almost invariably executed to completion (Moltz, 1961). The fixed action pattern can be seen as an extremely deterministic type of action sequence; other behaviors, such as different types of birdsong, have more probabilistic transitions between actions (Slater, 1973). More recent well-studied action sequences include *Drosophila* courtship (Dankert et al., 2009; Dickson, 2008) and grooming (Seeds et al., 2014). The importance of serial action sequencing is underscored by its diverse utility and ubiquity across both animal species (invertebrates and vertebrates) and behavioral goals (e.g. mating and grooming).

Despite this ubiquity, how nervous systems enable serially sequenced behavior remains a contested issue. At least four competing models have been proposed, each with support from recent studies in different species and behavioral settings (*Drosophila* courtship (McKellar et al., 2019), *Drosophila* grooming (Seeds et al., 2014), mouse learned lever presses (Murray and Escola, 2017), and zebrafinch singing (Long et al., 2010); different models summarized in (Seeds et al., 2014) and (McKellar et al., 2019)). For example, an excitatory synaptic chain mechanism is thought to underlie birdsong (Long et al., 2010), while a single-neuron ramp-to-threshold model has been proposed for *Drosophila* courtship, in which increasing thresholds of neuronal activity drive subsequent behaviors (McKellar et al., 2019). The particularities of each of these action sequences might necessitate different implementations, accounting for this diversity of findings (McKellar et al., 2019). Still, all previous studies remain limited with

regard to their access to comprehensive neuronal activity data. Only a small fraction of neurons residing in a single brain region are typically recorded in any given study. While manipulation experiments also inform these models, these are again limited to the targeted neuron type and brain region. These limitations are potentially severe, as recent studies suggest that behavior is encoded in a brain-wide manner (Ahrens et al., 2012; Musall et al., 2019; Stringer et al., 2019). Therefore, to ensure that the proposed model is not dependent on the neuron type or brain region examined, researchers should ideally take advantage of new technologies enabling brain-wide neuronal activity recordings (Ahrens et al., 2013; Schrödel et al., 2013). While these methodologies do have limitations, which are discussed below, they enable an unprecedentedly unbiased and comprehensive mapping of the neuronal dynamics driving action sequences.

3.3 Behavioral organization: Hierarchy

In his seminal analyses of animal behavior, Nikolaas Tinbergen hypothesized hierarchical organization as a fundamental principle of animal behavior (Tinbergen, 1951). Using the reproductive instinct of the three-spined stickleback as a model, he observed that specific sets of actions appear to be grouped together, in that they occur only in the context of a specific longer-lasting behavioral goal (Tinbergen, 1951). Different timescales of behavior therefore occupy different levels of the hierarchy: the stickleback's reproductive instinct lasts over several days and occupies the uppermost hierarchy level; fighting and nesting are behavioral programs within the reproductive instinct, and they occupy an intermediate hierarchy level; each of these behavioral programs consists of its own set of faster-timescale actions such as biting or digging, at the lowest hierarchy level (Fig. 1a) (Tinbergen, 1951). Importantly, this type of hierarchy is non-overlapping, meaning that no lower-level element is accessible via two different upper-level ones (each element has only one "boss" (Dawkins, 1976); Fig. 1a shows a non-overlapping hierarchy, Fig. 1b shows an overlapping hierarchy).

As a result, if the animal were to switch from biting (part of the fighting program) to digging (part of the nesting program), it would have to switch between the upper-level programs as well (Fig. 1a). This feature provides a testable prediction: if such a constraint were found to be common in the nervous system's implementation of behavior, it would provide strong evidence in favor of Tinbergen's hierarchy model.

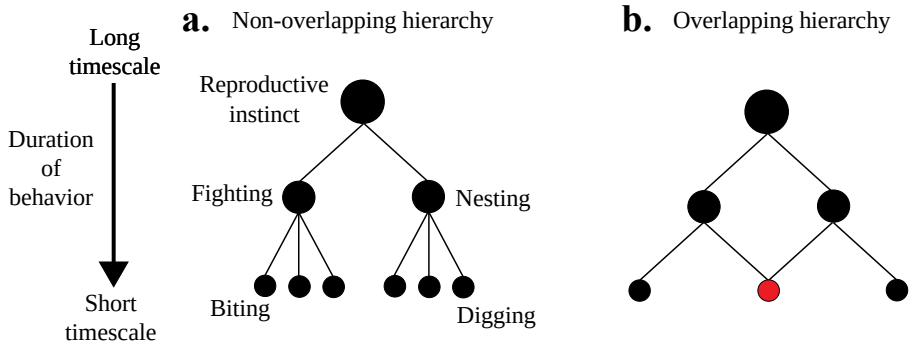

Figure 1. Hierarchical models of behavior. For both (a) and (b), circle size corresponds to relative behavioral timescale. (a) A non-overlapping hierarchy model, with behaviors labelled according to a subset of three-spined stickleback behaviors reported by (Tinbergen, 1951). (b) An overlapping hierarchy model, as distinguished by (Dawkins, 1976). The element colored red has two "hierarchs" or "bosses," making this an overlapping hierarchy model unlike that shown in (a).

Despite increasing behavioral evidence in favor of the hierarchy model, few neurophysiological investigations have directly addressed multi-timescale behavioral organization. Human language and birdsong exhibit clear hierarchical structures (Berwick et al., 2011; Glaze and Troyer, 2007), as does locomotory behavior in mouse (Markowitz et al., 2018), zebrafish (Marques et al., 2018), and *Drosophila* (Berman et al., 2016). However, only the study in *Drosophila* rigorously tested whether a hierarchical organization can better explain behavior compared to other models (Berman et al., 2016). More convincing evidence, such as a test of the aforementioned prediction, could come from neuronal activity recordings. One study identified a hierarchical relationship between breathing and whisking behavior in mice

and found that the brain regions driving these behaviors exhibit a unidirectional connection in accordance with hierarchical control (Moore et al., 2013). Studies in mice examining basal ganglia circuits delineated different timescale activity patterns coordinated with different behavioral timescales (Jin and Costa, 2015; Markowitz et al., 2018). Still, none of these studies showed how different activity patterns interact to coordinate behavior across timescales. Despite strong evidence for hierarchical structure in birdsong (Berwick et al., 2011; Glaze and Troyer, 2007), neurophysiological studies suggest a serial sequential encoding scheme (Long et al., 2010). One further complication is that these studies examined hierarchical organization between motor actions, whereas Tinbergen's original model described motor actions only at the lowest hierarchy level, with different behavioral "drives" at higher levels [in modern parlance, drives might be called behavioral programs (fighting, mating) or states (reproductive)]. It is easy to rule out non-overlapping hierarchies at levels "lower" than motor actions: for example, some of the same leg muscles may be used during both fighting and mating, so these muscles are accessible by two different upper-level states. Whether hierarchies organize motor actions, behavioral states, or both, however, remains unclear. Altogether, several fundamental gaps remain in our understanding of how behavior is organized across timescales, especially with regard to the most prominent model, the behavioral hierarchy.

3.4 Neuronal mechanisms: central pattern generators

Despite ethology's long-standing emphasis on organizational principles of behavior, neurophysiology has historically focused elsewhere. This was likely due to technical limitations. Early electrophysiological studies, such as the fundamental contributions of Hubel & Wiesel, were performed in anesthetized animals which lacked behavioral output, and were focused on neuronal responses to sensory inputs. While these studies revealed several foundational neuroscientific principles (see, for example (Hubel and Wiesel, 1962)), they left

animal behavior relatively unexamined. Other early researchers circumvented the need for anesthesia by removing parts of the nervous system from the animal completely, and recording from neurons *ex vivo* (Goulding, 2009; Marder and Bucher, 2001). These preparations, for example of cat spinal cord, miraculously produced dynamic nerve activity that resembled muscle activity during walking, including oscillatory patterns and coordination between nerves driving different limbs (Goulding, 2009). Thus it was discovered that mammalian locomotion is driven by a central pattern generator (CPG), a neuron or circuit that produces intrinsic activity that resembles patterns of behavior, even in the absence of sensory input (Marder and Bucher, 2001). CPGs have been demonstrated as a neuronal basis for other simple rhythmic behaviors in addition to mammalian locomotion, such as insect flight and mammalian breathing (Marder and Bucher, 2001). These results have demonstrated that the rhythms and patterns of muscle contraction typical of these behaviors do not require time-varying sensory feedback for their occurrence: even in isolated preparations lacking such feedback, activity patterns similar to behavioral patterns are produced (Marder and Bucher, 2001). Still, it is clear that sensory input has a strong effect on CPG output, because the frequencies and amplitudes of these behaviors are typically very different in isolated versus intact preparations (Marder and Bucher, 2001). For example, the cycle period is often strongly reduced in isolated preparations, by as much as an order of magnitude (Fox, 2006; Goulding, 2009). In many cases, experiments have shown that such differences are due to sensory effects such as proprioception (Ausborn et al., 2007; Marder and Bucher, 2001). Researchers studying CPGs have therefore been able to tease apart how network activity (in the isolated preparation) and sensory input (in the intact animal) each contribute to the behavior in question. As a result, CPGs have enabled perhaps the most comprehensive understanding to date of how neuronal dynamics drive behavior.

However, CPG mechanisms have so far been observed only for simple rhythmic behaviors. It remains unclear whether higher-order behavioral phenomena such as action sequences or multi-timescale organization might also be observed in preparations isolated from time-varying sensory input. Indeed, some models propose that sensory input is a key determinant in action sequence progression (Seeds et al., 2014), precluding the involvement of CPG-like mechanisms. If, however, some components of higher-order behavioral organization were indeed found observable in the absence of sensory input, then, as with CPGs, researchers could examine the underlying neuronal circuit interactions that produce the organization separately from the influence of sensory input. CPG research could therefore provide a roadmap toward a deeper understanding of neuronal mechanisms underlying higher-order behavioral organization (Yuste et al., 2005).

3.5 Neuronal mechanisms: population dynamics

With the development of technology to record neuronal activity in behaving animals, more complex relationships between neurophysiology and behavior were observed. O'Keefe reported the discovery of place cells, a class of neurons in the hippocampus identifiable by their activity during behavior (O'Keefe, 1976). Recorded as rats explored a behavioral arena, these neurons became active only when the animal is located at a particular position in space (O'Keefe, 1976). This not only revealed that individual neurons can represent high-level behavioral parameters like location, but also that crucial information exists at the level of the neuronal population. Because each place cell fired only at a small restricted location in the arena, the experimenter could read out the animal's position only when several place cells coding for different locations were co-recorded. Likewise, any downstream brain area concerned with the animal's position would need to receive information from the population of place cells. The crucial role of population coding for behavior became more apparent with

analyses of primate motor cortex activity during goal-directed reaching, by Georgopolous and colleagues (Georgopoulos and Carpenter, 2015). While individual neurons represented particular reach directions, only with the activity of several neurons at once, summarized by the "population vector," could the animal's reach direction be precisely decoded (Georgopoulos and Carpenter, 2015). These early studies therefore demonstrated that insight into brain function would come not only from recording the activity of individual neurons during behavior, but also from recording many of them.

As researchers began recording populations of neurons simultaneously, it became clear that population activity is more than simply a combination of signals representing, for example, different reach directions or locations in space. Rather, neurons share a lot of information, tending to covary in time on a single-trial basis. One particularly pioneering study was in the leech, where Briggman and colleagues were able to record from intact ganglia using a voltage-sensitive optical dye in an *ex vivo* preparation (Briggman, 2005). In response to an electrical stimulation, the ganglia would stochastically generate either a swim-like or crawl-like activity pattern. The authors asked whether single-cell or population-level analyses could better predict the outcome of this behavioral "choice." To analyze population activity, they used principal components analysis (PCA), a dimensionality reduction technique that uses co-variations between the activity of co-recorded neurons to find latent dimensions (shared activity patterns); the resulting dimensions are ranked according to the percentage of variance in the data that they explain. Using only the three highest-ranked dimensions, they found that this population-level information could predict behavioral choice well in advance of information from any single cell alone. Crucially, they then tested the hypothesis that this population-level information was more relevant than any single-cell information: they manipulated a neuron that did not show an early (relative to other cells) discrimination of behavioral choice, but still contributed strongly to the population-wide dynamics. This manipulation biased behavioral

choice, whereas manipulating neurons that did show early discrimination of behavioral choice did not affect behavior. This suggested that these latter neurons were perhaps only early readouts of the population-wide activity, whose evolution was the more relevant factor (Briggman, 2005). Another study used PCA to analyze motor cortex activity in primates during reaching, and similarly found that shared low-dimensional activity patterns best described the behavior (Churchland et al., 2012). As neuronal population recording and analysis techniques have become more widely available, low-dimensional representations have been observed underlying diverse behaviors (Ahrens et al., 2012; Allen et al., 2019; Bruno et al., 2015; Stringer et al., 2019). However, few studies have yet examined how neuronal population dynamics underlying these individual behaviors are coordinated into the types of higher-order organizations described above.

3.6 *C. elegans* as a model organism for neuroscience research

Since its establishment as a model organism in the 1960s, by Sydney Brenner, the nematode worm *Caenorhabditis elegans* has been used to unveil several fundamental principles of biology. It has extremely diverse utility, illustrated well by the three Nobel prizes that have been awarded for *C. elegans* research: (1) organ development and programmed cell death (2002), (2) the discovery of RNA interference (2006), and (3) the development of GFP as a genetic research tool (2008). Brenner chose *C. elegans* specifically as a model for both development and neuroscience research (Wood and researchers, 1988). While neuroscience research in *C. elegans* has led to the discovery of several highly conserved genes and associated molecular mechanisms (e.g. synaptic release machinery (Barclay et al., 2012)), and has yielded the first and most complete connectome to date (White et al., 1986), a unified understanding of the worm's nervous system function at the level of animal behavior remains elusive. This underscores the difficult questions that face neuroscience as a whole. In mammalian

neuroscience, for example, several active areas of research, such as cell type classification and structural connectivity, have been essentially solved in the worm: every cell type has been identified and classified, and all connections have been mapped. The worm's nervous system and its behavior are less complex than most other animals, especially mammals, arguably by orders of magnitude. Remarkably, despite all these advantages, how the worm's nervous system generates its behavior remains largely unclear.

Brenner's choice was carefully considered, resulting in a model system particularly well-suited for experimentation in the newborn age of molecular biology. *C. elegans* is 1mm long as an adult and has an extremely fast generation time of only about three days. A single hermaphrodite produces hundreds of offspring, enabling experiments with very high statistical power. *C. elegans* has extreme numerical simplicity at the cellular level: the hermaphrodite is made up of only 959 cells, 302 of which are neurons; each cell has been given an identity and can be found with little to no variation in every wild-type animal (Sulston and Horvitz, 1977). Transgenes are easily produced by gonad injection, using enhancer or promoter elements targeting specific neuron classes cloned upstream of effector genes. In standard laboratory conditions, only a fraction of a percent of animals are males (the rest are hermaphrodites), yet this fraction can be increased by various methods to enable crosses. Finally, the worm's transparence makes it ideal for optical tools such as calcium indicators. Altogether, these features make *C. elegans* a premier model organism for modern experimental neuroscience research.

3.7 The *C. elegans* nervous system

The *C. elegans* hermaphrodite nervous system consists of 302 neurons split into 118 identifiable cell classes. All of the synapses between these neurons, and between the neurons and muscles, have been mapped by electron microscopy (White et al., 1986); this includes 6393

chemical synapses, 890 gap junctions, and 1410 neuromuscular junctions (Varshney et al., 2011). While this unique dataset is rich in useful information, at least two important issues preclude a more complete understanding of neuronal mechanisms in the worm. First, the signs of the chemical synapses, whether excitatory or inhibitory, are not known; there is also evidence that gap junctions can act in a rectifying, i.e. directional manner (Liu et al., 2017; Marder, 2009). Efforts to ameliorate this issue have been made, especially by the Hobert lab, which has mapped the neurotransmitter identities based on gene expression data (see, for example, (Gendrel et al., 2016)). Still, gene expression data must be complemented with functional studies to understand the impact of an upstream neuron on a downstream neuron. A second issue is that neuropeptides and neuromodulators (e.g. dopamine, serotonin) have been shown to act extrasynaptically, in the worm as well as in other organisms (Bentley et al., 2016). These signaling molecules form an extrasynaptic network perhaps as complex as the synaptic connectome, including ~250 predicted neuropeptides and ~100 receptors, several of which have been shown to exert strong behavioral effects (e.g. (de Bono and Bargmann, 1998)) (Bentley et al., 2016). Further, the extrasynaptic connectome has been shown to be mostly orthogonal to the synaptic connectome (Bentley et al., 2016). The functional timescales and effects of these extrasynaptic connections remain to be explored. Any network-level model of *C. elegans* nervous system function based on current data is therefore necessarily impoverished.

While the known connectome can and does act as an invaluable resource, its utility is often limited to one- or two-step connections rather than large-scale pathways for information relay. This is due to the high degree of recurrency in the worm connectome, providing many possible paths by which neurons can impact one another (Varshney et al., 2011). Despite this complexity, a few general principles of the worm's nervous system organization are apparent. Nearly all neurons can be classified as sensory neuron, motor neuron, or interneuron (Varshney

et al., 2011). Sensory neurons are defined either by the presence of anatomical features such as processes to sensory sites at the worm's nose or tail, or by functional evidence, while motor neurons are defined by the presence of neuromuscular junctions (Varshney et al., 2011). Any non-sensory and non-motor neuron is referred to as an interneuron. It is important to note that many motor neurons synapse not only onto muscle but also onto other motor neurons, and in some cases onto interneurons as well. This raises the possibility that individual neurons in the compact *C. elegans* nervous system might be capable of a high degree of multifunctionality, e.g. acting as both motor neurons and interneurons. Another feature of the nervous system is that eight motor neuron classes each consist of between six and 15 anatomically similar individual neurons; these classes are repeated throughout the body of the worm in an iterated fashion, defining functional segments of motor control along the worm's body (Haspel and O'Donovan, 2011). These 75 total motor neurons reside in the ventral nerve cord (VNC) and target either ventral or dorsal body wall muscle, but not both. Worms lie on their left or right sides and move primarily along their dorsal/ventral body axis. Several additional motor neuron classes in the head target specifically head muscle, and allow for movement on the left/right body axis as well as the dorsal/ventral axis (Kwon et al.; 2013; Shaw et al., 2018).

The majority of the rest of the worm's neurons, including most sensory and interneurons, have their cell bodies located in the head. Strikingly, just five interneuron classes in the head (ten individual neurons) are responsible for the vast majority (83.4%) of synapses onto the most functionally important motor neuron classes in the VNC (VB, DB, VA, and DA motor neurons; synapses onto these neurons by other VNC motor neurons were excluded in this count). These five interneurons (AVA, AVB, AVD, AVE, and PVC) therefore represent a significant bottleneck in the crucial connection between the highly recurrent interneuron network in the head and the iterated motor control network in the body. They are therefore referred to as "command" or "pre-motor" interneurons by much of the literature to date. In a

recent peer-reviewed opinion article, my colleagues and I argued that "pre-motor" is a more appropriate title for these neurons, partially based on findings presented in this thesis (see section 6.2). The pre-motor interneurons' primary role in locomotion has been confirmed several times over by a variety of experimental approaches (Chalfie et al., 1985; Gray et al., 2005; Kawano et al., 2011; Piggott et al., 2011; Rakowski et al., 2013; Roberts et al., 2016; Tsalik and Hobert, 2003).

3.8 Neuronal mechanisms underlying behavior in *C. elegans*

C. elegans locomotion behavior consists of dorso-ventral rhythmic undulatory bends, which propagate from head to tail during forward locomotion and from tail to head during reverse locomotion. The frequencies and durations of forward and reverse locomotion periods are highly flexible depending on internal state and environmental conditions (see, for example, (Ben Arous et al., 2009; Gray et al., 2005; Luo et al., 2014b; Skora et al., 2018)). The work presented in this thesis primarily focused on animals that have recently been removed from their food source, and are thus in an exploratory search mode in which forward locomotion predominates, with reversals occurring once every ~15 seconds and lasting ~3 seconds each. However, even in this particular setting, these behaviors occur in a stochastic manner, such that both much longer and much shorter forward and reverse periods can be observed (Roberts et al., 2016). A third discrete behavior type that has been described is the omega turn, in which the worm's body curves into the shape of the Greek letter omega, thus causing a large reorientation; omega turns typically follow reversals (Gray et al., 2005). However, whether omega turns are truly a discrete behavior type or simply the extreme end of a continuum of possible turn angles remains unclear (Broekmans et al., 2016; Donnelly et al., 2013; Hums et al., 2016). Altogether, forward locomotion, reverse locomotion, and turn maneuvers enable the worm to navigate its environment, for example to find food or avoid predators. Additional

details of these behaviors, such as differences in forward locomotion speed or steering, are also used for navigation and are discussed below.

Significant progress has been made in understanding how forward and reverse locomotion behaviors are generated and coordinated across the worm's body. Different sets of VNC neurons and upstream pre-motor interneurons have been specifically implicated in either forward or reverse locomotion (Chalfie et al., 1985; Gray et al., 2005; Kawano et al., 2011; Wicks et al., 1996). Based on anatomy and laser ablation studies, it was found that DB and VB neurons drive dorsal and ventral bending respectively, specifically during forward locomotion, while DA and VA neurons drive dorsal and ventral bending during reverse locomotion (Chalfie et al., 1985; Wicks et al., 1996). As mentioned above, the five pre-motor interneurons form a connectivity bottleneck between head ganglia neurons and these VNC motor neurons: DB and VB motor neuron classes receive most of their input from pre-motor interneurons AVB and PVC, while DA and VA classes receive input primarily from AVA, AVD, and AVE. One particularly elegant study showed that the antagonistic control of forward versus backward locomotion requires intact gap junction communication between these pre-motor interneurons and their respective motor neuron classes, such that the two pools of neurons maintain imbalanced activity during locomotion in either direction (Kawano et al., 2011). Using genetically encoded calcium indicators, this study provided clear neuronal activity evidence that forward and reverse locomotion programs are implemented by a flip-flop-like mechanism, with heightened activity in either the forward or reverse pre-motor interneuron classes as well as the respective motor neurons themselves (Kawano et al., 2011). Two major questions remained: (1) how are these locomotory programs implemented at the level of individual bends coordinated across the body? and (2) how is the frequency of flip-flops between these programs controlled to enable e.g. chemotactic behaviors?

Both forward and reverse locomotion consist of rhythmic body bends, with forward locomotion bends propagating from head to tail and reverse locomotion bends propagating from tail to head. Rhythmic locomotory behaviors are typically driven by CPGs (see section 3.4); however, only very recently have experiments been undertaken to identify CPGs for *C. elegans* locomotory programs. One study found rhythmic activity patterns under various immobilized animal conditions in a posterior A-class motor neuron, which may be responsible for generating individual bends during reverse locomotion (Gao et al., 2018). For forward locomotion, such neuronal activity evidence is lacking. In a series of careful laser ablation and optogenetic experiments, one study showed that different parts of the worm's body can simultaneously show bending oscillations at different frequencies if communication through intervening segments is disrupted (Fouad et al., 2018). B-class motor neurons (B-MNs, including both DB and VB classes) appear responsible for driving at least some of these bending patterns, while the authors also posit an additional non-B-MN oscillator in the worm's head (Fouad et al., 2018). However, all oscillations observed in this study could be the product of a reflex chain mechanism, whereby proprioception is responsible for the rhythmic bending pattern rather than internally generated CPG activity. The crucial missing evidence for a forward locomotion CPG is rhythmic activity patterns in immobilized animals that resemble the same neurons' activity patterns during locomotion. Evidence for such activity in immobilized animals, specifically in the SMDs, a head motor neuron class, has been shown in an earlier study (Hendricks et al., 2012), however the authors did not explore whether the SMDs may indeed act as CPGs for specific behaviors. In the absence of more complete evidence, it remains possible that proprioception plays an indispensable role in *C. elegans* forward locomotion. Proprioceptive signals have been reported in the B-MNs (Wen et al., 2012), the SMDs (Yeon et al., 2018), and the highly connected interneuron DVA (Li et al., 2006b). It is likely that these signals are important for coordinating bending across the worm's

body, and indeed the proprioceptive B-MN signals are capable of doing so in some settings (Wen et al., 2012). However, how the motor system of the worm integrates local proprioceptive signals into coordinated locomotion across its entire body remains unclear. Altogether, the generation of body bending by either CPG elements or proprioceptive mechanisms, as well as the coordination of bending across the body, remain important future directions.

Finally, sensorimotor integration in *C. elegans* could potentially serve as a model for neuronal computations (Lockery, 2011). The worm efficiently performs chemotaxis to a variety of cues, which requires the continuous integration of sensory and motor information, both time-varying as the animal moves in a sensory gradient (Chalasani et al., 2007; Gabel et al., 2007; Gray et al., 2004; Iino and Yoshida, 2009; Pierce-Shimomura et al., 1999). The worm employs several behavioral strategies for chemotaxis. By varying the frequency of stochastically occurring reverse-and-turn events according to the change in sensory input, the worm implements a biased random walk strategy: with increasing concentration of an attractant, reversal frequency is reduced, and vice versa, with decreasing attractant concentration, reversal frequency is increased (Pierce-Shimomura et al., 1999). Indeed, reversal frequency is strongly modulated by a variety of sensory cues, either in a gradient or when presented as step changes, in line with this model (Chalasani et al., 2007; 2010; Luo et al., 2014b; Pierce-Shimomura et al., 1999; Zimmer et al., 2009). Therefore, one primary question is how the nervous system uses sensory input to control reversal frequency. A large body of literature has suggested or identified transformations of sensory information between sensory neurons and so-called "first-layer" or "second-layer interneurons," one or two synapses downstream of the sensory neuron (Chalasani et al., 2007; 2010; Clark et al., 2006; Gabel et al., 2007; Gray et al., 2005; Guillermin et al., 2017; Iino and Yoshida, 2009; Larsch et al., 2015; Oda et al., 2011; Tsalik and Hobert, 2003). However, other studies have reported that these same neurons show activity changes tightly coordinated with behavior (Laurent et al., 2015; Li

et al., 2014; Luo et al., 2014b; Piggott et al., 2011), and one study reported coordinated activity changes across the pre-motor interneuron AVA and first- and second-layer interneurons AIB and RIM (Gordus et al., 2015). The computations identified in the first set of studies were largely either inferred by laser ablation or determined by neuronal activity recordings in immobilized animals; how such computations occur in the context of neurons that are strongly modulated by ongoing activity patterns during behavior remains unclear.

A similar issue has arisen regarding a different behavioral strategy the worm uses for chemotaxis, termed weathervaning. Specifically within forward locomotion periods, worms can make curved trajectories to steer toward an attractant sensory cue (Iino and Yoshida, 2009). This steering is implemented by a head-bend bias, either dorsal or ventral. As for other neurons in the aforementioned studies, it was found that the interneuron RIA shows signals relating to both sensory and motor information; however, in RIA, these signals are compartmentalized along the neuronal process (Hendricks et al., 2012). Whether such compartmentalization occurs in the interneurons implicated in reversal frequency control has not been systematically examined. A genetically encoded calcium indicator revealed that RIA's motor signals correlate with the instantaneous head-bend angle of the worm, with dorsal and ventral bending showing positive correlations with signals from different regions of the RIA process (Hendricks et al., 2012). Changes in concentration of the attractant isoamyl alcohol induce changes in activity in a third region of RIA's process (Hendricks et al., 2012). An elegant follow-up study examined this compartmentalization in the context of chemotaxis: the authors showed that weathervaning can be implemented by sensory suppression of RIA motor-related activity, reducing RIA's inhibition onto head motor neurons, thus enabling stronger head-bending in the direction of the odor (Liu et al., 2018). Together, these studies provide a detailed understanding of one way in which the worm implements weathervaning. One important lesson from these studies can be applied to the more confusing case of reversal frequency control. Crucial to understanding the

interplay of RIA sensory and motor signals was an examination of RIA activity in a no-odor condition, in comparison to the odor condition. RIA's pure motor signals would be difficult to distinguish from sensory signals in a gradient environment where head-bend oscillations are tightly coupled to sensory input oscillations. The work in this thesis similarly benefits from examining motor-related signals in the absence of sensory stimuli, prior to examining how any ongoing motor-related activity interacts with sensory signals; it would be prudent for future work on *C. elegans* interneurons to follow these examples (Kaplan et al., 2018).

3.9 Behavioral organization in *C. elegans*

The organization of behavior in *C. elegans* is an active topic of research, with several interesting findings but no consensus. Two major efforts have examined worm behavior in constant environments, both with and without food present (Brown et al., 2013; Stephens et al., 2008). Quantifications of worm body posture timeseries have led, on one hand, to the conclusion that worm behavior is highly low-dimensional (Stephens et al., 2008), and on the other hand, to a large database of diverse worm behaviors (Brown et al., 2013; Yemini et al., 2013). While these results are not necessarily in direct disagreement with one another, due to the different methods used, it is clear that the field is far from a consensus on the most relevant description of behavior. Ultimately, a satisfying description of behavior should reveal plainly the knobs of control that the nervous system uses to engage with its environment. Therefore, beyond pure analysis of behavioral data, joint inference of behavior and accompanying neuronal activity patterns is one way forward (Brown and de Bivort, 2018). In the work presented in this thesis, my colleagues and I have taken this type of approach, letting neuronal activity patterns guide us to relevant descriptions of behavior.

The two types of behavioral organization described above, action sequences and multi-timescale hierarchies, have partially been described thus far in *C. elegans*. However, several

aspects of both types of organization remain ambiguous. First, while it is clear that switches between reverse and forward locomotion are important, two behaviors hardly constitute an "action sequence." The omega turn represents a third behavior, and interestingly, reversals are only occasionally followed by omega turns (Gray et al., 2005). This suggests a behavioral choice point at the end of the reversal, where the action sequence can proceed to an omega turn or not. Altogether, the worm engages in a cyclical action: sequence of forward – reverse – omega turn – forward (Donnelly et al., 2013; Pirri et al., 2009). However, as mentioned above, it remains unclear whether omega turns are truly discrete behaviors, or simply part of a continuum of turn angles. Second, *C. elegans* behavior has indeed been described on a variety of interacting timescales. Forward and reverse locomotion each consist of faster-timescale body bending behaviors. Slower timescale modulations of forward speed and reversal frequency are also commonly reported, for example during roaming and dwelling switches (Ben Arous et al., 2009) or the switch from local to global search strategies (Calhoun et al., 2014; Gray et al., 2005). While worm behavior is clearly modulated across multiple timescales, how these different timescales of behavior are organized with respect to one another remains an open question. One analysis of behavior has indeed hinted at a hierarchical organization of worm body postures (Gomez-Marin et al., 2016). As mentioned above, our approach has been to let neuronal activity recordings guide us toward more concrete descriptions of sequenced and multi-timescale behavior, ultimately allowing for both a description of behavior that is clearly relevant to nervous system control, as well as an account of underlying neuronal mechanisms.

3.10 Neuronal activity imaging techniques in *C. elegans*

C. elegans is especially amenable to modern optical techniques for recording neuronal activity, thanks to its genetic tractability and its transparency. Transgenic animals expressing

genetically encoded calcium indicators such as GCaMP (Chen et al., 2013; Nakai et al., 2001) are quickly and easily produced, and they can be imaged through the transparent cuticle without the need for surgery. Further, *C. elegans* neurons are mostly non-spiking, so the graded signals obtained using such indicators are perhaps more faithful representations of underlying electrical activity and synaptic release compared to recordings in spiking neurons. Early developments in *C. elegans* optical recording techniques included the development of microfluidic devices to hold the worm in place and provide tight control over sensory cues such as odors or atmospheric gases (Chronis et al., 2007; Zimmer et al., 2009). These recordings are often combined with a paralytic agent such as tetramisole, an acetylcholine receptor agonist that contracts the worm's muscles so that it remains almost completely immobile. Whether tetramisole affects neuronal dynamics via its drug action (i.e. beyond its immobilizing effects) remains unclear. Several groups have also developed methods enabling optical recordings in moving animals (Clark et al., 2007; Collins and Koelle, 2013; Faumont et al., 2011; Kawano et al., 2011; Larsch et al., 2013; Laurent et al., 2015; Li et al., 2014; Liu et al., 2018; Luo et al., 2014a; Nguyen et al., 2016; Piggott et al., 2011; Venkatachalam et al., 2016). These recordings are typically performed in animals moving between an agar surface and a coverglass, though some have made recordings of animals in microfluidic devices with pillars allowing movement, or open agar plates.

One major recent development in neuronal activity imaging is the advent of whole-brain calcium imaging (Schrödel et al., 2013). In this study, a nuclear-localized GCaMP was developed and employed to enable segmentation of individual neurons during data analysis. This enabled the simultaneous recording of dozens of ~70% of head ganglia neurons with single-cell resolution at ~5 Hz. The authors confirmed the efficacy of nuclear-localized GCaMP, compared to signals recorded from the soma with cytoplasmic GCaMP, using sensory responses in two neuron classes. These experiments confirmed that nuclear localization caused

only slight alterations in signal dynamics and amplitudes, at least for the neurons tested. The authors reported correlated dynamics across interneuron and motor neuron classes, the function of which awaited further testing, which is partly presented in this thesis. Two later studies demonstrated brain-wide imaging in freely moving animals (Nguyen et al., 2016; Venkatachalam et al., 2016), though results from these methods remain so far largely unreported (except for (Scholz et al., 2018), discussed below). As mentioned above, the RIA interneuron acts via signals compartmentalized within its neuronal process; such signals, which have also been reported for other behaviorally relevant interneurons such as AIY, are not captured by current whole-brain imaging approaches measuring activity in the soma or nucleus. Despite this fundamental limitation, whole-brain imaging is a major technical advance and has enabled several important discoveries (Nichols et al., 2017; Skora et al., 2018), some of which are discussed below.

3.11 Aims of the study

The work presented in this thesis aims to provide an understanding of behavioral organization in *C. elegans*, for both an action sequence (Article 1) and a behavioral hierarchy (Article 2), in terms of underlying neuronal dynamics. Beyond the importance of such behavioral organization (described in sections 3.1-3.3), my colleagues and I have come to appreciate the need for understanding ongoing neuronal dynamics prior to the analysis of how these dynamics interact with sensory stimuli (Kaplan et al., 2018). Because these ongoing dynamics strongly relate to behavior in the worm, a thorough investigation of their coordination in the context of behavioral organization is essential. Both Article 1 and Article 2 are efforts in this direction. A strikingly similar conclusion was recently reached by researchers working in mice, who uncovered a brain-wide encoding of multiple behavioral variables during spontaneous behavior as well as task performance or visual stimulation (Musall et al., 2019;

Stringer et al., 2019). These dynamics are much higher-dimensional than those observed in *C. elegans*, and therefore less straightforwardly understood (Stringer et al., 2019). Thus, the efforts presented in this thesis toward understanding the structure of ongoing dynamics, their relationship to behavior, and their interaction with sensory stimulation have the potential to forge a path forward for neuroscience research more broadly.

My first aim was to understand how the worm's major motor commands are organized into an action sequence by its neuronal activity patterns. In Article 1, my colleagues and I investigated the ongoing brain-wide dynamics reported in (Schrödel et al., 2013) and their relationship to the *C. elegans* action sequence. As mentioned above, we were guided by our whole-brain neuronal activity data toward an understanding of the behavioral variables the nervous system is concerned with. As a result, we proposed a new characterization of the worm's post-reversal turn: we observed a bifurcation in brain-wide dynamics at the end of reversal command periods, such that head-bends occurred either in a ventral or dorsal direction, potentially leading to large reorientations like omega turns. We found that this cyclical action sequence, forward – reverse – dorsal/ventral turn – forward, is encoded in low-dimensional population dynamics spread across the worm's interneurons and motor neurons. We showed that the most interconnected neuron in the worm's brain, the pre-motor interneuron AVA, previously thought to be the primary generator of reversals, is in fact not required for the generation of the reversal motor command. Finally, we investigated how a salient sensory input interacts with these dynamics to cause changes in reversal frequency. We found that the brain-wide dynamics are robust to stimulation, failing to show anything beyond subtle quantitative changes, despite modulations of reversal command frequency. Thus, we concluded that the worm's action sequence is embedded in global brain dynamics as a motor command sequence; these coordinated dynamics persist both in the absence of movement, reminiscent of CPGs for simple, rhythmic behaviors, as well as in response to a salient acute sensory input.

My second aim was to test Tinbergen's long-standing hierarchical model for multi-timescale behavior. In Article 2, I first identified a three-level, non-overlapping hierarchy in *C. elegans* that described how behaviors are coordinated across three timescales. This hierarchy obeyed the aforementioned prediction, in which switches between lower-level behaviors with different "hierarchs" requires switching at the upper level. My colleagues and I next aimed to demonstrate how this hierarchical organization is encoded in the neuronal dynamics underlying the behaviors. We first sought to identify neurons specifically responsible for driving each behavior; in doing so, we found strong evidence in favor of B-MNs and SMD neurons as CPG components for two different types of forward state locomotory maneuvers. We then showed that these neurons' activity patterns are strictly nested within one another, with faster-timescale oscillations occurring within specific phases of slower-timescale dynamics; this nesting enforced the hierarchical behavioral relationships we observed. Importantly, these nested patterns were found even in immobilized animals, indicating that they are the product of neuronal circuit interactions. Thus, the worm's nervous system produces dynamics that implement a behavioral hierarchy, providing crucial evidence in favor of Tinbergen's decades-old model.

4. Article 1: Global brain dynamics embed the motor command sequence of *Caenorhabditis elegans*

Status: published article

2015 in Cell 163, 1-50 doi: 10.1016/j.cell.2015.09.034

Authors: Saul Kato*, Harris S. Kaplan*, Tina Schrödel*, Susanne Skora, Theodore H. Lindsay, Eviatar Yemini, Shawn Lockery, and Manuel Zimmer

*Co-first authors

Contributions: S.K. designed experiments, developed analytical methods for whole-brain imaging datasets, and analyzed data. H.S.K. designed experiments, generated transgenic strains, performed Ca^{2+}-imaging experiments in freely moving an- imals, developed analytical methods, and analyzed data. T.S. designed experiments, generated transgenic strains, performed whole-brain imaging experiments, and analyzed data. S.S. performed population behavioral re- cordings and analyzed data. T.H.L. and S.L. performed electrical recordings; E.Y. wrote code for behavioral analysis; and M.Z. designed experiments, developed analytical methods, and led the project. S.K., H.S.K., T.S., and M.Z. wrote the manuscript.

Article

Cell

Global Brain Dynamics Embed the Motor Command Sequence of *Caenorhabditis elegans*

Graphical Abstract

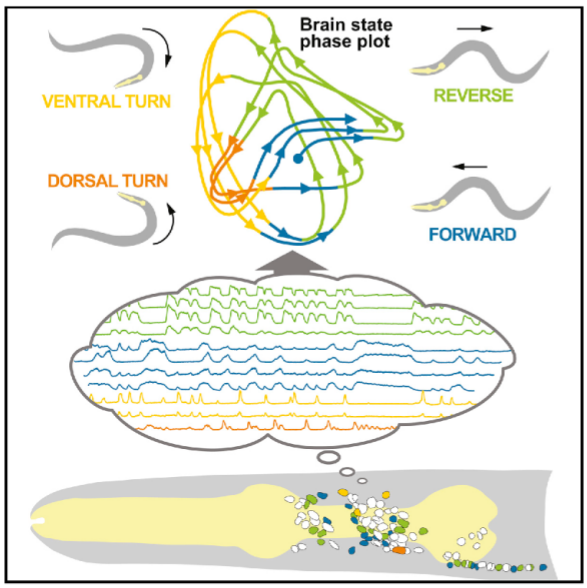

Authors

Saul Kato, Harris S. Kaplan, Tina Schrödel, ..., Eviatar Yemini, Shawn Lockery, Manuel Zimmer

Correspondence

zimmer@imp.ac.at

In Brief

Simultaneously recording the activity of nearly all neurons in the *C. elegans* brain reveals that most active neurons share information by engaging in coordinated, dynamical network activity that corresponds to the sequential assembly of motor commands.

Highlights

- Most active neurons in the brain participate in coordinated dynamical activity
- Smooth, cyclical dynamics continuously represent action sequences and decisions
- Internal representation of behavior persists when decoupled from its execution
- Brain dynamics provide a robust scaffold for sensory-driven action selection

Kato et al., 2015, Cell *163*, 1–14
October 22, 2015 ©2015 Elsevier Inc.
http://dx.doi.org/10.1016/j.cell.2015.09.034

CellPress

Please cite this article in press as: Kato et al., Global Brain Dynamics Embed the Motor Command Sequence of *Caenorhabditis elegans*, Cell (2015), http://dx.doi.org/10.1016/j.cell.2015.09.034

Article

Global Brain Dynamics Embed the Motor Command Sequence of *Caenorhabditis elegans*

Saul Kato,[1,4] Harris S. Kaplan,[1,4] Tina Schrödel,[1,4] Susanne Skora,[1] Theodore H. Lindsay,[2,5] Eviatar Yemini,[3] Shawn Lockery,[2] and Manuel Zimmer[1,*]
[1]Research Institute of Molecular Pathology IMP, Vienna Biocenter VBC, Dr. Bohr-Gasse 7, 1030 Vienna, Austria
[2]Institute of Neuroscience, University of Oregon, Eugene, OR 97403, USA
[3]Department of Biochemistry and Molecular Biophysics, Howard Hughes Medical Institute, Columbia University Medical Center, New York, NY 10032, USA
[4]Co-first author
[5]Present address: Division of Biology and Biological Engineering, California Institute of Technology, Pasadena, CA 91125, USA
*Correspondence: zimmer@imp.ac.at
http://dx.doi.org/10.1016/j.cell.2015.09.034

SUMMARY

While isolated motor actions can be correlated with activities of neuronal networks, an unresolved problem is how the brain assembles these activities into organized behaviors like action sequences. Using brain-wide calcium imaging in *Caenorhabditis elegans*, we show that a large proportion of neurons across the brain share information by engaging in coordinated, dynamical network activity. This brain state evolves on a cycle, each segment of which recruits the activities of different neuronal sub-populations and can be explicitly mapped, on a single trial basis, to the animals' major motor commands. This organization defines the assembly of motor commands into a string of run-and-turn action sequence cycles, including decisions between alternative behaviors. These dynamics serve as a robust scaffold for action selection in response to sensory input. This study shows that the coordination of neuronal activity patterns into global brain dynamics underlies the high-level organization of behavior.

INTRODUCTION

Behavior is composed of individual motor actions and motifs, such as limb movements or gaits, which do not achieve organismal goals unless they are orchestrated into longer-lasting action sequences and behavioral strategies, like navigation, grooming, or courtship (Anderson and Perona, 2014; Gray et al., 2005; Seeds et al., 2014). Ethologists often make quantitative descriptions of this higher-level organization using state transition diagrams, consisting of distinct, repeatable high-level motor states and switches between them (Anderson and Perona, 2014). The brain's representation of behavior must account for both detailed metrics of individual actions (e.g., strength and extent of movement or speed of gait), as well as for their higher level orchestration. Identifying how these aspects of behavior correspond to measurable neural activity is a necessary step toward understanding how the brain encodes and produces behavior. Recent studies in invertebrate motor ganglia and mammalian cortex show that selection, execution, and shaping of motor programs correspond to neural activity patterns across large neuronal populations. These studies show that, despite the participation of hundreds of sampled neurons, their activity is coordinated, and meaningful signals can thus be reduced to far fewer dimensions. Moreover, neuronal populations encode information dynamically (Briggman et al., 2005; Bruno et al., 2015; Churchland et al., 2012; Cunningham and Yu, 2014; Harvey et al., 2012; Jin et al., 2014; Mante et al., 2013). For practical reasons, recordings in these studies have been performed over short intervals that encompass individual motions or brief behavioral tasks. Hence, the neuronal mechanisms that govern the continuous control of behavior and its time course, encompassing long-lasting and repeated action sequences, remain enigmatic. Furthermore, approaches have been typically limited by the need to average across trials or to sub-sample from local brain regions or motor ganglia. Recently, the first brain-wide single-cell-resolution functional imaging studies, in zebrafish and fly larvae and adult *C. elegans*, revealed motor-related population dynamics correlated across distant brain regions. These data suggest that behaviorally relevant neural representations might occur at the level of global population dynamics and highlight the benefit of brain-wide sampling (Ahrens et al., 2012, 2013; Lemon et al., 2015; Panier et al., 2013; Prevedel et al., 2014; Schrödel et al., 2013).

The nematode *C. elegans* is an attractive model system to address these problems, due to its stereotypic nervous system of just 302 identifiable neurons grouped into 118 anatomical symmetry classes (White et al., 1986). However, prior to the availability of whole-brain imaging, past studies had not explored distributed or population dynamics in *C. elegans*. Instead, identified interneurons and pre-motor neurons have been described as dedicated encoders of specific sensory inputs or motor outputs and are commonly placed in a context of isolated sensory-to-motor pathways (see the following references for examples: Chalasani et al., 2007; Donnelly et al., 2013; Gray et al., 2005; Ha et al., 2010; Iino and Yoshida, 2009; Kimata et al., 2012). However, these pathways largely overlap and are embedded in a horizontally organized and recurrently connected neuronal wiring diagram (Varshney et al., 2011; White et al., 1986). Moreover, recent functional imaging

Please cite this article in press as: Kato et al., Global Brain Dynamics Embed the Motor Command Sequence of *Caenorhabditis elegans*, Cell (2015), http://dx.doi.org/10.1016/j.cell.2015.09.034

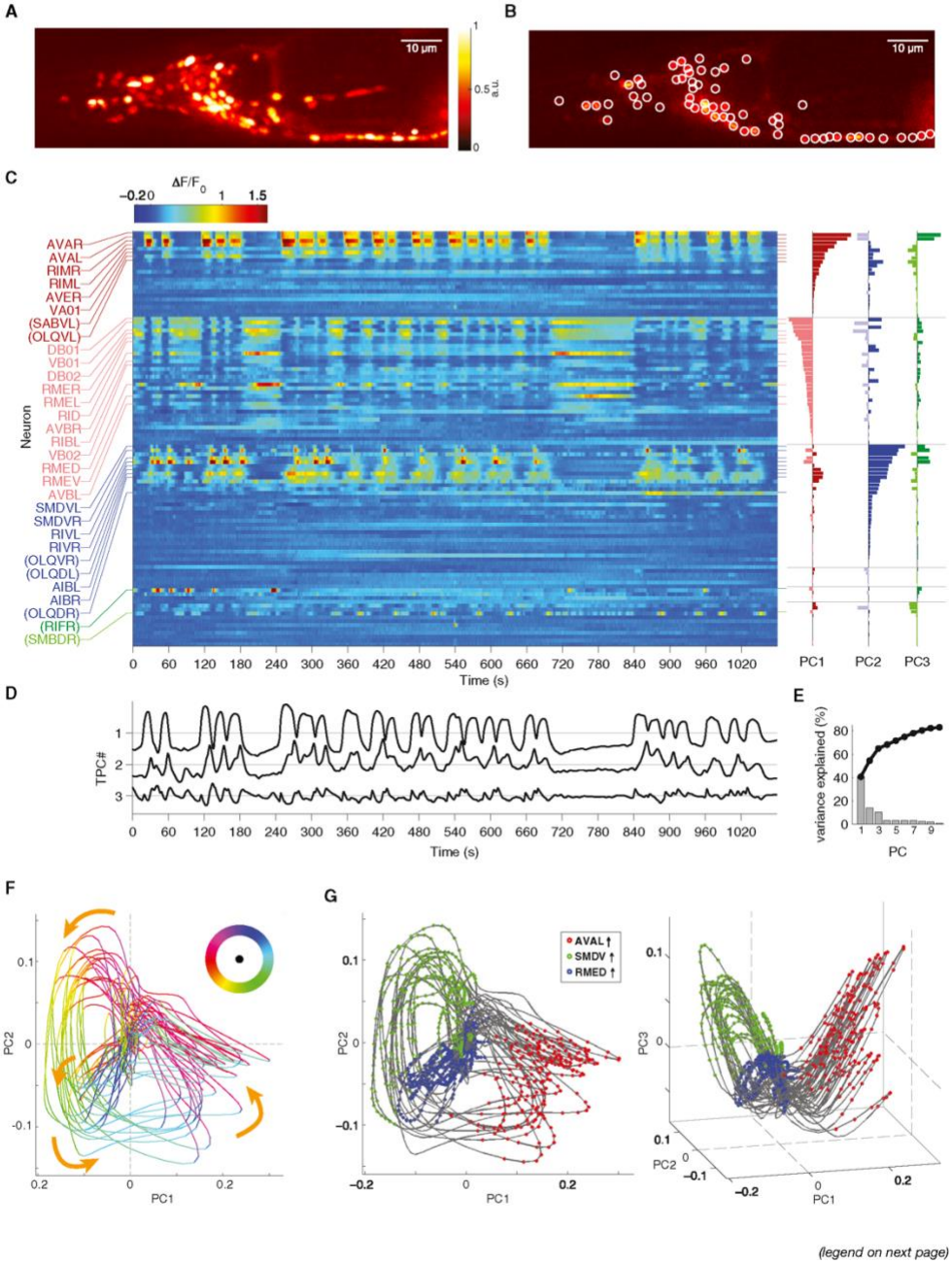

(legend on next page)

Please cite this article in press as: Kato et al., Global Brain Dynamics Embed the Motor Command Sequence of *Caenorhabditis elegans*, Cell (2015), http://dx.doi.org/10.1016/j.cell.2015.09.034

studies revealed that many of these circuit elements encode motor rather than sensory related signals (Gordus et al., 2015; Hendricks et al., 2012; Laurent et al., 2015; Li et al., 2014; Luo et al., 2014). Taken together, these considerations argue against separable feed-forward sensory pathways and instead support the hypothesis that sensorimotor processing is performed by distributed, shared networks operating on widespread motor representations.

In the present study, we provide evidence for this hypothesis by showing that many neurons in the *C. elegans* brain participate in a pervasive dynamic population state, collectively representing the major motor commands of the animal. The time evolution of the neural state is directional and cyclical, corresponding to the sequential order of the animals' repeated actions. These network dynamics interface with sensory representations as early as at the first synapse downstream of sensory neurons and provide a robust scaffold for sensory inputs to modulate behavior. Our work suggests that high-level organization of behavior is encoded in the brain by globally distributed, continuous, and low-dimensional dynamics.

RESULTS

Brain-wide Activity Evolves on a Low-Dimensional Attractor-like Manifold

We performed whole-brain single-cell-resolution Ca^{2+} imaging with a pan-neuronally expressed nuclear Ca^{2+} sensor in animals immobilized in a microfluidic device (Schrödel et al., 2013). In each animal ($n = 5$), we recorded the brain activity under environmentally constant conditions for 18 min at a rate of ~2.85 volumes per second. The imaging volume spanned all head ganglia, including most of the worm's sensory neurons and interneurons, as well as all head motor neurons and the most anterior ventral cord motor neurons (White et al., 1986) (Figures 1A and 1B). In each recording, we detected 107–131 neurons and were able to determine the cell class identity of most of the active neurons. Figures 1C and S1A show a typical multi-neuron time series during which a large proportion of imaged neurons exhibited discernable Ca^{2+}-activity patterns. We performed principal components analysis (PCA) on the time derivatives of the normalized Ca^{2+} traces (Figures 1C–1E). This method produces neuron weight vectors, termed principal components (PCs); here, PCs are calculated based on the covariance structure found in the normalized data (Jolliffe, 2002). For each PC, a corresponding time series (temporal PC) was calculated by taking the weighted average of the full multi-neural time series. Temporal PCs represent signals shared by neurons that cluster based on their correlations. We found a low-dimensional, widely shared, dominant signal: the first three PCs accounted for 65% of the full dataset variance (Figure 1E). We performed PCA on the time derivatives of Ca^{2+} traces because the resulting PCs produced more spatially organized state space trajectories, described below.

The time integral of temporal PC1 displayed a strong oscillatory time course with variable period, sharp transitions, and prolonged plateaus and troughs. This pattern derived from the antagonistic activity of two groups of interneurons and motor neurons (Figure 1C, right) previously implicated in controlling the switch between forward- and backward-directed crawling (Table S1 summarizes published results). Neurons previously reported to have opposing roles were observed to have opposing signs of their PC1 weights—e.g., AVA promoting backward crawling and AVB promoting forward crawling. PC2 and PC3 received high contributions from head motor neurons. Two of these neurons (SMDV and RIV) have been implicated in postural changes required for navigational re-orientation maneuvers (termed omega turns) (Gray et al., 2005). However, the neuronal weights of all three PCs indicated contributions from many neurons (Figure 1C). PC1–3 weights and their variance contributions were consistent across the five datasets (Figures S2A–S2D).

The phase plot of temporal PC1–3 showed that the neural state's time evolution was cyclical—i.e., the same states were repeatedly revisited within a trial, such that successive trajectory cycles formed spatially coherent bundles (Figure 1F and Movie S1). Consequently, the entire neural state trajectory traced out a manifold, which is defined here as the sub-volume in PCA space occupied by the neural state trajectory. When mapped onto the neural trajectory, individual neurons' activity rise and fall phases occupied class-specific sub-regions on the manifold (Figures 1G and S1B). All five recordings displayed a similarly structured manifold (Figure S2E). Thus, a large group of interneurons and motor neurons produces a cyclical, low-dimensional population state time-varying signal.

Interneurons and Head Motor Neurons Reliably Encode Motor State and Graded Motion Parameters

Next, we aimed for a functional interpretation of the neural state manifold and its properties. Each manifold sub-region was labeled specifically and consistently by different subsets of neurons, some of which have been previously implicated in the action sequence termed a pirouette (Table S1), which is central to navigation (Gray et al., 2005; Pierce-Shimomura et al., 1999). During pirouettes, worms switch transiently from

Figure 1. Brain-wide Activity Is Organized in a Low-Dimensional, Cyclical Neural State Space Trajectory

(A) Maximum intensity projection of a representative sample recorded under constant conditions.

(B) Single z plane overlaid with segmented neuronal regions.

(C) Heat plot of fluorescence ($\Delta F/F$) time series of 109 segmented head neurons, one neuron per row. Labeled neurons indicate putative cell IDs. Ambiguous neuron IDs are in parentheses (see Figure S1 for additional candidates). Neurons are colored and grouped by their principal component (PC1–3) weights and signs, which are shown by the bar plots on the right.

(D) Integrals of the first three temporal PCs.

(E) Variance explained by first ten PCs, black line indicates cumulative variance explained.

(F) Phase plot of first two temporal PCs colored by direction of time evolution indicated by color key.

(G) Phase plots of first two (left) and first three (right) temporal PCs. Colored balls indicate Ca^{2+} rises of three example neurons indicated by legend.

See also Movie S1 and Figures S1 and S2.

Please cite this article in press as: Kato et al., Global Brain Dynamics Embed the Motor Command Sequence of *Caenorhabditis elegans*, Cell (2015), http://dx.doi.org/10.1016/j.cell.2015.09.034

forward- to backward-directed crawling, termed a reversal (Figures 2A and 2B). They then resume forward crawling with a concomitant turn along the dorsal or ventral body axis; worms crawl lying on their left or right side (Figures 2C and 2D). We performed Ca^{2+} imaging experiments of representative neurons in freely moving worms while simultaneously recording their behavior with an infrared (IR) camera (Faumont et al., 2011). We selected neurons based on their PC weights and availability of specific promoters to drive GCaMP expression. As with brain-wide imaging experiments, animals were recorded 5–10 min after removal from food, a paradigm in which pirouettes contribute to a local search strategy (Gray et al., 2005). Behavioral analysis of the IR movies showed that reversal initiations were each preceded by a reduction in crawling speed (slowing bout), though 20% of slowing bouts did not lead to a reversal (Figures S3A and S3B). We thus defined slowing as an additional behavioral state and represent pirouettes together with forward crawling as action sequences composed of forward run, slowing, reversal, resume forward via dorsal turn, and resume forward via ventral turn actions, which is depicted in a state transition diagram (Figure 2E).

We first examined Ca^{2+} dynamics in neurons with high positive or negative PC1 weight. An example trace of RIM neurons is shown in Figure 2F. We found that the Ca^{2+} signals of RIM resided in stable low states during forward-directed crawling and that Ca^{2+} rises occurred exclusively during reversals (Figure 2F). The slope of these signals correlated with the speed of reverse crawling (Figure 2G). Although reversals are of variable duration (Gray et al., 2005; Pokala et al., 2014) (Figure S3B), RIM Ca^{2+} rise onsets precisely aligned with reversal start, and RIM Ca^{2+} fall onsets aligned with reversal end. This relationship was highly reliable—approximately 90% of reversals were associated with a detectable RIM Ca^{2+} rise phase (Figure 2H, top), and the remainders were very short reversals where small Ca^{2+} signals might have been occluded by noise (Figure 2F). All clearly discernible RIM Ca^{2+} rises above our signal-to-noise threshold occurred during reversals. We found such a relationship of Ca^{2+} rise and fall phases with respect to reversal events for all tested neurons with positive PC1 weight (RIM, AVA, AVE, AIB), while neurons with negative PC1 weight (RIB, AVB, RMEV) showed the inverse relationship (Figures 2H and S3C–S3H). All these neurons' activities changed as reliably as RIM at both forward-reverse and reverse-forward transitions.

Besides this common property of PC1 neurons, class-specific relationships between neuronal activity and locomotion were revealed by freely moving Ca^{2+} imaging. RIM and AVA Ca^{2+} rise slopes, and AVE Ca^{2+} signal magnitude, were graded and correlated with reverse crawling speed (Figures 2G, S3I, and S3J). Unlike RIM, AVA, and AVE, the activity of AIB did not show strong correlations with reverse crawling speed (Figures S3E and S3K); however, small AIB Ca^{2+} transients co-occurred with forward slowing bouts, even when no reversal followed (Figures S3E and S3Q). Consistent with this, AIB Ca^{2+} rise phases preceded the forward-to-reversal transition by ~1 s on average (Figure 2H). The continuous activity of AVB and RIB, unlike RMEV, showed strong correlations with forward crawling speed (Figures S3L–S3P; see also Li et al., 2014). Consistent with this, AVB and RIB Ca^{2+} fall phases preceded the forward to reverse transition by ~1 s on average (Figure 2H).

Next, we examined the activity of SMDV head motor neurons as representative neurons with strong PC2/3 weight. Resumption of forward crawling begins with a dorsal or ventral bend, which was biased (71%/29%) in the ventral direction. The head flexure during post-reversal turns is graded and increased compared to normal forward crawling, especially for ventral bends (Figure 3A). SMDV exhibited Ca^{2+} rises at the transition from reverse to forward crawling; importantly, these rises occurred exclusively during ventrally and not dorsally directed events (Figures 3B–3D). The magnitude of these signals correlated with ventral head-bending flexure (Figure 3E).

The major qualitative divergence in neural activity patterns between the freely moving single neuron and restrained whole-brain setups that we observed was the absence, in freely moving worms, of prolonged high phases in neurons with positive PC1 weight. Using RIM as an exemplar, we first ruled out that this difference was a consequence of nuclear localization of the Ca^{2+} reporter used in whole-brain imaging (Figures S3R–S3T). We then dissociated the two major differences in these experimental conditions by performing experiments in either pharmacologically or physically immobilized worms. While low doses of the paralyzing agent tetramisole caused RIM high phases in conjunction with prolonged slowly executed reversals, physical immobilization alone also caused RIM high phases (Figures S3U–S3X). These data suggest that impeded motor execution leads to a prolongation of the reversal, which is correlated with sustained Ca^{2+} levels in reversal-promoting neurons.

In summary, the investigated neuronal activities showed both (1) sharp transitions depending on discrete motor state (i.e., forward versus backward crawling, ventral versus dorsal turning direction) and (2) graded information about motion parameters (i.e., forward and reverse crawling speed and head bending flexure). Acute motor state reliably matched the activities of the associated neurons on a single event basis. Importantly, when examining neuron activity periods mapped onto the neural state manifold, we observed that neurons encoding the same behavioral state in freely moving animals shared the same manifold sub-regions with rare exception (Figure S1B).

Manifold Branches and Bundles Exhibit Distinct Neuronal Recruitment Patterns

Having determined that the neural state manifold is a composite of motor related signals, we next aimed for a quantitative description thereof. We first segmented the global brain cycle into four behaviorally relevant phases using the left AVA neuron (AVAL) as a reference: a trough in AVAL Ca^{2+} defined the LOW state, a Ca^{2+} increase the RISE state, a Ca^{2+} plateau the HIGH state, and a Ca^{2+} decrease the FALL state (Figure 4A). We chose this single neuron class because it is among the highest PC1 contributors, participated in every brain cycle, and, unlike temporal PCs, exhibited sharply discernible transitions; however, other strongly PC1-contributing neurons such as RIM could also be used for this purpose. We validated that the appearance of lasting plateau and smooth transition states was not due to temporal filtering effects of Ca^{2+} imaging: all four states were readily discernible in AVA membrane voltage recordings, and

Please cite this article in press as: Kato et al., Global Brain Dynamics Embed the Motor Command Sequence of *Caenorhabditis elegans*, Cell (2015), http://dx.doi.org/10.1016/j.cell.2015.09.034

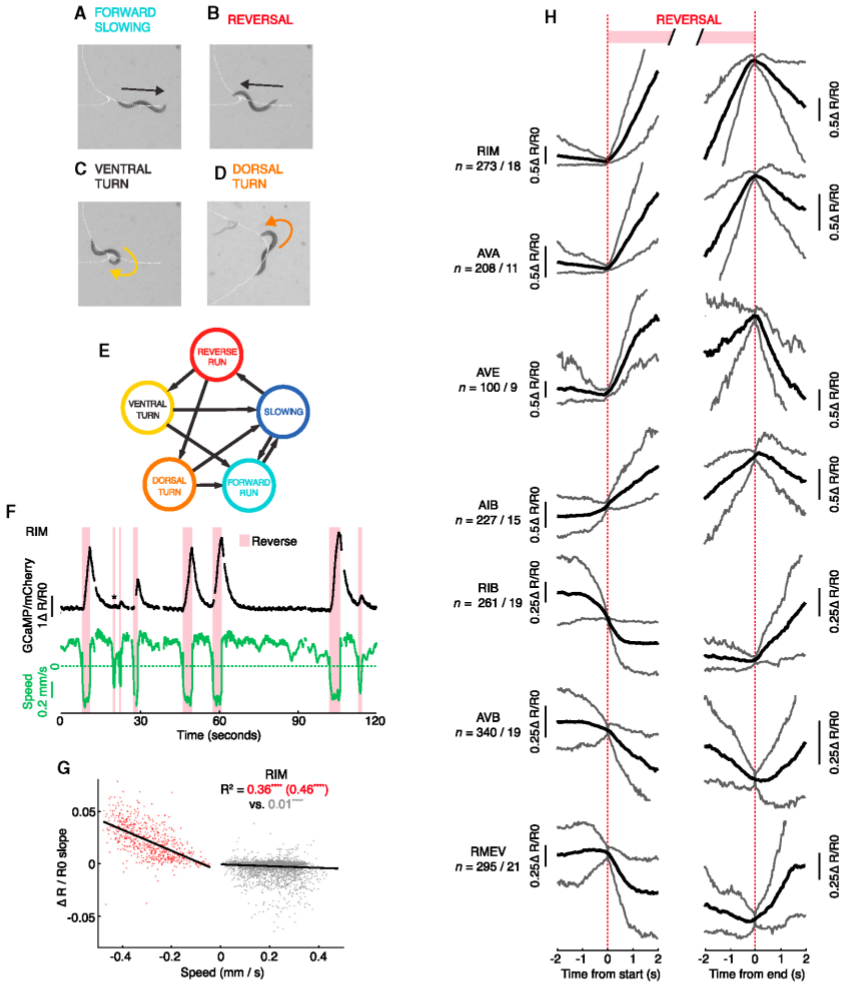

Figure 2. Distributed Encoding of Motor State and Crawling Speed by Interneurons in Freely Moving Worms

(A–D) Motor states of pirouette action sequence. White dotted lines show crawling trajectory. Arrows indicate crawling direction.

(E) Behavioral state transition diagram indicating motor states as circles and possible transitions as arrows.

(F–H) Ca^{2+} imaging in freely moving animals.

(F) Example trace showing RIM activity as normalized GCaMP/mCherry fluorescence ratio (black) and corresponding crawling speed (green). Pink bars overlay reverse crawling periods. Asterisk indicates reversal with no detectable RIM activity peak.

(G) Regression analysis of crawling speed versus RIM Ca^{2+} signal slope. R^2 indicates goodness of linear fit for instantaneous and maximum (in parentheses) reverse speed (red) and instantaneous forward speed (gray). Permutation test p value ****$p < 0.0001$ indicates probability that correlation was obtained by chance.

(H) Average Ca^{2+} signals of the indicated neurons triggered to reversal start (left) or end (right). Upper and lower traces represent 90^{th} and 10^{th} percentile of all data, respectively. Number of recorded worms and reversal events are indicated.

See also Figure S3.

Please cite this article in press as: Kato et al., Global Brain Dynamics Embed the Motor Command Sequence of *Caenorhabditis elegans*, Cell (2015), http://dx.doi.org/10.1016/j.cell.2015.09.034

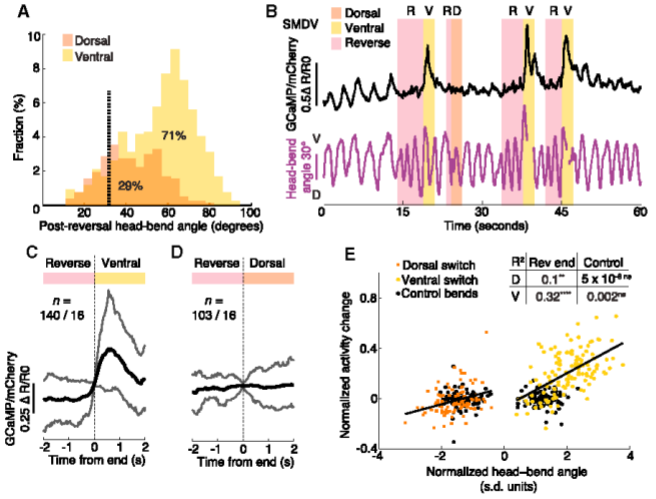

Figure 3. SMDV Signals during Ventral, but Not Dorsal, Post-Reversal Turns

(A) Fractional histogram showing postural angle of first post-reversal head bend (ventral, yellow; dorsal, orange). Numbers indicate percentage of all post reversal head bends. Dashed vertical black line shows median of all other head bends (no difference between ventral and dorsal).

(B–E) SMDV Ca^{2+} imaging in freely moving animals.

(B) Example trace showing SMDV activity as normalized GCaMP/mCherry fluorescence ratio (black) and corresponding head-bend angle (purple). Pink bars overlay reverse crawling; yellow and orange bars overlay ventral and dorsal post-reversal head-bends, respectively.

(C and D) Average SMDV Ca^{2+} signals triggered to reversals ending with ventral (C) or dorsal (D) head bends. Upper and lower traces represent 90th and 10th percentile of all data, respectively. Number of recorded worms and events are indicated.

(E) Regression analysis of normalized peak post-reversal head-bend angle versus SMDV Ca^{2+} signal. Ventral and dorsal bends are shown in yellow and orange, respectively. Black open circles show an equal number of randomly selected head-bend peaks during regular forward movement. R^2 indicates goodness of linear fits to ventral (V), dorsal (D), and respective control groups. Permutation test p values (****$p < 0.0001$, **$p < 0.01$, ^{ns} not significant) indicate probability that R^2 value was obtained by chance.

we calculated an estimate of low-pass filtering caused by nuclear Ca^{2+}-imaging, producing a maximum delay in signal peaks of less than 1.1 s (Figure S4). Although neurons with a common relationship to behavior were recruited to the same sub-regions of the manifold, their precise phase onsets and offsets varied. In order to quantify this observation, for each onset of RISE and FALL, we created a vector containing the phase delays of all recruited neurons (Figure S5) (see Supplemental Experimental Procedures for details). Across the five datasets, we detected 121 RISE and 123 FALL transitions and observed characteristic phase delay distributions for each neuronal class (Figure S5). Next, we searched for structure across neuronal classes by performing k-means clustering separately for the RISE and FALL phase timing vectors; we found that both could be significantly clustered into two groups each, which we termed RISE1/2 and FALL1/2, respectively. RISE1 differed from RISE2 mostly based on different timing of neurons; e.g., AIB and RIB activity exhibited phase advances during RISE1 (Figure S5). FALL1 and FALL2 mostly differed by mutually exclusive head motor neuron recruitments, SMDV/RIV versus RMED/ventral ganglion head motor neuron (likely SMB, SMDD, or RMF) (Figure S5). The precise ordering detected by this method may be affected by differential Ca^{2+} dynamics in different cells; however, the reproducible clustering would be preserved. Using this six-state classification (LOW, RISE1/2, HIGH, and FALL1/2), we labeled the neural state trajectory and found that each state classifies a distinct bundle of trajectory segments (Figures 4A and 4B and Movie S2). Thus, the two methods (PCA and phase timing analysis) revealed the same dynamical structure in the neural data. Bundle classification enabled us to calculate average neural state trajectories illustrating the canonical brain cycle (Figure 4C). Note that, without this single-trial clustering analysis, the cycle-averaged trajectory would be reduced to a single loop in neural state space. Furthermore, bundle classification enabled us to estimate a contour surface of the manifold (Figure 4D and Movie S3), where the extents correspond to the standard deviations (SDs) by which the trajectory path diverges from the canonical (average) path. The trajectory segments across all cycles are strongly bundled; the mean pairwise distance of points across any two phase-registered trajectory time points within a bundle is ~10% of the diameter of the full trajectory, and their mean angular divergence is 22° versus 90° expected from uncorrelated orientations. In summary, we find that many active neurons across the brain are tightly bound to reproducible and smooth population dynamics.

The Motor Command Sequence Is Embedded in Neural State Space

Remarkably, the relationships neurons exhibited with behavioral transitions (Figures 2H, 3C, and 3D) matched their phase relationships with the six state global brain cycle without exception. Assembling all of the neuronal-behavioral correlate information gathered via Ca^{2+} imaging in freely moving worms enabled us to unambiguously map the worm's major motor command states onto separate bundles of the neural state manifold (Figures 4B–4E)—RISE1 or RISE2, in conjunction with HIGH, correspond to reversals, with HIGH corresponding to the sustained reversal seen only in immobilized animals. FALL1 corresponds to the post-reversal ventral turn and FALL2 to the dorsal turn. FALL1 and FALL2, in conjunction with LOW, correspond to forward crawling. Slowing mapped to final sections of LOW

Please cite this article in press as: Kato et al., Global Brain Dynamics Embed the Motor Command Sequence of *Caenorhabditis elegans*, Cell (2015), http://dx.doi.org/10.1016/j.cell.2015.09.034

preceding RISEs (Figures 4B–4E, see Experimental Procedures for the detailed mapping rules). Thus, the neural state manifold, on a single trial basis, embeds the pirouette command sequence described in the state transition diagram (Figures 2A–2E). The neural trajectory follows the same unidirectional sequence through manifold sub-regions as the corresponding behavioral sequence executed by freely moving worms during pirouettes. This observation motivated us to redraw the state transition diagram (Figure 2E) as a continuous flow graph (Figure 4E). The neuronal manifold, in addition to embedding the command sequence, also contains information about graded locomotion parameters like the drive underlying crawling speed (Figure 4F, see Experimental Procedures for the detailed mapping rules). Both motor command states, as well as speed drive, appear organized on the manifold; i.e., separable sub-regions unambiguously delimit the distinct command states (Figure 4B) and proximal traversals on the manifold exhibit similar speed drives (Figure 4F). This manifold organization was clearly apparent in all five recordings (Figure S2E).

Each branching region of the manifold represents a decision where the subsequent motor state is determined. To explore the process of decision execution, we quantified the time course of trajectory separation when branching into RISE1 versus RISE2 and FALL1 versus FALL2 and subsequent merging. This approach calculates how significantly trajectory segments bundle in PCA space when tested against random shuffling of membership in RISE1 versus RISE2 or FALL1 versus FALL2 clusters (see Supplemental Experimental Procedures for details). Consistent with the significant clustering of neuronal recruitment vectors described above, there was significant separation during the RISE and FALL phases (Figures 4G and 4H). Interestingly, this also uncovered memory effects: a RISE1 versus RISE2 branch choice could, on average, be predicted during the preceding FALL period (Figure 4G), and consistent with the previous, FALL1 versus FALL2 trajectories remained significantly unmixed in the following RISE phases (Figure 4H). Moreover, RISE1 and RISE2 are associated, respectively, with long and short preceding LOW states (Figure 4I). Both results indicate that the trajectory path history influences the future branch choice decision.

In contrast to the state transition diagram, the neural state manifold captures the continuous dynamical structure of motor commands and their transitions and contains additional information about graded metrics of motion, like crawling speed and postural flexure. Here, we define the terms command state and speed drive as the brain's internal high-level representations of the underlying motor programs, since these are readily observable in immobilized animals in the absence of motor execution.

Neural State Dynamics Persist When a Hub Output Neuron Is Inhibited

The presence of a representation of the pirouette sequence in immobilized animals suggests that the neuronal population dynamics are primarily internally driven and thus represent descending motor commands that can operate in the absence of motor feedback. We sought to further test this hypothesis. Despite the largely recurrent connectivity of the *C. elegans* wiring diagram, a bottleneck exists from the head ganglia to body motor neurons—AVA pre-motor interneurons are anatomical network hubs linking head ganglia neurons to A-class ventral cord motor neurons, which mediate the reversal motor program (Chalfie et al., 1985; Kawano et al., 2011; Varshney et al., 2011). Acutely silencing AVA via transgenic expression of a histamine-gated chloride channel (HisCl) (Pokala et al., 2014) abolished reversals in freely moving worms (Figure 5A). As expected, similarly silenced animals under whole-brain imaging (n = 5 recordings) showed substantial attenuation of AVA activity and strong uncoupling of AVA from the global brain cycle (Figures 5B and S6A). Additionally, activity of the reverse interneurons AVE and RIM, which are connected to AVA via gap junctions (White et al., 1986) was slightly attenuated (Figure 5B). However, their phase relationships with most other neurons appeared normal (Figure S6C). A-class ventral cord motor neurons, the principal output targets of AVA, also showed significant attenuation (Figure 5B). Despite these effects, the cyclical dynamics and neuronal recruitment patterns were largely preserved (Figures 5C, 5D, and S6). The distributions of network state durations were unchanged, with the exception of a decrease in HIGH state duration, suggesting that network HIGH state prolongation was due in part to reinforcement from AVA (Figure 5E). These observations raised the possibility that the global brain cycle was also intact in freely moving worms with AVA, and therefore reversals, inhibited. Unlike in wild-type animals, where 92.5% of turns occurred in conjunction with a preceding reversal, in worms with silenced AVA neurons, none of the turns were preceded by reversals; instead, 68% of turns (32 out of 47) were preceded by prolonged slowing or pauses, while the rest occurred during apparently normal forward locomotion. Imaging RIM in AVA-silenced freely moving animals revealed the presence of sustained RIM activity during these prolonged slowing or pauses preceding normal turning events (Figures 5F–5H). Such transients were never seen in controls, where RIM was only active during reversals. In AVA-silenced animals, RIM activity often entered HIGH states during prolonged pauses, further supporting the above interpretation that the HIGH state occurs due to the absence of effectual motor execution (Figures 5F and S3U–S3X). These results show that the cyclical time course of the brain-wide motor command is maintained in the absence of reversal execution, the only effect of which is a prolonged HIGH state duration. Analogously, behaviors that are not AVA-output mediated (slowing and turns) are also preserved. Further, these data imply that AVA is not a privileged generator of motor commands but should instead be characterized as an output-facing member of the collectively oscillating interneuron group.

Entrainment of the Global Brain Cycle by Sensory Stimulation

Next, we investigated how these collective network dynamics interact with a chemosensory input. Under whole-brain imaging, we stimulated oxygen chemosensory neurons with consecutive oxygen up- and down-shifts (21% versus 4%), a protocol previously shown to reliably activate BAG, URX, and AQR oxygen sensory neurons and to entrain pirouette behavior with high pirouette probability at 21% oxygen and low at 4% (Figures S7A and S7B; see also references Busch et al., 2012; Schrödel et al., 2013; Zimmer et al., 2009). To our surprise, with the exception of one ventral ganglion neuron class (RIG or RIF)

Cell

Please cite this article in press as: Kato et al., Global Brain Dynamics Embed the Motor Command Sequence of *Caenorhabditis elegans*, Cell (2015), http://dx.doi.org/10.1016/j.cell.2015.09.034

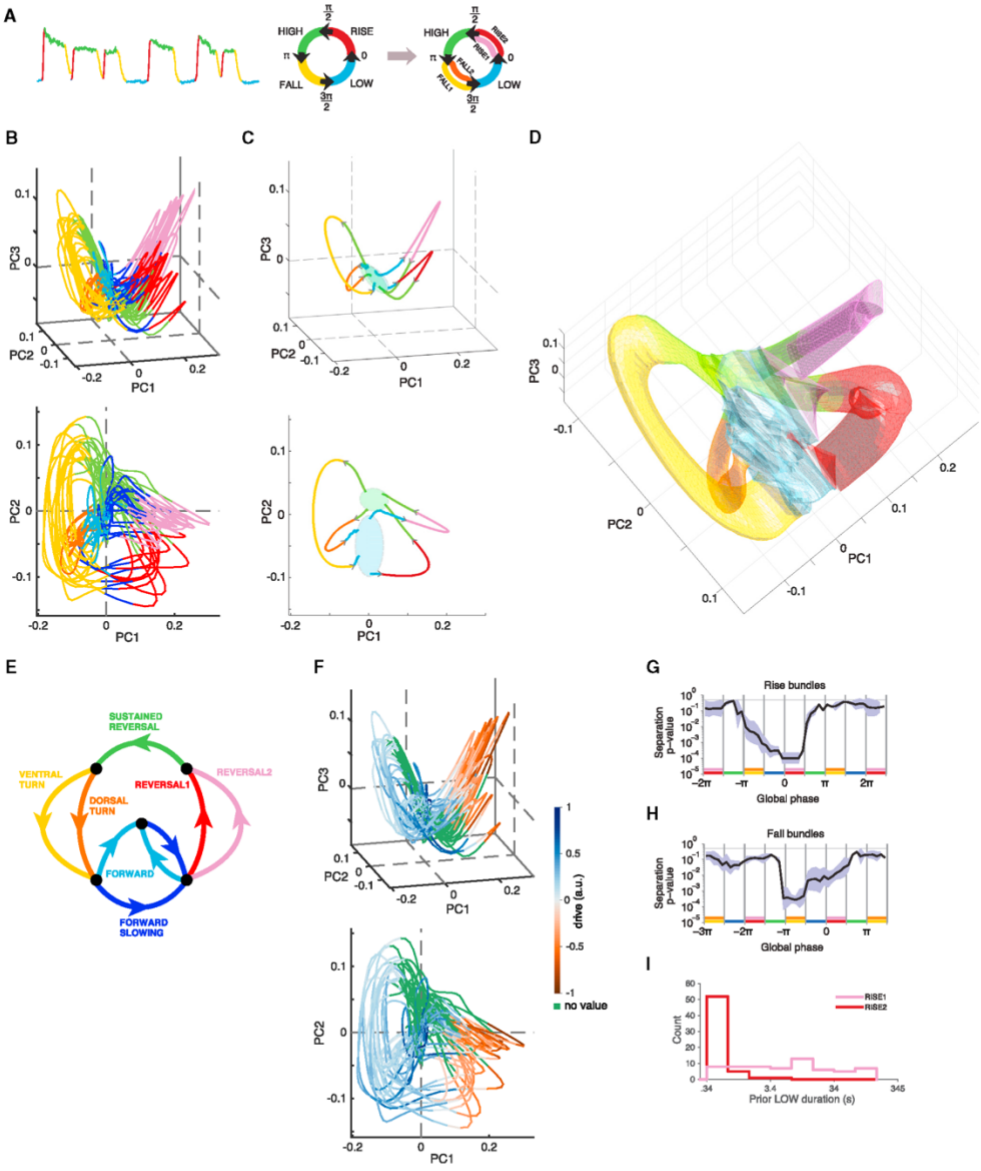

Figure 4. The Neural State Manifold Embeds the Action Sequence and Exhibits Organized Analog Speed Drive

(A) Phase segmentation of example AVAL trace (left). Four-state brain cycle (middle). Phase timing analysis and clustering leads to six-state brain cycle (right). See also Figures S4 and S5.

(B) Phase plot of the same trial shown in Figure 1, colored by six-state brain cycle plus FORWARD SLOWING command state in purple (see below).

(legend continued on next page)

Please cite this article in press as: Kato et al., Global Brain Dynamics Embed the Motor Command Sequence of *Caenorhabditis elegans*, Cell (2015), http://dx.doi.org/10.1016/j.cell.2015.09.034

(Figure S7C), we did not detect single-neuron representations of sensory stimulus downstream of sensory neurons (n = 13 recordings). Moreover, the topology of the neural state manifold did not change upon stimulation; however, there were some magnitude effects on the amplitude of temporal PC1 (Figure 6A). Based on the strong entrainment effect the stimulation protocol has on pirouette behavior, we expected that oxygen concentration should affect bundle occupancy on the manifold. Indeed, the stimulus protocol entrained the global phase of the brain cycle so that the probability of the reverse motor command state declined during 4% oxygen periods and increased during 21% oxygen periods (Figures 6B and 6C), indicating a successful sensorimotor transformation in our preparation. Consistent with these findings, Ca^{2+} rises in BAG neurons during the HIGH state evoked immediate FALL1 or FALL2 transitions in 56% (30/54, n = 13 recordings) of all instances (see Figure S7C for an example). Interestingly, in 22 out of the 24 remaining instances, secondary BAG Ca^{2+}-rises coincided with a FALL1 or FALL2 transition; these were the only times when we observed secondary BAG transients (see Figure S7C as an example). This finding suggests the existence of a feedback mechanism eliciting or gating secondary Ca^{2+} rises in the BAG sensory neurons, demonstrating that variability in the BAG sensory response profile (Zimmer et al., 2009) can be explained when the underlying brain state is known to the observer.

Finally, we looked for sensory-evoked Ca^{2+} activity in the major PC1 neuron classes AVA, AVE, and RIB in freely moving animals. Together AVE and RIB receive 47% of BAG neuron synapses (White et al., 1986). Consistent with our whole-brain imaging results, these neurons retained a tight correlation with motor state and movement metrics and lacked obvious sensory encoding activity; the magnitude of Ca^{2+} signals was subtly modulated during the stimulation periods (Figures S7D–S7U).

In summary, neural state manifold organization is robust to a salient sensory input and thus stably encodes the motor command sequences of the worm under these conditions. The major effect of sensory input was to modulate the probability that the neural state resides on a particular segment bundle by driving the neural state along a lawful trajectory. The result is an entrainment of the global brain cycle, which is consistent with the entrainment of corresponding motor behaviors in freely moving worms.

DISCUSSION

In this work, we identify and characterize a brain-wide signal in *C. elegans* that dominates the neural activity time series. Although our approach required the use of a nuclear localized Ca^{2+} indicator, omitting the detection of subcellular Ca^{2+} signals (Chalasani et al., 2007; Hendricks et al., 2012; Li et al., 2014), it reveals a pervasive motor state representation that is shared among most interneuron and motor neuron layers. The neural state trajectory exhibits directional, cyclical flow (Figure 1F) confined to a low-dimensional manifold (Figure 4D), organized into bundles (Figures 4B–4D) composed of stereotyped and smoothly changing neural activity vectors (Figure S5). Each motor command within the pirouette action sequence is reliably represented across several neurons. Neurons additionally encode graded parameters of locomotion, e.g., crawling speed and postural flexure (Figures 2, 3, and S3). These data enable us to unambiguously map behavioral commands onto sub-regions of the neural state manifold, enabling instantaneous behavioral decoding throughout an experimental trial (Figures 4B and 4E). We interpret these dynamics as corresponding to motor commands, as they can be decoupled from motor output either by restraint (during whole-brain imaging) or manipulation of a major output neuron (Figure 5). Organized flow along the neural state manifold mediates the assembly of motor commands into action sequences (Figures 4B and 4E); it thus represents the high-level temporal organization of behavior upstream of the generation of the animal's undulatory gait. This contrasts with population dynamics in the motor ganglia of crustaceans, mollusks, and lampreys that generate peristaltic and movement rhythms (Bruno et al., 2015; Grillner, 2006; Marder and Bucher, 2007). Interestingly, the brain's forward and reversal motor commands are coupled to corresponding rise, high, fall, and low states in the B- and A-class ventral nerve cord (VNC) motor neurons (Figures 1 and S1), which is consistent with previous studies performed in moving *C. elegans*. Additionally, VNC motor neuron activity exhibits gait-related rhythmic activity superimposed on these command states (Kawano et al., 2011; Wen et al., 2012), which requires proprioceptive coupling to movement (Wen et al., 2012). Taken together, we propose that behavioral state is encoded in the brain and coupled to the motor periphery and that this coupling co-occurs with locally maintained rhythmic activity.

These continuous neural dynamics embed behavioral motifs, described by the state transition diagram, and permit their superposition with graded motion metrics (Figure 4F). The process of decision making leading to execution of alternate behaviors can be observed as the time evolution of neural trajectories before the branches (Figures 4B–4D, 4G, and 4H). We propose that the phenomenon of global dynamics robustly and continuously encoding action sequence commands may be present in

(C) Phase-registered averages of the two RISE phase and two FALL phase bundles colored by six-state brain cycle. Semi-transparent ovals denote trajectory bundle mixing regions.
(D) Contour surface illustrating the neural state manifold colored by six-state brain cycle.
(E) Flow diagram indicating the motor command states corresponding to the six-state brain cycle plus FORWARD SLOWING command state (purple).
(F) The same phase plot colored by forward- and reverse-speed drive inferred from neural correlate decoding. Green trajectory segments indicate the SUSTAINED REVERSAL state, for which no drive correspondence is made. See Figure S2 for more examples.
(G and H) Quantification of inter-bundle separation and mixing for RISE (G) and FALL (H) clusters. Traces show trial-averaged p values (shading indicates SEM; n = 5 animals) of mean normalized pairwise distance at instantaneous points in the past or future, which indicate the probability that the observed separation between bundles occurred by chance. This calculation was done in six dimensions (PC1–3 plus their derivatives) to incorporate directional information from the trajectory paths.
(I) Distribution of LOW state durations preceding RISE1 or RISE2 segments.
See also Movies S2 and S3.

Please cite this article in press as: Kato et al., Global Brain Dynamics Embed the Motor Command Sequence of *Caenorhabditis elegans*, Cell (2015), http://dx.doi.org/10.1016/j.cell.2015.09.034

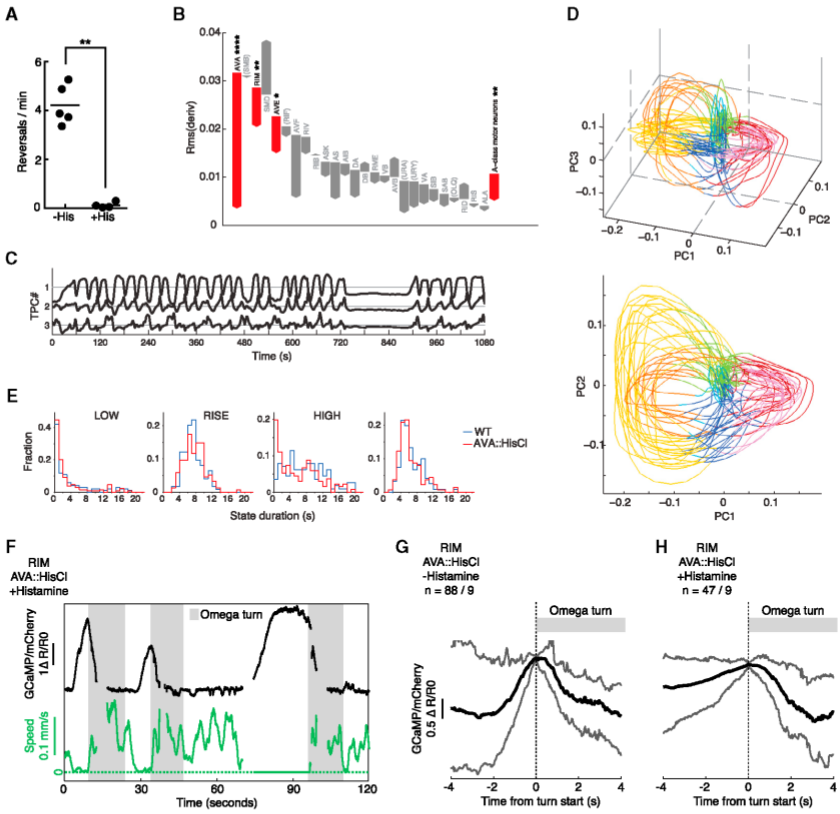

Figure 5. Global Brain Dynamics Persist when Decoupled from Motor Output

(A) Reversal events per minute for AVA::HisCl worms without (−His) or with (+His) histamine treatment. Each data point represents a single assay, n = 20–25 worms per assay. Horizontal lines show means. Mann-Whitney test, $^{**}p < 0.01$.

(B) Shifts in trial-averaged root-mean-squared power of neuronal trace derivatives of AVA::HisCl worms with histamine treatment, relative to wild-type control (n = 5). Gray bars indicate non-significant power shifts, red bars indicate significant power shifts. Class-A motor neurons, typically 1–2 visible per recording, were combined. Significance was determined using a permutation test, $^{****}p < 0.0001$, $^{**}p < 0.01$, $^{*}p < 0.05$.

(C and D) Integrated temporal PCs (C) and phase plots (D) of an example AVA::HisCl dataset.

(E) Distributions of state durations of AVA::HisCl (red) versus wild-type (blue) across multiple trials (n = 5).

(F–H) Ca^{2+} imaging of RIM in freely moving animals expressing HisCl in AVA.

(F) Example trace showing RIM activity in an AVA::HisCl worm after histamine treatment. Normalized GCaMP/mCherry fluorescence ratio (black) and corresponding crawling speed (green) are shown. Omega turns are indicated with gray overlaid bars. These worms did not exhibit reversals.

(G and H) Averages of RIM Ca^{2+} signals in AVA::HisCl worms triggered to omega turn onset, for worms pre-incubated without (G) or with (H) histamine. Upper and lower traces represent 90^{th} and 10^{th} percentile of all data, respectively. Number of recorded worms and omega turns are indicated.

See also Figure S6.

higher animals with more sophisticated behavioral repertoires. This hypothesis is supported by the observation of smooth population dynamics maintaining navigational plans in rodents (Harvey et al., 2012). Its generality could be further tested by studying the basis of well-described sequential courtship and grooming behaviors in fruit flies (Dankert et al., 2009; Seeds et al., 2014).

The ability to find dynamical structure solely on the basis of neural event timing (Figure S5) suggests that the structure we observe is not a particular consequence of the graded, non-spiking, nature of *C. elegans* neurons. We speculate that neuronal population trajectories associated with action selection in leeches (Briggman et al., 2005), limb movement in monkey

Please cite this article in press as: Kato et al., Global Brain Dynamics Embed the Motor Command Sequence of *Caenorhabditis elegans*, Cell (2015), http://dx.doi.org/10.1016/j.cell.2015.09.034

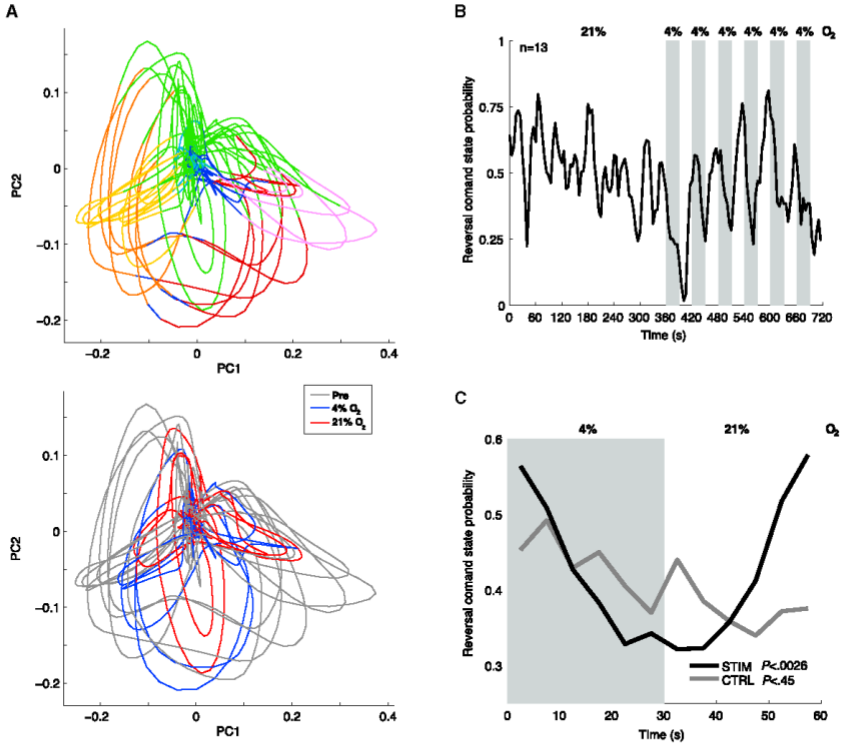

Figure 6. Entrainment of the Global Brain Cycle by Sensory Stimulation

Animals were recorded and stimulated with the oxygen profile indicated in (B).

(A) Phase plots of temporal PCs 1–2 from a representative recording. Top: behavioral command state coloring as in Figure 4B. Bottom: trajectory segments during the pre-stimulus period are labeled gray; segments during the 4% and 21% shift periods are labeled blue and red, respectively.

(B) The trace shows the probability of reversal command state (REVERSAL1 + REVERSAL2 + SUSTAINED REVERSAL) calculated over n = 13 recordings.

(C) Reversal command state probability as in (B) but averaged over the six down- and up-shift periods. p values are calculated by a resampling test and indicate the probability that the stimulus-synced profile shape occurred from a randomly time-shifted stimulus pattern.

See also Figure S7.

cortical areas (Georgopoulos and Carpenter, 2015; Shenoy et al., 2013), and speech in humans (Bouchard et al., 2013) may be sparsely sampled windows onto similarly well-organized, smooth global dynamics.

Our work establishes a framework for future studies aimed at embedding more fine-scaled behaviors beyond the discrete classifications of the state transition diagram, such as gradual steering commands (Iino and Yoshida, 2009) and locomotory gait (Stephens et al., 2008). By exploring more sophisticated sensory input paradigms and studying the animal in different contexts and life stages, we expect that the neural state manifold will be further sub-dividable and support the mapping of other behavioral parameters. Additionally, in-depth analysis of whole-brain activity may uncover previously hidden aspects of behavior; for example, we found two types of reversals (corresponding to RISE1 and RISE2) in whole-brain activity that currently lack known behavioral correlates. Although AVA inhibition had only subtle effects, systematically expanding this approach to other neurons and combinations thereof should reveal whether individual neurons or sub-ensembles are causal to brain dynamics. By probing the system with acute perturbation using optogenetics and imaging at finer timescales and sub-neuronal spatial resolution, it should be possible to uncover the neuronal logic governing trajectory control and branch selection, which underlies decision making in this system. Measuring manifold geometry changes over longer timescales may uncover the characteristics of brain states such as hunger-satiety or sleep-wakefulness.

Please cite this article in press as: Kato et al., Global Brain Dynamics Embed the Motor Command Sequence of *Caenorhabditis elegans*, Cell (2015), http://dx.doi.org/10.1016/j.cell.2015.09.034

Our results argue against models of largely feed-forward sensory-to-motor flow where intermediate neuronal layers perform sequential processing and the behavioral state is only ultimately represented within the nervous system at the motor periphery. Instead, our data support a model of an early interface between sensory and motor representations as was suggested by recent single-neuron studies (Hendricks et al., 2012; Luo et al., 2014).

Moreover, motor command representations affect responsiveness of sensory neurons and early interneurons to sensory inputs via feedback mechanisms (Figure S7) that remain to be identified (see also Gordus et al., 2015). Consistent with recent distributed models of sensorimotor action selection in mammals, including primates (Cisek and Kalaska, 2010), our work suggests that the brain's outputs—i.e., its intents and actions—make up a large fraction of its dynamic activity state.

Our findings reveal that a large collection of neuronal classes with distinct morphologies and connectivities (White et al., 1986), distinct molecular compositions and neurotransmitter expression patterns (Hobert, 2013), distinct synaptic transmission properties (Li et al., 2014), and distinct subcellular signal processing capacities (Chalasani et al., 2007; Hendricks et al., 2012; Li et al., 2014) nevertheless collectively share a low-dimensional, pervasive neuronal signal. The class-specific phase relationships with respect to the global brain cycle (Figures S1B and S5) suggest that neurons differentially interact with this shared mode. We therefore propose that the neural state manifold influences and binds local activity to a global reference framework, establishing a consensus that produces stable, coherent behavior.

EXPERIMENTAL PROCEDURES

The Supplemental Experimental Procedures contain more detailed information on each procedure, and in addition, they include descriptions of region of interest detection and neural time series extraction from volumetric Ca^{2+} imaging data, electrophysiology, simulation of nuclear GCaMP signals from voltage traces, population behavior assays, statistics applied in this study, strain genotypes, and molecular biology constructs.

Whole-Brain Ca^{2+} Imaging of *C. elegans* Head Ganglia Neurons

Animals were immobilized with 1 mM tetramisole in microfluidic devices that allow controlled O_2 stimuli as previously described (Schrödel et al., 2013; Zimmer et al., 2009). Recordings were started within 5 min after removal from food. Worms were either imaged for 18 min at constant 21% O_2 or, for the stimulus protocol, imaged for 12 min with the first 6 min at 21% O_2 and the remaining 6 min with 30 s consecutive shifts between 4% and 21% O_2. Data were acquired using an inverted spinning disc microscope (UltraViewVoX, PerkinElmer) equipped with an EMCCD camera (C9100-13, Hamamatsu).

Identification of Head Ganglia Neurons

In each recording, we detected 107–131 neurons, covering 55%–67% of expected neurons in the imaging area. Neurons were identified taking into account their anatomical positions, also in relation to surrounding neurons (http://www.wormatlas.org), and their activity patterns. To confirm ambiguous neuron identities, marker lines expressing red fluorophores in neurons of interest were generated and crossed to the imaging line expressing GCaMP5K pan-neuronally in the nucleus (ZIM504).

Time Series Analysis: PCA, Numerical Differentiation, 4-Phase Segmentation, Phase Timing Analysis, and Clustering

PCA was performed on the time derivatives of $\Delta F/F_0$ neural traces, each normalized by its peak magnitude. To compute de-noised time derivatives without the need of smoothing that can affect precise timing of sharp transitions, the total-variation regularization method (Chartrand, 2011) was applied. To segment individual neuronal activity into 4-phase sequences, first RISE and FALL phases for neurons were identified as periods when the time derivative was greater or lower than a small threshold, respectively. HIGH and LOW phases were then inferred in the remaining gaps. For trajectory segment averaging (Figures 4C, 4D, and S2E) and generation of Movies S2 and S3, neuronal time series were registered to a common phase clock by matching phase segment starts and ends to the reference neuron (AVA or RIM) rise onsets and fall offsets, respectively, followed by linearly interpolating within phase segments. To perform phase timing analysis, first a set of global transitions, either RISE or FALL onsets, were defined by the transitions of a reference neuron (AVA or RIM in this study). Then, relative time delays of the nearest transitions found in other neurons were used to compose a feature vector for each global transition. In the absence of a matching transition within 7 s of the reference neuron transition, a time delay of −10 s was used for the purposes of clustering, since the absence of neurons was also considered an important feature of transitions. *K*-means clustering was applied to transition feature vectors for each full trial using L_1 distance and $k = 2$. Detailed explanations of the above computational analyses may be found in the Supplemental Experimental Procedures.

Behavioral Decoding of Whole-Brain Recordings

Each time point of the phase plot trajectory was first assigned to a global brain cycle HIGH, LOW, RISE1, RISE2, FALL1, or FALL2 segment as described above and in the main text, then mapped to motor command states as follows. RISE1 and RISE 2 segments were mapped to REVERSAL1 and REVERSAL2 command states, respectively. HIGH segments were mapped to the SUSTAINED REVERSAL state. FALL1 and FALL2 segments were mapped to VENTRAL TURN and DORSAL TURN, respectively. LOW segments were mapped to FORWARD except that RIB FALL phases present during global LOW segments were mapped to FORWARD SLOWING command states. A speed drive was assigned to each point on the trajectory as follows, aside from those in SUSTAINED REVERSAL phases for which no speed drive was inferred. During VENTRAL TURN, DORSAL TURN, FORWARD, and FORWARD SLOWING phases, positive speed drive was taken to be the magnitude of RIB activity, normalized to its most negative value during the trial. During REVERSAL1 and 2 phases, negative speed drive was taken to be the derivative of RIM neuron activity, normalized to its highest value during the trial.

Ca^{2+} Imaging in Freely Moving Animals

Ca^{2+} imaging recordings were made using the automatic re-centering system described previously (Faumont et al., 2011) with custom modifications. Young adult worms (0–8 eggs) expressed both mCherry and GCaMP in the neuron of interest. Animals were recorded while freely crawling on agar in a custom built microscope stage containing an airtight chamber with inlet and outlet connectors for gas flow delivery. Images were acquired using two CCD cameras (Evolve 512, Photometrics) connected via a DualCam DC2 beam splitter (Photometrics). A long-distance 63× objective (Zeiss LD Plan-Neofluar 63×, 0.75 NA) was used to obtain unbinned images streamed at 30.3 frames per second (fps) acquisition rate. Simultaneous behavior recordings under infrared illumination (780 nm) were made using a CCD camera (Manta Prosilica GigE, Applied Vision Technologies) at 4× magnification and 10 fps acquisition rate.

SUPPLEMENTAL INFORMATION

Supplemental Information includes Supplemental Experimental Procedures, seven figures, one table, and three movies and can be found with this article online at http://dx.doi.org/10.1016/j.cell.2015.09.034.

AUTHOR CONTRIBUTIONS

S.K. designed experiments, developed analytical methods for whole-brain imaging datasets, and analyzed data. H.S.K. designed experiments, generated transgenic strains, performed Ca^{2+}-imaging experiments in freely moving animals, developed analytical methods, and analyzed data. T.S. designed

Please cite this article in press as: Kato et al., Global Brain Dynamics Embed the Motor Command Sequence of *Caenorhabditis elegans*, Cell (2015), http://dx.doi.org/10.1016/j.cell.2015.09.034

Cell

experiments, generated transgenic strains, performed whole-brain imaging experiments, and analyzed data. S.S. performed population behavioral recordings and analyzed data. T.H.L. and S.L. performed electrical recordings; E.Y. wrote code for behavioral analysis; and M.Z. designed experiments, developed analytical methods, and led the project. S.K., H.S.K., T.S., and M.Z. wrote the manuscript.

ACKNOWLEDGMENTS

We thank Cori Bargmann, Larry Abbott, Alipasha Vaziri, Andrew Straw, Hagai Lalazar, Omri Barak, and Sean Escola for critically reading the manuscript, Richard Latham for technical support, and Martin Colombini for manufacturing of mechanical components. The research leading to these results has received funding from the European Community's Seventh Framework Programme (FP7/2007-2013)/ERC grant agreement number 281869 (acronym: *elegans Neurocircuits*) to M.Z., the Simons Foundation (grant number 324958 to M.Z.), an EMBO Long Term Fellowship to S.K. (number ALTF 345-2014), an NIH training grant to T.H.L. (number F31 NS061697), an NIH T32 training grant to E.Y. (number T32 MH015174-38), and the Research Institute of Molecular Pathology (IMP). The IMP is funded by Boehringer Ingelheim.

Received: July 2, 2015
Revised: August 14, 2015
Accepted: September 2, 2015
Published: October 15, 2015

REFERENCES

Ahrens, M.B., Li, J.M., Orger, M.B., Robson, D.N., Schier, A.F., Engert, F., and Portugues, R. (2012). Brain-wide neuronal dynamics during motor adaptation in zebrafish. Nature *485*, 471–477.

Ahrens, M.B., Orger, M.B., Robson, D.N., Li, J.M., and Keller, P.J. (2013). Whole-brain functional imaging at cellular resolution using light-sheet microscopy. Nat. Methods *10*, 413–420.

Anderson, D.J., and Perona, P. (2014). Toward a science of computational ethology. Neuron *84*, 18–31.

Bouchard, K.E., Mesgarani, N., Johnson, K., and Chang, E.F. (2013). Functional organization of human sensorimotor cortex for speech articulation. Nature *495*, 327–332.

Briggman, K.L., Abarbanel, H.D., and Kristan, W.B., Jr. (2005). Optical imaging of neuronal populations during decision-making. Science *307*, 896–901.

Bruno, A.M., Frost, W.N., and Humphries, M.D. (2015). Modular deconstruction reveals the dynamical and physical building blocks of a locomotion motor program. Neuron *86*, 304–318.

Busch, K.E., Laurent, P., Soltesz, Z., Murphy, R.J., Faivre, O., Hedwig, B., Thomas, M., Smith, H.L., and de Bono, M. (2012). Tonic signaling from O_2 sensors sets neural circuit activity and behavioral state. Nat. Neurosci. *15*, 581–591.

Chalasani, S.H., Chronis, N., Tsunozaki, M., Gray, J.M., Ramot, D., Goodman, M.B., and Bargmann, C.I. (2007). Dissecting a circuit for olfactory behaviour in Caenorhabditis elegans. Nature *450*, 63–70.

Chalfie, M., Sulston, J.E., White, J.G., Southgate, E., Thomson, J.N., and Brenner, S. (1985). The neural circuit for touch sensitivity in Caenorhabditis elegans. J. Neurosci. *5*, 956–964.

Chartrand, R. (2011). Numerical differentiation of noisy, nonsmooth data. ISRN Applied Mathematics *2011*, 1–11.

Churchland, M.M., Cunningham, J.P., Kaufman, M.T., Foster, J.D., Nuyujukian, P., Ryu, S.I., and Shenoy, K.V. (2012). Neural population dynamics during reaching. Nature *487*, 51–56.

Cisek, P., and Kalaska, J.F. (2010). Neural mechanisms for interacting with a world full of action choices. Annu. Rev. Neurosci. *33*, 269–298.

Cunningham, J.P., and Yu, B.M. (2014). Dimensionality reduction for large-scale neural recordings. Nat. Neurosci. *17*, 1500–1509.

Dankert, H., Wang, L., Hoopfer, E.D., Anderson, D.J., and Perona, P. (2009). Automated monitoring and analysis of social behavior in Drosophila. Nat. Methods *6*, 297–303.

Donnelly, J.L., Clark, C.M., Leifer, A.M., Pirri, J.K., Haburcak, M., Francis, M.M., Samuel, A.D.T., and Alkema, M.J. (2013). Monoaminergic orchestration of motor programs in a complex C. elegans behavior. PLoS Biol. *11*, e1001529.

Faumont, S., Rondeau, G., Thiele, T.R., Lawton, K.J., McCormick, K.E., Sottile, M., Griesbeck, O., Heckscher, E.S., Roberts, W.M., Doe, C.Q., and Lockery, S.R. (2011). An image-free opto-mechanical system for creating virtual environments and imaging neuronal activity in freely moving Caenorhabditis elegans. PLoS ONE *6*, e24666.

Georgopoulos, A.P., and Carpenter, A.F. (2015). Coding of movements in the motor cortex. Curr. Opin. Neurobiol. *33*, 34–39.

Gordus, A., Pokala, N., Levy, S., Flavell, S.W., and Bargmann, C.I. (2015). Feedback from network states generates variability in a probabilistic olfactory circuit. Cell *161*, 215–227.

Gray, J.M., Hill, J.J., and Bargmann, C.I. (2005). A circuit for navigation in Caenorhabditis elegans. Proc. Natl. Acad. Sci. USA *102*, 3184–3191.

Grillner, S. (2006). Biological pattern generation: the cellular and computational logic of networks in motion. Neuron *52*, 751–766.

Ha, H.I., Hendricks, M., Shen, Y., Gabel, C.V., Fang-Yen, C., Qin, Y., Colón-Ramos, D., Shen, K., Samuel, A.D.T., and Zhang, Y. (2010). Functional organization of a neural network for aversive olfactory learning in Caenorhabditis elegans. Neuron *68*, 1173–1186.

Harvey, C.D., Coen, P., and Tank, D.W. (2012). Choice-specific sequences in parietal cortex during a virtual-navigation decision task. Nature *484*, 62–68.

Hendricks, M., Ha, H., Maffey, N., and Zhang, Y. (2012). Compartmentalized calcium dynamics in a C. elegans interneuron encode head movement. Nature *487*, 99–103.

Hobert, O. (2013). The neuronal genome of Caenorhabditis elegans (WormBook), pp. 1–106.

Iino, Y., and Yoshida, K. (2009). Parallel use of two behavioral mechanisms for chemotaxis in Caenorhabditis elegans. J. Neurosci. *29*, 5370–5380.

Jin, X., Tecuapetla, F., and Costa, R.M. (2014). Basal ganglia subcircuits distinctively encode the parsing and concatenation of action sequences. Nat. Neurosci. *17*, 423–430.

Jolliffe, I.T. (2002). Principal Component Analysis, Second Edition (Springer).

Kawano, T., Po, M.D., Gao, S., Leung, G., Ryu, W.S., and Zhen, M. (2011). An imbalancing act: gap junctions reduce the backward motor circuit activity to bias C. elegans for forward locomotion. Neuron *72*, 572–586.

Kimata, T., Sasakura, H., Ohnishi, N., Nishio, N., and Mori, I. (2012). Thermotaxis of C. elegans as a model for temperature perception, neural information processing and neural plasticity. Worm *1*, 31–41.

Laurent, P., Soltesz, Z., Nelson, G.M., Chen, C., Arellano-Carbajal, F., Levy, E., and de Bono, M. (2015). Decoding a neural circuit controlling global animal state in C. elegans. eLife *4*, 4.

Lemon, W.C., Pulver, S.R., Höckendorf, B., McDole, K., Branson, K., Freeman, J., and Keller, P.J. (2015). Whole-central nervous system functional imaging in larval Drosophila. Nat. Commun. *6*, 7924.

Li, Z., Liu, J., Zheng, M., and Xu, X.Z.S. (2014). Encoding of both analog- and digital-like behavioral outputs by one C. elegans interneuron. Cell *159*, 751–765.

Luo, L., Wen, Q., Ren, J., Hendricks, M., Gershow, M., Qin, Y., Greenwood, J., Soucy, E.R., Klein, M., Smith-Parker, H.K., et al. (2014). Dynamic encoding of perception, memory, and movement in a C. elegans chemotaxis circuit. Neuron *82*, 1115–1128.

Mante, V., Sussillo, D., Shenoy, K.V., and Newsome, W.T. (2013). Context-dependent computation by recurrent dynamics in prefrontal cortex. Nature *503*, 1–19.

Marder, E., and Bucher, D. (2007). Understanding circuit dynamics using the stomatogastric nervous system of lobsters and crabs. Annu. Rev. Physiol. *69*, 291–316.

Please cite this article in press as: Kato et al., Global Brain Dynamics Embed the Motor Command Sequence of *Caenorhabditis elegans*, Cell (2015), http://dx.doi.org/10.1016/j.cell.2015.09.034

Panier, T., Romano, S.A., Olive, R., Pietri, T., Sumbre, G., Candelier, R., and Debrégeas, G. (2013). Fast functional imaging of multiple brain regions in intact zebrafish larvae using selective plane illumination microscopy. Front. Neural Circuits *7*, 65.

Pierce-Shimomura, J.T., Morse, T.M., and Lockery, S.R. (1999). The fundamental role of pirouettes in Caenorhabditis elegans chemotaxis. J. Neurosci. *19*, 9557–9569.

Pokala, N., Liu, Q., Gordus, A., and Bargmann, C.I. (2014). Inducible and titratable silencing of Caenorhabditis elegans neurons in vivo with histamine-gated chloride channels. Proc. Natl. Acad. Sci. USA *111*, 2770–2775.

Prevedel, R., Yoon, Y.-G., Hoffmann, M., Pak, N., Wetzstein, G., Kato, S., Schrödel, T., Raskar, R., Zimmer, M., Boyden, E.S., and Vaziri, A. (2014). Simultaneous whole-animal 3D imaging of neuronal activity using light-field microscopy. Nat. Methods *11*, 727–730.

Schrödel, T., Prevedel, R., Aumayr, K., Zimmer, M., and Vaziri, A. (2013). Brain-wide 3D imaging of neuronal activity in Caenorhabditis elegans with sculpted light. Nat. Methods *10*, 1013–1020.

Seeds, A.M., Ravbar, P., Chung, P., Hampel, S., Midgley, F.M., Jr., Mensh, B.D., and Simpson, J.H. (2014). A suppression hierarchy among competing motor programs drives sequential grooming in Drosophila. eLife *3*, e02951.

Shenoy, K.V., Sahani, M., and Churchland, M.M. (2013). Cortical control of arm movements: a dynamical systems perspective. Annu. Rev. Neurosci. *36*, 337–359.

Stephens, G.J., Johnson-Kerner, B., Bialek, W., and Ryu, W.S. (2008). Dimensionality and dynamics in the behavior of C. elegans. PLoS Comput. Biol. *4*, e1000028.

Varshney, L.R., Chen, B.L., Paniagua, E., Hall, D.H., and Chklovskii, D.B. (2011). Structural properties of the Caenorhabditis elegans neuronal network. PLoS Comput. Biol. *7*, e1001066.

Wen, Q., Po, M.D., Hulme, E., Chen, S., Liu, X., Kwok, S.W., Gershow, M., Leifer, A.M., Butler, V., Fang-Yen, C., et al. (2012). Proprioceptive coupling within motor neurons drives C. elegans forward locomotion. Neuron *76*, 750–761.

White, J.G., Southgate, E., Thomson, J.N., and Brenner, S. (1986). The structure of the nervous system of the nematode Caenorhabditis elegans. Philos. Trans. R. Soc. Lond. B Biol. Sci. *314*, 1–340.

Zimmer, M., Gray, J.M., Pokala, N., Chang, A.J., Karow, D.S., Marletta, M.A., Hudson, M.L., Morton, D.B., Chronis, N., and Bargmann, C.I. (2009). Neurons detect increases and decreases in oxygen levels using distinct guanylate cyclases. Neuron *61*, 865–879.

Cell

Supplemental Figures

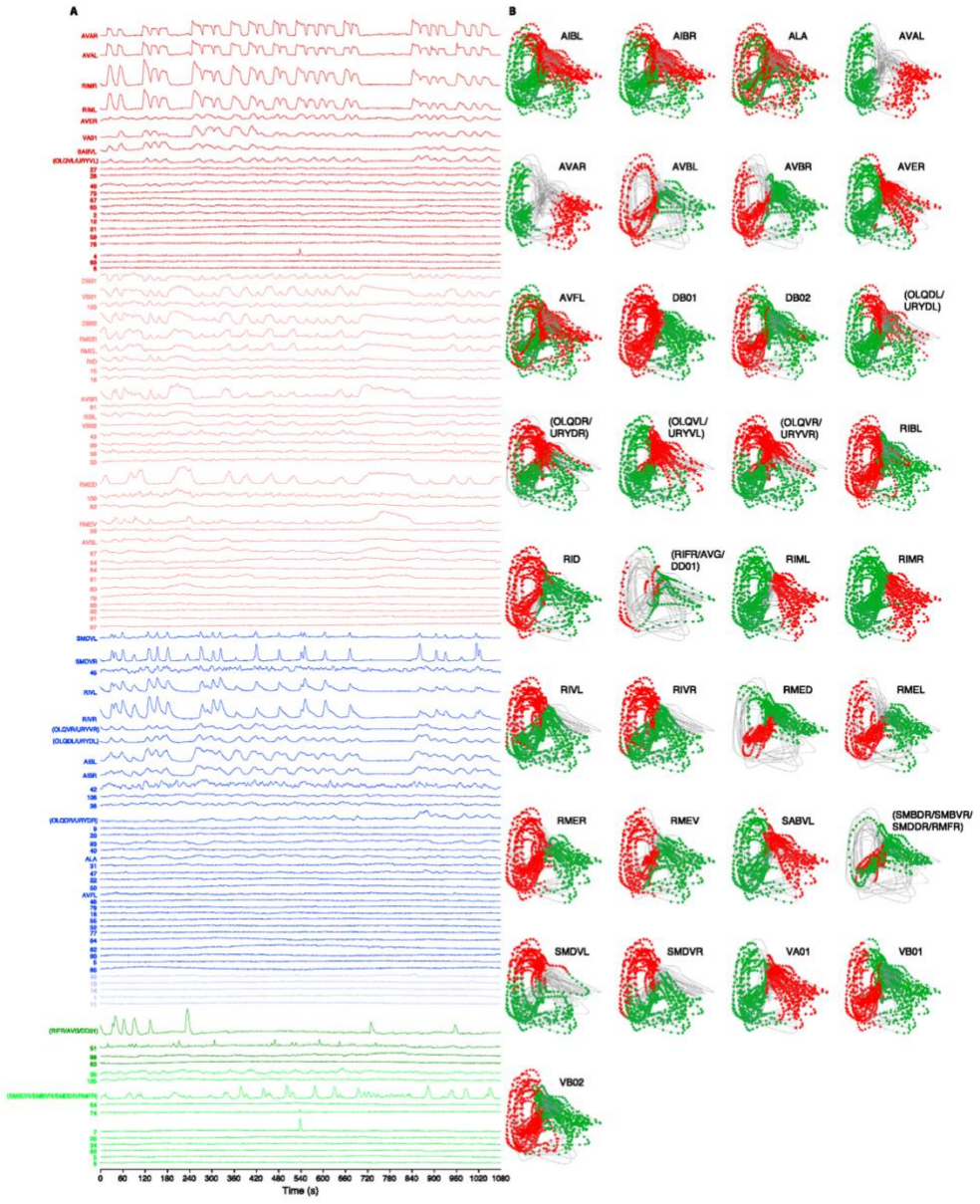

(legend on next page)

Cell

Figure S1. Patterns of Neuronal Recruitment Map to Sub-regions of the Neural State Manifold, Related to Figure 1

Data are from the same example recording shown in Figure 1.

(A) Single traces of all recorded neurons colored and grouped by their maximum principal component weight (out of PC1–3) and sign as in Figure 1.

(B) Each panel is a phase plot of the first two temporal PCs as in Figure 1G. All panels are labeled by the Ca^{2+} rise (red balls) and fall (green balls) phases of the indicated neurons. Note that each neuron is recruited to a class-specific sub-region on the manifold. Ambiguous neuron IDs are shown in parentheses.

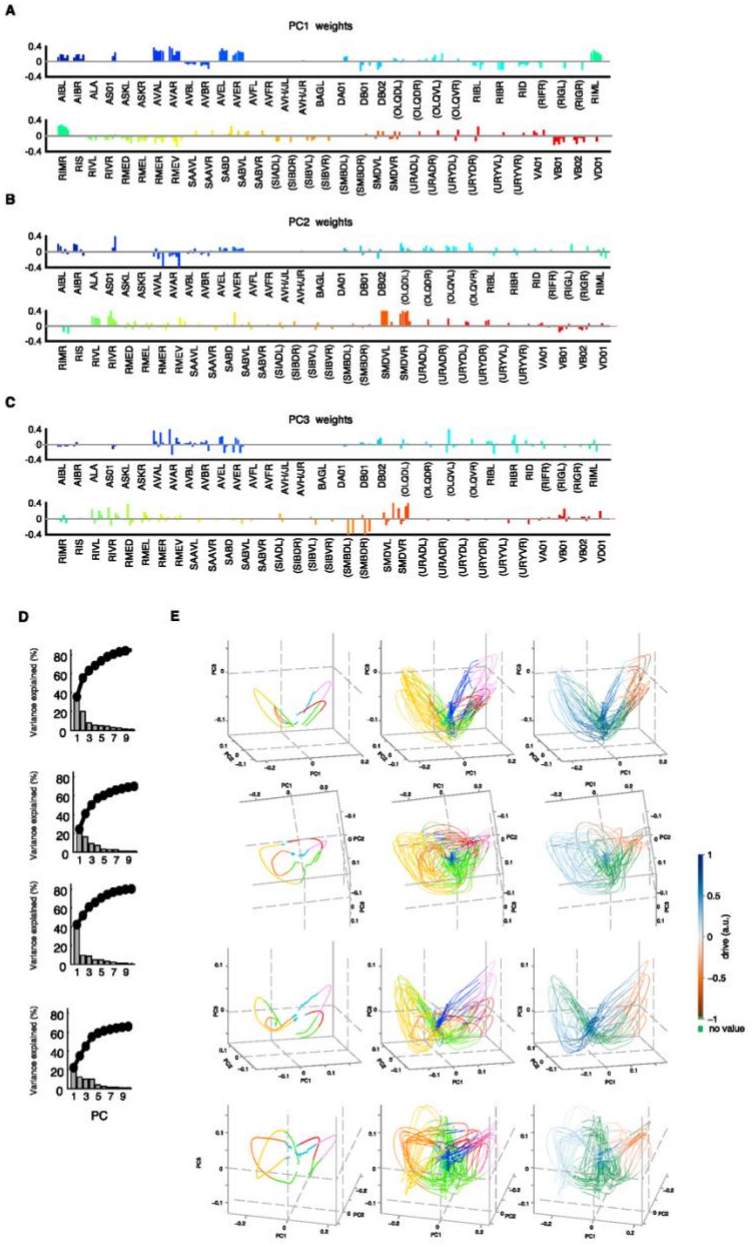

(legend on next page)

Figure S2. Inter-trial Variability of PC1–3 Compositions and Manifold Structure, Related to Figure 1

(A) PC1 coefficients for the 5 trials, grouped by neuron identity, and in order of trial.

(B and C) (B) PC2 coefficients, (C) PC3 coefficients. Not every neuron was identified in all 5 trials; blank values indicate that the neuron was not identified in that trial. Inter-trial regularity of coefficients show that the same neuron-specific dynamical features tend to dominate the global brain signal. Ambiguous neuron class IDs are in parentheses. Additional candidates: URA: URY; OLQ: URY; URY: OLQ; RIF: AVG/DD01; SMB: SMD/RMF; SIA: SIB; SIB: SIA; RIG: RIF/DB.

(D) Percentage variance explained for the 4 additional trials; same analysis as in Figure 1E.

(E) Repetitions of the state space trajectory analysis in Figures 4B, 4C, and 4F on the 4 additional animals included in all analysis. RISE/FALL bundle separations are visible. The orientation of the manifold relative to the PC2 and PC3 axes varied, so the camera viewpoint was rotated to visually match manifold geometry between trials.

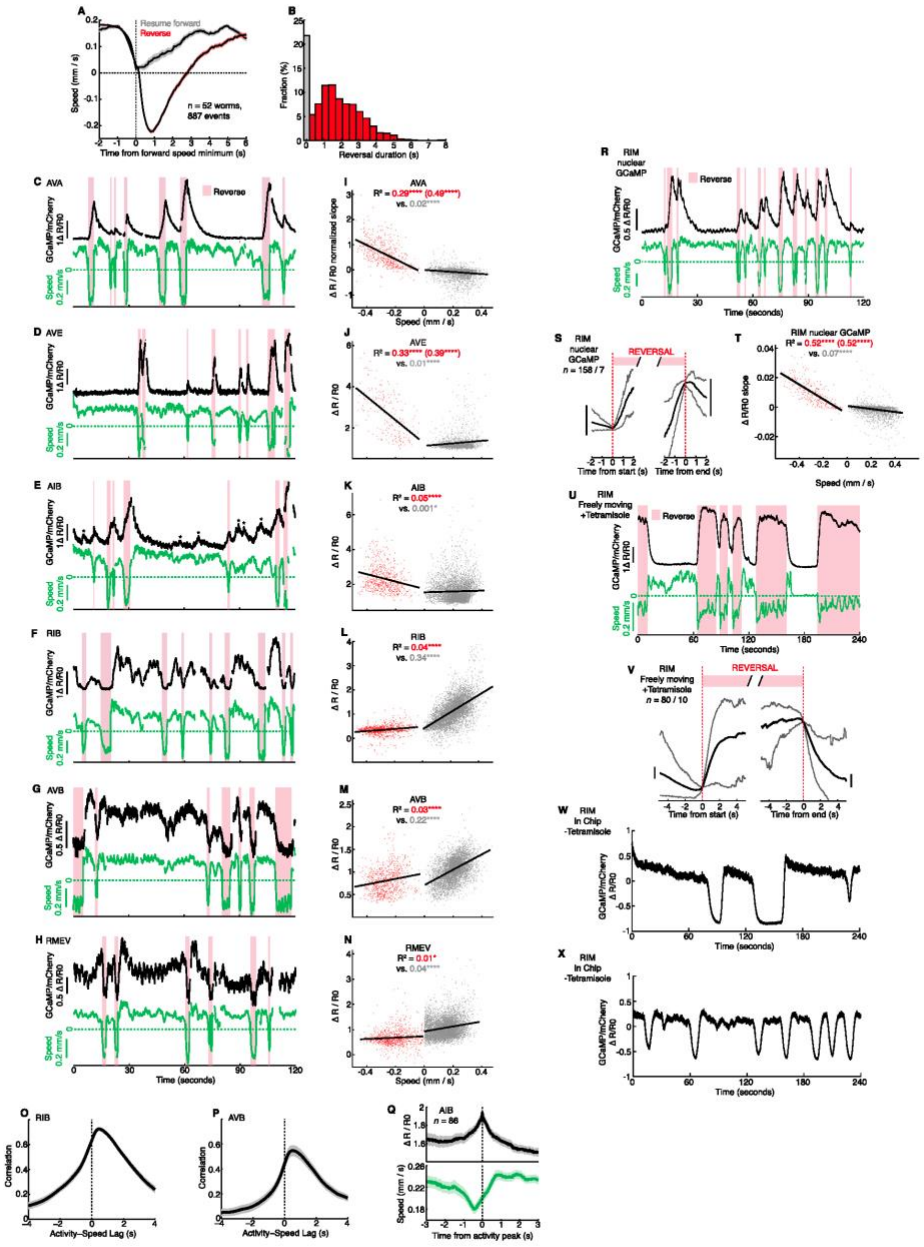

(legend on next page)

Figure S3. Several Interneurons Encode Motor State and Crawling Speed, and HIGH States Are Caused by Tetramisole or Confinement Alone, Related to Figures 2 and 4

(A) Crawling speed during spontaneous slowing events. Traces show event-triggered average speed (±SEM) aligned to forward speed minimum before transition to reversal (red) or resumption of forward crawling (gray). Reversal speed is shown as negative.

(B) Fractional histogram of reversal duration after slowing events; 0 bin corresponds to no reversal.

(C–Q) Ca^{2+} imaging in freely moving animals (same recordings as in Figure 2H).

(C–H) Example traces showing the activities of indicated neurons by normalized GCaMP/mCherry fluorescence ratio (black) and corresponding crawling speed (green). Pink bars overlay reverse crawling periods. (C) AVA, co-recorded with RIM (Figure 2F). Synchronous activity between AVA and RIM was seen across 5 such co-recordings. (D) AVE. (E) AIB. (F) RIB. (G) AVB. (H) RMEV.

(I–N), Regression analysis of crawling speed versus normalized Ca^{2+} signal slope (I) or absolute Ca^{2+} signal (J-N) for the indicated neurons. R^2 indicates goodness of fit for linear fits to reverse (red; parentheses indicate R^2 for one maximum value for each individual reversal) and forward (gray) groups. Number of recordings is the same as in Figure 2H. Permutation test p-value: ****$p < 0.0001$ *$p < 0.05$.

(O and P) Average cross-correlation (±SEM) between Ca^{2+}-signal and crawling speed during forward movement, for RIB (O) and AVB (P). Sharp drop in correlation magnitude from t = 0 indicates that these neurons correlate with forward speed as it changes on the order of seconds.

(Q) Event-triggered averages of AIB activity (±SEM, upper panel) and crawling speed (±SEM, lower panel) aligned to activity peaks detected during forward movement, as shown by asterisks in (E).

(R–T) RIM Ca^{2+}-imaging recorded using nuclear-localized GCaMP.

(R) Example trace showing normalized GCaMP/mCherry fluorescence ratio (black) and corresponding crawling speed (green). Pink bars overlay reverse crawling periods.

(S) Event-triggered averages of Ca^{2+}-signals aligned to reversal onset (left) or reversal end (right). Number of recorded worms and events are indicated. Vertical line next to each trace indicates 0.5 $\Delta R/R_0$. Compare to Figure 2H, top row.

(T) Regression analysis of crawling speed versus Ca^{2+}-signal. R^2 indicates goodness of fit for linear fits to reverse (red; parentheses indicate R^2 for one maximum value for each individual reversal) and forward (gray) groups. Compare to Figure 2G.

(U and V) RIM Ca^{2+}-imaging in worms able to move freely on the imaging pad, after application of tetramisole.

(U) Example trace showing normalized GCaMP/mCherry fluorescence ratio (black) and corresponding crawling speed (green). Pink bars overlay reverse crawling periods.

(V) Event-triggered average of neuronal activity aligned to reversal onset (left) or reversal end (right). Upper and lower traces represent 90^{th} and 10^{th} percentile of all data, respectively. Number of recorded worms and events are indicated. Vertical line next to each trace indicates 0.5 $\Delta R/R_0$. Compare to Figure 2H, top row; note different x-axes. (W-X) Two example traces of RIM Ca^{2+}-activity in worms confined to the imaging chip ("in chip") without tetramisole application. High states are observed in all such worms (n = 8).

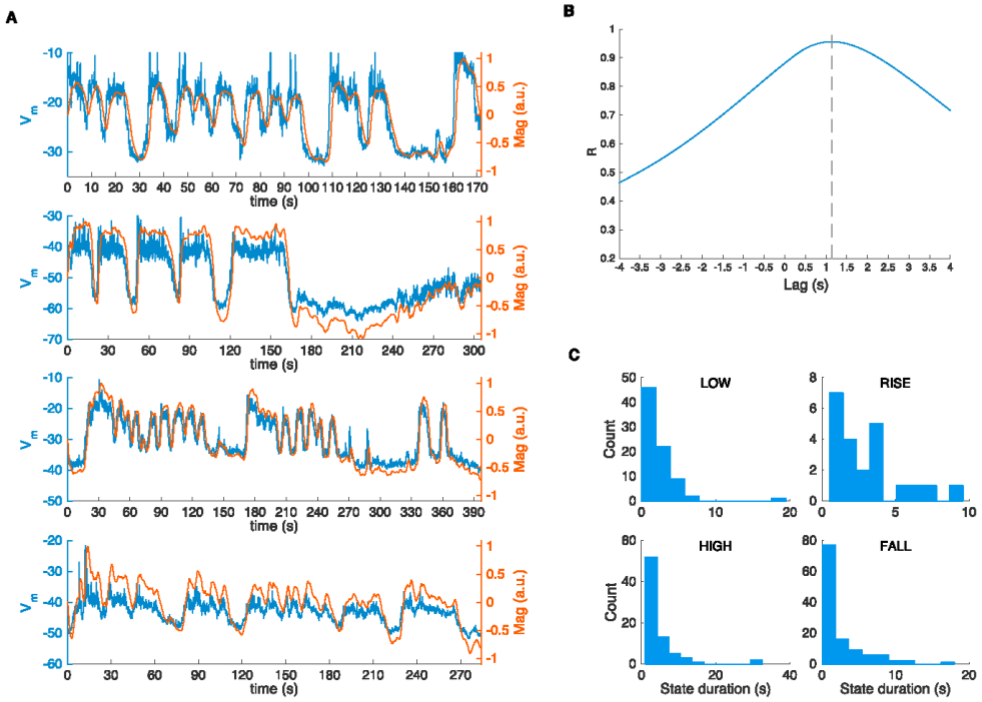

Figure S4. AVA Membrane Voltage Displays Four Long-Lived Phases Similar to Nuclear GCaMP, Related to Figure 4

(A) Membrane voltage V_m in blue and simulated nuclear GCaMP traces in orange. Membrane voltage was measured using the electrophysiological preparation used in reference Lindsay et al. (2011). The nuclear GCaMP signal was simulated by convolving V_m with an alpha-function filter based on kinetic parameters (.06 s rise $t_{1/2}$, 0.28 s fall $t_{1/2}$) of GCaMP5K reported elsewhere (Chen et al., 2013) to simulate a cytoplasmic GCaMP signal, followed by convolution with a single-exponential filter with a time constant of 0.9 s to model the temporal filtering due to nuclear localization. This filter timescale was estimated by fitting the transformation between trial-averaged sensory-evoked transient responses using GCaMP5K and NLS-GCaMP5K from Schrödel et al. (2013) in BAG and URX sensory neurons. Both neurons gave similar estimates.

(B) Cross-correlation between V_m and simulated nuclear GCaMP5K signals yields a lag of 1.16 s. This represents the upper bound of the delay between V_m and Ca^{2+} phase onsets.

(C) Distributions of state durations measured from the V_m traces in (A). Note that all 4 states are long-lived.

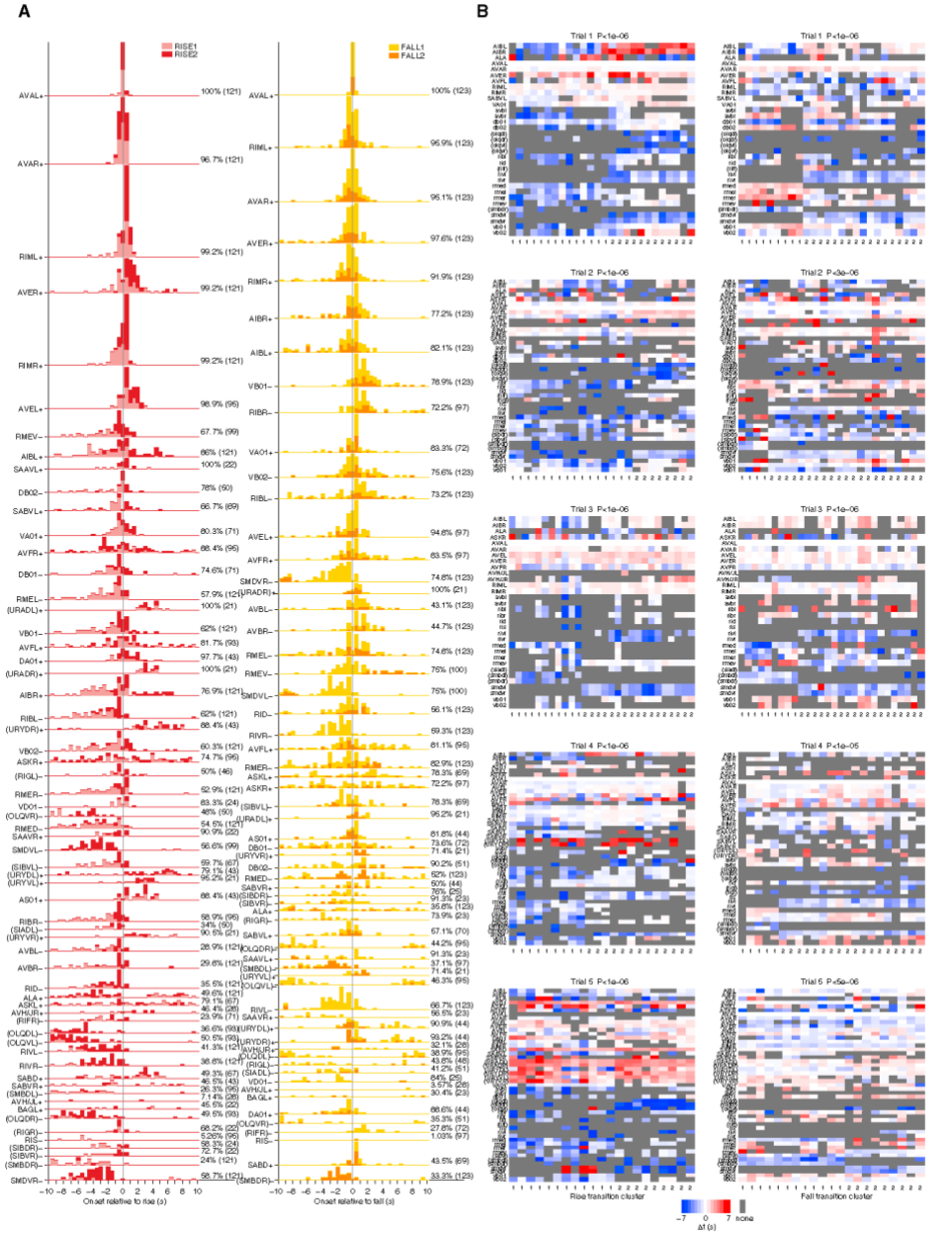

(legend on next page)

Figure S5. Phase Timing Analysis and Clustering, Related to Figure 4

(A) Cumulative histograms of rise-phase onset times (left column) and fall-phase onset times (right column) for all identified neurons, relative to AVA reference neuron transitions across 5 datasets, limited to transitions within −10 to +10 s of reference transition. Colors are assigned to each histogram point by its cluster membership as indicated by the legend; histograms for each cluster are stacked. Each neuron was assigned a polarity based on the sign of its largest PC contribution, indicated by + or -. Transitions were matched to transitions of the same kind (fall-to-fall, rise-to-rise) for + polarity neurons, whereas transitions were matched to transitions of the opposite kind (fall-to-rise, rise-to-fall) for - polarity neurons. Percentage indicates proportion of transitions in which that neuron displayed a transition in the relative time window, and number in parenthesis indicates the total number of transitions across the trials for which that neuron was identified. Left column shows rise-phase histograms, right column shows fall-phase histograms.

(B) Results of k-means clustering, using L_1 distance, on transition timing vectors for all labeled neurons, for 5 datasets. Each column corresponds to a reference transition, composed of a relative transition time for each labeled neuron, and clustering re-orders the columns into two groups. Grey squares indicate that there was no transition detected in the −7 to 7 s window for that neuron, for which a value of −10 was assigned for the purposes of computing vector distances. Left column shows rise-phase transition timing; right column shows fall-phase transition timing. Ambiguous neuron class IDs are in parentheses. Additional candidates: URA: URY; OLQ: URY; URY: OLQ; RIF: AVG/DD01; SMB: SMD/RMF; SIA: SIB; SIB: SIA; RIG: RIF/DB. p values are calculated by a permutation test and indicate the probability that the ratio of the average pairwise inter-cluster distance to the average pairwise intra-cluster distance occurred by chance, under a random cluster assignment.

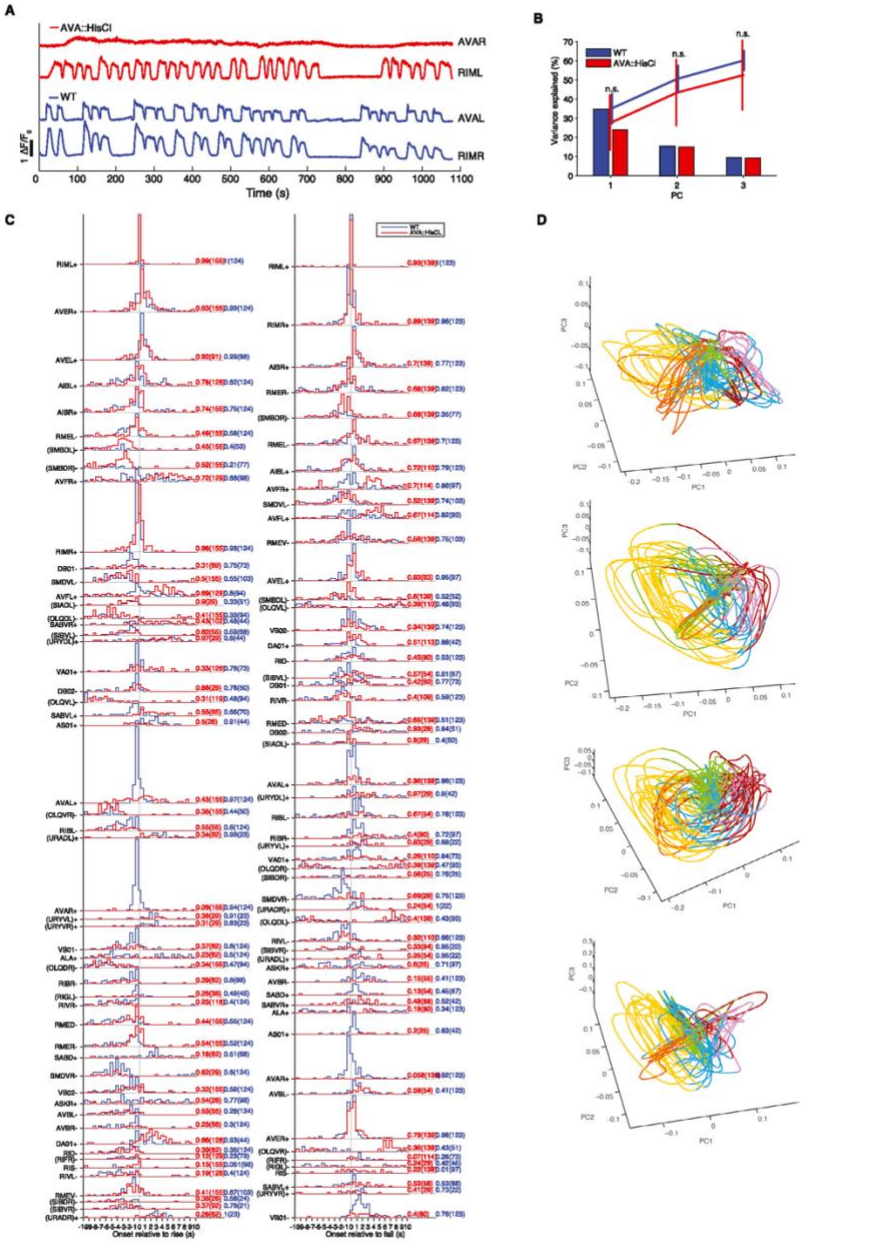

(legend on next page)

Figure S6. Phase Relationships Are Preserved Despite AVA Silencing, Related to Figure 5

(A) HisCl applied to AVA::HisCl worms silenced most transient activity in AVAR while RIM dynamics retained wild-type appearance.

(B) Variance explained of the top 3 PCs in AVA::HisCl (red) versus wild-type (blue), with cumulative variance explained shown as a line, and SEM as vertical lines (n = 5 for both). 3 dimensions still dominated the activity time series in AVA silenced trials.

(C) Cumulative histograms of relative phase transition times similar to Figure S5 for AVA::HisCl worms versus wild-type, using RIML as the timing reference instead of AVAL for both groups, since AVA neurons were inactivated in AVA::HisCl trials. Aside from AVA, most phase relationships to the global brain cycle were intact.

(D) Phase plots of repeated trials from AVA silenced worms.

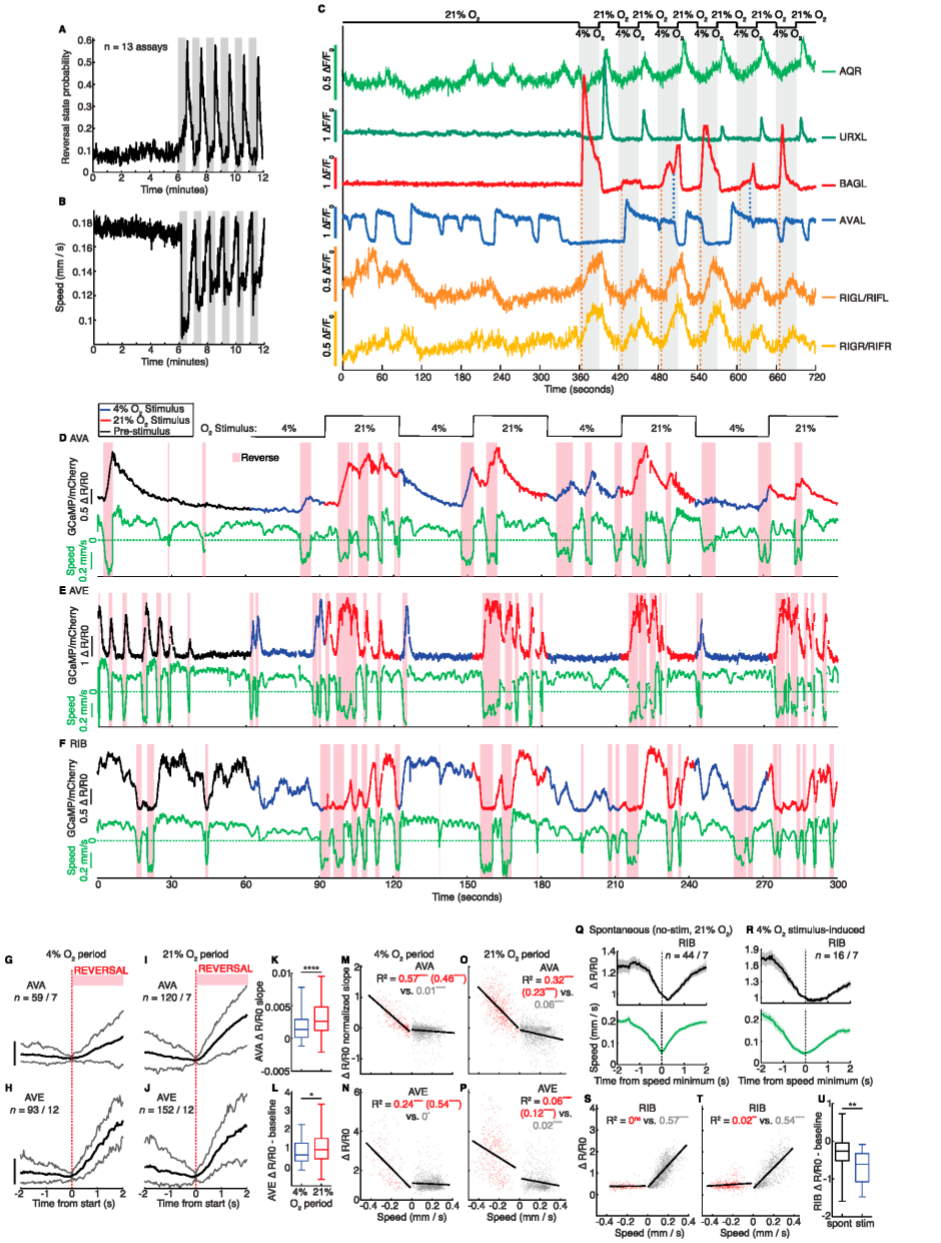

(legend on next page)

Figure S7. O_2 Stimulation Probabilistically Modulates Behavior and Brain State, Which Feeds Back onto Sensory Neuron Activity, and Interneurons Are Modified by O_2 Stimulation but Maintain Strict Motor State Relationships, Related to Figure 6

(A and B) Population behavior assays using the same O_2 stimulation protocol as in Figure 6. Grey bars mark 4% O_2; all other periods are at 21% O_2. 20-25 worms per assay; number of assays is indicated.

(A) Reversal state probability is entrained by stimulus.

(B) Average forward crawling speed is also entrained.

(C) Example traces of neuronal activity during O_2 stimulation protocol. Gray bars indicate 4% O_2. AQR and URX are reliably activated upon O_2 upshifts whereas BAG is activated upon O_2 downshifts. Dashed blue lines mark secondary BAG transients coincident with AVA FALLs. One ventral ganglion neuron class, RIG or RIF, was the only non-sensory neuron found to represent the O_2 stimulus. Using marker lines we confirmed that this neuron class expresses *sra-11* but not *flp-18*, yet this did not allow unambiguous identification. However, the strong synaptic coupling to BAG suggests RIG as the strongest candidate.

(D–U) Ca^{2+} imaging in freely moving animals under O_2 stimulation. Data are divided into pre-stimulus (black, constant 21% O_2 after pre-incubation at 21% O_2), 4% O_2 stimulus (red), and 21% O_2 stimulus (blue) periods.

(D–F) Example traces showing the activities of AVA (D), AVE (E), and RIB (F). Corresponding crawling speed is shown in green. Pink bars overlay reverse crawling periods.

(G–J) Event-triggered average of AVA (G, I) or AVE (H, J) neuronal activity aligned to reversal onset during either 4% O_2 (G–H) or 21% O_2 (I–J) stimulus periods. Number of recorded worms and events is indicated. Vertical line next to each trace indicates 0.25 $\Delta R/R_0$ (G, I) or 1 $\Delta R/R_0$ (H, J).

(K–L), Quantifications of interneuron activities during events shown in (G–J). Boxes show median and 25th to 75th percentiles, and whiskers show min to max.

(K) Average AVA Ca^{2+} signal slope for reversals that occurred during either 4% (blue) or 21% (red) O_2 stimulus periods. Mann-Whitney test $p < 0.0001$.

(L) Average AVE Ca^{2+} signal change minus pre-reversal baseline for reversals that occurred during either 4% (blue) or 21% (red) O_2 stimulus periods. Mann-Whitney test $p < 0.05$.

(M–P) Regression analysis using all AVA and AVE recordings of crawling speed versus normalized Ca^{2+}-signal slope (M, O) or absolute Ca^{2+} signal (N, P) during either 4% (M-N) or 21% (O-P) O_2 stimulus periods for the indicated neurons. R^2 indicates goodness of fit for linear fits to reverse (red; parentheses indicate R^2 for one maximum value for each individual reversal) and forward (gray) groups. Permutation test p-value: ****$p < 0.0001$ **$p < 0.01$ *$p < 0.05$ ^{ns}not significant. Compare to Figures S3I and S3J, respectively. Interestingly, AVE loses its relationship with reverse crawling speed during 21% O_2 stimulation, indicating a more complex effect of stimulus on AVE than on AVA or RIB.

(Q–R) Event-triggered averages of RIB activity (±SEM, upper panels) and crawling speed (±SEM, lower panels) aligned to speed minima of slowing events without reversals, made either spontaneously (Q: constant 21% O_2 after pre-incubation at 21% O_2) or induced by O_2 downshift (R: event occurs within first 5 s following shift to 4% O_2). Number of recorded worms and events is indicated.

(S and T) Regression analysis of crawling speed versus absolute Ca^{2+} signal for all RIB recordings during either 4% (S) or 21% (T) O_2 stimulus periods. R^2 indicates goodness of fit for linear fits to reverse (red) and forward (gray) groups. Compare to Figure S3L.

(U) RIB Ca^{2+} signal change from baseline during slowing events that occurred spontaneously (black) or induced by O_2 downshift (blue). Average Ca^{2+} signal was calculated from a 0.5 s window surrounding either the slowing minimum or two seconds earlier (baseline). Quantifications of interneuron activities during events shown in (Q–R). Boxes show median and 25th to 75th percentiles, and whiskers show min to max. Mann-Whitney test $p < 0.01$.

Cell
Supplemental Information

Global Brain Dynamics Embed the Motor Command Sequence of *Caenorhabditis elegans*

Saul Kato, Harris S. Kaplan, Tina Schrödel, Susanne Skora, Theodore H. Lindsay, Eviatar Yemini, Shawn Lockery, and Manuel Zimmer

Supplemental Experimental Procedures

Whole-brain Ca^{2+} imaging of *C. elegans* head ganglia neurons

Two-layer PDMS microfluidic devices were manufactured as described previously (Zimmer et al., 2009). The chip design was comprised of a curved worm channel to laterally align animals as described previously (Cáceres et al., 2012) with a straight elongation of the channel after the curve to obtain a straight body posture of the worm during imaging. Gas flow (50 ml/min) in the device was controlled using a static gas mixer connected to mass flow controllers (Vögtling Instruments) operated by LabView software. Different O_2 concentrations were balanced with N_2. The worm channel was connected by Tygon or polyethylene tubing to a reservoir containing nematode growth medium (NGM) and 1 mM tetramisole. Adult worms (carrying zero to four eggs) were picked on food-free NGM agar plates in a drop of NGM with 1mM tetramisole and aspirated into the worm channel. Recordings were started within 5 minutes after removal from food. Illumination and piezo stage were switched on 2 minutes prior to recording. Worms were either imaged for 18 minutes at constant 21% O_2, or for the stimulus protocol, they were imaged for 12 minutes with the first 6 minutes at 21% O_2 and the remaining 6 minutes with 30 s consecutive shifts between 4% and 21% O_2. Data was acquired using an inverted spinning disc microscope (UltraViewVoX, PerkinElmer) equipped with an EMCCD camera (C9100-13, Hamamatsu). Read-out area on the camera chip was 150-170 x 512 pixels, translating to a field of view of 50-56 x 170 µm on the sample, which was divided into 11-12 z-planes spaced by 2 µm. These settings allowed an imaging rate of 2.6 – 3 volumes per second. To inhibit AVA in HisCl expressing lines, worms were incubated for 30-45 min on OP50 seeded NGM agar plates including 20 mM histamine (histamine dihydrochloride, Sigma-Aldrich) before loading them into the worm channel filled with NGM containing 10 mM histamine.

Electrophysiology

Records of AVA membrane potential were extracted from a database of current clamp recordings collected but not reported in previous studies. Briefly, recording pipettes were pulled and pressure-polished to achieve resistances of 10–20 MΩ when filled with normal internal saline. The AVA neuron was identified by targeted expression of tdTomato using the *nmr-1* promoter followed by assessment of the time and voltage dependence of cell-intrinsic currents as described previously (Lindsay et al., 2011). Pulses used to calculate whole-cell capacitance and series resistance were filtered at 50 kHz and sampled at 125 kHz. All cells reported here had a whole cell capacitance of > 0.2 pF. Current-clamp recordings of membrane potential, were filtered at 2 kHz, sampled at 10 kHz and corrected for the liquid junction potential post-hoc. Depending on the resting membrane potential, 0-3 pA of constant negative current was injected to compensate for the large depolarizing effect of the leak conductance generated when patching high input resistance cells (Barry and Lynch, 1991). Internal saline consisted of 143 mM K-gluconate , 1 mM CaCl2,, 4 mM NaCl, 1 mM MgCl2, 10 mM HEPES, 10 mM EGTA, pH 7.2 (KOH). External saline consisted of 5 mM KCl, 10 mM HEPES, 8 mM CaCl2, 143 mM NaCl, 30 mM glucose, pH 7.2 (NaOH).

Simulation of nuclear GCaMP signals from voltage traces

To simulate the nuclear GCaMP5K signal that would be generated from an underlying membrane voltage signal, we convolved voltage traces with a kernel based on GCaMP5K dynamical parameters reported elsewhere (Chen et al., 2013), followed by convolution with a single exponential kernel with =0.9 sec, to model the transformation between the cytoplasmic GCaMP signal and a nuclear localized GcaMP signal. This time constant was determined by an optimization procedure, minimizing the difference between trial-averaged nuclear localized GcaMP5K step responses of BAG neurons versus putatively convolved trial-averaged cytoplasmic

GcaMP5K step responses, data taken from (Schrödel et al., 2013). We neglect the transformation between voltage and Ca^{2+}, which we expect to be much faster than the other processes and thus not appreciably affect the overall temporal effects.

Ca^{2+} imaging in freely moving animals

Ca^{2+} imaging recordings were made using the automatic re-centering system described previously (Faumont et al., 2011). Young adult worms (0-8 eggs) expressed both mCherry and GCaMP in the neuron of interest; mCherry expression was optimized to allow sufficient signal intensities required for efficient tracking, while GCaMP expression was kept relatively low, which in our experience leads to higher dynamic range signals in neurons. Animals were picked and transferred onto a growth medium (NGM) plate to allow crawling away from food, then placed on a NGM agarose pad and sealed in a custom built microscope stage containing an airtight chamber with inlet and outlet connectors for gas flow delivery. Worms were given five minutes to acclimate to the pad and to the 21% O_2 flow conditions before recordings began. For **Figure 2**, **Figure 3**, and **Figure S3**, each worm was recorded for 3-4 minutes. For **Figure S7**, each worm was recorded for 1 minute at 21% O_2 prior to either 8 (AVE) or 12 (AVA, RIB) consecutive O_2 up- and down-shifts lasting 30 s each.

Preparation of homogeneously thick NGM agarose pads required for imaging was achieved as follows: agarose was melted and poured into a ring 2.45 mm thick and 50 mm in diameter and enclosed with glass on both sides to harden into a smooth surface. A ring of 38 mm diameter was pressed onto the agarose to produce an indentation into which a repellent $CuCl_2$ (20 mM) solution was pipetted to restrict the worm to the pad center. The pad was placed inside the chamber, which was sealed shut and covered with a 0.55 mm thick glass slide 0.7 mm from the agarose surface. This created a perpendicular homogeneous surface below the flow chamber both

within the working distance of the objective lens. The chamber was then placed into a motorized stage with associated controller (MS-2000-PhotoTrack, Applied Scientific Instrumentation). Images were acquired on an inverted compound microscope (Zeiss Axio Observer.Z1) using two CCD cameras (Evolve 512, Photometrics). Excitation light (470nm and 585nm) was provided by a CoolLED pE excitation system simultaneously using an ET-EGFP/mCherry filter set (59022x, Chroma) and dichroic (59022bs, Chroma). A long-distance 63x objective (Zeiss LD Plan-Neofluar 63x, 0.75 NA) was used to obtain unbinned images at 33 ms exposure time with VisiView software (Visitron Systems GmbH, Germany). A dichroic mirror (620 spxr, Chroma) directed high wavelength mCherry emission to a four-quadrant photomultiplier tube (Hamamatsu) for re-centering. The remaining emission was split by a DualCam DC2 cube (565 lpxr, Photometrics) to each of the two CCD cameras, one for mCherry emission (641/75nm, Brightline) and one for GCaMP emission (520/35nm, Brightline). mCherry emission was further reduced by 50% via a neutral density filter to prevent signal saturation. Simultaneous behavior recordings under infrared illumination (780nm) were made using a CCD camera (Manta Prosilica GigE, Applied Vision Technologies) at 4x magnification and 100 ms exposure time.

GCaMP and mCherry signals were quantified either by custom MATLAB scripts (The MathWorks) if the neuron was the only or brightest cell expressing mCherry or by MetaMorph software (Molecular Devices) if several neurons were labeled. The brighter mCherry signals were used as analysis tracking targets to determine a region of interest (ROI) used to record the dimmer GCaMP signals. Signals were measured as integrated fluorescence over the ROI, subtracting a background value computed per recording, taken from the first frame using the same sized ROI on a region in the worm's head lacking labeled neurons. The GCaMP/mCherry ratio was then divided by an R_0 value calculated within each recording as either the mean ratio over the entire recording (for fluctuating neurons RIB, SMDV, AVB, RMEV, or RID) or

the mean of the lowest 10% of ratio values (for occasional spiking neurons RIM, AVA, AVE, and AIB) to avoid biasing by variability in animal behavior.

Ca^{2+} signals used to calculate event-triggered averages had their $\Delta R/R_0$ values shifted (added or subtracted) such that all events had the same value at t = 0. RIM and AVA slopes were calculated as de-noised time derivatives as described below. AVA slope and SMDV activity, for **Figures S3I**, **S7M, S7O** and for **Figure 3E** respectively, were peak-normalized within recordings. For **Figure 3E** head-bend angle was normalized to the standard deviation within each recording. Data in speed versus activity scatterplots were found by binning each individual reverse and forward locomotion period into 0.5 s bins and averaging within bins. To avoid spurious correlations due to coincident rise-phases of Ca^{2+} activity and reversal speed, single values for speed and rise-phase slope (RIM, AVA) or magnitude (AVE) were calculated for each reversal by averaging all data above median speed or Ca^{2+} activity; R^2 for these data are given in parentheses in each figure panel. Ca^{2+} activity data in **Figure 3E** were found by averaging data points within 1.5 s on either side of the head-bend peak angle frame, and control bend Ca^{2+} activity data were found using the same procedure on Ca^{2+} activity occurring with the head-bend peak found following randomly selected time points during forward movement, as if these random time points were reversal offsets. All p-values for R^2 were determined by bootstrapping: data were randomly permuted and R^2 was calculated 10^6 times, and p-value was calculated as the fraction of R^2 values greater than the R^2 of the non-permuted data. Activity peaks (after peak-normalization) and speed minima in **Figure S3Q** and **S7Q-R** were found using a peak-detection algorithm.

Freely moving + tetramisole recordings were made by applying 1-5mM tetramisole to worms placed on the imaging pad. Freely moving + or - histamine recordings were made by placing worms on food-seeded NGM plates + or - 20mM histamine 30-45

minutes prior to imaging and, in both experimental and control cases, recording them on pads lacking histamine.

Behavior tracking in single freely moving animals

Reversals and omega turns were identified manually, blind to corresponding neural activity data, by examining infrared movies and x-y plots of stage position captured with every Ca^{2+} imaging frame. All time points not marked as reversals were considered forward movement for computing speed correlations. Bends where the worm's head touched or nearly touched its tail were classified as omega turns. Body angles were determined using a skeletonization procedure on the infrared movies (Yemini et al., 2013), and the first of nine resulting segment angles was selected as the head-bend angle. The post-reversal head-bend was marked as the first peak in head-bend angle following reversal offset, and often closely or exactly coincided with reversal offset. Ventral vs. dorsal direction was determined by the co-recorded mCherry expression pattern. Speed was calculated according to x-y stage position, smoothed, and marked as negative wherever worms were reversing. Speed minima in **Figure S7Q-R** were found using a peak-detection algorithm on these data.

Region of interest (ROI) detection from volumetric Ca^{2+}-imaging data

Inter-frame motion was computed for each time step of each image plane using discrete Fourier transform based sub-pixel image registration (Guizar-Sicairos et al., 2008). A reference ROI movie was composed for each image plane by averaging successive blocks of 100 movie frames to reduce noise. Each frame of the reference movie was adaptively thresholded based on the median image brightness plus an offset and median filtered with a 3x3 block to de-noise, then local maxima pixels were found. Local maxima closer than 5 pixels were merged using a greedy algorithm to produce single plane, single frame ROI centers. For each ROI center in each frame, a 5-pixel radius circular ROI was defined. Overlapping ROI areas were

removed using Voronoi tessellation with area shrinkage applied to leave a 0.5 pixel margin between ROIs, thereby leaving a thin frame of pixels not in any ROI to be used for background subtraction described below. ROIs in adjacent reference movie frames were adjoined using a greedy algorithm based on closest distance relative to global inter-frame motion, subject to a maximum x-y acceleration of 5 pixels/frame^2, to produce time-varying ROIs spanning the time range of the movie for which the ROI center was detectable. To track cells that fell below the detection threshold for spans of time, then reappeared, the positions of ROIs that terminated mid-movie were extrapolated based on the motion of neighboring ROIs within 20 pixels and adjoined to proximate ROIs that appeared mid-movie. Finally, time-varying, multi-plane regions of interest ("4D-ROIs") were created by adjoining the time-varying ROIs present in adjacent Z-planes with overlapping x-y extent, producing one spacetime voxel set. Ambiguities in the ROI adjoining process were resolved by human judgment during a proof-checking phase. ROIs that identified non-neuronal recording artifacts, such as gut autofluorescence, were removed during this phase. Occasionally, additional neurons were observed that were not identified using the above detection scheme. ROI centers for these neurons were determined by measuring a fixed displacement from an existing ROI nearby and maintaining that relative spatial displacement throughout the recording, and 5-pixel radius, single-Z plane time-varying ROIs were defined for these neurons.

Neural time series extraction

For each 4D-ROI, a single-cell fluorescence intensity F was computed by taking the average of the brightest 75 voxels at every time point after subtracting a z-plane specific background fluorescence intensity. Background values were computed by averaging pixels not belonging to any ROI (see prior section) within a radius of 16 pixels from the ROI center. $\Delta F/F_0$ was computed for each neuron with F_0 taken as the mean fluorescence intensity across the trial.

Identification of head ganglia neurons

In each recording we detected 107-131 neurons, covering 55-67% of expected neurons in the imaging area. As previously determined (Schrödel et al., 2013), many neurons remain undetected due to inactivity and low Ca^{2+}-levels, as well as lack of neuronal marker expression. Neurons were identified taking into account their anatomical positions, also in relation to surrounding neurons (www.wormatlas.org), and their activity patterns. To confirm ambiguous neuron identities, marker lines expressing red fluorophores in neurons of interest were generated and crossed to the imaging line expressing GCaMP5K pan-neuronally in the nucleus (ZIM504). Immediately before recording Ca^{2+} traces in these lines one dual-color stack was acquired allowing unambiguous mapping of red fluorophore expression to tracked ROIs. Neurons with identities confirmed by marker expression that showed specific activity patterns and similar anatomical positions could then also be identified in recordings without markers. In some cases neuron identities were ambiguous if no specific marker could be found or if, within the same anatomical region, there were more than one neuron class showing a similar activity pattern. In these cases we denote neuron class identities in parentheses and provide all additional possible candidates in figure legends. All neurons that could not be assigned to a certain class, but had well defined locations and distinct activity patterns were labelled identically across different recordings. Marker lines are provided in the strain list below.

Population behavioral assays

For behavior assays (**Figure 5A**; **Figure S7A-B**) 20-25 adult worms grown on OP50 seeded food plates were picked food free on a NGM agar plate without food. The 36 mm x 36 mm assay arena was confined by Whatman paper soaked with 20 mM $CuCl_2$, a repellent, to prevent worms from leaving the arena. Gas flow (25 ml/min)

was delivered through a transparent plexiglas device with a flow arena of 39 mm x 39 mm x 0.7 mm placed on top of the assay arena and controlled using a static gas mixer connected to mass flow controllers (Vögtling Instruments) operated by LabView software. The 12 min stimulus protocol was the same as for whole-brain imaging experiments (6 min at 21% O_2 followed by six consecutive 30 s shifts to 4% O_2 and back to 21%). During illumination with red LED animals were recorded at 10 fps using a 4 megapixel CCD (Jai) camera and Streampix software. Movie analysis and reversal detection was performed using Matlab-based tracking software as described before (Chalasani et al., 2007; Ramot et al., 2008; Zimmer et al., 2009). Worms were pre-incubated at constant 21% O_2 on the assay arena for 5 min before recordings were started to accustom them to the gas flow.

For inhibition of AVA in HisCl expressing lines, worms were treated as described in (Pokala et al., 2014). Briefly, they were incubated for 30-45 min on OP50 seeded NGM agar plates including 20 mM histamine (histamine dihydrochloride, Sigma-Aldrich) before picking them on NGM agar assay plates also containing 20 mM histamine.

Derivatives and PCA on neural time series data

PCA was performed on the time derivatives of $\Delta F/F_0$ neural traces, each normalized by the peak magnitude of corresponding $\Delta F/F_0$ trace. Total-variation regularization (Chartrand, 2011) was used to compute de-noised time derivatives while preserving accuracy of state transition times to within one frame. This numerical differentiation method was also used during 4-phase analysis of neural $\Delta F/F_0$ traces and voltage traces. A 3-sample sliding-average filter was applied to each phase plot trajectory to aid visualization, though all analysis was performed on unfiltered traces. Activity traces of the sensory neurons BAG, URX, and AQR were removed from the analysis

in recordings with sensory stimulus applied. Variance explained for each PC in Figures 1E, S2D and S6 was calculated as described previously (Kato, 2014); here, we defined measured data to be the derivatives of the full neural time series, and we defined reconstructed data to be the sums of projections of the derivative time series onto each temporal PC1 to 10.

4-phase segmentation analysis

Rise phases for neurons were identified as periods when the time derivative was greater than a small threshold, typically 5% of each neuron's full dynamic range, and fall phases for neurons were identified as regions of when the time derivative was less than a small negative threshold, typically 5% of full dynamic range. Using regularization when computing the derivative, in combination with the use of thresholds, rather than simply using any infinitesimal deviation in the derivative from zero, eliminated the presence of spurious short-lived state fluctuations but varying thresholds, up to 10% of the full dynamic range of each neuron, did not significantly affect transition timing relationships. HIGH and LOW phases were then assigned to the remaining periods based on a threshold and lawful phase order, producing a state time series for the neuron in question. For trajectory averaging and generation of phase-registered movies, neuronal time series were registered to a common phase clock by matching phase segment starts and ends followed by linearly interpolating within segments.

Phase timing analysis and clustering

A set of global transitions, either RISE or FALL onsets, were defined by the transitions of a reference neuron (AVA or RIM in our study), since these transitions were sharper than those of the temporal PCs themselves. For each global transition,

each neuron's state time series was scanned to find the nearest transition of matching or opposite type, depending on the neuron's polarity (see below), and was paired with the reference transition. Neurons were assigned to have positive or negative polarity based on the sign of their PC1 weight, or a negative polarity if their PC2 or PC3 weights exceeded that of PC1. For example, AVB falls were paired with AVA rises, and SMDV falls were paired with AVA falls. The relative delays of each of these paired transitions were composed into a vector thus representing the differential activation/deactivation times of the neurons for that brain-wide transition. Each vector was classified as RISE1 vs. RISE2 and FALL1 vs. FALL2 by *K*-means clustering, which was applied to phase timing vectors for a full trial using Euclidean distance and k=2. Missing delay values, indicating a neuron lacking a paired transition within +/- 7 seconds of the reference neuron transition, were assigned a value of -10 for the purposes of computing vector distances. In **Figure 4G-H** we estimated the time course of trajectory separation during RISE1 vs. RISE2 and FALL1 vs. FALL2, including their two adjoining full brain cycles. First we calculated a 6 dimensional vector in PCA phase space for each time point of a trajectory by adjoining a vector of the top 3 temporal PCs instantaneous amplitudes with their derivatives to include also directional information. Next, we calculated the Euclidean distances between trajectories for each time point. Clustering ratio, a normalized measure of separation, was defined as the average inter-cluster distance across all possible pairs of vectors divided by the average intra-cluster distance across all possible pairs of vectors within the same cluster, averaged across both clusters. P-values indicate the probability by which the resultant or higher distance ratios occurred by random cluster assignment. They were computed using an exact permutation test, shuffling cluster labels and recomputing the clustering ratio, 10^6 times.

Canonical trajectory calculation and manifold contour surface extraction

Sets of phase-registered trajectory points, one set for each RISE and each FALL cluster, were extracted at 300 evenly spaced intervals of the phase clocks using linear interpolation, assigning equal clock intervals of π/2 to RISE, HIGH, FALL, and LOW segments. Canonical trajectories were produced by taking the means of each set. For each set, a normal plane to the canonical trajectory was determined by the tangent and position of the mean trajectory for that cluster. Points in the set were projected onto this plane, and PCA was performed on their intrinsic plane coordinates to determine the two principal axes for the point set. These principal axes defined a plane ellipse; the length of the axes was set to the square root of the corresponding eigenvalue, so that each ellipse represented a one-standard-deviation contour line. A triangular-mesh tube for each clustered trajectory in 3D PCA space was generated to connect consecutive elliptical rings sampled at 24 points each.

Behavioral decoding of whole-brain recordings

Each time point of the trajectory was first assigned to a global brain cycle HIGH, LOW, RISE1, RISE2, FALL1, or FALL2 segment as described above, then mapped to motor command states as follows. RISE1 and RISE 2 segments were mapped to REVERSAL1 and REVERSAL2 command states respectively. HIGH segments were mapped to SUSTAINED REVERSAL. FALL1 and FALL2 segments were mapped to VENTRAL TURN and DORSAL TURN respectively. LOW segments were mapped to FORWARD, except that RIB fall phases present during global LOW segments were mapped to FORWARD SLOWING command states.

A speed drive was assigned to each point on the trajectory as follows, aside from those in SUSTAINED REVERSAL phases for which no speed drive was inferred. During VENTRAL TURN, DORSAL TURN, FORWARD, and FORWARD SLOWING phases, positive speed drive was taken to be the magnitude of RIB activity, normalized to its most negative value during the trial. During REVERSAL1 and

REVERSAL2 phases, negative speed drive was taken to be the derivative of RIM neuron activity, normalized to its highest value during the trial.

Entrainment resampling test

To improve statistical power, more datasets (n=13 animals for the stimulus group and n=13 animals for the control group) were generated. At least one AVA neuron was identified in each dataset to determine the brain cycle. For entrainment analysis, resampling for group (stimulus and control) P-value computation was performed by applying the stimulus profile with random phase shifts to either the pre-stimulus period (0 to 6 min) or the stimulus period (6-12 min) to each dataset's state time series, then trial-averaged to produce a 12 point (binning 5 s) time series *p(t)*, like in **Figure 6C**. The procedure was repeated 10^6 times. The test statistic computed for each sample was the accumulated finite difference symmetrized around the midpoint stimulus change time:

$$\sum_{t=2}^{6} p(t) - p(t-1) - \sum_{t=8}^{12} p(t) - p(t-1)$$

which results in high values for data oscillating in phase with the stimulus profile and which results in small values for non-entrained, i.e. random or monotonically drifting data.

Statistical tests

Unless otherwise stated in the figure legends, all p-values of statistical quantities were computed using permutation tests performed by random relabeling of experimental groups or cluster assignments. Following standard statistical procedure, p-values indicated the probability that the measured or greater value of a

given test statistic would occur by drawing from an empirically generated distribution of randomly labelled data.

All computations were performed using custom code in MATLAB.

Strains

Strain name	Experiment	Genotype	Construct (pasmid no.) injection concentrations	Reference for promoter expression pattern
ZIM458	RIM freely-moving imaging	*mzmEx299; lite-1 (xu7)*	P*cex-1*::mCherry (pHK19) 50 ng/µL P*cex-1*::GCaMP5K (pHK21) 50 ng/µL	(Cohen et al., 2009)
ZIM347	AVA & RIM freely-moving imaging	*mzmEx243; lite-1 (xu7)*	P*flp-18*::mCherry (pHK48) 30 ng/µL P*flp-18*::GCaMP5K (pRL62) 30 ng/µL	(Cohen et al., 2009)
ZIM601	AVE freely-moving imaging	*mzmEx389; lite-1(xu7)*	P*opt-3*::tagRFP (pHK146) 50 ng/µL P*opt-3*::GCaMP5K (pRL66) 50 ng/µL	www.wormatlas.org
ZIM519	AIB freely-moving imaging	*mzmEx337; lite-1(xu7)*	P*npr-9*::mCherry (pHK105) 50 ng/µL P*inx-1*::GCaMP5K (pHK55) 50 ng/µL	P*npr-9*: (Luedtke et al., 2010) P*inx-1*: (Altun et al., 2009)
ZIM583	RIB freely-moving imaging	*mzmEx376; lite-1(xu7)*	P*sto-3*::mCherry (pHK129) 20 ng/µL P*sto-3*::G-CaMP6FOPT (pHK130) 5 ng/µL	www.wormatlas.org
ZIM498	AVB freely-moving imaging	*mzmEx324; lite-1(xu7)*	P*sra-11*::mCherry (pHK56) 50 ng/µL P*sra-11*::GCaMP5K (pHK57) 50 ng/µL	(Troemel et al., 1995)
ZIM698	RMEV freely-moving imaging	*mzmEx437; lite-1(xu7)*	P*ser-2*prom2::NLSwCherryNLS (pHK163) 50 ng/µL P*ser-2*prom2::NLSGCaMP6FcodoptNLS (pHK164) 10 ng/µL	(Tsalik et al., 2003)
ZIM813	SMDV freely-moving imaging	*mzmEx488; lite-1(xu7)*	Complex array using bacterial DNA P*unc-7S*::mCherry (pHK173) 5 ng/µL P*unc-7S*::GCaMP6Fcodopt (pHK189) 2 ng/µL	(Starich et al., 2009)
ZIM814	RIM freely-moving imaging + AVAHisCl	*mzmEx299; kyEx4863; lite-1(xu7)*	P*cex-1*::mCherry (pHK19) 50 ng/µL P*cex-1*::GCaMP5K (pHK21) 50 ng/µL P*rig-3*::HisCl1::SL2::mCherry (pNP471) 50 ng/µL	P*rig-3*: (Pokala et al., 2014)
ZIM660	RIM freely-moving nuclear imaging	*mzmEx419; lite-1(xu-7)*	P*cex-1*::NLSwCherryNLS (pHK141) 25 ng/µL P*cex-1*::NLSGCaMP5K (pHK162) 37.5 ng/µL	(Cohen et al., 2009)
ZIM504	Whole-brain	*mzmEx199;*	P*unc-31*::NLSGCaMP5K (pTS36)	(Schrödel et al.,

	imaging	*lite-1 (xu7)*	30ng/µL; *Punc-122*::gfp 15ng/µL	2013)
ZIM756	Whole-brain imaging AVAHisCl	*mzmEx199; kyEx4863; lite-1 (xu7)*	P*unc-31*::NLSGCaMP5K (pTS36) 30ng/µL; P*unc-122*::gfp 15ng/µL; P*rig-3*::HisCl1::SL2::mCherry (pNP471) 50 ng/µL	P*rig-3*: (Pokala et al., 2014)
ZIM871	Whole brain imaging SMDV AVE marker	*mzmEx199; mzmEx536; lite-1 (xu7)*	P*unc-31*::NLSGCaMP5K (pTS36) 30ng/µL; Punc-122::gfp 15ng/ul P*unc-7S*::mCherry::His58 (pHK174) 50ng/µL	P*unc-7S*: (Starich et al., 2009)
ZIM651	Whole brain imaging AIB marker	*mzmEx199; mzmEx412; lite-1 (xu7)*	P*unc-31*::NLSGCaMP5K (pTS36) 30ng/µL; P*unc-122*::gfp 15ng/ul P*inx-1*::NLSwCherryNLS (pHK140) 30ng/µL P*unc-122*::DsRed 20ng/µL	P*inx-1*: (Altun et al., 2009)
ZIM650	Whole brain imaging RIM marker	*mzmEx199; mzmEx411; lite-1 (xu7)*	P*unc-31*::NLSGCaMP5K (pTS36) 30ng/µL; P*unc-122*::gfp 15ng/ul P*cex-1*::NLSwCherryNLS (pHK141) 25ng/µL ;P*unc-122*::DsRed 20ng/µL	(Cohen et al., 2009)
ZIM730	RIB marker	*mzmEx447; lite-1 (xu7)*	P*sto-3*::NLSwCherryNLS (pTS105) 30ng/µL + P*unc-122*::dsRed 15ng/µL	www.wormatlas.org
ZIM895	Whole brain imaging AVB marker	*mzmEx199; mzmEx432; lite-1 (xu7)*	P*unc-31*::NLSGCaMP5K (pTS36) 30ng/µL; P*unc-122*::gfp 15ng/µL P*sra-11*::NLSwCherryNLS (pHK143) 25ng/µL + P*unc-122*::dsRed 15ng/µL	P*sra-11*: (Troemel et al., 1995)
ZIM888	Whole brain imaging ASK marker	*mzmEx199; mzmEx545; lite-1 (xu7)*	P*unc-31*::NLSGCaMP5K (pTS36) 30ng/µL+ Punc-122::gfp 15ng/µL P*srbc-64*::NLSwCherryNLS (pTS113) 25ng/µL + P*unc-122*::dsRed 15ng/µL	P*srbc-64*: (Kim et al., 2009)
ZIM764	Whole brain imaging AWB AWC marker	*mzmEx199; mzmEx433; lite-1 (xu7)*	P*unc-31*::NLSGCaMP5K (pTS36) 30ng/µL+ P*unc-122*::gfp 15ng/µL P*odr-1*::NLSwCherryNLS (pTS104) 40ng/µL + P*unc-122*::dsRed 15ng/µL	P*odr-1*: (Yu et al., 1997)
ZIM759	Whole brain imaging AVH/J marker	*mzmEx199; mzmEx446; lite-1 (xu7)*	P*unc-31*::NLSGCaMP5K (pTS36) 30ng/µL; Punc-122::gfp 15ng/µL P*hlh-34*::NLSwCherryNLS (pSS22) 20ng/µL + P*unc-122*::dsRed 15ng/µL	P*hlh-34*: (Cunningham et al., 2012)
ZIM773	Whole brain imaging AVF marker	*mzmEx199; mzmEx367; lite-1 (xu7)*	P*unc-31*::NLSGCaMP5K (pTS36) 30ng/µL; P*unc-122*::gfp 15ng/µL P*pdfr-1*::NLSwCherryNLS (pTS92) 15ng/µL; P*unc-122*::dsRed 20ng/µL	P*pdfr-1*: (Barrios et al., 2012)
ZIM811	Whole brain imaging OLQ marker	*mzmEx199; mzmEx480; lite-1 (xu7)*	P*unc-31*::NLSGCaMP5K (pTS36) 30ng/µL+ P*unc-122*::gfp 15ng/µL P*ocr-4*::NLSwCherryNLS (pAN17) 30ng/µL P*unc-122*::dsRed 15ng/µL	P*ocr-4*: (Tobin et al., 2002)

Primers

Promoter	P1 (5'->3')	P2 (5'->3')
P*cex-1*	ATGAACATTCCATGGGTTGTG	CACCAACCTGGAAAACTACAC
P*flp-18*	TCTGTCACATACTGCTCGAA	GTTGCWTGTCTAACCCTGAA
P*opt-3*	GATAAAAATAACAGAATTAG	GGGAGAGGCGGAATTAATTT
P*npr-9*	GTTGAATCATCCAAAACGGT	CAACGACATTTCCCAGGAAG
P*inx-1*	GACAAGAACTGCAATGAAAAC	CAGATTCATAACTGTCTATG
P*sto-3*	AGCCAAACCAAGTGAGAAG	CACCAAAATCATCACGCTG
P*sra-11*	GTTTTGCACAAATCCCCTGT	TTGTGTGTTGCGGAGATGTG
P*ser-2*prom2	GTCTGGTAAGTTGAACATGGAGTC	TTTTGCAAATTACTTGAGGCTGC
P*unc-7S*	ACCGTCGACAGTCCATCGAA	GGAAGACGTGTTTGATAGCG
P*unc-31*	GTGCATTTTTGGCATTTTCC	AACAAGGAGACTTGAAATTG
P*srbc-64*	TGCAAGAGTCGGTTGCAAATA	TTTTCAGACTGTGACAAGAAAACT
P*odr-1*(P*gcy-10*)	AGCTTTTCAGCATTGAGGG	CGAAGAGCACACCAATTCA
P*hlh-34*	TGAGCAACTTTCTCTTGGAACA	TTCTCAAGTGGTTATAAGTCAAG
P*pdfr-1* (proximal)	CCCACCCTCCAAATGTCTTG	GGTGACGTGGCATCCGCCAT
P*ocr-4*	ACTCATCGACCAGGAATAAC	ATTAATACAAGTTAGATTCAGAG

Table S1

Neuron class	Ablation effect	Inhibition effect	Activation effect
AIA	R´[a]		
AIB	F[bc], T[bc]	F[d]	R[cd]
AIY	R[b], T[b]	R[d], T[d]	F[d], T[d]
AIZ	F[b], T[e]	F´[a]	R´[a], T[d]
AVA	F[bcf]		R[g]
AVB	R[h]		
AVD	F[h]		
DVA	R[h]		
RIA	F[b]		
RIB	R[i], F[b]	⊘´[a]	F´[a]
RIM	R[bi]	R´[c]	R[j]
RIV	T[b]		
RMD	R[b]		
RME	T[b]		T[d]
SIB	F[b]		
SMB	T[b]		T[d]
SMD	R[b], T[b]		

Table S1. Single-interneuron manipulations in previous studies nearly always affect reversal frequency and/or turning, related to Figure 1. Literature review of single interneuron perturbations that affect spontaneous reversals and turns. Listed are the effects of cell ablations, inhibition via Archaerhodopsin or Halorhodopsin, and activation by Channelrhodopsin; R = increased reversal frequency, F = decreased reversal frequency, T = turning affected, ⊘ = no effect. ´Experiment performed on food. [a](Li et al., 2014). [b](Gray et al., 2005). [c](Piggott et al., 2011). [d](Kocabas et al., 2012). [e](Iino and Yoshida, 2009). [f](Chalfie et al., 1985). [g](Schmitt et al., 2012). [h](Rakowski et al., 2013). [i](Tsalik and Hobert, 2003). [j](Gordus et al., 2015). For additional functional studies, see (Kawano et al., 2011) and (Luo et al., 2014).

Supplemental References

Altun, Z.F., Chen, B., Wang, Z.-W., and Hall, D.H. (2009). High resolution map of Caenorhabditis elegansgap junction proteins. Developmental dynamics : an official publication of the American Association of Anatomists *238*, 1936-1950.

Barrios, A., Ghosh, R., Fang, C., Emmons, S.W., and Barr, M.M. (2012). PDF-1 neuropeptide signaling modulates a neural circuit for mate-searching behavior in C. elegans. Nature Neuroscience *15*, 1675-7682.

Barry, P.H., and Lynch, J.W. (1991). Liquid junction potentials and small cell effects in patch-clamp analysis. The Journal of membrane biology *121*, 101-117.

Cáceres, I.d.C., Valmas, N., Hilliard, M.A., and Lu, H. (2012). Laterally Orienting C. elegans Using Geometry at Microscale for High-Throughput Visual Screens in Neurodegeneration and Neuronal Development Studies. PLoS ONE *7*, e35037.

Chalasani, S.H., Chronis, N., Tsunozaki, M., Gray, J.M., Ramot, D., Goodman, M.B., and Bargmann, C.I. (2007). Dissecting a circuit for olfactory behaviour in Caenorhabditis elegans. Nature *450*, 63-70.

Chalfie, M., Sulston, J.E., White, J.G., Southgate, E., Thomson, J.N., and Brenner, S. (1985). The neural circuit for touch sensitivity in Caenorhabditis elegans. The Journal of neuroscience : the official journal of the Society for Neuroscience *5*, 956-964.

Chartrand, R. (2011). Numerical Differentiation of Noisy, Nonsmooth Data. ISRN Applied Mathematics *2011*, 1-11.

Chen, T.-W., Wardill, T.J., Sun, Y., Pulver, S.R., Renninger, S.L., Baohan, A., Schreiter, E.R., Kerr, R.A., Orger, M.B., Jayaraman, V., *et al.* (2013). Ultrasensitive fluorescent proteins for imaging neuronal activity. Nature *499*, 295-300.

Cohen, M., Reale, V., Olofsson, B., Knights, A., Evans, P., and de Bono, M. (2009). Coordinated Regulation of Foraging and Metabolism in C. elegans by RFamide Neuropeptide Signaling. Cell Metabolism *9*, 375-385.

Cunningham, K.A., Hua, Z., Srinivasan, S., Liu, J., Lee, B.H., Edwards, R.H., and Ashrafi, K. (2012). AMP-Activated Kinase Links Serotonergic Signaling to Glutamate Release for Regulation of Feeding Behavior in C. elegans. Cell Metabolism *16*, 113-121.

Faumont, S., Rondeau, G., Thiele, T.R., Lawton, K.J., McCormick, K.E., Sottile, M., Griesbeck, O., Heckscher, E.S., Roberts, W.M., Doe, C.Q., *et al.* (2011). An image-free opto-mechanical system for creating virtual environments and imaging neuronal activity in freely moving Caenorhabditis elegans. PLoS ONE *6*, e24666.

Gordus, A., Pokala, N., Levy, S., Flavell, S.W., and Bargmann, C.I. (2015). Feedback from network states generates variability in a probabilistic olfactory circuit. Cell *161*, 215-227.

Gray, J.M., Hill, J.J., and Bargmann, C.I. (2005). A circuit for navigation in Caenorhabditis elegans. Proceedings of the National Academy of Sciences of the United States of America *102*, 3184-3191.

Guizar-Sicairos, M., Thurman, S.T., and Fienup, J.R. (2008). Efficient subpixel image registration algorithms. Optics letters *33*, 156-158.

Iino, Y., and Yoshida, K. (2009). Parallel Use of Two Behavioral Mechanisms for Chemotaxis in Caenorhabditis elegans. Journal of Neuroscience *29*, 5370-5380.

Kawano, T., Po, M.D., Gao, S., Leung, G., Ryu, W.S., and Zhen, M. (2011). An Imbalancing Act: Gap Junctions Reduce the Backward Motor Circuit Activity to Bias C. elegans for Forward Locomotion. Neuron *72*, 572-586.

Kato, S., Xu, Y., Cho, C.E., Abbott, L.F., and Bargmann, C.I. (2014). Temporal responses of *C. elegans* chemosensory neurons are preserved in behavioral dynamics. Neuron *81*, 616-628.

Kim, K., Sato, K., Shibuya, M., Zeiger, D.M., Butcher, R.A., Ragains, J.R., Clardy, J., Touhara, K., and Sengupta, P. (2009). Two chemoreceptors mediate developmental effects of dauer pheromone in C. elegans. Science (New York, NY) *326*, 994-998.

Kocabas, A., Shen, C.-H., Guo, Z.V., and Ramanathan, S. (2012). Controlling interneuron activity in Caenorhabditis elegans to evoke chemotactic behaviour. Nature *490*, 273-277.

Li, Z., Liu, J., Zheng, M., and Xu, X.Z.S. (2014). Encoding of both analog- and digital-like behavioral outputs by one C. elegans interneuron. Cell *159*, 751-765.

Lindsay, T.H., Thiele, T.R., and Lockery, S.R. (2011). Optogenetic analysis of synaptic transmission in the central nervous system of the nematode Caenorhabditis elegans. Nature Communications *2*, 306.

Luedtke, S., O'Connor, V., Holden-Dye, L., and Walker, R.J. (2010). The regulation of feeding and metabolism in response to food deprivation in Caenorhabditis elegans. Invertebrate Neuroscience *10*, 63-76.

Luo, L., Wen, Q., Ren, J., Hendricks, M., Gershow, M., Qin, Y., Greenwood, J., Soucy, E.R., Klein, M., Smith-Parker, H.K., *et al.* (2014). Dynamic Encoding of Perception, Memory, and Movement in a C. elegans Chemotaxis Circuit. Neuron *82*, 1115-1128.

Piggott, B.J., Liu, J., Feng, Z., Wescott, S.A., and Xu, X.Z.S. (2011). The neural circuits and synaptic mechanisms underlying motor initiation in C. elegans. Cell *147*, 922-933.

Pokala, N., Liu, Q., Gordus, A., and Bargmann, C.I. (2014). Inducible and titratable silencing of Caenorhabditis elegans neurons in vivo with histamine-gated chloride channels. Proceedings of the National Academy of Sciences *111*, 2770-2775.

Rakowski, F., Srinivasan, J., Sternberg, P.W., and Karbowski, J. (2013). Synaptic polarity of the interneuron circuit controlling C. elegans locomotion. Frontiers in computational neuroscience *7*.

Ramot, D., Johnson, B.E., Berry, T.L., Carnell, L., and Goodman, M.B. (2008). The Parallel Worm Tracker: a platform for measuring average speed and drug-induced paralysis in nematodes. PLoS ONE *3*, e2208.

Schmitt, C., Schultheis, C., Pokala, N., Husson, S.J., Liewald, J.F., Bargmann, C.I., and Gottschalk, A. (2012). Specific expression of channelrhodopsin-2 in single neurons of Caenorhabditis elegans. PLoS ONE *7*, e43164.

Schrödel, T., Prevedel, R., Aumayr, K., Zimmer, M., and Vaziri, A. (2013). Brain-wide 3D imaging of neuronal activity in Caenorhabditis elegans with sculpted light. Nature methods *10*, 1013-1020.

Starich, T.A., Xu, J., Skerrett, I.M., Nicholson, B.J., and Shaw, J.E. (2009). Interactions between innexins UNC-7 and UNC-9 mediate electrical synapse specificity in the Caenorhabditis elegans locomotory nervous system. Neural Development *4*, 16-28.

Tobin, D., Madsen, D., Kahn-Kirby, A., Peckol, E., Moulder, G., Barstead, R., Maricq, A., and Bargmann, C. (2002). Combinatorial expression of TRPV channel proteins defines their sensory functions and subcellular localization in C. elegans neurons. Neuron *35*, 307-318.

Troemel, E.R., Chou, J.H., Dwyer, N.D., Colbert, H.A., and Bargmann, C.I. (1995). Divergent seven transmembrane receptors are candidate chemosensory receptors in C. elegans. Cell *83*, 207-218.

Tsalik, E.L., and Hobert, O. (2003). Functional mapping of neurons that control locomotory behavior in Caenorhabditis elegans. Journal of neurobiology *56*, 178-197.

Tsalik, E.L., Niacaris, T., Wenick, A.S., Pau, K., Avery, L., and Hobert, O. (2003). LIM homeobox gene-dependent expression of biogenic amine receptors in restricted regions of the C. elegans nervous system. Developmental biology *263*, 81-102.

Yemini, E., Jucikas, T., Grundy, L.J., Brown, A.e.E.X., and Schafer, W.R. (2013). A database of Caenorhabditis elegans behavioral phenotypes. Nature methods, 1-7.

Yu, S., Avery, L., Baude, E., and Garbers, D.L. (1997). Guanylyl cyclase expression in specific sensory neurons: a new family of chemosensory receptors. Proceedings of the National Academy of Sciences of the United States of America *94*, 3384-3387.

Zimmer, M., Gray, J.M., Pokala, N., Chang, A.J., Karow, D.S., Marletta, M.A., Hudson, M.L., Morton, D.B., Chronis, N., and Bargmann, C.I. (2009). Neurons detect increases and decreases in oxygen levels using distinct guanylate cyclases. Neuron *61*, 865-879.

5. Article 2: Nested neuronal dynamics orchestrate a behavioral hierarchy across timescales

Status: in revision

Submitted on February 4, 2019 to Neuron

Authors: Harris S. Kaplan*, Oriana Salazar Thula*, Niklas Khoss, and Manuel Zimmer

*Co-first authors

Contributions: H.S.K. and O.S.T. performed experiments, developed analytical methods, analyzed data and wrote the manuscript. N.K. performed experiments. M.Z. led the project, developed analytical methods and wrote the manuscript.

Main manuscript file

Nested neuronal dynamics orchestrate a behavioral hierarchy across timescales

Harris S. Kaplan[1,2,3], Oriana Salazar Thula[1,2,3], Niklas Khoss[1,2], & Manuel Zimmer[1,2,4*]

[1]Department of Neurobiology, University of Vienna, Althanstrasse 14, 1090 Vienna, Austria

[2]Research Institute of Molecular Pathology (IMP), Vienna Biocenter (VBC), Campus-Vienna-Biocenter 1, 1030 Vienna, Austria

[3]These authors contributed equally

[4]Lead contact

[*]Correspondence: manuel.zimmer@univie.ac.at

SUMMARY

Classical and modern ethological studies suggest that animal behavior is organized hierarchically across timescales, such that longer-timescale behaviors are composed of specific shorter-timescale actions. Despite progress relating neuronal dynamics to single timescale behavior, it remains unclear how different timescale dynamics interact to give rise to such higher-order behavioral organization. Here we show, in the nematode *Caenorhabditis elegans*, that a behavioral hierarchy spanning three timescales is implemented by nested neuronal dynamics. At the uppermost hierarchy level, slow neuronal

population dynamics spanning brain and motor periphery control two faster motorneuron oscillations, toggling them between different activity states and functional roles. These faster oscillations are further nested, in a manner that enables flexible behavioral control in an otherwise rigid hierarchical framework. Our findings establish nested neuronal activity patterns as a repeated dynamical motif of the *C. elegans* nervous system, which together implement a controllable hierarchical organization of behavior.

INTRODUCTION

Animal behavior unfolds over a wide range of timescales, from sub-second muscle contractions to circadian rhythms. Nervous systems must not only act on each of these timescales, but also coordinate across them, in order to implement long-term behavioral strategies and avoid interfering actions. Classical (Dawkins, 1976; Tinbergen) and modern (Anderson, 2016; Berman et al., 2016; Glaze and Troyer, 2006; Gomez-Marin et al., 2016; Marques et al., 2018) ethological studies posit that such inter-timescale coordination is achieved via hierarchical control, with longer timescales at higher hierarchy levels. Specific shorter-timescale actions are then constrained to occur only in the context of a hierarch, a longer-timescale motor program or behavioral state (Dawkins, 1976). For example, Tinbergen described stickleback behavior as hierarchical, with the reproductive instinct encompassing sub-behaviors like nest-building or defensive fighting; each of these, in turn, consists of specific sub-actions like digging or biting, respectively (Tinbergen, 1951). Modern quantitative analyses suggest that behaviors as diverse as birdsong and *Drosophila* locomotion are organized hierarchically (Berman et al., 2016; Glaze and Troyer, 2006), in contrast to a serially sequential, or Markovian, organization.

Importantly, sequentially or hierarchically organized behavior would require fundamentally different neuronal control mechanisms. However, despite substantial progress relating neuronal dynamics to behavior on single timescales, few studies have described how different timescale dynamics orchestrate a higher-order behavioral organization. In rodents, distinct behavioral timescales are represented by separable neuronal populations (Jin and Costa, 2015; Moore et al., 2013), which could potentially provide a substrate for inter-timescale coordination. Additional behavioral and anatomical evidence suggested that rhythmic orofacial behaviors operating at different frequencies, like breathing and whisking, are coordinated by a hierarchical phase-resetting mechanism (Moore et al., 2013). Still, it remains unclear how the underlying neuronal dynamics interact across timescales to implement a hierarchical organization of behavior; i.e. whether these dynamics or underlying circuit architectures are indeed hierarchically organized. For example, while birdsong can be described hierarchically in terms of behavior (Glaze and Troyer, 2006), neurophysiological evidence thus far suggests a sequential chain model of neuronal activities (Long et al., 2010).

Addressing this question necessitates fine-grained analysis of both behavior and neuronal activity, as well as precise circuit manipulation tools (Krakauer et al., 2017). We therefore examined *C. elegans* locomotion. *C. elegans* behaviors include sub-second body-bends, seconds- to minutes-long motor states such as forward and reverse crawling, and longer-lasting states of exploration, exploitation or quiescence. Detailed analyses of postural dynamics have hinted at an underlying hierarchical organization of motor actions (Gomez-Marin et al., 2016). Physiological studies, however, have thus far focused on relating neuronal activity to behaviors on single timescales; for example, calcium imaging studies have described motor neuron

dynamics underlying the oscillatory gait (Gao et al., 2018; Shen et al., 2016; Wen et al., 2012; Xu et al., 2018), or interneuron dynamics underlying forward/reverse locomotion switches (Kato et al., 2015; Kawano et al., 2011; Li et al., 2014; Piggott et al., 2011). These technological and conceptual advances regarding single-timescale behaviors present a unique opportunity to investigate neuronal orchestration of behaviors across timescales.

Here, we use high-resolution quantitative behavior analysis, nervous-system-wide single-cell-resolution functional imaging, and circuit manipulations to reveal nested neuronal activity dynamics giving rise to a behavioral hierarchy in *C. elegans*. At the uppermost hierarchy level, a ~0.05 Hz nervous-system-wide neuronal activity cycle drives switches between forward and reverse crawling states and also controls two faster neuronal oscillations, toggling them between different dynamical states and functional roles. At the intermediate hierarchy level, nested within forward states, B-class motor neurons (B-MNs) drive ~0.5 Hz crawling undulations. At the lowest hierarchy level, SMD-class motor neurons drive ~1 Hz head-casts, which are further nested within specific phases of the mid-level oscillation. Experimentally varying the duration of these phase-windows alters head-cast probability, suggesting a mechanism for flexible behavioral regulation in an otherwise rigid hierarchical framework. Crucially, by comparing neuronal activity in moving versus immobilized animals, we show that these nested dynamics persist in the absence of behavioral execution and therefore must be intrinsic properties of the neurons and their circuit interactions. Our work identifies nested neuronal activity as a repeated dynamical motif of the *C. elegans* nervous system, which serves to implement a controllable hierarchical organization of behavior.

RESULTS

A multi-timescale behavioral hierarchy of motor actions

To identify behaviors with well-defined relationships across timescales, we video-tracked animals to measure motor programs and associated gaits. *C. elegans* locomotion switches stochastically between forward- or reverse-directed crawling (Roberts et al., 2016); each of these motor programs consists of alternating dorsal/ventral undulatory bends. During the predominant forward locomotion state, bends originate in the head and propagate posteriorly. We quantified 24 bend angles along the worm's body for each video frame (Figure 1A) and traced each head-bend's propagation to its posterior-most segment (Figures 1B and S1A). This revealed a bimodal distribution, indicating two distinct types: one propagating completely to the tail (henceforth “propagated-bends”) and another terminating anterior to the mid-body (henceforth “head-casts”) (Figure 1B-C). Our subsequent analyses (below) indicated that head-casts were a distinct class of actions, as opposed to simply stalled propagated bends. Furthermore, head-casts were also distinct from previously described "foraging" movements of the nose, which are restricted to the most anterior part of the head (Huang et al., 2008), while head-casts typically extend to or beyond the neck (posterior pharyngeal bulb) (Figure 1B-C). Forward locomotion consisted primarily of propagated-bends, intermittently superimposed with episodes of head-cast oscillations (Figures S1A-B); when they did occur, head-cast oscillations were faster than propagated-bend oscillations (Figure 1D). Together with locomotion direction switches (forward + reverse state duration), these behaviors occurred on three distinct timescales (Figure 1D).

125 Nevertheless, these behaviors were considerably coupled. Head-cast
126 oscillations were ventral- or dorsal-biased, depending on the direction of the previous
127 propagated-bend (Figures 1E, upper, and S1C). To investigate this relationship
128 further, we calculated the phase of the propagated-bend cycle: we assigned the dorsal
129 propagated-bend initiation as the start of the cycle (0 or 2π rad) and the ventral
130 propagated-bend initiation as the cycle's midpoint (π rad), and interpolated the phase
131 between them (Figure 1E, lower). This revealed that head-cast episodes were only
132 initiated at restricted phases (Figure 1F). This phase dependence, henceforth "phase-
133 nesting," suggests a brief window of opportunity for head-casts within each
134 propagated-bend cycle. Indeed, head-casts preferentially occurred during the longest-
135 duration propagated-bend cycles, consistent with longer cycles having wider windows
136 of opportunity (Figures S1D-F). Alternatively, head-cast occurrence could stall and
137 therefore lengthen the propagated-bend cycle, a possibility we examine below. Both
138 head-bend types occurred exclusively during forward locomotion: during reversals,
139 bends propagate from tail to head, and no head-casts occurred (Figures S1G-H).
140 Together, these data suggest a hierarchical organization of behavior, in which shorter-
141 timescale behaviors are strictly constrained by specific longer-timescale behavioral
142 phases or states (Figure 1G).
143
144 **A nervous-system-wide representation of slow behavioral dynamics at the**
145 **uppermost hierarchy level**
146 We next sought neuronal correlates for this organization. In our previous work
147 we developed a single-cell-resolution real-time whole-brain Ca^{2+}-imaging approach in
148 immobilized animals. Given the stereotypy in *C. elegans* nervous system anatomy and
149 reproducible cell-class specific activity patterns, the cell class identity of a large

proportion of neurons can be determined in these data (Kato et al., 2015; Schrödel et al., 2013). Using principal components analysis (PCA), we reported a low-dimensional brain-wide activity cycle that dominates head ganglia, including descending (and other) interneurons (Kato et al., 2015). In freely moving animals, these interneurons were strictly active during forward or reverse locomotion, the uppermost level of our hierarchy model. Because these same neurons show coordinated dynamics despite immobilization, specific neuronal activity patterns in immobilized worms can be ascribed to forward or reverse motor command states (Kato et al., 2015).

Here, we expanded our immobilized worm Ca^{2+}-imaging recordings beyond head ganglia to the entire nervous system, including ventral nerve cord (VNC, containing motor neurons) and tail ganglia (Figures 2A-B and S2A, movie S1). We performed multiple (n=5) such nervous-system-wide recordings and, using PCA, we found low-dimensional dynamics strikingly similar to those restricted to head ganglia (Figures 2B-D and S2B). Notably, interneuron and motor neuron activities were equally well-represented in this low-dimensional PCA space (Figure 2E) and both neuron classes showed strong modulations by forward/reverse command state (Figure S2C). Network activity corresponding to motor commands therefore extends from head ganglia to the motor periphery; this is consistent with previous work showing descending interneuron control of VNC motor neurons (Kawano et al., 2011; Xu et al., 2018). Moreover, previous activity recordings in freely moving animals confirmed that interneuron dynamics indeed occur at this slow forward/reverse timescale (Kato et al., 2015; Kawano et al., 2011; Li et al., 2014; Luo et al., 2014). In conclusion, a long-timescale nervous-system-wide neuronal activity cycle underlies the uppermost hierarchy level.

Identification of candidate central pattern generator circuits for lower hierarchy levels

PCA is sensitive to global correlations in timeseries data but does not necessarily reveal more local and transient interactions between neuronal activity fluctuations. Therefore, we sought additional approaches to screen our datasets for shorter-timescale activities potentially underlying the lower hierarchy levels. Rhythmic behaviors such as head-bending are typically driven by central pattern generators (CPGs), neurons or circuits that can generate motor-pattern-like activity without proprioceptive feedback (Kiehn, 2011; Marder and Bucher, 2001). As our pan-neuronal immobilized (i.e. muscle-paralyzed) worm recordings lack fluctuating proprioceptive inputs, they are particularly well-suited for identifying CPG candidates. Behavioral studies have implicated B-MNs, along with an unknown head neuron class, as potential CPGs for forward locomotion (Fouad et al., 2018; Xu et al., 2018) (A-MN oscillators drive reverse locomotion (Gao et al., 2018)). 18 B-MNs distributed along the VNC synapse locally onto either dorsal (DB-subclass) or ventral (VB-subclass) muscle and are crucial for forward locomotion (Chalfie et al., 1985) (Figure 2A). Based on anatomical features (described in methods), we were able to identify most individual B-MNs in our data. Nested within forward command periods, we indeed found shorter-timescale fluctuations: some neuron classes, including certain B-MNs, showed several Ca^{2+} peaks per forward command period (Figure 3A). Most of these neurons rarely peaked during reverse command periods (Figure S2D). We focused on rhythmically active neuron classes, i.e. those with non-random inter-peak intervals (Figure 3A, methods). Two of these were excitatory motor neuron classes targeting head and neck muscle, making them top head-bend CPG candidates: SMD neurons

199 (dorsal-projecting SMDD and ventral-projecting SMDV) and dorsal-projecting B-MNs
200 DB01 and DB02 (Figures 2D and 3B).

201 To determine whether SMD and DB01/02 were part of larger oscillator circuits,
202 we performed an appropriate variant of cross-correlation analysis (Brody, 1999)
203 across all neurons (Figure 3C). First, a histogram was generated of the timing offsets
204 of each "target" neuron's activity peak relative to each "reference" neuron's activity
205 peak (reference neurons here are left/right SMDD and SMDV, DB01, and DB02). The
206 same procedure was applied to shuffled timeseries and then subtracted from the
207 actual data, so that the resulting histograms indicate increased or decreased activity
208 peak frequency relative to chance levels. Target neurons were all neurons that could
209 be identified reliably across recordings, which includes nearly all neurons showing
210 activity changes. Only long forward command periods were used, to isolate
211 interactions within this state. This analysis delineated three small oscillator circuits
212 (highlighted in different colors in Figure 3C): (1) SMDD and GABAergic ventral-
213 projecting RMED head motor neurons oscillate in synchrony, (2) SMDV, dorsal-
214 projecting RMEV, and VB01 B-MNs oscillate in synchrony and antagonistically with
215 the SMDD oscillator (also see (Hendricks et al., 2012; Shen et al., 2016)), and (3)
216 DB01 and DB02 oscillate in synchrony with weak correlations with the SMDV
217 oscillator.

218 In the absence of proprioception, CPGs typically show both rhythm- and
219 pattern-generating activity (here, we use the term rhythm-generation for any regularly
220 repeated neuronal activity and pattern-generation for circuit activity that corresponds
221 to the coordination of multiple, e.g. antagonistic, muscles, as was discussed in ref.
222 (Kiehn, 2011)). SMDD/V oscillator antagonism is consistent with both rhythm and
223 pattern generation, for antagonistic dorsal/ventral head-bending. In contrast, DB01/02

oscillations showed positive correlations with VB01 activity (Figure 3C), despite targeting opposing muscles. Other B-MNs also exhibited rhythmic activity (Figure 3A), but we found no significant coordination among them (Figure S2E). These data are consistent with previous studies implicating B-MNs as distributed rhythm generators (Fouad et al., 2018), and they further suggest that proprioceptive feedback (described in (Wen et al., 2012; Xu et al., 2018)) is required to coordinate intrinsic rhythms into complete motor-patterned activity in freely crawling animals. SMDs were also reported to be proprioceptive (Yeon et al., 2018), presumably in addition to the activity we report in immobilized animals. We suggest that proprioception is required for both SMD and B-MN frequency entrainment, as we observed a ~10-fold reduction of frequency upon immobilization (compare Figure 3A with Figure 1D); such a reduction is consistent with CPG studies in other species (Fox et al., 2006; Goulding, 2009). In summary, in addition to slow global dynamics, immobilized animal recordings also revealed faster-timescale local dynamics: the head motor neurons SMD and DB01/02 are candidates CPG components, exhibiting largely independent rhythmic activity with correlations to very few other neurons.

SMDs and body motor neurons are required for head-casts and propagated-bends, respectively

To interrogate SMD and DB function, we transiently inhibited each using the histamine-gated chloride channel hisCl (Pokala et al., 2014). We first asked whether each can oscillate independently in immobilized worms, using whole-brain imaging (n=5 recordings per genotype). These recordings revealed DB01/02 oscillations in the absence of SMD activity (Figure 4A). To examine SMD activity in DB01/02-inhibited animals, we generated VNC_{ACh}::hisCl animals, in which all B-MNs including DB01/02

249 are inhibited, among other cholinergic VNC neurons (no specific DB01/02 genetic
250 driver is available). Whole-brain imaging in VNC_{ACh}::hisCl animals showed that SMDD
251 oscillations persisted, while SMDV oscillation frequency was reduced (Figure 4A).
252 These data show that SMD and DB01/02 can affect one another, but can also operate
253 as independent oscillators. We next used behavioral experiments in these hisCl
254 strains to examine how oscillator inhibition affects locomotion. SMD::hisCl animals
255 exhibited normal propagated-bend frequency but largely reduced head-casting
256 (Figures 4B and S3A-B). VNC_{ACh}::hisCl animals exhibited reduced propagated-bend
257 frequency and increased head-casting (Figures 4B and S3A-B). Combining
258 VNC_{ACh}::hisCl and SMD::hisCl rendered animals almost completely immobile, with
259 abnormally non-rhythmic head-cast-like bends (Figures 4B and S3A-E). This suggests
260 a prominent role for SMDs and anterior VNC_{ACh} neurons in head-bending, since 11
261 head motor neuron classes were not targeted for inhibition but could not compensate
262 for SMD and VNC_{ACh} inhibition. Altogether, these data suggest that the SMD and
263 DB01/02 oscillator circuits are separable head-bend rhythm generators, with SMDs
264 driving head-casts and B-MNs driving propagated-bends.

265 These behavior experiments also provided support for two predictions of our
266 hierarchy model. First, reduced head-cast frequency in SMD::hisCl animals did not
267 result in shorter propagated-bend cycle periods (Figure S3C-D), suggesting that head-
268 cast occurrence does not stall or lengthen the propagated-bend cycle. Second,
269 VNC_{ACh}::hisCl showed a reciprocal effect on propagated-bends and head-casts,
270 consistent with longer propagated-bend cycles (Figure S3D) permitting wider windows
271 of opportunity for head-casts. By contrast, reduced head-casting in SMD::hisCl
272 animals did not affect propagated-bend frequency, consistent with a top-down effect
273 of longer-timescale behaviors but not vice versa. Finally, the apparent discrepancy

between the head-cast increase (Figure 4B) and SMDV frequency decrease (Figure 4A) in VNC_{ACh}::hisCl animals suggests that head-casts are not simply represented by an increase in SMD activity frequency, which we investigate below.

Hierarchy level I and II interaction: SMD neurons are multi-functional

To determine how these circuits interact to drive hierarchical behaviors, we performed Ca^{2+} imaging of SMDs and DB02 in freely moving animals (Figures 5B-C, movie S2). We first asked how the uppermost hierarchy level, i.e. forward/reverse locomotion state, impacts faster-timescale activities (Figure 5A). As both SMDs and DB02 target head muscle, we examined neuronal activity relative to the head-bend oscillation, corresponding to propagated-bends during forward locomotion and anterior-propagating bends during reverse locomotion (the only reversal head-bend type we observed). During forward locomotion, consistent with their lateralized neuromuscular innervation, SMDD and DB02 peaked during dorsal bends, SMDV peaked during ventral bends, and each neuron peaked during nearly every head-bend cycle (Figures 5D, 5F and 5H). During reverse locomotion, DB02 was inactive (Figures 5B and 5H-I), while SMDs peaked at altered head-bend phases (Figure 5G), less reliably (Figure 5H), and with lower frequency and amplitude (Figure 5I) compared to forward periods. These altered SMD activity patterns suggest altered SMD function during reversals. Indeed, SMD inhibition reduced head-bend angle only during forward locomotion, and slightly increased head-bend angle during reverse locomotion (Figure 5J).

If SMD activity during reversals does not promote head-bending, what function does it serve? We reliably observed SMD Ca^{2+} peaks at reverse-to-forward transitions (Figure S4A). These transitions are typically accompanied by reorientation

299 turns(Donnelly et al., 2013; Gray et al., 2005); the amplitude of these post-reversal
300 turns correlated with SMD Ca^{2+}-peak amplitude (Figures S4A-B), with mutually
301 exclusive SMDV activity during ventral turns and SMDD activity during dorsal turns
302 (Figure S4A). We therefore hypothesized that SMD reversal activity increases
303 reverse-to-forward transition probability and promotes post-reversal turn amplitude.
304 Indeed, SMD::hisCl animals showed increased reversal duration (Figures 5K and
305 S4C) and lacked large-amplitude post-reversal turns (Figures S4D-F). SMDs therefore
306 change their roles depending on the long-timescale forward/reverse switch: during
307 forward states, they increase head-bend amplitude and drive head-casts, and during
308 reversals they promote state termination. The latter suggests a potential interneuron-
309 like role, consistent with SMDs synapsing onto interneurons in addition to their
310 neuromuscular synapses (White et al., 1986).
311 We next asked whether these characteristic activity patterns arise from intrinsic
312 circuit properties or from proprioceptive feedback. To distinguish these possibilities,
313 we examined SMD and DB activity during forward versus reverse command state in
314 whole-brain recordings of immobilized animals. As in behaving animals, mutually
315 exclusive SMDD/V peaks were coincident with reversal command state termination
316 (Figure S4G). Indeed, SMD::hisCl animals showed increased reverse command state
317 durations (Figure 5L), confirming that this SMD function persists in the absence of
318 behavior. Further, DB02 frequency and SMD peak amplitudes were reduced during
319 reverse command states (Figure S4H), as they are during reversal behaviors (Figure
320 5I). In conclusion, SMD and DB oscillations are hierarchically nested within the slower
321 forward/reverse command cycle via circuit interactions: these nervous-system-wide
322 state switches toggle DB02 neurons between oscillatory and inactive states and SMD
323 neurons between different activity patterns and functional roles.

Hierarchy level II and III interaction: neuronal phase-nesting

We next examined neuronal activity in freely moving animals separately during the different head-bend types (Figure 6A). All three neurons showed oscillations synchronized with propagated-bends: DB02 and SMDD were active during dorsal propagated-bends, and SMDV was active during ventral propagated-bends (Figure 6B-C). SMDD and SMDV therefore showed alternating activity peaks with alternating dorsal/ventral propagated-bends (Figure 6C). During head-casts, DB02 typically did not oscillate (Figure 6D; excepting a minority of especially posterior-propagating head-casts, Figure S5A). In contrast, SMDs consistently showed oscillations during head-casts, superimposed onto their propagated-bend activity (Figure 6E). Unlike SMDD/SMDV alternations during propagated-bends, SMD head-cast oscillations were strictly unilateral: SMDD oscillated during dorsal head-casts while SMDV remained inactive; likewise, SMDV oscillated during ventral head-casts while SMDD remained inactive (Figures 6E and S5B-D; dotted lines in Figure 5C). SMDs therefore exhibited distinct activity signatures for different behaviors: SMDD/SMDV alternations during propagated-bends and unilateral SMDD-only or SMDV-only oscillations during head-casts.

We next asked whether these SMD activity signatures were phase-nested like their co-occurring behaviors. We quantified the phase of the SMDD/SMDV alternation cycle by assigning SMDD alternating peaks as the start of the cycle (0 or 2π rad) and SMDV alternating peaks as the cycle's midpoint (π rad), and interpolating the phase between them (Figure 6F). This revealed that unilateral SMD oscillations were initiated at restricted phases (Figure 6G, compare with Figure 1F). This suggests that phase-nested SMD activity may be causal for phase-nested behavior; if so, phase-nested

SMD activity should persist in the absence of behavior. Indeed, in the whole-brain recordings of immobilized animals, SMD activity showed the same phase-nested relationship (Figure 6H). Further, unilateral SMD oscillations preferentially occurred during the longest-duration SMD alternation cycles in both immobilized and freely crawling animals (Figures S5E-F, compare with Figure S1E, lower); hence, SMD activity represents a neuronal correlate for the proposed window of opportunity. Taken together, by recapitulating these characteristic neuronal activity patterns in immobilized animals, our data indicate that nested neuronal dynamics are the cause, rather than consequence, of nested behaviors. Nested neuronal activity patterns are therefore a repeated dynamical motif of the *C. elegans* nervous system, which together constitute a hierarchical organization of neuronal activity and behavior across three timescales (Figures 7A-B).

A hierarchical control mechanism for behavioral flexibility

Phase-nesting implies a mechanism for behavioral regulation: our results thus far suggest that head-cast occurrence may be controlled by manipulating the propagated-bend oscillation speed, thereby widening or narrowing the head-cast window of opportunity. Propagated-bend oscillation speed correlated strongly with locomotion speed (Figure S6A); we therefore manipulated the RIB interneuron, a forward-active neuron previously implicated in locomotion speed control (Kato et al., 2015; Li et al., 2014). Indeed, RIB inhibition slowed the propagated-bend cycle and, consistent with our model, increased head-casting (Figures 7C-E). Conversely, optogenetic RIB activation accelerated the propagated-bend cycle, and decreased head-casting (Figures 7F-H). To determine whether this antagonistic regulation occurs in more naturalistic conditions, we examined behaviors involving locomotion speed

regulation. Off food, animals exposed to ambient O_2 downshifts slow their locomotion (Zimmer et al., 2009), presumably to explore locally (Hums et al., 2016). Upon O_2 downshift, we observed that the slowed propagated-bend cycle was coupled with increased head-casting (Figures 7I-K and S6B, movie S3). On food, animals switch spontaneously between low-speed exploitative dwelling and high-speed explorative roaming states (Fujiwara et al., 2002). We found that roaming animals exhibited faster propagated-bend cycles and rarely head-casted compared to dwelling animals (Figures 7L-N and S6C-D, movie S4). These results suggest context-dependent functions for head-casts, serving either exploration (off food) or exploitation (on food). They further implicate phase-nesting as a mechanism for controlling behavioral output downstream of both sensory neurons and internal state regulators.

DISCUSSION

Here we showed that nested neuronal dynamics coordinate different timescale behaviors into a hierarchy in *C. elegans*. As opposed to a sequential model, we observe persistent phases of neuronal activity driving higher-level behaviors, which gate the occurrence of faster neuronal activity fluctuations driving specific lower-level behaviors. The uppermost level of the behavioral hierarchy impacts the entire nervous system: many interneurons in the brain can be classified into two major groups that are only active either during forward or reverse motor command states ((Kato et al., 2015) and Figures 2B and S2C). This principle extends to the B-class motor neurons in the periphery, which switch from a silent state to a high activity state during forward commands ((Kato et al., 2015) and Figures 2B-E and S2C) and are required for forward locomotion (Chalfie et al., 1985). A-class motor neurons, in contrast, exhibit higher activity during reverse command states ((Kato et al., 2015) and Figures 2B-E)

399 and are required for reverse locomotion (Chalfie et al., 1985); however, A-MNs were
400 not the focus of this study. Towards the lower hierarchy levels, neurons show
401 dynamics that span multiple time-scales. The slow timescale reverse-to-forward
402 switches not only modulate basal activity levels but also gate additional faster activity
403 fluctuations in a myriad of motor neurons (Figure 3A), which potentially correspond to
404 dorsal-ventral propagated bends, as was confirmed for DB02 in freely moving worms
405 (Figure 6B). SMD activity changes span all three timescales. They show fast head-
406 cast-driving oscillations (level III) superimposed onto a slower propagated-bend-
407 correlated activity oscillation (level II), which enables phase-nested behaviors (Figure
408 6). Upon switch to reverse locomotion (level I), SMDs execute completely different
409 functions, contributing to the termination of reversals and mediating subsequent
410 reorientation turns (Figures 5K and S4F). In this respect, SMDs are highly
411 multifunctional, executing both motor- and interneuron-like functions, with hierarchical
412 control preventing interference between these different roles. Nearly all of the nested
413 activity patterns we observed in freely moving animals were recapitulated in paralyzed
414 worms, suggesting that nesting is a property of the underlying circuits and not
415 dependent on proprioception or behavioral execution. Altogether, these results
416 conceptually reveal an organizational principle in which upper hierarchy behavioral
417 programs are represented by slow global dynamics spread across many neurons,
418 while lower hierarchy behaviors are represented by fast local dynamics in a few multi-
419 functional neurons. These inter-timescale dynamics are tied together in a nested
420 fashion; nesting is therefore a repeated dynamical motif of the *C. elegans* nervous
421 system, and is crucial to the neuronal control of *C. elegans* behavior.

422 A defining feature of this hierarchical organization is a rigid framework, in which
423 lower level behaviors may only be accessed via switches between certain upper level

424 states. In the hierarchy we describe (Figure 7A-B), upper-level neuronal activity
425 patterns indeed provide strict control over lower-level ones. For example, DB02 nearly
426 never showed activity peaks during reversal command states, while constantly
427 oscillating during forward states; therefore, when the network is in the reversal
428 command state, mid-level DB02 oscillations may only be executed by switching the
429 upper level from the reverse to the forward command state. Similarly, SMDV nearly
430 never exhibited head-cast activity during dorsal propagated-bends (when DB02 and
431 SMDD were active); therefore, when the worm is in a dorsal propagated-bend phase,
432 low-level ventral head-casts may only be executed by first switching the mid-level
433 phase to ventral. This rigid framework is, however, accessible to additional neuronal
434 control, via either sensory input or behavioral state (Figure 7I-N); both of these can
435 modulate the crawling phase velocity of the animal and therefore the window of
436 opportunity for head-casting. Given the ubiquity of neuronal activity oscillations as well
437 as hierarchically organized behavior, the circuit interactions and control principles we
438 describe may be relevant for other species.

439 We also examined an even longer timescale of behavior above the forward-
440 reverse switch: roaming and dwelling behavioral states. In contrast to the strict, all-or-
441 none relationships of the motor hierarchy, actions within roaming and dwelling are not
442 exclusive to those states, but rather show differences in frequency: dwelling exhibits
443 high frequencies of forward-reverse transitions and head-casts, while roaming
444 consists of long stretches of propagated-bend forward movement with low head-cast
445 and reversal frequencies (Figure 7I-N and (Gallagher et al., 2013), respectively). We
446 therefore suggest that such longer-timescale behavioral states, which rely on
447 neuromodulation (Ben Arous et al., 2009; Flavell et al., 2013), act in a non-hierarchical
448 manner. While Tinbergen's proposal of hierarchy in stickleback behavior included

449 longer-lasting states that are typically controlled by neuromodulators, such as a
450 reproductive instinct, our data are more in line with recent studies describing
451 hierarchies at the level of motor actions (Berman et al., 2016; Duistermars et al., 2018;
452 Glaze and Troyer, 2006; Gomez-Marin et al., 2016; Marques et al., 2018). A primary
453 benefit of hierarchical behavior may be to coordinate the activities of motor neurons
454 that target overlapping body parts, in order to prevent interfering actions. Indeed,
455 DB01/02 and SMDD target overlapping muscles, as do motor neurons for whisking
456 and breathing in rodents. In contrast to the rigid framework studied here, longer lasting
457 behavioral states could gain flexibility by re-utilizing a combinatorial set of actions.

458 The strict, nested relationships we uncovered bear striking resemblance to
459 neuronal dynamics underlying multi-timescale rodent behaviors. For example, CPGs
460 driving whisking and breathing appear to interact in a hierarchical manner: breathing
461 resets the whisking phase, but not vice versa, and a strictly unidirectional anatomical
462 pathway has been identified from the breathing CPG to the whisking CPG. Such a
463 phase-resetting mechanism may also explain the impact of B-MNs on SMD activity,
464 whereby B-MN oscillations may drive the SMDs into particular phases that restrict their
465 unilateral oscillation and therefore head-casts. Further, basal ganglia circuits in mice
466 show independent coding of different timescales during learned action sequences
467 (Luo et al., 2014), suggesting a hierarchical "chunking" with theoretical advantages
468 compared to serial sequencing (Jin and Costa, 2015). Our study demonstrates how
469 circuits acting on different timescales can interact to implement hierarchical behavior,
470 and could therefore provide a starting point to search for similar circuit interactions in
471 rodents or flies.

472 The motor neuron dynamics showed a strong dependence on oscillation phase
473 (Figure 6H). Oscillation phase is crucially important for the effect of motor neurons

474 during insect locomotion (Fayyazuddin and Dickinson, 1999; Sponberg and Daniel,
475 2012), and has been proposed to act as a window for integrating inputs in flies (Gupta
476 et al., 2016) and mammals (Buzsáki and Draguhn, 2004; Yuste et al., 2005). While
477 forward and reverse state switches in *C. elegans* appear to be stochastic rather than
478 oscillatory (Roberts et al., 2016), non-oscillatory phase-coding has been demonstrated
479 in the bat (Eliav et al., 2018). It has also been suggested that CPG circuits can, at a
480 minimum, foretell principles of cortical circuits (Yuste et al., 2005). Throughout the
481 mammalian brain, longer-timescale oscillations spread across larger neuronal
482 populations influence more local, shorter-timescale oscillations in a hierarchical
483 manner (Buzsáki et al., 2013). Coupling between these nested oscillations could serve
484 myriad functions (Hyafil et al., 2015); for example, the widening and narrowing of an
485 alpha-oscillation window of opportunity has been proposed to enable gamma-
486 oscillatory communication between neuronal populations (Hahn et al., 2019). Our work
487 demonstrates that such hierarchically nested dynamics can indeed organize neuronal
488 activity patterns, and consequently animal behavior, across timescales.
489 In conclusion, nested neuronal activity patterns implement a three-level
490 hierarchy of behavior across timescales in *C. elegans*. Future work should examine
491 the molecular and synaptic bases of these crucial circuit interactions. Neuronal activity
492 oscillations on different timescales are ubiquitous in neuroscience; we therefore
493 speculate that such hierarchically nested activity patterns may be a common
494 mechanism for organizing and regulating neuronal dynamics across timescales.
495
496 **Acknowledgements**
497

We thank Marie Gendrel, Oliver Hobert, Kyuhyung Kim and Ken Miller for plasmids, Shawn Lockery, Max Jösch, Andrew Straw, Mara Andrione, Ulises Rey and Charlie Fieseler for critically reading the manuscript and the Zimmer lab for critical feedback, Annika Nichols for technical support. The research leading to these results has received funding from the European Community's Seventh Framework Programme (FP7/2007-2013)/ERC grant agreement 281869, the Vienna Science and Technology Fund (#LS14-084), the University of Vienna, and the Research Institute of Molecular Pathology (IMP). M.Z. is supported by the Simons Foundation (#543069) and the International Research Scholar Program by the Wellcome Trust and Howard Hughes Medical Institute (#208565/Z/17/Z). The IMP is funded by Boehringer Ingelheim.

Author contributions

H.S.K. and O.S.T. performed experiments, developed analytical methods, analyzed data and wrote the manuscript. N.K. performed experiments. M.Z. led the project, developed analytical methods and wrote the manuscript.

References

Anderson, D.J. (2016). Circuit modules linking internal states and social behaviour in flies and mice. Nature reviews Neuroscience *17*, 692-704. doi: 10.1038/nrn.2016.125.

Ben Arous, J., Laffont, S., and Chatenay, D. (2009). Molecular and sensory basis of a food related two-state behavior in C. elegans. PLoS ONE *4*, e7584. doi: 10.1371/journal.pone.0007584.

Benjamini, Y., Yekutieli, D., and 2001 The control of the false discovery rate in multiple testing under dependency. Annals of Statistics. doi: 10.2307/2674075.

529
530 Berman, G.J., Bialek, W., and Shaevitz, J.W. (2016). Predictability and hierarchy in
531 Drosophila behavior. Proceedings of the National Academy of Sciences *113*, 11943-
532 11948. doi: 10.1073/pnas.1607601113.
533
534 Bhatla, N., and Horvitz, H.R. (2015). Light and hydrogen peroxide inhibit C. elegans
535 Feeding through gustatory receptor orthologs and pharyngeal neurons. Neuron *85*,
536 804-818. doi: 10.1016/j.neuron.2014.12.061.
537
538 Brenner, S. (1974). The genetics of Caenorhabditis elegans. Genetics *77*, 71-94. doi:
539
540 Brody, C. (1999). Correlations without synchrony. Neural computation *11*, 1537-
541 1551. doi:
542
543 Buzsáki, G., and Draguhn, A. (2004). Neuronal oscillations in cortical networks.
544 Science (New York, NY) *304*, 1926-1929. doi: 10.1126/science.1099745.
545
546 Buzsáki, G., Logothetis, N., and Singer, W. (2013). Scaling brain size, keeping
547 timing: evolutionary preservation of brain rhythms. Neuron *80*, 751-764. doi:
548 10.1016/j.neuron.2013.10.002.
549
550 Cáceres, I.d.C., Valmas, N., Hilliard, M.A., and Lu, H. (2012). Laterally Orienting C.
551 elegans Using Geometry at Microscale for High-Throughput Visual Screens in
552 Neurodegeneration and Neuronal Development Studies. PLoS ONE *7*, e35037. doi:
553 10.1371/journal.pone.0035037.g006.
554
555 Chalfie, M., Sulston, J.E., White, J.G., Southgate, E., Thomson, J.N., and Brenner,
556 S. (1985). The neural circuit for touch sensitivity in Caenorhabditis elegans. The
557 Journal of neuroscience : the official journal of the Society for Neuroscience *5*, 956-
558 964. doi:
559
560 Charlie, N.K., Schade, M.A., Thomure, A.M., and Miller, K.G. (2006). Presynaptic
561 UNC-31 (CAPS) is required to activate the G alpha(s) pathway of the Caenorhabditis
562 elegans synaptic signaling network. Genetics *172*, 943-961. doi:
563 10.1534/genetics.105.049577.
564
565 Chartrand, R. (2011). Numerical Differentiation of Noisy, Nonsmooth Data. ISRN
566 Applied Mathematics *2011*, 1-11. doi: 10.1152/ajpregu.00055.2010.
567
568 Chen, T.-W., Wardill, T.J., Sun, Y., Pulver, S.R., Renninger, S.L., Baohan, A.,
569 Schreiter, E.R., Kerr, R.A., Orger, M.B., Jayaraman, V., *et al.* (2013). Ultrasensitive
570 fluorescent proteins for imaging neuronal activity. Nature *499*, 295-300. doi:
571 10.1038/nature12354.
572
573 Collins, K.M., and Koelle, M.R. (2013). Postsynaptic ERG potassium channels limit
574 muscle excitability to allow distinct egg-laying behavior states in Caenorhabditis
575 elegans. Journal of Neuroscience *33*, 761-775. doi: 10.1523/JNEUROSCI.3896-
576 12.2013.
577

578 Dawkins, R. (1976). Hierarchical organisation: A candidate principle for ethology. In
579 Growing points in ethology P. Bateson, and R. Hinde, eds. (Oxford, England:
580 Cambridge U Press SN -), pp. 7-45. doi:
581
582 Donnelly, J.L., Clark, C.M., Leifer, A.M., Pirri, J.K., Haburcak, M., Francis, M.M.,
583 Samuel, A.D.T., and Alkema, M.J. (2013). Monoaminergic orchestration of motor
584 programs in a complex C. elegans behavior. PLoS biology *11*, e1001529. doi:
585 10.1371/journal.pbio.1001529.
586
587 Duistermars, B.J., Pfeiffer, B.D., Hoopfer, E.D., and Anderson, D.J. (2018). A Brain
588 Module for Scalable Control of Complex, Multi-motor Threat Displays. Neuron *100*,
589 1474-1490.e1474. doi: 10.1016/j.neuron.2018.10.027.
590
591 Eliav, T., Geva-Sagiv, M., Yartsev, M.M., Finkelstein, A., Rubin, A., Las, L., and
592 Ulanovsky, N. (2018). Nonoscillatory Phase Coding and Synchronization in the Bat
593 Hippocampal Formation. Cell *175*, 1119-1130.e1115. doi:
594 10.1016/j.cell.2018.09.017.
595
596 Faumont, S., Rondeau, G., Thiele, T.R., Lawton, K.J., McCormick, K.E., Sottile, M.,
597 Griesbeck, O., Heckscher, E.S., Roberts, W.M., Doe, C.Q., *et al.* (2011). An image-
598 free opto-mechanical system for creating virtual environments and imaging neuronal
599 activity in freely moving Caenorhabditis elegans. PLoS ONE *6*, e24666. doi:
600 10.1371/journal.pone.0024666.
601
602 Fayyazuddin, A., and Dickinson, M.H. (1999). Convergent mechanosensory input
603 structures the firing phase of a steering motor neuron in the blowfly, Calliphora.
604 Journal of Neurophysiology *82*, 1916-1926. doi: 10.1152/jn.1999.82.4.1916.
605
606 Flavell, S.W., Pokala, N., Macosko, E.Z., Albrecht, D.R., Larsch, J., and Bargmann,
607 C.I. (2013). Serotonin and the neuropeptide PDF initiate and extend opposing
608 behavioral states in C. elegans. Cell *154*, 1023-1035. doi:
609 10.1016/j.cell.2013.08.001.
610
611 Fouad, A.D., Teng, S., Mark, J.R., Liu, A., Alvarez-Illera, P., Ji, H., Du, A., Bhirgoo,
612 P.D., Cornblath, E., Guan, S.A., *et al.* (2018). Distributed rhythm generators underlie
613 Caenorhabditis elegans forward locomotion. eLife *7*, 713. doi: 10.7554/eLife.29913.
614
615 Fox, L.E., Soll, D.R., and Wu, C.-F. (2006). Coordination and modulation of
616 locomotion pattern generators in Drosophila larvae: effects of altered biogenic amine
617 levels by the tyramine beta hydroxlyase mutation. Journal of Neuroscience *26*, 1486-
618 1498. doi: 10.1523/JNEUROSCI.4749-05.2006.
619
620 Fujiwara, M., Sengupta, P., and McIntire, S.L. (2002). Regulation of body size and
621 behavioral state of C. elegans by sensory perception and the EGL-4 cGMP-
622 dependent protein kinase. Neuron *36*, 1091-1102. doi:
623
624 Gallagher, T., Bjorness, T., Greene, R., You, Y.-j., and Avery, L. (2013). The
625 Geometry of Locomotive Behavioral States in C. elegans. PLoS ONE *8*, e59865. doi:
626 10.1371/journal.pone.0059865.s013.
627

628 Gao, S., Guan, S.A., Fouad, A.D., Meng, J., Kawano, T., Huang, Y.-C., Li, Y.,
629 Alcaire, S., Hung, W., Lu, Y., *et al.* (2018). Excitatory motor neurons are local
630 oscillators for backward locomotion. eLife *7*, 1936. doi: 10.7554/eLife.29915.
631
632 Gendrel, M., Atlas, E.G., and Hobert, O. (2016). A cellular and regulatory map of the
633 GABAergic nervous system of C. elegans. eLife *5*, 1395. doi: 10.7554/eLife.17686.
634
635 Glaze, C.M., and Troyer, T.W. (2006). Temporal structure in zebra finch song:
636 implications for motor coding. Journal of Neuroscience *26*, 991-1005. doi:
637 10.1523/JNEUROSCI.3387-05.2006.
638
639 Gomez-Marin, A., Stephens, G.J., and Brown, A.E.X. (2016). Hierarchical
640 compression of Caenorhabditis elegans locomotion reveals phenotypic differences in
641 the organization of behaviour. Journal of The Royal Society Interface *13*, 20160466-
642 20160469. doi: 10.1098/rsif.2016.0466.
643
644 Goulding, M. (2009). Circuits controlling vertebrate locomotion: moving in a new
645 direction. Nature reviews Neuroscience *10*, 507-518. doi: 10.1038/nrn2608.
646
647 Gray, J.M., Hill, J.J., and Bargmann, C.I. (2005). A circuit for navigation in
648 Caenorhabditis elegans. Proceedings of the National Academy of Sciences of the
649 United States of America *102*, 3184-3191. doi: 10.1073/pnas.0409009101.
650
651 Gupta, N., Singh, S.S., and Stopfer, M. (2016). Oscillatory integration windows in
652 neurons. Nature Communications *7*, 13808. doi: 10.1038/ncomms13808.
653
654 Hahn, G., Ponce-Alvarez, A., Deco, G., Aertsen, A., and Kumar, A. (2019). Portraits
655 of communication in neuronal networks. Nature reviews Neuroscience, 1-11. doi:
656 10.1038/s41583-018-0094-0.
657
658 Haklai-Topper, L., Soutschek, J., Sabanay, H., Scheel, J., Hobert, O., and Peles, E.
659 (2011). The neurexin superfamily of Caenorhabditis elegans. Gene expression
660 patterns : GEP *11*, 144-150. doi: 10.1016/j.gep.2010.10.008.
661
662 Hendricks, M., Ha, H., Maffey, N., and Zhang, Y. (2012). Compartmentalized calcium
663 dynamics in a C. elegans interneuron encode head movement. Nature *487*, 99-103.
664 doi: 10.1038/nature11081.
665
666 Huang, K.-M., Cosman, P., and Schafer, W.R. (2008). Automated detection and
667 analysis of foraging behavior in Caenorhabditis elegans. Journal of neuroscience
668 methods *171*, 153-164. doi: 10.1016/j.jneumeth.2008.01.027.
669
670 Hums, I., Riedl, J., Mende, F., Kato, S., Kaplan, H.S., Latham, R., Sonntag, M.,
671 Traunmüller, L., and Zimmer, M. (2016). Regulation of two motor patterns enables
672 the gradual adjustment of locomotion strategy in Caenorhabditis elegans. eLife *5*,
673 1951. doi: 10.7554/eLife.14116.
674
675 Hyafil, A., Giraud, A.-L., Fontolan, L., and Gutkin, B. (2015). Neural Cross-Frequency
676 Coupling: Connecting Architectures, Mechanisms, and Functions. Trends in
677 Neurosciences *38*, 725-740. doi: 10.1016/j.tins.2015.09.001.

678
679 Jin, X., and Costa, R.M. (2015). Shaping action sequences in basal ganglia circuits.
680 Current opinion in neurobiology *33*, 188-196. doi: 10.1016/j.conb.2015.06.011.
681
682 Kato, S., Kaplan, H.S., Schrödel, T., Skora, S., Lindsay, T.H., Yemini, E., Lockery,
683 S., and Zimmer, M. (2015). Global Brain Dynamics Embed the Motor Command
684 Sequence of Caenorhabditis elegans. Cell *163*, 1-50. doi:
685 10.1016/j.cell.2015.09.034.
686
687 Kawano, T., Po, M.D., Gao, S., Leung, G., Ryu, W.S., and Zhen, M. (2011). An
688 imbalancing act: gap junctions reduce the backward motor circuit activity to bias C.
689 elegans for forward locomotion. Neuron *72*, 572-586. doi:
690 10.1016/j.neuron.2011.09.005.
691
692 Kiehn, O. (2011). Development and functional organization of spinal locomotor
693 circuits. Current opinion in neurobiology *21*, 100-109. doi:
694 10.1016/j.conb.2010.09.004.
695
696 Kim, K., and Li, C. (2004). Expression and regulation of an FMRFamide-related
697 neuropeptide gene family in Caenorhabditis elegans. The Journal of comparative
698 neurology *475*, 540-550. doi: 10.1002/cne.20189.
699
700 Klapoetke, N.C., Murata, Y., Kim, S.S., Pulver, S.R., Birdsey-Benson, A., Cho, Y.K.,
701 Morimoto, T.K., Chuong, A.S., Carpenter, E.J., Tian, Z., *et al.* (2014). Independent
702 optical excitation of distinct neural populations. Nature methods *11*, 338-346. doi:
703 10.1038/nmeth.2836.
704
705 Krakauer, J.W., Ghazanfar, A.A., Gomez-Marin, A., MacIver, M.A., and Poeppel, D.
706 (2017). Neuroscience Needs Behavior: Correcting a Reductionist Bias. Neuron *93*,
707 480-490. doi: 10.1016/j.neuron.2016.12.041.
708
709 Li, Z., Liu, J., Zheng, M., and Xu, X.Z.S. (2014). Encoding of both analog- and digital-
710 like behavioral outputs by one C. elegans interneuron. Cell *159*, 751-765. doi:
711 10.1016/j.cell.2014.09.056.
712
713 Liu, J., Ward, A., Gao, J., Dong, Y., Nishio, N., Inada, H., Kang, L., Yu, Y., Ma, D.,
714 Xu, T., *et al.* (2010). C. elegans phototransduction requires a G protein-dependent
715 cGMP pathway and a taste receptor homolog. Nature Neuroscience *13*, 715-722.
716 doi: 10.1038/nn.2540.
717
718 Long, M.A., Jin, D.Z., and Fee, M.S. (2010). Support for a synaptic chain model of
719 neuronal sequence generation. Nature *468*, 394-399. doi: 10.1038/nature09514.
720
721 Luo, L., Wen, Q., Ren, J., Hendricks, M., Gershow, M., Qin, Y., Greenwood, J.,
722 Soucy, E.R., Klein, M., Smith-Parker, H.K., *et al.* (2014). Dynamic Encoding of
723 Perception, Memory, and Movement in a C. elegans Chemotaxis Circuit. Neuron *82*,
724 1115-1128. doi: 10.1016/j.neuron.2014.05.010.
725

726 Maier, W., Adilov, B., Regenass, M., and Alcedo, J. (2010). A neuromedin U receptor
727 acts with the sensory system to modulate food type-dependent effects on C. elegans
728 lifespan. PLoS biology *8*, e1000376. doi: 10.1371/journal.pbio.1000376.
729
730 Marder, E., and Bucher, D. (2001). Central pattern generators and the control of
731 rhythmic movements. Current Biology *11*, R986-996. doi:
732
733 Marques, J.C., Lackner, S., Félix, R., and Orger, M.B. (2018). Structure of the
734 Zebrafish Locomotor Repertoire Revealed with Unsupervised Behavioral Clustering.
735 Current Biology, 1-34. doi: 10.1016/j.cub.2017.12.002.
736
737 McCloskey, R.J., Fouad, A.D., Churgin, M.A., and Fang-Yen, C. (2017). Food
738 responsiveness regulates episodic behavioral states in Caenorhabditis elegans.
739 Journal of Neurophysiology *117*, 1911-1934. doi: 10.1152/jn.00555.2016.
740
741 Moore, J.D., Deschênes, M., Furuta, T., Huber, D., Smear, M.C., Demers, M., and
742 Kleinfeld, D. (2013). Hierarchy of orofacial rhythms revealed through whisking and
743 breathing. Nature *497*, 205-210. doi: 10.1038/nature12076.
744
745 Nichols, A.L.A., Eichler, T., Latham, R., and Zimmer, M. (2017). A global brain state
746 underlies C. elegans sleep behavior. Science (New York, NY) *356*, eaam6851. doi:
747 10.1126/science.aam6851.
748
749 Piggott, B.J., Liu, J., Feng, Z., Wescott, S.A., and Xu, X.Z.S. (2011). The neural
750 circuits and synaptic mechanisms underlying motor initiation in C. elegans. Cell *147*,
751 922-933. doi: 10.1016/j.cell.2011.08.053.
752
753 Pokala, N., Liu, Q., Gordus, A., and Bargmann, C.I. (2014). Inducible and titratable
754 silencing of Caenorhabditis elegans neurons in vivo with histamine-gated chloride
755 channels. Proceedings of the National Academy of Sciences of the United States of
756 America *111*, 2770-2775. doi: 10.1073/pnas.1400615111.
757
758 Ramot, D., Johnson, B.E., Berry, T.L., Carnell, L., and Goodman, M.B. (2008). The
759 Parallel Worm Tracker: A Platform for Measuring Average Speed and Drug-Induced
760 Paralysis in Nematodes. PLoS ONE *3*, e2208-2207. doi:
761 10.1371/journal.pone.0002208.
762
763 Roberts, W.M., Augustine, S.B., Lawton, K.J., Lindsay, T.H., Thiele, T.R., Izquierdo,
764 E.J., Faumont, S., Lindsay, R.A., Britton, M.C., Pokala, N., *et al.* (2016). A stochastic
765 neuronal model predicts random search behaviors at multiple spatial scales in C.
766 elegans. eLife *5*, 489. doi: 10.7554/eLife.12572.
767
768 Ruijtenberg, S., and van den Heuvel, S. (2015). G1/S Inhibitors and the SWI/SNF
769 Complex Control Cell-Cycle Exit during Muscle Differentiation. Cell *162*, 300-313.
770 doi: 10.1016/j.cell.2015.06.013.
771
772 Schrödel, T., Prevedel, R., Aumayr, K., Zimmer, M., and Vaziri, A. (2013). Brain-wide
773 3D imaging of neuronal activity in Caenorhabditis elegans with sculpted light. Nature
774 methods *10*, 1013-1020. doi: 10.1038/nmeth.2637.
775

776 Shen, Y., Wen, Q., Liu, H., Zhong, C., Qin, Y., Harris, G., Kawano, T., Wu, M., Xu,
777 T., Samuel, A.D., *et al.* (2016). An extrasynaptic GABAergic signal modulates a
778 pattern of forward movement in Caenorhabditis elegans. eLife *5*, 2290. doi:
779 10.7554/eLife.14197.
780
781 Skora, S., Mende, F., and Zimmer, M. (2018). Energy Scarcity Promotes a Brain-
782 wide Sleep State Modulated by Insulin Signaling in C. elegans. CellReports *22*, 953-
783 966. doi: 10.1016/j.celrep.2017.12.091.
784
785 Sohal, V.S., Zhang, F., Yizhar, O., and Deisseroth, K. (2009). Parvalbumin neurons
786 and gamma rhythms enhance cortical circuit performance. Nature *459*, 698-702. doi:
787 10.1038/nature07991.
788
789 Sponberg, S., and Daniel, T.L. (2012). Abdicating power for control: a precision
790 timing strategy to modulate function of flight power muscles. Proceedings Biological
791 sciences / The Royal Society *279*, 3958-3966. doi: 10.1098/rspb.2012.1085.
792
793 Starich, T.A., Xu, J., Skerrett, I.M., Nicholson, B.J., and Shaw, J.E. (2009).
794 Interactions between innexins UNC-7 and UNC-9 mediate electrical synapse
795 specificity in the Caenorhabditis elegans locomotory nervous system. Neural
796 Development *4*, 16. doi: 10.1186/1749-8104-4-16.
797
798 Tinbergen, N. (1951). The study of instinct (Oxford Eng.: Clarendon Press).
799
800 Turek, M., Lewandrowski, I., and Bringmann, H. (2013). An AP2 transcription factor
801 is required for a sleep-active neuron to induce sleep-like quiescence in C. elegans.
802 Current biology : CB *23*, 2215-2223. doi: 10.1016/j.cub.2013.09.028.
803
804 Von Stetina, S.E., Fox, R.M., Watkins, K.L., Starich, T.A., Shaw, J.E., and Miller,
805 D.M. (2007). UNC-4 represses CEH-12/HB9 to specify synaptic inputs to VA motor
806 neurons in C. elegans. Genes & development *21*, 332-346. doi:
807 10.1101/gad.1502107.
808
809 Wen, Q., Po, M.D., Hulme, E., Chen, S., Liu, X., Kwok, S.W., Gershow, M., Leifer,
810 A.M., Butler, V., Fang-Yen, C., *et al.* (2012). Proprioceptive coupling within motor
811 neurons drives C. elegans forward locomotion. Neuron *76*, 750-761. doi:
812 10.1016/j.neuron.2012.08.039.
813
814 White, J.G., Southgate, E., Thomson, J.N., and Brenner, S. (1986). The structure of
815 the nervous system of the nematode Caenorhabditis elegans. Philosophical
816 transactions of the Royal Society of London Series B, Biological sciences *314*, 1-
817 340. doi:
818
819 Winnier, A.R., Meir, J.Y., Ross, J.M., Tavernarakis, N., Driscoll, M., Ishihara, T.,
820 Katsura, I., and Miller, D.M. (1999). UNC-4/UNC-37-dependent repression of motor
821 neuron-specific genes controls synaptic choice in Caenorhabditis elegans. Genes
822 & development *13*, 2774-2786. doi:
823
824 Xu, T., Huo, J., Shao, S., Po, M., Kawano, T., Lu, Y., Wu, M., Zhen, M., and Wen, Q.
825 (2018). Descending pathway facilitates undulatory wave propagation in

826 Caenorhabditis elegans through gap junctions. Proceedings of the National
827 Academy of Sciences *115*, E4493-E4502. doi: 10.1073/pnas.1717022115.
828
829 Yeon, J., Kim, J., Kim, D.-Y., Kim, H., Kim, J., Du, E.J., Kang, K., Lim, H.-H., Moon,
830 D., and Kim, K. (2018). A sensory-motor neuron type mediates proprioceptive
831 coordination of steering in C. elegans via two TRPC channels. PLoS biology *16*,
832 e2004929. doi: 10.1371/journal.pbio.2004929.
833
834 Yuste, R., MacLean, J.N., Smith, J., and Lansner, A. (2005). The cortex as a central
835 pattern generator. Nature reviews Neuroscience *6*, 477-483. doi: 10.1038/nrn1686.
836
837 Zimmer, M., Gray, J.M., Pokala, N., Chang, A.J., Karow, D.S., Marletta, M.A.,
838 Hudson, M.L., Morton, D.B., Chronis, N., and Bargmann, C.I. (2009). Neurons detect
839 increases and decreases in oxygen levels using distinct guanylate cyclases. Neuron
840 *61*, 865-879. doi: 10.1016/j.neuron.2009.02.013.
841
842
843 **Figure legends**
844
845
846 **Figure 1. A multi-timescale behavioral hierarchy of motor actions. (A)** Body
847 angle measurement. A: anterior, P: posterior, V: ventral, D: dorsal. **(B)** Lower:
848 example posture timeseries kymogram. Head-bend propagations traced by black
849 lines. Upper: worm images with propagated-bends (filled arrows) and head-casts
850 (open arrows) indicated. Scale bar, 0.4 mm. **(C)** Fractional and cumulative
851 distributions of each head-bend's most posterior propagation segment. n = 45,129
852 head bends pooled from 28 assays, ~20 animals per assay. **(D)** Median,
853 interquartile and range of cycle periods for forward/reverse (forward + reverse bout
854 duration, n=1,259), propagated-bend (n=25,817), and head-cast cycles (n=341)
855 pooled from 14 assays, ~20 animals per assay. ****p<0.0001, Mann-Whitney Test.
856 **(E)** Example head-bend angle timeseries illustrating propagated-bend phase
857 measurement. Red and blue dashed lines indicate initial head-cast phases,
858 quantified in (**F**). **(F)** Fractional distributions of initial dorsal or ventral head-casts
859 binned according to their propagated-bend oscillation phases. n = 427 dorsal and
860 194 ventral head-casts pooled from 21 animals. $p<10^{-6}$ for both distributions,

861 indicating the probability that each is drawn from the full data distribution shown in
862 grey (Methods). **(G)** Hierarchical model of behavior with corresponding cycle
863 frequencies from **(D)**. See also Figure S1.
864
865 **Figure 2. A nervous-system-wide representation of slow behavioral dynamics**
866 **at the uppermost hierarchy level.** **(A**) Worm schematic. **(B-D)** Example whole-
867 nervous-system GCaMP6f recording. **(B)** Upper: motor command states inferred
868 from neuronal activity (Methods). Lower: Fluorescence timeseries of 129 neurons,
869 sorted by correlation. **(C)** Low-dimensional representation of nervous-system-wide
870 activity cycle, from principal components analysis (PCA). Color key in lower panel
871 indicates motor command state inferred from neuronal activity (Methods;
872 arrowheads indicate directional flow). Coordinates depict PC axes orientations and
873 % variance explained. **(D)** Activity traces of selected neurons. **(E)** Mean ± SEM
874 correlation coefficient between neuronal activity traces and traces reconstructed
875 using indicated top PCs. n = 5 datasets. See also Figure S2 and Movie S1.
876
877 **Figure 3. Identification of candidate central pattern generator circuits for lower**
878 **hierarchy levels.** **(A)** Activity peak frequencies per forward command period for all
879 identified neurons, pooled from n = 5 whole-nervous-system and n= 5 head ganglia
880 recordings. Median, interquartile, and 5-95% range shown. “Baseline” distribution
881 for one peak per forward command period, red line indicates its median. Neurons
882 above “baseline” peaked multiple times within forward command periods; of those,
883 red labels indicate significantly non-random inter-peak interval distributions
884 (Methods). See **Table S2** for multiple-comparison corrected p-values and n
885 numbers. #ambiguous IDs, see Methods for alternatives. **(B)** Worm head schematic

illustrating positions and lateralized muscle innervations of CPG candidate motor neurons. Cell bodies and projections not shown to scale. **(C)** Covariograms of SMD and DB with all coordinated neurons. All identified neurons were tested, but shown are only those with significant correlation with at least one SMD or DB01/02. Panels show the relative frequencies of Ca^{2+}-peaks of neurons in columns triggered to Ca^{2+}-peaks of neurons in rows. Data are shuffle-corrected so that positive/negative values show higher/lower correlation than chance (Methods). Opaque plots differ significantly from random surrogate distributions (Methods; p-values in **Table S3**). Colored borders denote significant positive relationships consistent within neuron classes. See also Figure S2.

Figure 4. SMDs and body motor neurons are required for head-casts and propagated-bends, respectively. (A) Frequencies as in **(Fig. 3A)** for the indicated neurons in control, VNC_{ACh}-inhibited, and SMD-inhibited animals, pooled across paired neurons, and across n = 5 (control, SMD::HisCl) or 4 (VNC_{ACh}::HisCl) recordings. *p<0.05, ****p<0.0001, Mann-Whitney Test. n.s., not significant. Box plots show median, interquartile and range. **(B)** Effects of SMD (n=9), VNC_{ACh} (n=6), and SMD+VNC_{ACh} (n=6) inhibition on propagated-bends (upper) and head-casts (lower), mean ± SD. Each data point is the mean of an experimental repeat with ~20 animals each. **p<0.01, ****p<0.0001, Mann-Whitney Test. n.s., not significant. See also Figure S3.

Figure 5. Hierarchy level I and II interaction: SMD neurons are multi-functional. **(A)** Hierarchy levels investigated. **(B-C)** Example DB02 **(B)** and SMD **(C)** Ca^{2+}-imaging in moving animals. Lower: posture kymograms. Dotted vertical lines:

unilateral SMDD- or SMDV-only oscillations. **(D-G)** Fractional distributions of DB02 **(D-E)** or SMD **(F-G)** Ca^{2+} peaks binned by head-bend phase during forward **(D, F)** or reverse **(E, G)** locomotion. n = 595 **(D)**, 5 **(E)**, 547 **(F,** SMDD**)**, 437 **(F,** SMDV**)**, 147 **(G,** SMDD**)**, 134 **(G,** SMDV**)**. $p<10^{-6}$ for all distributions except SMDV (p=0.000728) and DB02 (n.s.) during reverse locomotion, indicating the probability that distributions are drawn randomly (Methods). Probability that SMDD and SMDV reversal distributions were drawn from the respective forward distributions: $p<10^{-6}$ (Methods). **(H)** Percentage of head-bend cycles with at least one activity peak. Total head-bend cycles, from left to right: n = 639, 80, 517, 290, 386, 291. **(I)** Frequency (upper) and average amplitude (lower) of activity peaks. **p<0.01, ***p≤0.001, Wilcoxon matched-pairs signed rank test. Each data point from one animal, n=11 (SMD) and n=10 (DB02). N.A., not applicable, no amplitude measurement possible in the absence of peaks in several animals. **(J)** Peak head-bend amplitudes in SMD::hisCl animals, mean ± SD. **p<0.01, ****p<0.0001 Mann-Whitney Test. **(K)** Reversal duration in SMD::hisCl animals, ****p<0.0001, Mann-Whitney Test. Each data point in **(J-K)** is the mean of an experimental repeat (n=9) with ~20 animals each. **(L)** Reversal command duration from head ganglia imaging in immobilized animals. Each data point is the mean of an experimental repeat, n=5 each. **p<0.01, Mann-Whitney test. Data in **(D-H)** pooled across 11 (SMD) and 10 (DB02) animals. See also Figure S4 and Movie S2.

Figure 6. Hierarchy level II and III interaction: neuronal phase-nesting. **(A)** Hierarchy levels investigated. **(B-E)** DB02 **(B, D)** and SMD **(C, E)** trigger-averaged GCaMP/mCherry traces and kymograms. Alignment to either propagated-bend without subsequent head-casts **(B-C)** or initial head-casts **(D-E)**. Left to right, n =

669, 680, 303, 101 **(B,D)** and n = 377, 360, 178, 119 **(C,E)**. In **(E)**, activity peaks during propagated-bends (filled arrowheads) and head-casts (open arrowheads) denoted. **(F)** Example SMD activity timeseries illustrating SMD alternation phase measurement. Red and blue dashed lines indicate unilateral SMDD-only or SMDV-only oscillations, quantified in **(G-H). (G-H)** Fractional distributions of unilateral SMDD-only or SMDV-only oscillations binned according to SMD alternation cycle phase, in freely moving **(G)** or immobilized **(H)** animals. n = 102 **(G,** SMDD**)**, 68 **(G,** SMDV**)**, 33 **(H,** SMDD**)** and 14 **(H,** SMDV). $p \leq 10^{-6}$ for each SMD distribution in **(G)** and **(H)** indicates the probability that distributions are drawn randomly from the full data distribution shown in grey (Methods). Data in **(H)** pooled from 10 animals. Data in **(B-E, G)** pooled across 11 (SMD) and 10 (DB02) animals. See also Figure S5.

Figure 7. A hierarchical control mechanism for behavioral flexibility. (A) Neuron classes (F = forward-active neurons, R = reverse-active neurons) underlying each behavior. **(B)** Model traces (upper) and corresponding behavioral and neuronal hierarchy states (lower). **(C)** RIB inhibition model: longer propagated-bend cycle period results in increased head-cast frequency. **(D-E)** Propagated-bend cycle period **(D)** and head-cast frequency **(E)** in RIB::hisCl animals, mean ± SD. n=8 assays each. ***p<0.001, Mann-Whitney Test. **(F)** RIB activation model: shorter propagated-bend cycle period results in decreased head-cast frequency. **(G-H)** Propagated-bend cycle period **(G)** and head-cast frequency **(H)** in RIB::Chrimson animals during yellow light exposure. n=8 assays each. **p<0.01, ***p<0.001, Mann-Whitney Test. **(I)** Representative O_2 downshift kymogram. **(J-K)** Propagated-bend cycle period **(J)** and head-cast frequency **(K)** 30s pre- and post-O_2 downshift. n=14 assays. ***p<0.001, ****p≤0.0001, Wilcoxon matched-pairs signed rank test.

961 **(L)** Example kymogram during dwelling to roaming switch. **(M-N)** Propagated-bend
962 cycle period **(M)** and head-cast frequency **(N)** in dwelling or roaming animals. n=19
963 assays. ****p<0.0001, Wilcoxon matched-pairs signed rank test. All data points
964 show the mean of an experiment repeat with ~20 animals each. See also Figure S6
965 and Movies S3 and S4.
966
967
968 **STAR Methods**
969
970 **CONTACT FOR REAGENT AND RESOURCE SHARING**
971 Further information and requests for resources and reagents should be directed to and
972 will be fulfilled by the Lead Contact, Manuel Zimmer (manuel.zimmer@univie.ac.at).
973
974 **EXPERIMENTAL MODEL AND SUBJECT DETAILS**
975 All experiments were performed in *lite-1 (ce314)* animals to reduce light responses
976 (Liu et al., 2010). Young adult hermaphrodites were used for all experiments. Worms
977 were maintained using standard methods (Brenner, 1974) and grown at 20°C on
978 nematode growth media (NGM) plates, which were seeded with *Escherichia Coli*
979 OP50 as a food source. A detailed list of all transgenic strains used is provided in the
980 Key Resources table and Table S1.
981
982 **METHOD DETAILS**
983 **Population behavior assays**
984 For on-food assays (**Fig. 7G-H, L-N**, **S6C-D**), ~20 animals (young adults, 0 eggs to 1
985 row of eggs) were transferred to a 15cm NGM assay plate seeded with OP50
986 (previously grown for 16 hours at room temperature). For off-food assays (all other

behavior experiments) animals were picked onto a food-free NGM plate, immersed in 1mL S-basal to remove transferred food, and picked again onto a food-free 15cm NGM assay plate. Data in **Fig. 1D** are combined from an equal number of on- and off-food experiments, because head-casts make up the majority of bends on-food and propagated-bends make up the majority off-food. In both cases, a 36mm x 36mm assay arena was delineated by Whatman paper soaked with 20mM $CuCl_2$, a repellent used to prevent worms from leaving the arena. A custom transparent plexiglass gas flow device (Hums et al., 2016) of 39mm x 39mm x 0.7mm was placed on top of this arena, through which 21% O_2 was delivered at 25mL/min via a static gas mixer connected to mass flow controllers (Vögtlin Instruments), operated by custom written LabVIEW scripts (National Instruments). For off-food assays, 21% O_2 was switched to 4% O_2 to examine sensory responses; for on-food assays, 21% O_2 was required to observe significant roaming periods. Arenas were illuminated with red LEDs and movies were recorded at 10fps on 5 megapixel CMOS cameras (Teledyne DALSA) with a pixel resolution of 0.0129 mm/pixel. Animals were allowed to acclimate for either 5min (off-food) or 1h (on-food) prior to recordings.

For histamine assays, prior to picking onto the assay plates, animals were incubated for 30-45min on plates with NGM agar including either 20mM histamine (+His; histamine dihydrochloride, Sigma-Aldrich) or an equal volume of water (-His) and seeded with OP50 across the entire agar surface to enhance histamine uptake. Recordings were performed on +His and -His assay plates. For optogenetics assays, animals expressing the optogenetic activator Chrimson (Klapoetke et al., 2014) were grown on NGM plates seeded with OP50 plus either 100μM all-trans retinal (ATR) or an equal volume of ethanol lacking ATR (Control). One day prior to assays, L3 and L4 animals were picked onto fresh ATR or Control plates. After 30min without light,

constant 591nm light was delivered, via a custom-made ring of LEDs above the assay plate, at ~45 $\mu W/mm^2$ for 30min.

Movies were analyzed using custom image processing and tracking code in MATLAB (Mathworks), built upon previously published scripts (Ramot et al., 2008). Briefly, worms were detected by gray level thresholding, and trajectories were found by adjoining nearby centroid coordinates in adjacent frames. These centroid data were used for speed, angular speed, reversal, and heading change quantifications. To measure bend angles, worm images were analyzed as described in (Hums et al., 2016). Briefly, binarized worm images were skeletonized to produce splines tracing the midline of each worm. Splines were smoothed and divided into 25 equally spaced body segments. Head vs. tail positions were determined by direction of centroid movement. Angles were measured between adjacent segments as in **Fig. 1A** to produce 24 angle measurements for each frame in each worm's trajectory. Power spectra in **Fig. S3C** were calculated using the MATLAB (Mathworks) function fft. For experiments in which manipulations caused a loss of animal movement, it was important to exclude time-averaged background subtraction prior to gray level thresholding, and to assign head position manually. Ventral and dorsal were indistinguishable in these lower-resolution recordings, so angle sign was assigned randomly; all panels distinguishing ventral and dorsal directions made use of higher-resolution movies recorded along with Ca^{2+} imaging (see below).

<u>Ca^{2+} imaging in immobilized animals</u>

For immobilized Ca^{2+} imaging whole-brain and whole-nervous system experiments, transgenic adult *C. elegans* (1 day after larval L4 stage, 0-10 eggs) expressing

genetically-encoded calcium indicator NLS-GCaMP6f (Chen et al., 2013) panneuronally (using the *Punc-31* promoter) were recorded as described previously (Kato et al., 2015) with following modifications. Previously, we found that forward command periods occasionally terminate in quiescence periods (Kato et al., 2015; Nichols et al., 2017). Thus, to increase forward command period occurrence, we expressed the *Drosophila* hisCl channel (Pokala et al., 2014) in the quiescence-promoting neuron RIS (Nichols et al., 2017; Turek et al., 2013) with the *Pnlr-1* (Gendrel et al., 2016; Haklai-Topper et al., 2011) promoter. To silence the SMDs, hisCl was expressed specifically in these neurons using a Cre-lox strategy. To this end, we expressed Cre with the P*unc-7S* promoter (Starich et al., 2009) and the *HisCl::SL2::mCherry* construct within a double inverted open reading frame (DIO) with the *Pflp-22* promoter (Kim and Li, 2004). SMD inhibition was confirmed using the mCherry marker co-expressed with HisCl to co-record GCaMP from the SMD neurons; animals showing residual SMD activity (~50%) were excluded from further analysis. Residual SMD activity often observed in mCherry-positive neurons (data not shown) may explain residual head-casting in SMD::hisCl animals (**Fig. 4B**). Body MNs were silenced by expressing hisCl and mCherry in VNC cholinergic motor neuron classes AS, DA, DB, VA, VB with promoter *Punc-17β* (Charlie et al., 2006); this promoter is referred to as VNC_{ACh} throughout. While we could not use the mCherry marker to unambiguously identify DB01 and DB02 in these animals, we confirmed that all mCherry-positive neurons in the retrovesicular ganglion (where DB01 and DB02 nuclei reside) showed little to no activity.

Immobilized Ca^{2+} imaging experiments were performed with custom-made microfluidic two-layer PDMS devices as previously described (Kato et al., 2015; Schrödel et al., 2013), with modifications. In addition to the curve in the worm channel

used to align worms laterally (Cáceres et al., 2012), a straightening of the channel was followed by a second curve designed to fit a young adult worm. This curve was designed to align the animal's head and tail, thus reducing the necessary imaging area to record the activity of all neurons in the *C. elegans* body; it also contains a narrowing in order to keep the animal's head in place. A technical drawing of the design is provided in **Fig. S2A**.

As previously described (Hums et al., 2016; Zimmer et al., 2009), the worm channel of the microfluidic device was connected to a syringe containing nematode growth medium (NGM) buffer with 1 mM tetramisole and 20 mM histamine (his-tet-NGM). All components were connected using Tygon tubing (0.02 in ID, 0.06 in OD; Norton) or polyethylene tubing (0.066 in ID, 0.095 in OD; Intramedic) using 23G Luer-stub adapters (Intramedic). Constant gas delivery at 21% O_2 at a flow rate of 50ml/min was regulated with a gas mixer attached to mass flow controllers (Vögtling Instruments) that mixed oxygen and nitrogen from pressurized gas tanks, using LabView software.

Well-fed worms were transferred onto NGM agar plates seeded with OP50 *E. coli* mixed with 20 mM histamine to feed on for 30-45 minutes. To rid them of bacteria covering the body, the animals were transferred into a drop of his-tet-NGM on a food-free NGM agar plate and then onto a second NGM plate with his-tet-NGM buffer. A vacuum was manually applied with the syringe to suck up individual animals into Tygon tubing; this tubing was subsequently reconnected to the worm inlet to arrange the worm in the curved channel. The fluorescence values were recorded 5 minutes after loading; the illumination and piezo stage were switched on 2-3 minutes before acquisition start. Animals were imaged at 21% O_2 for 30 minutes.

High-resolution data of neuronal activity in the head ganglia (whole-brain

recordings) was acquired with an inverted UltraViewVoX spinning disk confocal microscope (PerkinElmer) using an EMCCD camera (C9100-13, Hamamatsu) and a 40x 1.3 NA EC Plan-Neofluar oil-immersion objective (Zeiss). The volume spanning the animals' head ganglia was recorded in 13-15 2 µm z-planes, each illuminated for 10ms to record GCaMP6f fluorescence, resulting in acquisition rates of 1.55 - 2.23 volumes/sec. Whole-nervous system neuronal activity was recorded using an inverted fluorescence microscope (Observer Z1, Zeiss) with a 25x 0.8 NA LCI Plan-Neofluar multi-immersion objective (Zeiss) and recorded with a scientific complementary metal-oxide-semiconductor (sCMOS) camera (pco.edge 4.2, PCO) using Visiview software (Visitron Systems). The nervous system was recorded in 30 1 µm z-planes illuminated each for 10ms, resulting in an acquisition rate of 3.0303 volumes/sec. To increase the contrast and resolution of the image data, we used a deconvolution algorithm (classic maximum likelihood estimation) using Huygens software (signal/noise ratio, 8; automatic background estimation; iterations, 40; quality change stopping criterion, 0.1).

Simultaneous imaging of neuronal activity and behavior

Transgenic young adult worms (0-6 eggs) were placed onto a foodless NGM agar plate, allowed to crawl away from food, then picked onto another foodless NGM agar plate. Then, as in (Collins and Koelle, 2013), a ~40mm x 40mm chunk of agar surrounding the worm was removed and covered with a 45mm x 50mm #1.5 coverglass, so that the worm was between coverglass and agar. Under these conditions worms move slower but with qualitatively normal body shapes and behavior. The coverglass setup was placed into a motorized stage with associated controller (MS-2000-PhotoTrack, Applied Scientific Instrumentation). After a 5min

acclimation period including at least 2min excitation light exposure, each worm was recorded for 8min. Images were acquired using an inverted compound microscope (Ziess Axio Observer.Z1) with two Charge-Coupled Device cameras (Evolve 512, Photometrics). A CoolLED pE-2 excitation system provided dual wavelength excitation light (470 and 585 nm) with an ET-EGFP/mCherry filter set (59022x, Chroma) and dichroic (59022bs, Chroma). A 63x oil objective (Zeiss Plan-Apochromat, 1.4 NA) was used to stream unbinned images at 33ms exposure time (~30Hz) with Visiview software (Visitron Systems GmbH). The neuron(s) of interest were re-centered onto the objective using the system described in (Faumont et al., 2011): a dichroic mirror (620 spxr, Chroma) directed the high-wavelength portion of the mCherry emission to a four-quadrant photomultiplier tube (Hamamatsu). Remaining emission light was split by a DualCam DC2 cube (565 lpxr, Photometrics) to each CCD camera, one for mCherry (641/75nm, Brightline) and one for GCaMP (520/35nm, Brightline). Simultaneous behavior recordings were made under infrared illumination (780nm) using a CCD camera (Manta Prosilica GigE, Applied Vision Technologies) at 4x magnification and 100ms exposure time. Approximately 8 minutes of data were acquired for each animal.

Data Analysis

Neuronal time series extraction (pan-neuronal imaging)

As described before (Kato et al., 2015), neuronal activity traces were obtained by tracking the intensity maxima in each volume over time and calculating the single-cell fluorescence intensities (F). F_0 was calculated as the mean fluorescence intensity across the trial. After background subtraction, $\Delta F/ F_0$ was calculated for each neuron. $\Delta F/F_0$ neural traces were then detrended to correct for bleaching in a two-step

procedure which gave qualitatively better results compared to the previously described method (Kato et al., 2015). First, we performed and exponential fit to each trace, followed by fitting a single exponential function to peaks of the neural traces. Neural traces were manually inspected after the second detrending step; for those traces that were distorted by this method, we resorted to the single bleach-corrected version of the trace.

Neuronal identification (pan-neuronal imaging)

In whole-brain Ca^{2+} imaging data, the activity of 113-129 neurons was detected in the head ganglia, which corresponds to 49.7 - 66.15% of expected neurons. The rest likely were constitutively inactive and thus showed very low fluorescence levels; we further cannot exclude that the label is not expressed in a small fraction of neurons. In whole-nervous system Ca^{2+} imaging data, 103-129 neurons were detected across the whole body (39.4 - 42.7%).

The identification of the neurons of interest was done according to their activity patterns, anatomical location (www.wormatlas.org) and our experience with red fluorophore expression in specific marker lines reported in previous recordings (Kato et al., 2015; Nichols et al., 2017; Skora et al., 2018). In addition, the SMD neurons were identified by driving worm codon-optimized mCherry (wCherry) (Kawano et al., 2011) expression with the *Pflp-22* and *Punc-7s* promoters; henceforth, we disambiguated the uncertain cell class identity of these neurons reported in previous studies (SMDD vs. SMB or RMF)(Kato et al., 2015; Schrödel et al., 2013). B-MNs along the VNC were identified with the *Pacr-5* promoter (Winnier et al., 1999); PDA was identified with a Cre-lox strategy using the P*flp-7*::*Cre* and P*nmur-1*::*DIO-mCherry* constructs (Kim and Li, 2004; Maier et al., 2010). We denoted # cases in which reliably

observed activity patterns in distinct locations could not be unambiguously assigned to neuronal identities; their neuronal identities and possible alternatives are shown in brackets: URY (URA, IL1), RMD (SAA, RIA, SIB, RIH), SIB (SIA, RMD, RMH).

B-MN IDs were determined by a combination of position, activity, and specific marker line information. We consistently observed four neurons in the retrovesicular ganglion (RVG) with heightened activity during forward command periods; we labelled the anterior-most neuron VB02 and the posterior-most neuron DB01, in agreement with previous IDs (www.wormatlas.org). Of the remaining two neurons, we consistently found one with activity patterns like DB01 and VB02 (i.e. slow rises following AVA fall and activity plateaus throughout forward command periods) and one with more spike-like, unpredictable activity transients. We used P*ceh-12::mCherry* to label VB neurons (Von Stetina et al., 2007) while recording and found that the latter neuron is VB01; the former is therefore DB02. Other B-MNs are reported to occur in a specific pattern along the VNC: DB03 and VB04 are posterior to the RVG and separated by cell bodies of other neuron classes, and posterior to VB04 is a repeating pattern of consecutive (i.e. uninterrupted by other cell bodies) VB/DB pairs followed by single VB neurons. We used P*acr-5::mCherry* to label all B-MNs and their processes and confirmed this 2-1-2-1 pattern. This marker also showed that in VB/DB pairs, the VB neuron is always anterior (DB but not VB neurons have commissures that cross to the dorsal side). One exception to this rule was the posterior-most pair: 11/20 animals showed DB07 anterior to VB11. In whole-nervous-system recordings, we found the expected number of neurons in the expected anatomical pattern showing heightened activity during forward command periods in all recordings. This allowed us to assign IDs to all such neurons except DB07 and VB11; we labelled the anterior of this pair DB07a and the posterior VB11p.

Principal Component Analysis (PCA; pan-neuronal imaging)

Our previously reported neuronal activity studies in freely moving animals showed that behavioral parameters like motor state, crawling speed and turning strength can sometimes better be decoded either from the time derivatives or original Ca^{2+}-imaging traces, depending on neuronal class (Kato et al., 2015). Unlike in our previous work, where we performed PCA only on the time derivatives (Kato et al., 2015; Nichols et al., 2017; Skora et al., 2018), we here performed PCA on both original Ca^{2+}-imaging traces plus their derivatives, thus each neuron is represented by two variables (rather than one) where each recording frame is one observation. This procedure is less biased as it captures both instantaneous Ca^{2+}-levels as well as the dynamics of each neuron. First, a variance threshold of 0.0083 was set to neuronal activity traces to exclude low variance (and thus inactive) neurons. Then, the time derivatives of $\Delta F/F_0$ of the detrended neuronal activity traces were calculated using the total variation regularized differentiation method (Chartrand, 2011). The neural traces were normalized so that each trace and its time derivative had equal variance. PCA was performed on the detrended $\Delta F/F_0$ neural traces and their time derivatives simultaneously using the MATLAB (Mathworks) pca function, which also calculated variance explained for each PC. For visualization purposes, a 10-sample sliding average filter was applied to the PCA-phase plot trajectories. Command state coloring of the phase plot trajectories was performed similarly as described previously (Kato et al., 2015). Shortly, AVA, SMDD and SMDV activities were used to assign behavior state commands to population neuronal activity. For this, RISE, HIGH, FALL and LOW phases were identified for these neurons as follows: RISE and FALL phases were defined as time points when their time derivative was greater than a small positive

threshold or smaller than a negative threshold, respectively. The remaining time points were assigned to HIGH and LOW phases based on behavioral state order and a threshold. The time points in the trajectory of neuronal activity were then colored by AVA phase (AVA rise as reversal, high as sustained reversal, fall as a post-reversal turn, and low as forward command). Additionally, AVA falls coupled to SMDV rises were defined as ventral turns and AVA falls coupled to SMDD rises as dorsal turns. Note that SMDD vs. SMDV rises during AVA falls were mutually exclusive in 100% of all detected AVA falls.

Command period identification, duration quantification (pan-neuronal imaging)

Forward command periods were inferred from the activity of interneuron AVA, as previously described (Kato et al., 2015). Shortly, timepoints of falling Ca^{2+} transients and low intensity AVA Ca^{2+} signals were defined as forward command periods. Timepoints of rising Ca^{2+} transients and high intensity Ca^{2+} signals were defined as reversal command periods.

Mean activity difference quantification (pan-neuronal imaging)

In order to assess whether neuronal activity levels are modulated by the forward/reverse command state, we calculated for each neuron the mean $\Delta F/F_0$ of the Ca^{2+} imaging neural activity traces in all forward and reverse command periods, separately, and calculated the difference. As for the peak frequency quantification (see below), all neurons identified in at least three recordings were taken into account. We determined which neurons showed a significant difference between their mean activity levels in the forward vs. reverse command states with a paired T-test (p-values reported in Table S2).

1237

1238 Peak frequency quantification (pan-neuronal imaging)

1239 In order to identify neurons with activity fluctuations that could correspond to
1240 oscillations during the forward command period, Ca^{2+} imaging neural activity traces
1241 were analyzed to determine their peak frequencies per each forward command period.
1242 For all neurons identified in at least three recordings, we obtained their smoothed time
1243 derivatives with the total variation regularized differentiation method (Chartrand, 2011)
1244 and detected activity peaks as follows: for each trace, local maxima and minima were
1245 detected. Maximum peaks were found as maximal values that were preceded and
1246 followed by a value lower than parameter delta. For each Ca^{2+} imaging recording, one
1247 appropriate delta parameter was set for peak detection in all neurons.

1248 The distribution of forward command period duration was bimodal (data not
1249 shown) and periods shorter than 50 seconds rarely allowed for more than one
1250 fluctuation per period. In order to avoid a bias in our analysis because of lack of data,
1251 forward command periods shorter than 50 seconds were excluded from the analysis.
1252 Frequencies were calculated as the number of maximum peaks within each forward
1253 command period divided by the duration of each forward command period for each
1254 neuron. Instances where a neuron was identified but no peaks were detected were
1255 counted as zero.

1256

1257 Cross-correlation analysis (pan-neuronal imaging)

1258 Covariograms report the frequency, relative to chance levels, of a "target" neuron's
1259 peak at different time delays relative to a "reference" neuron's peak. We found
1260 covariogram analysis superior to standard cross-correlation analysis for our sparse
1261 data. For example, neurons often showed only one or two activity transients per

forward command period. Standard cross-correlation on sparse data would report a high value at a given lag for two neurons showing few activity transients each, despite having independent signals. For example, a toy dataset of two signals, one oscillatory and one with a single step or few step signals would result into a strong cross correlation signal, which would otherwise vanish, if the time-series could be expanded to capture many sparse signals, which often is experimentally unfeasible. Averaging max cross-correlation values across forward periods would therefore result in high correlations for neurons showing sparse activity. Covariograms, by contrast, take into account the number of peaks detected, thus enabling statistical testing to exclude cases with few peaks from significance.

Covariograms were computed as described in ref. (Brody, 1999) with some minor adjustments to account for variations in forward command period duration. For each neuron pair, we first computed raw cross-correlogram counts as follows. We used peaks identified as described in the above section, only during forward command periods longer than 50s. For each peak in the reference neuron (rows in **Fig. 3C and S2E**), all peaks in the target neuron (columns in **Fig. 3C and S2E**) during the same forward command period were considered; in 10s bins, the time delays of these target neuron peaks relative to the reference peak were accumulated. This procedure was used across all reference spikes within each period, and ultimately to accumulate the full raw cross-correlogram across all forward command periods across all recordings. To account for unequal trial durations, raw cross-correlogram counts were then converted to frequencies, by dividing by the number of available data for each bin (i.e. the number of possible frames in each bin in which spikes could have occurred, given the trial duration). 10^6 resampled raw cross-correlograms were computed by randomly selecting the same number of spike times of the target neuron within each forward

period and normalizing in the same manner. This resampling procedure accounts for trial-to-trial co-fluctuations in neuronal activity frequencies that may be independent of peak timing relationships (Brody, 1999). Covariograms were then computed by subtracting the average resampled raw cross-correlograms (which serve as the "shuffle corrector" or "shift predictor" (Brody, 1999)) from actual raw cross-correlograms.

Neuronal time series extraction and behavior analysis (freely moving imaging)

GCaMP and mCherry signals were extracted by first tracking the nucleus or cell body of interest using Metamorph software (Molecular Devices). Then, using custom MATLAB (Mathworks) scripts, the coordinates of the tracked regions were used to extract the average of the 50 brightest pixels. A background measurement from the first frame per channel per recording was subtracted. The GCaMP/mCherry ratio, henceforth "R," was then used to calculate an R_0 value as the mean of the lowest 10% of ratio values. $\Delta R/R_0$ was then calculated as $(R - R_0) / R_0$. For subsequent analyses, peaks were detected using a parameter delta determined by manual inspection. A maximum point must be preceded and followed by a value lower by at least delta, and vice versa, a minimum point must be preceded and followed by a value higher by at least delta. Data were further normalized by the 95th percentile in each recording for **Fig. 5I** and **Fig. S4B**.

Reversals were identified manually by examining infrared movies. All other time points were considered as forward periods. Custom MATLAB (Mathworks) scripts used a combination of edge detection and gray level thresholding to extract a binary worm image, which were used for subsequent skeletonization as described in (Hums et al., 2016) to quantify 24 angle measurements. Angle measurements were linearly

interpolated to match the 30Hz Ca^{2+} recording and manually inspected for correct ventral/dorsal assignment.

Propagation analysis, head-bend type classification, and cycle period quantification (behavior assays and freely moving imaging)

Note that data in **Fig. 1E-F** and **Fig. S1B-D** were obtained from Ca^{2+} imaging recordings, as these recordings were high enough resolution (and contained fluoresecent neuronal markers) to distinguish dorsal and ventral sides, and because head-casts were more prominent in these animals allowing us to quantify head-cast episodes containing more than two head-casts. All other data in these figures were obtained in population behavior assays. Kymograms from either population behavior assays or simultaneous Ca^{2+} imaging and behavior experiments were smoothed and, in the case of missing data due to poor skeletonization, linearly interpolated to fill gaps < 1s. All subsequent analyses were performed separately on forward and reverse locomotion periods. For each angle timeseries, local maxima and minima were detected using a parameter delta determined by manual inspection. A maximum point must be preceded and followed by a value lower by at least delta, and vice versa, a minimum point must be preceded and followed by a value higher by at least delta. Each angle timeseries was thereby transformed into an "angle peak timeseries" containing for each frame either a maximum (= 1), a minimum (= -1), or neither (= 0). Note that maxima (minima) can be dorsal (ventral) if the head-bend changes by at least delta but does not cross 0. The resulting matrix of all angle peak timeseries, or "peak kymogram," (**Fig. S1A**, lower) of the same size as the original kymogram, was analyzed to determine the propagation of each head-bend as follows.

Because the first (anterior-most) angle is typically noisier than the others, peaks in the second angle were initially defined as head-bends. Head-bends were then analyzed in temporal order, in the following manner. For each head-bend (angle #2 peak), if the previous (i.e. backward or simultaneous in time) peak in angle #1 is of the same sign as the current head-bend (maximum, = 1, or minimum, = -1), and hasn't been assigned to a previous head-bend, then that peak is assigned to the current head-bend. Similarly, if the next (i.e. forward or simultaneous in time) peak in angle #3 is of the same sign as the current head-bend (maximum, = 1, or minimum, = -1), and hasn't been assigned to a previous-head-bend, then that peak is assigned to the current head-bend. The next peak in angle #4 is examined with respect to the current peak in angle #3 in the same way; this process is iterated posteriorly until the final angle (see **Fig. S1A**, lower), or until the propagation is terminated as follows. If the next posterior peak is of the opposite sign as the current head-bend, the head-bend is terminated. If the next posterior peak (a) occurs >10s following the previous peak and/or (b) occurs following at least two unassigned peaks in the previous (i.e. anterior) angle, then it is likely not part of the current head-bend, so the head-bend propagation is terminated. In both above cases, if the final propagation angle was less than or equal to angle #13, then the head-bend is assigned as a head-cast. If the final propagation angle was angle #14 or greater, then the head-bend is assigned as a propagated-bend. If the animal reverses or if missing data are encountered, the head-bend is terminated as well; in this case, if the final propagation angle is #14 or greater, the head-bend is assigned as a propagated-bend, but if it is less than angle #14, it is ambiguous as to whether the head-bend would have propagated further and is therefore not classified. Head-bends that are not connected to bends in any other angle are also not classified as they are likely due to noise or artifacts in angle

measurement. To account for such measurement noise, which may be amplified by peak detection, each head-bend is allowed to propagate backward in time by 0.1s, and up to 1s only once per propagation (for example, see **Fig. S1A**, lower, t = 19s, angle #24). Additionally, two segments per propagation may be skipped if a peak of the correct sign is not detected before the termination condition (for example, see **Fig. S1A**, lower, t = 12s, angles #22-23). These heuristics enabled the most robust detection of head-bend propagation upon inspection.

Note that for the 2nd head-cast of each pair, there is some ambiguity with regard to whether posterior bends, which are of the same sign, should in fact be assigned to the previous propagated-bend as opposed to that head-cast (in which case that head-cast would instead be assigned as a propagated-bend). Our algorithm assigns these ambiguous posterior bends to the earliest possible head-bend; for example, see **Fig. S1A**, lower, first head-cast pair. Results from SMD and DB02 neuronal activity imaging during behavior suggest that this procedure meaningfully assigns different head-bend types, because neuronal activity during the earlier head-bend is indistinguishable from other propagated-bends, whereas neuronal activity during the later head-bend is markedly different (**Fig. 5C and 6E**).

Reversal periods were analyzed the same way, only with kymograms flipped left/right such that bends are quantified as if they propagated head-to-tail, as during forward locomotion, rather than tail-to-head. This allows the classification of bends propagating fully from tail to head as well as bends that start in the neck and propagate toward the head, which for **Fig. S1G** were considered head-casts. Also considered head-casts during reversals for **Fig. S1G** were bends that propagate as head-casts normally do, which were found by analyzing reversal periods without flipping left/right.

Because head-casts typically occurred in only half-cycles (i.e. two head-casts, one ventral and one dorsal, without a return to the side of the first head-cast), head-cast cycle period in **Fig. 1D** was calculated by doubling head-cast inter-bend intervals (only measured between two consecutive head-casts). For **Fig. 1D** propagated-bend cycle periods were calculated regardless of intervening head-cast interruption; note that a reduction in head-casts caused only a small change in propagated-bend inter-bend intervals (**Fig. S3D**). Note that head-casts were typically posterior to and slower than the 4-5Hz nose-tip movements previously described as "foraging," (Huang et al., 2008) and were more in line with head movements described in refs. (McCloskey et al., 2017; Skora et al., 2018).

For **Fig. 7**, propagated-bend cycle periods were calculated by doubling propagated-bend inter-bend intervals. For **Fig. 7G-H**, data are taken from 10min post-lights-on.

Phase quantifications

Phases in **Fig. 1F** and **Fig. 6G-H** were quantified by linearly interpolating between detected peaks for each half cycle (a similar procedure was used by (Eliav et al., 2018)). Interpolation enabled a phase calculation that was independent of intervening head-casts or non-alternating SMD oscillations. In **Fig. 1F**, 0 to π was interpolated from dorsal to ventral propagated-bend maxima (peaks in head-bend angle #2) and π to 2π was interpolated from ventral to dorsal propagated-bend maxima, regardless of any intervening head-casts. Ventral and dorsal head-casts were defined as head-casts following ventral or dorsal propagated-bends, respectively; each head-cast type was therefore restricted to a half cycle. Only the first head-cast following a propagated-bend was used to generate the histograms in **Fig. 1F**. In **Fig. 6G-H**, 0 to π was

interpolated from the first SMDD peak following an SMDV peak (i.e. SMDD alternating peak) to the first SMDV peak following an SMDD peak, regardless of any intervening SMDD peaks. Similarly, π to 2π was interpolated from the first SMDV peak following an SMDD peak to the first SMDD peak following an SMDV peak, regardless of any intervening SMDV peaks. Because of this definition, SMDD-only and SMDV-only oscillations were each restricted to half cycles. To best compare to **Fig. 1F**, we used the first trough (i.e. minimum, see **Fig. 3E**, t=~0s) of each SMDD-only or SMDV-only oscillation to generate the histograms, as these corresponded to the first head-cast following a propagated-bend.

Phases in **Fig. 5D-G** were calculated using the Hilbert transform of head-bend angle #4, smoothed, to remove head-cast signals. The Hilbert transform was applied individually to each period of forward or reverse locomotion, and border data were removed as these were often partial cycles. To quantify the proportion of cycles that contained neural activity peaks, individual cycles were segmented from 0 to 2π (SMDV) or from π to π (SMDD and DB02) so that the typical peak timing for each neuron was centered and was therefore unlikely to fall into a neighboring cycle due to noise. Only cycles without missing data in both angle and neural activity were considered.

QUANTIFICATION AND STATISTICAL ANALYSIS

Quantifications were performed using custom MATLAB (Mathworks) scripts. Standard statistical tests were performed using Graphpad Prism 7. These tests, along with the value of n and what n represents, are reported in the figure legends. Additional tests are described in detail in the following sections.

Reconstruction quality for neuronal subsets (pan-neuronal imaging)

To assess how well interneuron and motor neuron activity was captured in the top PC dimensions, we calculated for each neuron the Pearson's linear correlation coefficient between the original data (activity traces and their derivatives) and reconstructed traces after PCA. These reconstructed traces were obtained by matrix multiplication of the PC coefficients with the PC loadings of the top (i =1 to 5) PCs and addition of the mean of the original data, as follows:

$$Data_{recon} = [PC_{Coeff}{}^{1}{:}PC_{Coeff}{}^{i}] \times [PC_{Load}{}^{1}{:}PC_{Load}{}^{i}] + mean(OrigData).$$

We used the average correlation coefficient for all the traces of a neuronal cell type (inter neurons, motor neurons or other neurons) in a recording as a measure of how similar reconstructed traces are to their original counterparts. This measure, in contrast to mean-square-error, is insensitive to the magnitude of neuronal activity traces.

Peak frequency quantification (pan-neuronal imaging)

For neurons that peaked multiple times in at least one forward command period longer than 50s, we tested whether the inter-peak interval distribution between such peaks, across all such forward command periods, was significantly different from random, as follows. For each forward command period, we randomly selected the same number of spike times to accumulate a random inter-peak interval distribution. This procedure was repeated 10^6 times to obtain an average random distribution. To measure the magnitude of deviation from random, we summed the absolute difference, bin-by-bin, between the average random distribution and the actual inter-peak interval distribution. This measure was also determined for each of the 10^6

resampled distributions, and the p-value reported in Table S2 is the fraction of resampled distributions with at least as large of a deviation from random as the actual distribution. To correct for multiple comparisons, statistical significance was determined by the Benjamini-Hochberg-Yekutieli procedure (Benjamini et al.).

Cross-correlation analysis (pan-neuronal imaging)

Statistical significance was evaluated by comparing the actual and resampled covariograms to determine the probability of finding correlations as large as the maximum and minimum ones observed in the actual covariogram. This allowed us to use the same procedure regardless of whether peaks were correlated or anti-correlated. The absolute amplitudes of the highest and lowest correlation bins (regardless of timing offset) found in each resampled covariogram were summed, for each of the 10^6 resampled covariograms. The p-value reported in Tables S3, S4 is the fraction of summed amplitudes that are at least as large as the summed amplitudes obtained from the actual distribution. To correct for multiple comparisons across all neuron pairs, statistical significance was determined by the Benjamini-Hochberg-Yekutieli procedure (Benjamini et al.).

Polar histogram statistics

We tested the significance of the distributions in **Fig. 1F**, **Fig. 5D-G, and Fig. 6G-H** using resampling. We determined the probability of obtaining a distribution as skewed as the real one by chance. For each half-cycle (**Fig. 1F, Fig. 6G-H**) or full cycle (**Fig. 5D-G**) from which the real data had been extracted, we randomly selected one phase, to generate a random distribution of phases of the same number as the real distribution. Because peaks were detected using a parameter delta for **Fig. 1F**

and **Fig. 6G-H**, we restricted the time points that could be selected to those where peaks could possibly have been found (i.e. those at least delta away from the previous peak). We binned the data in the same manner as the real data and quantified the absolute difference, bin-by-bin, between the resampled distribution and the all-phases distribution, which was calculated using the same phases from which the random data was selected. These bin-by-bin absolute differences were summed to give a total difference between the resampled data and the all-phases distribution as a measure of sample distribution skewness. This procedure was repeated 10^6 times and the skewness of the real distribution was measured the same way. The p-value is the fraction of randomly sampled distributions that were at least as skewed as the actual distribution.

Significance between forward (**Fig. 5F**) and reverse (**Fig. 5G**) SMD peak distributions were determined by resampling independently for each SMD. The reverse distribution contained fewer peaks than the forward distribution, so we randomly selected, from the forward distribution, 10^6 samples of the same size as the reverse distribution. We binned the data in the same manner as the real data and quantified, bin-by-bin, the absolute difference between the resampled and real forward distribution. These bin-by-bin absolute differences were summed to give a total difference. The same procedure was done to measure the difference between the forward and reversal distributions, and the p-value is the fraction of randomly sampled forward distributions that differed from the actual forward distribution at least as much as the reversal distribution did.

DATA AND SOFTWARE AVAILABILITY

Data and custom code are available for distribution from the corresponding author upon request.

Supplemental Movie legends

Movie S1. Whole-nervous-system Ca^{2+} imaging, related to Figure 2. Maximum intensity projection of an example 30-minute whole-nervous-system Ca^{2+} imaging recording, 60x real-time. Worm orientation and curvature as in **Fig. S2A**: upper right neurons are in head ganglia, lower right are tail ganglia, and others are VNC.

Movie S2. SMD imaging in a freely moving animal, related to Figure 5. An example recording of neuronal activity and behaviour, same as **Fig. 5C**. Left: same animal with neural activity imaged at 63x (upper) and behaviour at 4x (lower, segments for angle measurements marked). Right: neuronal activity (upper) and posture kymogram (lower).

Movie S3. O_2-induced switch in head-bend type, related to Figure 7. Worm images and associated kymogram showing an example O_2-downshift response, same as **Fig. 7I**. Note the decrease in propagated-bend frequency and increase in head-cast frequency.

Movie S4. Dwelling/roaming switch in head-bend type, related to Figure 7.

Worm images and associated kymogram showing example dwelling and roaming periods, same as **Fig. 7L**. Note the increase in propagated-bend frequency and decrease in head-cast frequency as the animal switches from dwelling to roaming.

Key Resource Table

KEY RESOURCES TABLE

REAGENT or RESOURCE	SOURCE	IDENTIFIER
Experimental Models: Organisms/Strains		
C. elegans: Strain ZIM958: *lite-1 (ce314)*	This study	N/A
C. elegans: Strain ZIM1466: *lite-1 (ce314); mzmEx877[Pnlr-1(-150;-1)::HisCl::SL2::mCherry]; mzmIs52[Punc-31::NLSGCaMP6f]*	This study	N/A
C. elegans: Strain ZIM1564: *lite-1 (ce314); mzmEx929[Punc-7s::CreVDH; Pmyo-3::mCherry]*	This study	N/A
C. elegans: Strain ZIM1725: *lite-1 (ce314); mzmEx1018[Punc-7s::CreVDH; Pmyo-3::mCherry]*	This study	N/A
C. elegans: Strain ZIM1418: *lite-1 (ce314); mzmEx858--[Pflp-22::DIO-HisCl::SL2::mCherry; Pelt-2::NLSdsRedNLS]*	This study	N/A
C. elegans: Strain ZIM1473: *lite-1 (ce314); mzmIs28[Punc-17beta::HisCl::SL2::mCherry]*	This study	N/A
C. elegans: Strain ZIM1628: *lite-1 (ce314); mzmEx877[Pnlr-1(-150;-1)::HisCl::SL2::mCherry]; mzmEx929 [Punc-7s::CreVDH; Pmyo-3::mCherry]; mzmIs52 [Punc-31::NLSGCaMP6f]*	This study	N/A
C. elegans: Strain ZIM1748: *lite-1 (ce314); mzmEx877[Pnlr-1(-150;-1)::HisCl::SL2::mCherry]; mzmEx1018 [Punc-7s::CreVDH; Pmyo-3::mCherry]; mzmIs52 [Punc-31::NLSGCaMP6f]*	This study	N/A
C. elegans: Strain ZIM1562: *lite-1 (ce314); mzmEx877[Pnlr-1(-150;-1)::HisCl::SL2::mCherry]; mzmEx858 [Pflp-22::DIO-HisCl::SL2::mCherry; Pelt-2::NLSdsRedNLS]; mzmIs52 [Punc-31::NLSGCaMP6f]*	This study	N/A
C. elegans: Strain ZIM1574: *lite-1 (ce314); mzmEx877[Pnlr-1(-150;-1)::HisCl::SL2::mCherry]; mzmIs28 [Punc-17beta::HisCl::SL2::mCherry]; mzmIs52 [Punc-31::NLSGCaMP6f]*	This study	N/A
C. elegans: Strain ZIM1658: *lite-1 (ce314); mzmEx981[Punc-17beta::NLSGCaMP6f]*	This study	N/A
C. elegans: Strain ZIM1467: *lite-1 (ce314); mzmEx882[Punc-7S::CreVDH; Pflp-22::DIO-mCherry; Pflp-22::DIO-GCaMP6Fopt]*	This study	N/A
C. elegans: Strain ZIM1749: *lite-1 (ce314); mzmEx1041[Psto-3::HisCl::mCherry; Punc-122::GFP]*	This study	N/A
C. elegans: Strain ZIM1563: *lite-1 (ce314); mzmEx928[Psto-3::Chrimson::mCherry; Punc-122::GFP]*	This study	N/A

Figure 1

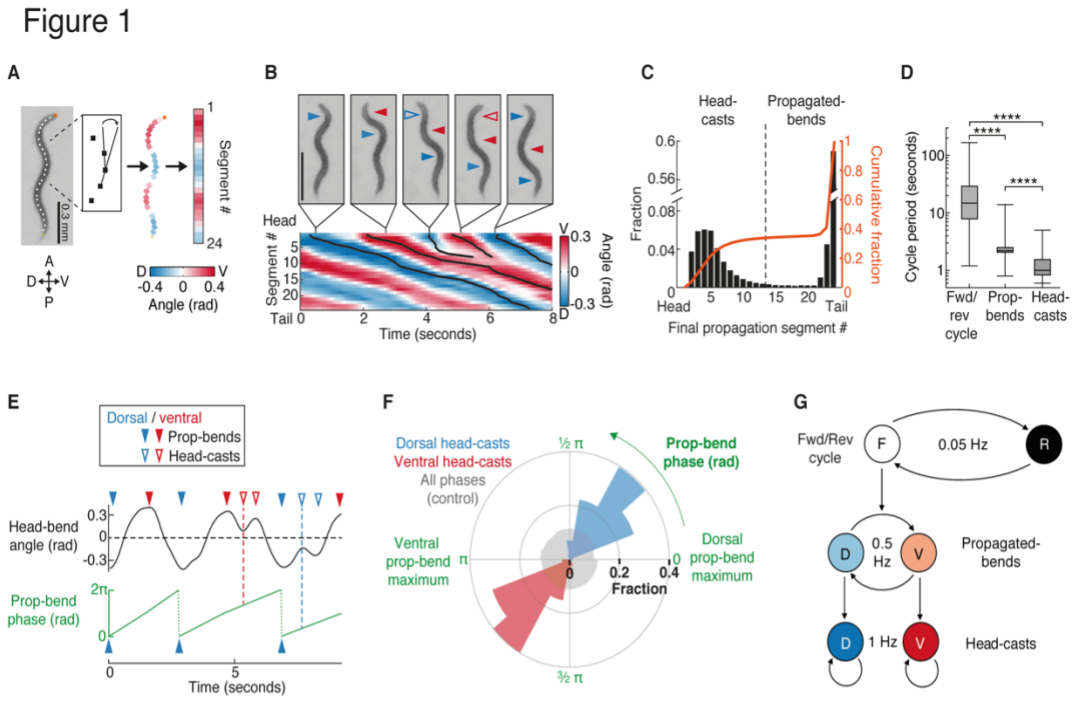
Figure 1
A
B
C
D
Segment #
Angle (rad)
Time (seconds)
Head-casts
Propagated-bends
Fraction
Cumulative fraction
Final propagation segment #
Cycle period (seconds)
Fwd/ rev cycle
Prop-bends
Head-casts
E
Dorsal / ventral
Prop-bends
Head-casts
Head-bend angle (rad)
Prop-bend phase (rad)
Time (seconds)
F
Dorsal head-casts
Ventral head-casts
All phases (control)
Prop-bend phase (rad)
Ventral prop-bend maximum
Dorsal prop-bend maximum
Fraction
G
Fwd/Rev cycle
0.05 Hz
0.5 Hz
1 Hz
Propagated-bends
Head-casts

Figure 2

Figure 2

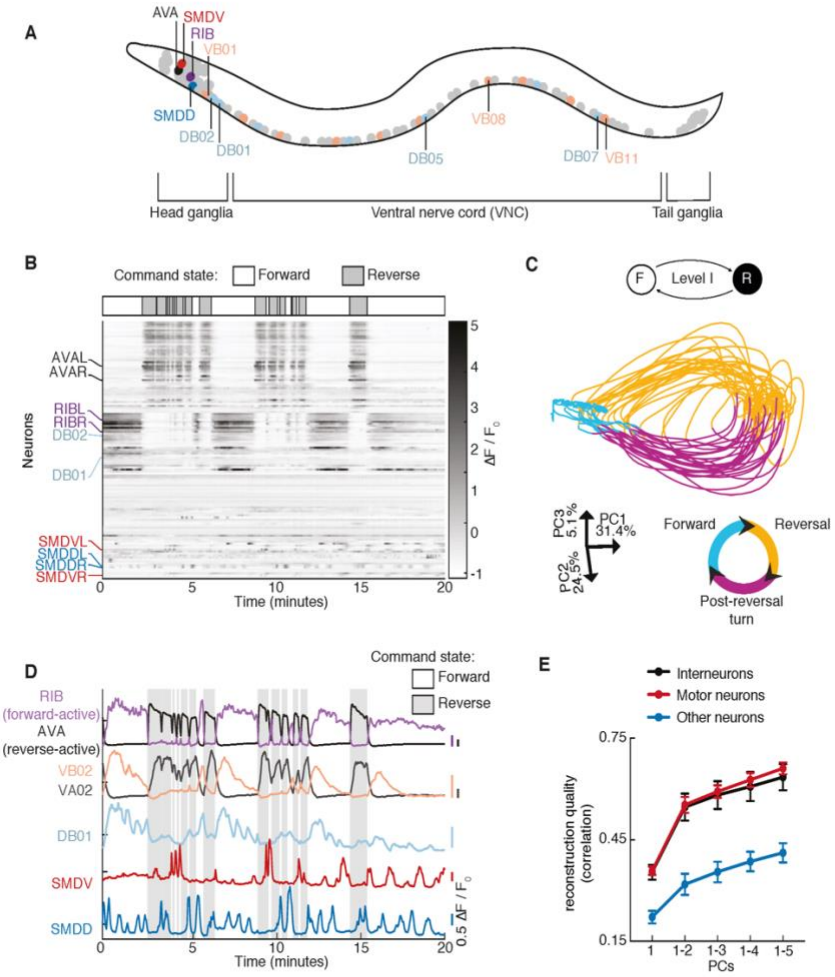

Figure 3

Figure 3

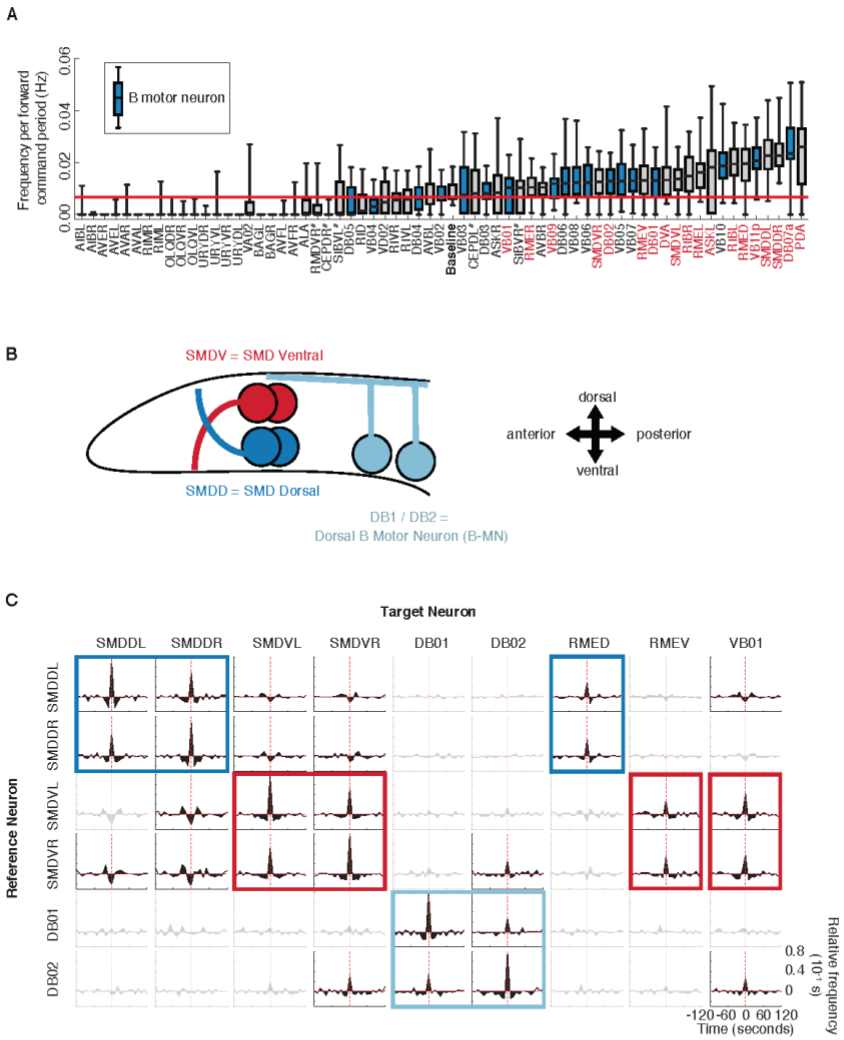

Figure 4

Figure 4

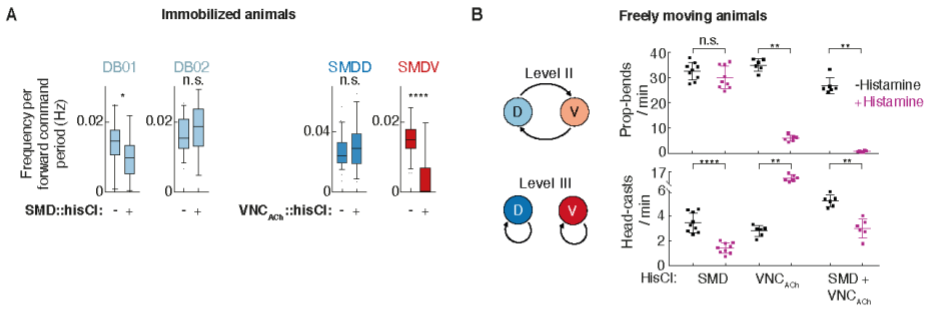

Figure 5

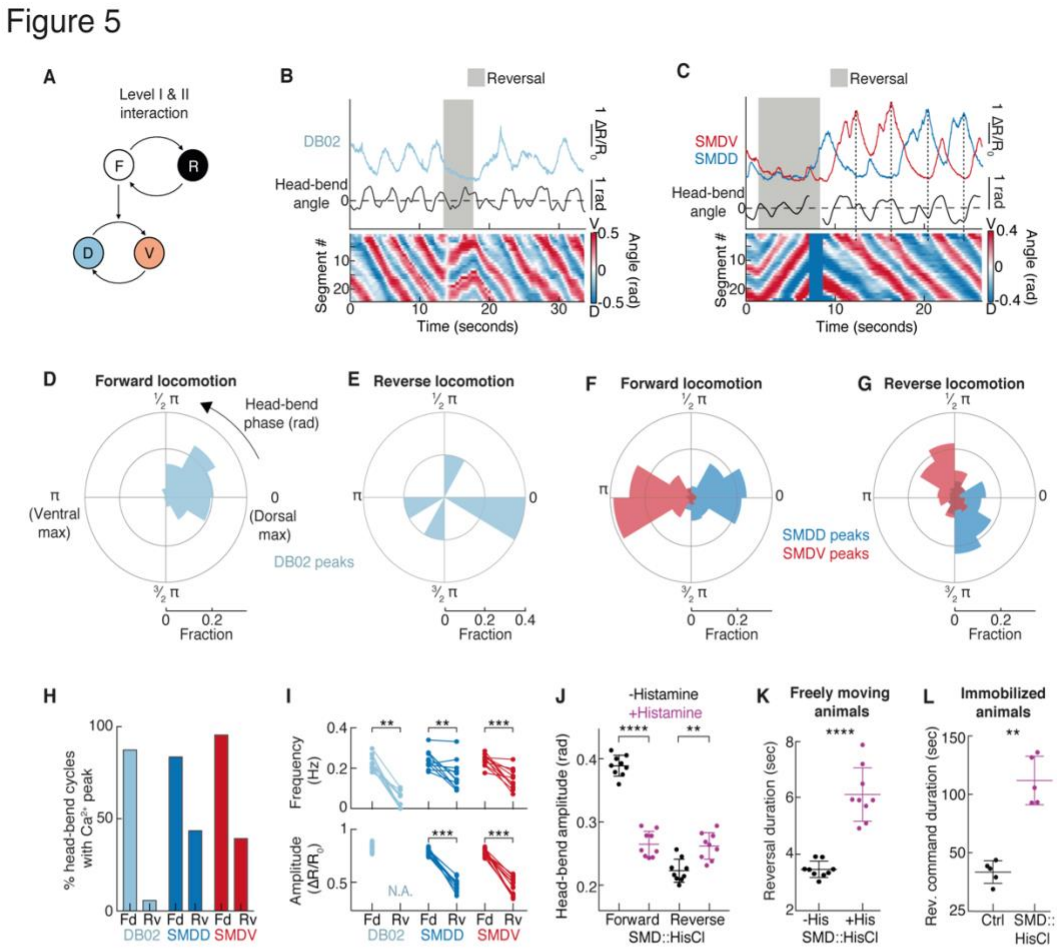
Figure 5
A
Level I & II interaction
F
R
D
V
B
Reversal
DB02
Head-bend angle
1 ΔR/R0
1 rad
Segment #
Time (seconds)
Angle (rad)
C
Reversal
SMDV
SMDD
Head-bend angle
Segment #
Time (seconds)
Angle (rad)
D
Forward locomotion
Head-bend phase (rad)
π (Ventral max)
0 (Dorsal max)
DB02 peaks
Fraction
E
Reverse locomotion
Fraction
F
Forward locomotion
SMDD peaks
SMDV peaks
Fraction
G
Reverse locomotion
Fraction
H
% head-bend cycles with Ca2+ peak
Fd Rv Fd Rv Fd Rv
DB02 SMDD SMDV
I
Frequency (Hz)
Amplitude (ΔR/R0)
N.A.
Fd Rv Fd Rv Fd Rv
DB02 SMDD SMDV
J
-Histamine
+Histamine
Head-bend amplitude (rad)
Forward Reverse
SMD::HisCl
K
Freely moving animals
Reversal duration (sec)
-His +His
SMD::HisCl
L
Immobilized animals
Rev. command duration (sec)
Ctrl SMD:: HisCl

Figure 6

Figure 6

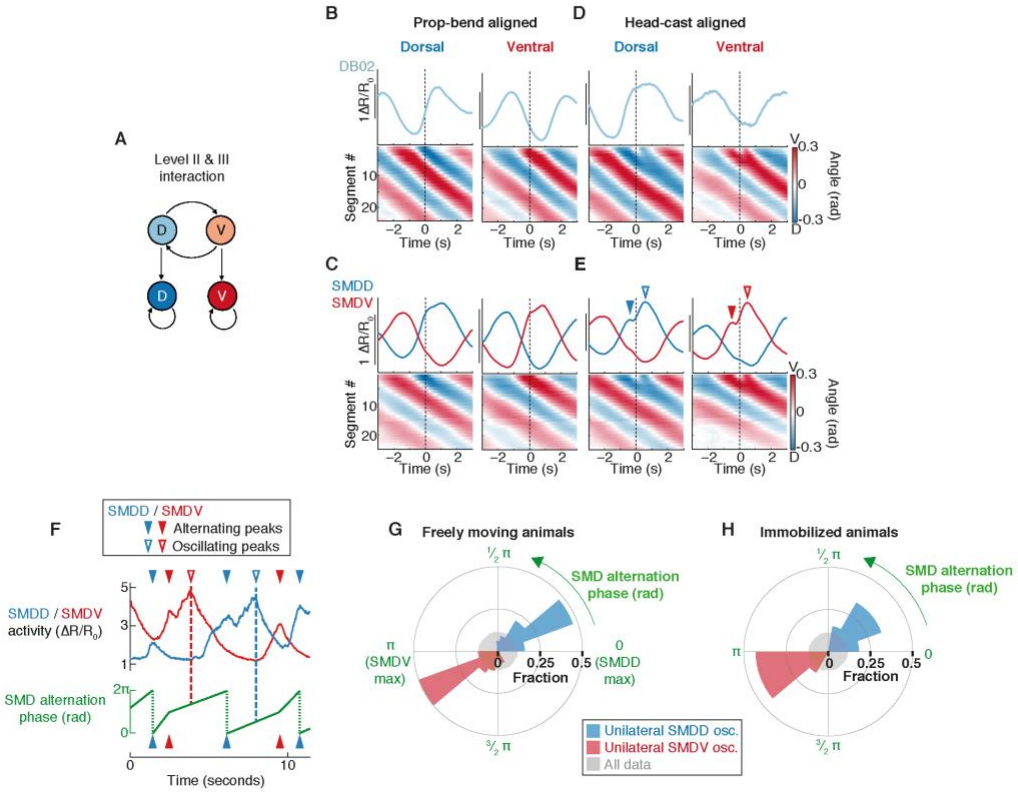

Figure 7

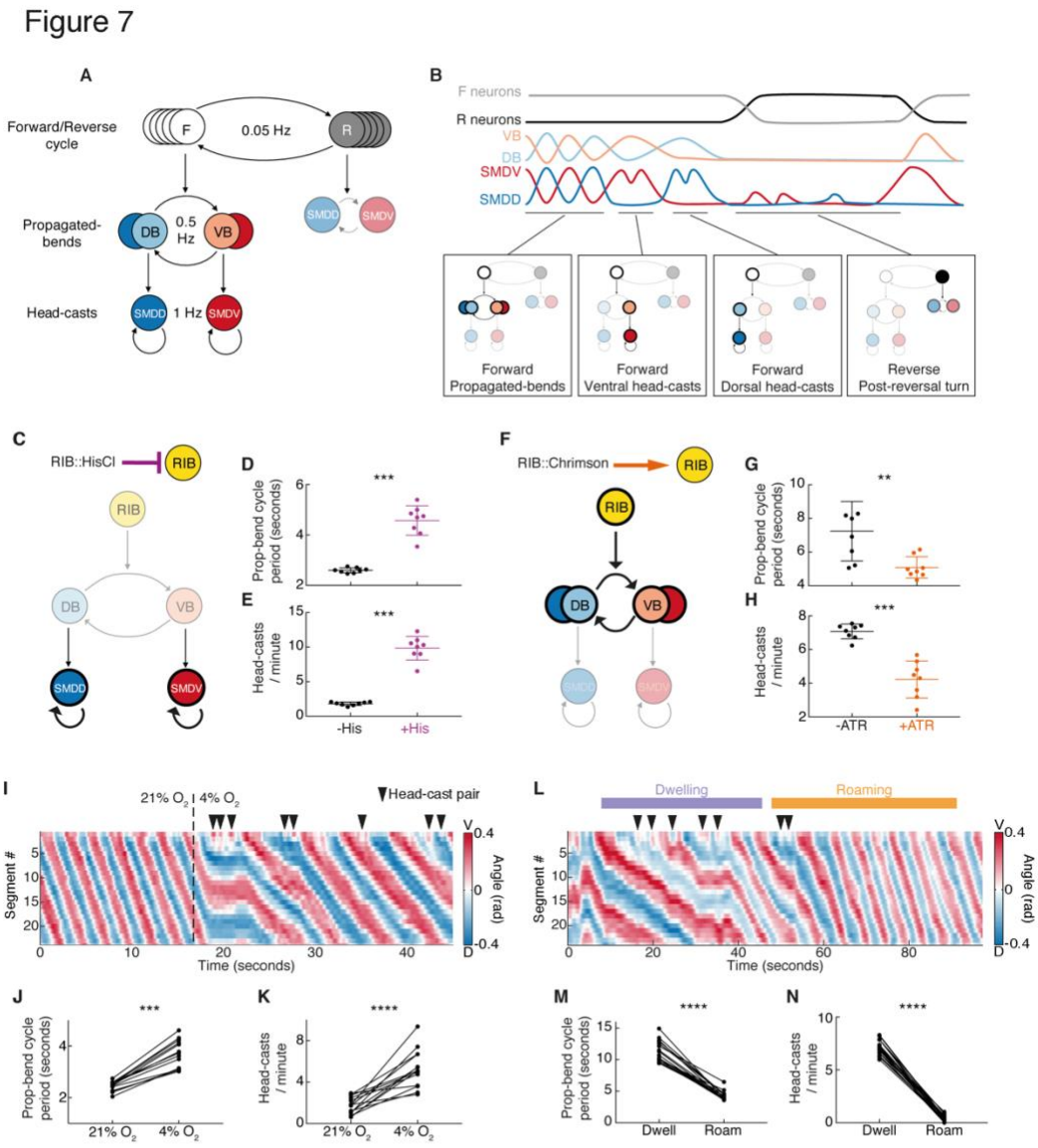
Figure 7
A
Forward/Reverse cycle
F
0.05 Hz
R
Propagated-bends
DB
0.5 Hz
VB
SMDD
SMDV
Head-casts
1 Hz
B
F neurons
R neurons
VB
DB
SMDV
SMDD
Forward Propagated-bends
Forward Ventral head-casts
Forward Dorsal head-casts
Reverse Post-reversal turn
C
RIB::HisCl
RIB
D
Prop-bend cycle period (seconds)
E
Head-casts / minute
-His
+His
F
RIB::Chrimson
G
H
-ATR
+ATR
I
21% O2
4% O2
Head-cast pair
Segment #
Time (seconds)
Angle (rad)
L
Dwelling
Roaming
J
21% O2
4% O2
K
M
Dwell
Roam
N

Supplemental Text and Figures

Figure S1

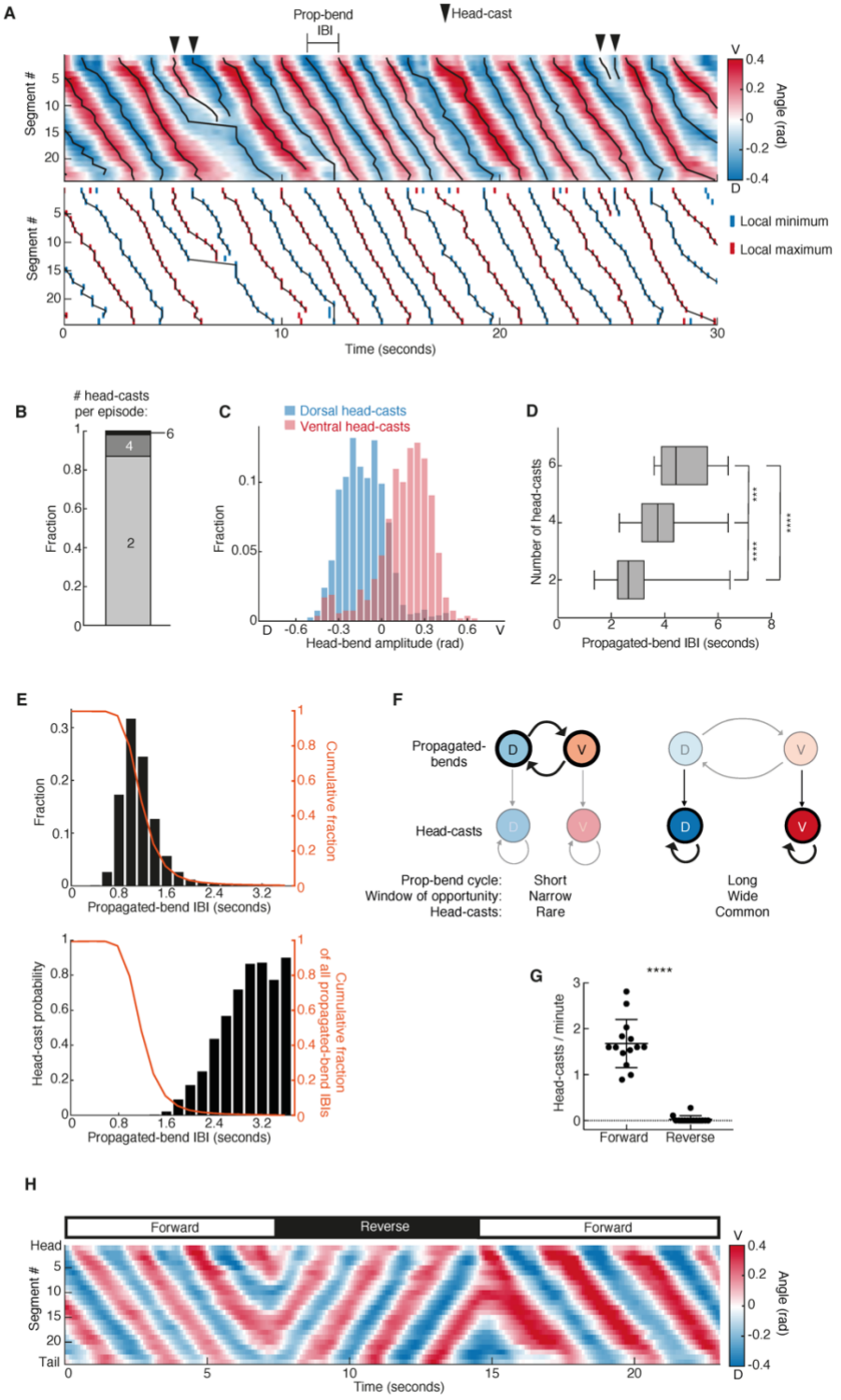

Figure S2

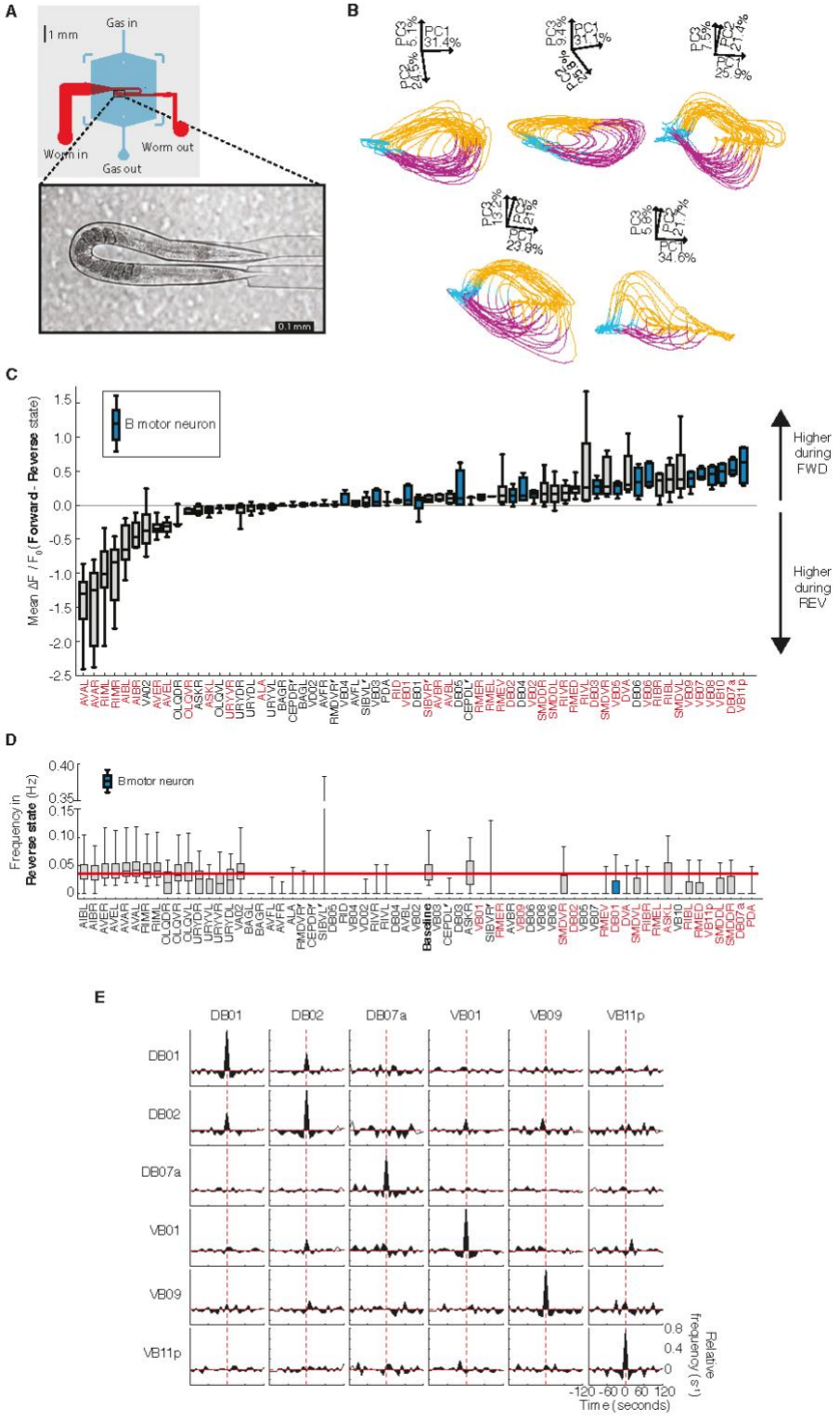
A
1 mm
Gas in
Worm out
Worm in
Gas out
0.1 mm
B
C
B motor neuron
Higher during FWD
Higher during REV
Mean ΔF / F0 (Forward - Reverse state)
D
B motor neuron
Frequency in Reverse state (Hz)
Baseline
E
DB01
DB02
DB07a
VB01
VB09
VB11p
Relative frequency (s-1)
Time (seconds)

Figure S3

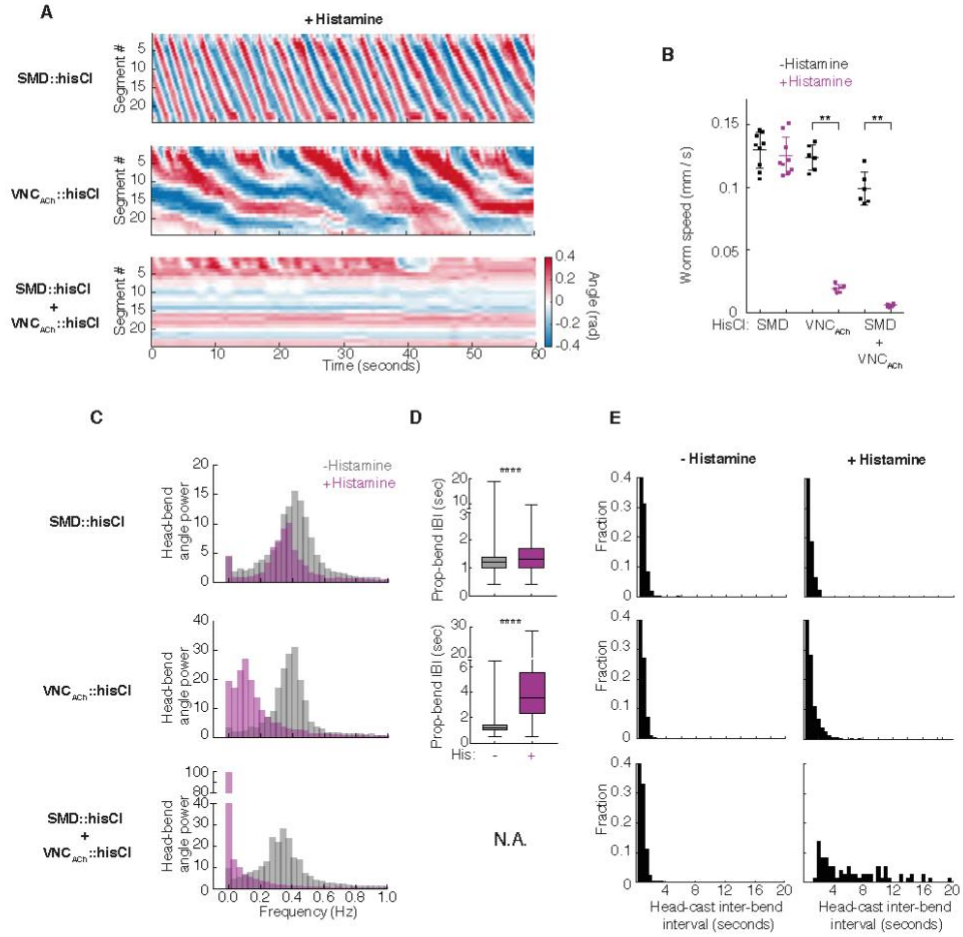
A
+Histamine
SMD::hisCl
VNCACh::hisCl
SMD::hisCl + VNCACh::hisCl
Segment #
Time (seconds)
Angle (rad)
B
-Histamine
+Histamine
Worm speed (mm / s)
HisCl: SMD VNCACh SMD + VNCACh
C
-Histamine
+Histamine
Head-bend angle power
Frequency (Hz)
D
Prop-bend IBI (sec)
His: - +
N.A.
E
- Histamine
+ Histamine
Fraction
Head-cast inter-bend interval (seconds)

Figure S4

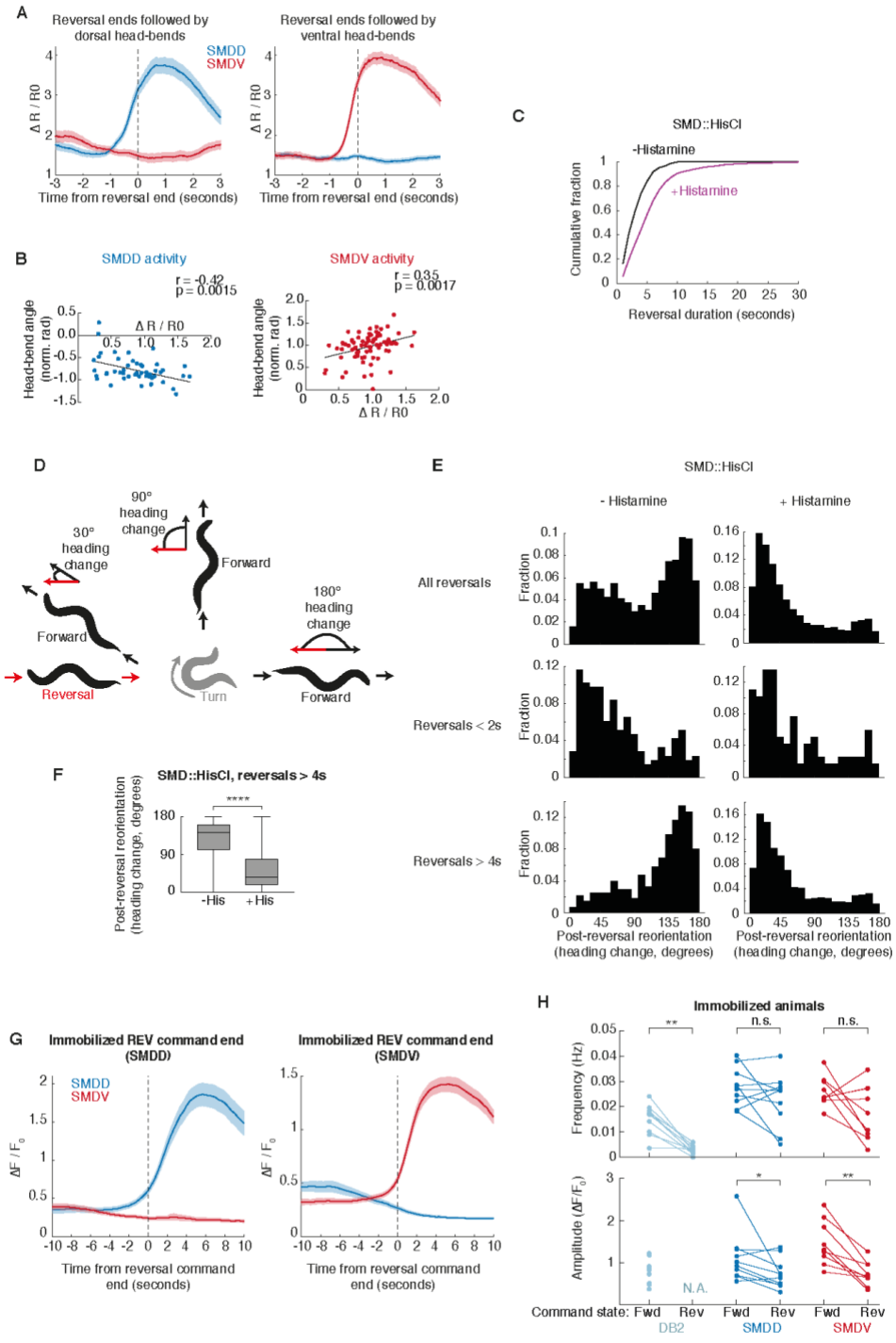
A
Reversal ends followed by dorsal head-bends
Reversal ends followed by ventral head-bends
SMDD
SMDV
Δ R / R0
Time from reversal end (seconds)
B
SMDD activity
SMDV activity
r = -0.42
p = 0.0015
r = 0.35
p = 0.0017
Head-bend angle (norm. rad)
Δ R / R0
C
SMD::HisCl
-Histamine
+Histamine
Cumulative fraction
Reversal duration (seconds)
D
90° heading change
30° heading change
Forward
Reversal
Turn
180° heading change
E
SMD::HisCl
- Histamine
+ Histamine
All reversals
Reversals < 2s
Reversals > 4s
Fraction
Post-reversal reorientation (heading change, degrees)
F
SMD::HisCl, reversals > 4s
****
Post-reversal reorientation (heading change, degrees)
-His
+His
G
Immobilized REV command end (SMDD)
Immobilized REV command end (SMDV)
SMDD
SMDV
ΔF / F0
Time from reversal command end (seconds)
H
Immobilized animals
**
n.s.
n.s.
Frequency (Hz)
*
**
Amplitude (ΔF/F0)
N.A.
Command state: Fwd Rev Fwd Rev Fwd Rev
DB2
SMDD
SMDV

Figure S5

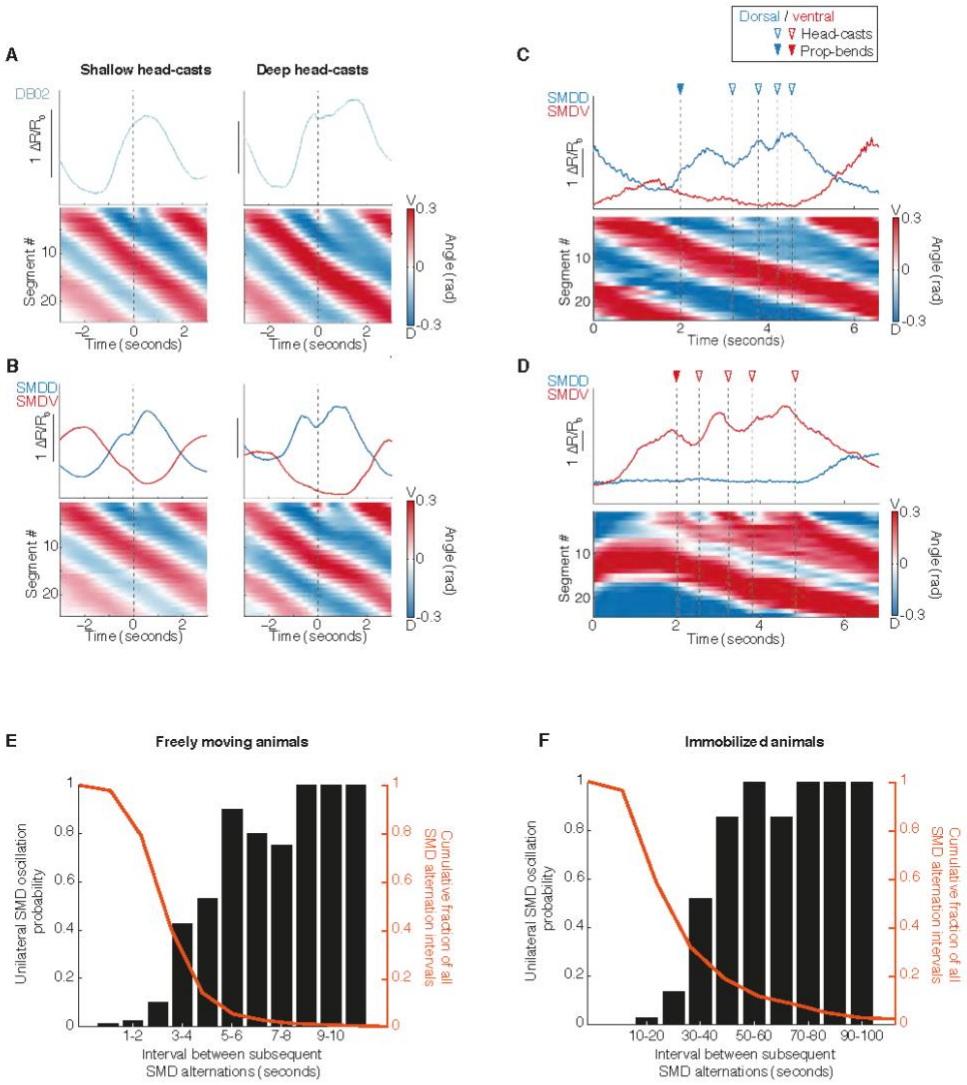
A
Shallow head-casts
Deep head-casts
DB02
1 ΔR/R0
Segment #
Time (seconds)
Angle (rad)
B
SMDD
SMDV
C
Dorsal / ventral
Head-casts
Prop-bends
D

E
Freely moving animals
Unilateral SMD oscillation probability
Cumulative fraction of all SMD alternation intervals
1-2
3-4
5-6
7-8
9-10
Interval between subsequent SMD alternations (seconds)
F
Immobilized animals
10-20
30-40
50-60
70-80
90-100

Figure S6

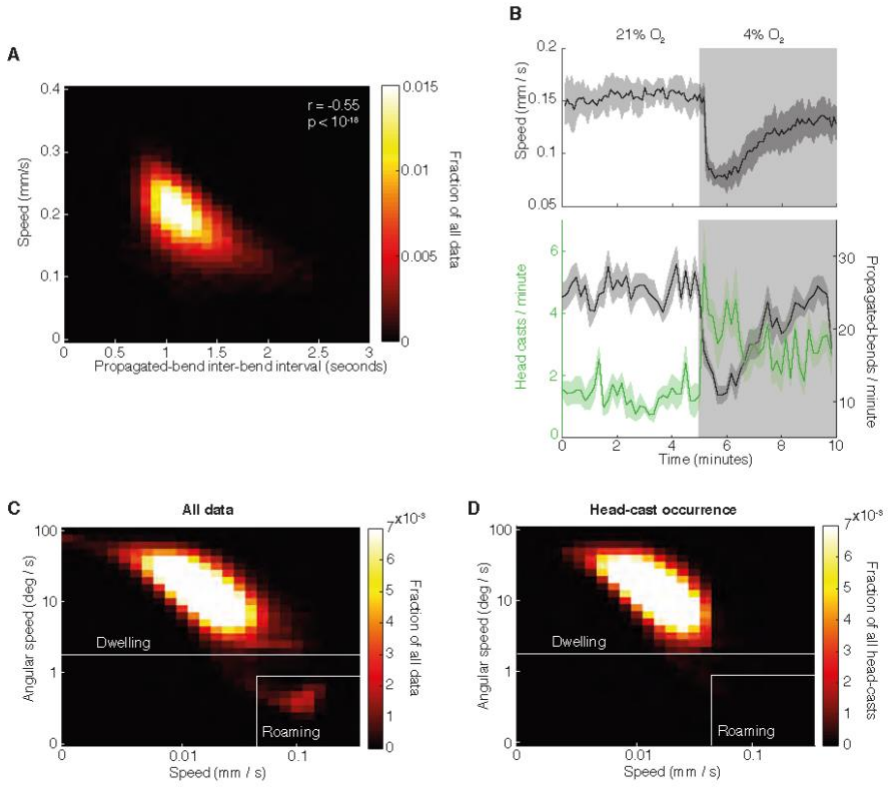
A
r = -0.55
p < 10⁻¹⁶
Speed (mm/s)
Propagated-bend inter-bend interval (seconds)
Fraction of all data
B
21% O2
4% O2
Speed (mm / s)
Head casts / minute
Propagated-bends / minute
Time (minutes)
C
All data
Angular speed (deg / s)
Dwelling
Roaming
Speed (mm / s)
Fraction of all data
D
Head-cast occurrence
Angular speed (deg / s)
Dwelling
Roaming
Speed (mm / s)
Fraction of all head-casts

Supplemental Figure Legends

Figure S1. Kinematic relationships between different timescale behaviors, related to Figure 1. (A) Upper: example kymogram showing a period of forward movement. Head-bend propagation traces shown by black lines. Arrowheads mark head-casts. Lower: peak kymogram showing detected maxima and minima used for propagation tracing (Methods). **(B)** Number of head-casts per head-cast episode. A head-cast episode is defined as a series of consecutive head-casts uninterrupted by propagated-bends or reversals (i.e. within one propagated-bend inter-bend interval (IBI), illustrated in **(A)**). n = 604 head-casts pooled from 21 animals. **(C)** Fractional histograms of maximal head-bend amplitude (angle #2) for dorsal or ventral head-casts, defined according to whether they followed dorsal or ventral propagated-bends, respectively. n = 427 dorsal and 194 ventral head-casts pooled from 21 animals. Note that head-casts can cross to the contralateral side of the previous propagated bend, but are largely restricted to the ipsilateral side. **(D)** Median, interquartile and range of propagated-bend inter-bend intervals (IBI, illustrated in **(A)**) for propagated-bend pairs with either 2, 4 or 6 intervening head casts. n = 525 (2 head-casts), 67 (4 head-casts) and 12 (6 head-casts) episodes pooled from 14 experimental repeats with ~20 animals each. ***p<0.001, ****p<0.0001, Mann-Whitney Test. **(E)** Upper: fractional and cumulative distribution of propagated-bend IBIs (illustrated in **(A)**). Lower: Probability of at least one head-cast occurrence between a pair of propagated-bends, binned according to the propagated-bend pair's IBI. Cumulative fraction of all propagated-bend IBIs (same as upper panel) overlaid in orange: note that head-casts are most probable during

the longest propagated-bend cycles. n=25815 propagated-bend pairs and 420 head-casts pooled from 14 assays, ~20 animals per assay. **(F)** Diagram illustrating how the propagated-bend cycle could act as a window of opportunity for head-casting, which may be widened or narrowed by decreasing or increasing cycle speed. **(G)** Head-cast frequency (regardless of propagation direction) in forward vs. reverse locomotion. Each data point is the mean of an experimental replicate, n = 14 with ~20 animals per replicate. ****p<0.0001, Mann-Whitney Test. **(H)** Example kymogram showing an animal switching between forward and reverse locomotion states. Note that during reverse locomotion, body undulations are initiated in the tail and propagate to the head, in contrast to forward locomotion "propagated-bends" which are propagated posteriorly.

Figure S2. Nervous-system-wide Ca^{2+} imaging reveals motor neuron activity nested within forward/reverse command switches, related to Figures 2 and 3. **(A)** Technical drawing of microfluidic device used for whole-brain and whole-nervous-system Ca^{2+} imaging experiments. Black box shows a zoom-in of an example worm immobilized in the imaging curve. **(B)** PC-phase plots for each of five nervous-system-wide recordings, as in **Fig. 2C**. Traces colored by instantaneous motor command state inferred from neuronal activity (Methods); color key in **Fig. 2C**, lower panel (arrowheads indicate directional flow). Coordinates depict PC axes orientations and % variance explained. Compare to Ref. 8 showing head ganglia PC-phase plots. **(C)** Difference in mean Ca^{2+} activity levels ($\Delta F / F0$) of all identified neurons during forward vs. reverse commands, pooled from n = 5 whole-nervous-system and n= 5 whole-brain recordings. Boxes: median and interquartile; whiskers: range. Blue boxes correspond to B motor neurons. Neurons labeled in red are those

with significantly different mean activity levels in forward vs. reverse commands (paired t-test); see **Table S2** for p-values and n numbers. #ambiguous IDs, see Methods for alternatives. **(D)** Frequencies of activity peaks of all identified neurons per reverse command period pooled from n=5 whole-nervous-system and n=5 whole-brain recordings. Boxplots show median and interquartile; whiskers show 5%-95% range. "Baseline" is the distribution for one peak per reversal command period; its median is indicated by the red line. Neurons ordered according to median frequency in forward state, see **Fig. 3A**. Note that more neurons appear active in the forward state because we only include neuron classes which we reliably identified; we focused on identifying forward-active B-MNs and not reverse-active A-MNs, although we observed strong signals in the latter (data not shown). **(E)** Covariograms of oscillatory motor neurons. Panels show the relative frequencies of Ca^{2+}-peaks of neurons in columns triggered to Ca^{2+}-peaks of neurons in rows. Data are shuffle-corrected so that positive/negative values show higher/lower correlation than chance (Methods). See **Table S4** for p-values.

Figure S3. Behavioral effects of neuronal inhibition, related to Figure 4. (A) Example kymograms from SMD::hisCl (upper), VNC_{ACh}::hisCl (middle) and SMD::hisCl + VNC_{ACh}::hisCl (lower) animals. Note that any coordination among body segments is lost in SMD::hisCl + VNC_{ACh}::hisCl animals. **(B)** Effects of indicated hisCl transgenes on locomotion speed. Bars show mean ± SD. Each data point is the mean of an experimental repeat with ~20 animals each. **p<0.01, Mann-Whitney Test. **(C-E)** Power spectra histograms of head-bend angle (angle #2) **(C)**, propagated-bend inter-bend interval (IBI; **D**), and fractional histograms of head-cast IBI **(E)** in SMD::hisCl (upper), VNC_{ACh}::hisCl (middle), and SMD::hisCl +

VNC_{ACh}::hisCl (lower) animals with or without histamine. Note that SMD inhibition slightly but significantly increased, rather than decreased, propagated-bend inter-bend interval, indicating that the head-cast reduction in SMD::hisCl did not result in faster propagated-bend cycles (i.e. head-cast occurrences do not stall the propagated-bend cycle, a possibility suggested by data in **Fig. S1E**). SMD::hisCl: n = 11952 (**D**, -his), 11230 (**D**, +his), 1481 (**E**, -his), 211 (**E**, +his). VNC_{ACh}::hisCl: n = 10511 (**D**, -his), 1062 (**D**, +his), 274 (**E**, -his), 1159 (**E**, +his). SMD::hisCl + VNC_{ACh}::hisCl: n = 492 (**E**, -his) and 73 (**E**, +his). Data are averaged **(B)** or pooled **(C-E)** across n = 6 (VNC_{ACh}::hisCl and SMD::hisCl + VNC_{ACh}::hisCl) or n = 9 (SMD::hisCl) experimental repeats with ~20 animals each. ****p<0.0001, Mann-Whitney test.

Figure S4. Interactions between global forward/reverse cycle and SMD/DB oscillators, related to Figure 5. (A) Trigger-averaged GCaMP/mCherry traces ± SEM from SMD recordings in freely moving animals aligned to reverse-to-turn transitions, separated by post-reversal dorsal (left) or ventral (right) head-bend. n = 55 dorsal and 96 ventral events, pooled from 11 animals. **(B)** Peak head-bend angle (angle #2, normalized to 95^{th} percentile within each recording) and GCaMP/mCherry signal amplitude for SMDD and post-reversal dorsal head-bends (left) or SMDV and post-reversal ventral head-bends (right). Pearson correlation coefficient and p-value indicated, n as in **(A)**. **(C)** Cumulative distribution of reversal duration in SMD::hisCl animals ±histamine. n = 1416 (control) and 1814 (histamine) reversals. p<0.0001, two-sample Kolmogorov-Smirnov test. Note that SMD inhibition led to reversal lengths beyond 10s that were never observed in non-inhibited controls. **(D)** Illustration of different heading changes upon reversal end as quantified in (**E-F**).

(E) Fractional histograms of absolute heading change (quantified as shown in **(D)**) resulting from reversals of the indicated durations, in SMD::hisCl animals ±histamine. Reversals > 4s were typically followed by strong reorientations, which were lost in SMD::hisCl animals. Control: n = 821 (all), 215 (<2s), and 275 (>4s) reversals; histamine: n = 1230 (all), 118 (<2s), and 848 (>4s) reversals. **(F)** Median, interquartile and range of heading change in SMD::hisCl animals for reversals >4s with or without histamine. n as in (**E**). ****p<0.0001, Mann-Whitney test. Data in (**C-F**) pooled from n = 9 experimental repeats from each condition, with ~20 animals each repetition. **(G)** Trigger-averaged SMD GCaMP traces ± SEM from immobilized worm recordings aligned to reverse-to-forward command state transitions, separated by SMDD (left) and SMDV (right) transition peaks. n = 64 (SMDD) and 158 (SMDV) pooled across 10 animals. **(H)** Frequency (upper) and mean amplitude (lower) of DB02 (n =10), SMDD (n =10) and SMDV (n = 9) GCaMP activity peaks in forward and reversal command periods across whole-brain and whole-nervous-system recordings. N.A., not applicable, too few peaks detected. *p<0.05, **p<0.01, Wilcoxon matched-pairs signed rank test. n.s., not significant.

Figure S5. Neuronal activity during deep vs. shallow head-casts, related to Figure 6. (A-B) Trigger-averaged GCaMP/mCherry traces and kymograms from DB02 (**A**) and SMD (**B**) neuronal activity recordings in freely moving animals during either shallow (left, up to angle #4) vs. deep (right, angle #5 and greater) head-casts following dorsal propagated-bends. n = 206 (DB02, shallow), 111 (DB02, deep), 161 (SMD, shallow) and 15 (SMD, deep). Data pooled from 11 animals for SMD and 10 animals for DB02. **(C-D)** Example SMD traces (upper) and kymograms (lower) with two dorsal (**C**) or ventral (**D**) head-cast pairs. **(E-F)** In freely moving (**E**) and

immobilized (**F**) animals, probability of at least one unilateral SMD oscillation between a pair of SMD alternations, binned according to the SMD alternation pair's time interval. Cumulative fraction of all SMD alternation pair time intervals shown in orange. Compare to **Fig. S1E**, lower panel. n = 996 (**E**) and 192 (**F**) SMD alternation pairs pooled across 11 (**E**) and 10 (**F**) animals.

Figure S6. Sensory input and internal state effects on head-bend type, related to Figure 7. (A) Fractional heat-map of locomotion speed versus propagated-bend inter-bend interval, averaged across 14 experimental repeats with ~20 animals each. Pearson correlation coefficient and p-value indicated. Correlation analysis between speed and inter-bend interval from the underlying unbinned data. **(B)** Population mean ± SD of locomotion speed (upper), propagated-bend frequency (lower, black) and head-cast frequency (lower, green) upon 21% to 4% O_2 shift. n =14 experimental repeats with ~20 animals each. The population mean is first calculated across all animals detected in each time point within an assay, then averaged across assays. **(C-D)** Fractional heat-map showing the distribution of all data (**C**) or all head-casts (**D**) as a function of locomotion speed and angular speed from behavioral assays on food, averaged across n = 19 experimental repeats with ~20 animals each. Each data point is averaged over a 10s sliding window. Data above upper white line are considered dwelling and data within lower right box are considered roaming. Note that roaming is devoid of head casting events.

Supplemental tables

Table S1. Detailed strain list, related to all figures, with specific figure panels listed.

Strain name	Genotype	Construct (plasmid no.) injection concentrations	Additional References	Figure panel
ZIM958	*lite-1 (ce314)*	-	(Bhatla and Horvitz, 2015)	1, 7I-N, S1, S6
ZIM1466	*lite-1 (ce314); mzmEx877; mzmIs52*	*Pnlr-1(-150;-1)::HisCl::SL2::mCherry* (pAN30) – linearized, 0.5ng/uL *Punc-122::dsred* – linearized, 4ng/uL *Punc-31::NLSGCaMP6f* (pTS100, codon-optimized and with introns) – linearized, 2.5ng/uL	*Pnlr-1* (Gendrel et al., 2016; Haklai-Topper et al., 2011) ; a gift from Drs. Marie Gendrel and Oliver Hobert, 150bp upstream of *nlr-1* ATG.	2A-F, 5L, 6H, S2, S4G-H, S5F
ZIM1564	*lite-1 (ce314); mzmEx929*	*Punc-7s::CreVDH* (pHK248) - 100ng/uL *Pmyo-3::mCherry* - 2ng/uL	*Punc-7s* (Starich et al., 2009) *CreVDH* (Ruijtenberg and van den Heuvel, 2015)	4B, 5J-K, S3, S5C
ZIM1725	*lite-1 (ce314); mzmEx1018*	*Punc-7s::CreVDH* (pHK248) - 40ng/uL *Pmyo-3::mCherry* - 2ng/uL	*Punc-7s* (Starich et al., 2009) *CreVDH* (Ruijtenberg and van den Heuvel, 2015)	4B, 5J-K, S3, S4C-E
ZIM1418	*lite-1 (ce314); mzmEx858*	*Pflp-22::DIO-HisCl::SL2::mCherry* (pHK244) - 60 ng/uL *Pelt-2::NLSdsRedNLS* - 5 ng/uL	*Pflp-22* (Kim and Li, 2004) ; a gift from Dr. Kyuhyung Kim *DIO* (Sohal et al., 2009)	4B, 3J-K, S3, S4C-E
ZIM1473	*lite-1 (ce314); mzmIs28*	*Punc-17beta::HisCl::SL2::mCherry* (pHK172) - 80ng/uL	*Punc-17beta* (Charlie et al., 2006) ; a	4B, S3

			gift from Dr. Kenneth Miller	
ZIM1628	*lite-1 (ce314); mzmEx877: mzmEx929; mzmIs52*	*Pnlr-1(-150;-1)::HisCl::SL2::mCherry* (pAN30) – linearized, 0.5ng/uL Punc-122::dsred – linearized, 4ng/uL *Punc-7s::CreVDH (pHK248)* - 100ng/uL *Pmyo-3::mCherry* - 2ng/uL *Punc-31::NLSGCaMP6f* (pTS100, codon-optimized and with introns) – linearized, 2.5ng/uL	*Pnlr-1* (Gendrel et al., 2016; Haklai-Topper et al., 2011) ; a gift from Drs. Marie Gendrel and Oliver Hobert *Punc-7s* (Starich et al., 2009) *CreVDH* (Ruijtenberg and van den Heuvel, 2015)	4A, 5L
ZIM1748	*lite-1 (ce314); mzmEx877: mzmEx1018; mzmIs52*	*Pnlr-1(-150;-1)::HisCl::SL2::mCherry* (pAN30) – linearized, 0.5ng/uL *Punc-122::dsred* – linearized, 4ng/uL *Punc-7s::CreVDH* (pHK248) - 40ng/uL *Pmyo-3::mCherry* - 2ng/uL *Punc-31::NLSGCaMP6f* (pTS100, codon-optimized and with introns) – linearized, 2.5ng/uL	*Pnlr-1* (Gendrel et al., 2016; Haklai-Topper et al., 2011) ; a gift from Drs. Marie Gendrel and Oliver Hobert *Punc-7s* (Starich et al., 2009) *CreVDH* (Ruijtenberg and van den Heuvel, 2015)	4A, 5L
ZIM1562	*lite-1 (ce314); mzmEx877; mzmEx858; mzmIs52*	*Pnlr-1(-150;-1)::HisCl::SL2::mCherry* (pAN30) – linearized, 0.5ng/uL *Punc-122::dsred* – linearized, 4ng/uL *Pflp-22::DIO-HisCl::SL2::mCherry* (pHK244) - 60 ng/uL *Pelt-2::NLSdsRedNLS* - 5 ng/uL *Punc-31::NLSGCaMP6f* (pTS100, codon-optimized and with introns) – linearized, 2.5ng/uL	*Pnlr-1* (Gendrel et al., 2016; Haklai-Topper et al., 2011) ; a gift from Drs. Marie Gendrel and Oliver Hobert *Pflp-22* (Kim and Li, 2004) ; a gift	4A, 5L

			from Dr. Kyuhyung Kim *DIO* (Sohal et al., 2009)	
ZIM1574	*lite-1 (ce314); mzmEx877; mzmIs28; mzmIs52*	*Pnlr-1(-150;-1)::HisCl::SL2::mCherry* (pAN30) – linearized, 0.5ng/uL *Punc-122::dsred* – linearized, 4ng/uL *Punc-17beta::HisCl::SL2::mCherry* (pHK172) - 80ng/uL *Punc-31::NLSGCaMP6f* (pTS100, codon-optimized and with introns) – linearized, 2.5ng/uL	*Pnlr-1* (Gendrel et al., 2016; Haklai-Topper et al., 2011) ; a gift from Drs. Marie Gendrel and Oliver Hobert *Punc-17beta* (Charlie et al., 2006) ; a gift from Dr. Kenneth Miller	4A
ZIM1658	*lite-1 (ce314); mzmEx981*	*Punc-17beta::NLSGCaMP6f* (pHK264, codon-optimized and with introns) – 20ng/uL *Punc-17beta::mCherry::his58* (pHK114) – 40ng/uL	*Punc-17beta* (Charlie et al., 2006) ; a gift from Dr. Kenneth Miller	5, 6B,D, S5A
ZIM1467	*lite-1 (ce314); mzmEx882*	*Punc-7S::CreVDH* (pHK248) - 100ng/uL *Pflp-22::DIO-mCherry* (pHK246) - 50ng/uL *Pflp-22::DIO-GCaMP6Fopt* (pHK247, codon-optimized and with introns) - 30ng/uL	*CreVDH* (Ruijtenberg and van den Heuvel, 2015) *Pflp-22* (Kim and Li, 2004) ; a gift from Dr. *CreVDH* (Ruijtenberg and van den Heuvel, 2015) *DIO* (Sohal et al., 2009)	5, 6, S4A-B, S5B-E
ZIM1749	*lite-1 (ce314); mzmEx1041*	*Psto-3::HisCl::mCherry* (pHK170) - 10ng/uL *Punc-122::GFP* - 15ng/uL	*Psto-3* (Kato et al., 2015)	7D-E
ZIM1563	*lite-1 (ce314); mzmEx928*	*Psto-3::Chrimson::mCherry* (pHK256) - 20ng/uL *Punc-122::GFP* - 20ng/uL	*Psto-3* (Kato et al., 2015)	7G-H

155

Table S2. Related to Figures 3 and S2. Second column: Number of instances where each neuron was identified in immobilized Ca^{2+} imaging recordings for the calculation of mean activity level differences in forward vs. reverse command periods (**Fig. S2C**). Third column: p-values for the paired t-test (**Fig. S2C**). Fourth column: number of forward periods per neuron for which peak frequencies were calculated (**Fig. 3A**). Fifth column: p-values for inter-peak interval distribution resampling test (**Fig. 3A**). This was calculated only for neurons with multiple peaks per forward period, and statistical significance is corrected for multiple comparisons (Methods).

Neuron name	# observations	P-value (Fig. S2C)	# forward periods	P-value (Fig. 3A)
AIBL	10	0.000119	56	-
AIBR	10	0.000056	56	-
ALA	10	0.041445	56	0.17
ASKL	8	0.007442	45	0.000648
ASKR	5	0.053196	25	0.1082
AVAL	10	0.000007	56	-
AVAR	10	0.000021	56	-
AVBL	8	0.003679	42	0.012
AVBR	5	0.004497	30	0.0859
AVEL	10	0.000001	56	-
AVER	9	0.000016	49	-
AVFL	7	0.077079	37	-
AVFR	8	0.293196	46	-
BAGL	7	0.700558	37	-
BAGR	7	0.831927	37	-
Baseline	-	-	56	-
CEPDL	3	0.153182	20	0.0102
CEPDR	3	0.730871	18	-
DB01	9	0.444463	49	$<10^{6}$
DB02	10	0.001824	56	0.000004
DB03	5	0.008244	26	0.0077
DB04	4	0.111655	21	0.3164
DB05	4	0.247590	21	0.0729
DB06	4	0.053807	22	0.183
DB07a	5	0.000419	26	0.000001

DVA	5	0.047722	26	0.0302
OLQDR	3	0.209337	18	-
OLQVL	3	0.249957	19	-
OLQVR	4	0.014049	25	-
PDA	3	0.303379	14	$<10^{6}$
RIBL	9	0.000788	51	0.000004
RIBR	9	0.001071	51	0.000009
RID	4	0.007461	24	-
RIML	10	0.000113	56	-
RIMR	9	0.000187	50	-
RIVL	9	0.041139	49	0.0105
RIVR	9	0.002213	49	0.041
RMDVR	3	0.465273	19	-
RMED	10	0.000043	56	$<10^{6}$
RMEL	3	0.000169	16	0.0023
RMER	4	0.009923	23	0.0015
RMEV	8	0.045459	46	0.000393
SIBVL	5	0.229044	30	0.2497
SIBVR	4	0.034030	24	0.0901
SMDDL	10	0.007962	56	$<10^{6}$
SMDDR	9	0.010916	49	$<10^{6}$
SMDVL	10	0.001672	56	$<10^{6}$
SMDVR	10	0.001490	56	0.000208
URYDL	10	0.080583	56	-
URYDR	8	0.107907	45	-
URYVL	9	0.122731	49	-
URYVR	8	0.003887	45	-
VA02	6	0.055074	31	-
VB01	10	0.012811	56	0.000155
VB02	10	0.000033	56	0.1596
VB03	6	0.120118	31	0.014
VB04	4	0.313493	19	0.4983
VB05	5	0.004762	26	0.031
VB06	5	0.005444	26	0.0495
VB07	4	0.001905	21	0.019
VB08	5	0.002505	26	0.0667
VB09	5	0.003075	26	0.0034
VB10	4	0.007944	23	0.0363
VB11p	5	0.007691	26	0.000363

VD02	3	0.464618	18	0.3707

Table S3. Related to Figure 3. P-values for covariogram significance test for covariograms shown in **Fig. 3C**. Statistical significance is corrected for multiple comparisons (Methods).

	SMDDL	SMDDR	SMDVL	SMDVR	DB01	DB02	RMED	RMEV	VB01
SMDDL	$<10^{-6}$	$<10^{-6}$	0.0011	0.00029	0.7246	0.7783	$<10^{-6}$	0.0544	0.000096
SMDDR	$<10^{-6}$	$<10^{-6}$	0.0003	0.001	0.1722	0.822	$<10^{-6}$	0.3796	0.0114
SMDVL	0.0039	0.0006	$<10^{-6}$	$<10^{-6}$	0.5386	0.0053	0.0222	0.000002	$<10^{-6}$
SMDVR	0.0001	0.001	$<10^{-6}$	$<10^{-6}$	0.0889	$<10^{-6}$	0.0094	$<10^{-6}$	$<10^{-6}$
DB01	0.1525	0.062	0.3691	0.0793	$<10^{-6}$	0.000001	0.7941	0.4473	0.6945
DB02	0.9148	0.8422	0.0193	$<10^{-6}$	0.000001	$<10^{-6}$	0.2117	0.4657	0.000025

Table S4. Related to Figure S2. P-values for covariogram significance test for covariograms shown in **Fig. S2E**. Statistical significance is corrected for multiple comparisons (Methods).

	DB01	DB02	DB07a	VB01	VB09	VB11p
DB01	$<10^{-6}$	$<10^{-6}$	0.2915	0.6938	0.4493	0.7896
DB02	$<10^{-6}$	$<10^{-6}$	0.9167	0.000599	0.2612	0.931
DB07a	0.6955	0.8963	$<10^{-6}$	0.382	0.2728	0.4725
VB01	0.6524	0.000156	0.6436	$<10^{-6}$	0.7389	0.024
VB09	0.5515	0.1337	0.841	0.8186	$<10^{-6}$	0.3242
VB11p	0.6768	0.7061	0.3653	0.0127	0.242	$<10^{-6}$

6. Discussion

6.1 The *C. elegans* action sequence is embedded in global brain dynamics

The first aim of this thesis was to understand how the worm's neuronal activity patterns are coordinated to enable its action sequence. In Article 1, my colleagues and I addressed this question using the novel tool of whole-brain calcium imaging. We unexpectedly discovered low-dimension, brain-wide, cyclical dynamics in immobilized animals. By identifying individual neurons contributing to these dynamics, some of which were previously shown to drive forward, reverse, or turn behaviors, we hypothesized that this cycle represents the worm's motor commands. Indeed, by imaging these neurons and others individually in freely moving animals, we found their activity to be reliably and precisely coordinated with the worm's instantaneous behavior. Thus, we were able to map different motor commands onto the activity patterns of immobilized animals. Crucially, these motor commands cycled through the same pattern as the worm's action sequence, forward – reverse – turn – forward; we were even able to distinguish alternative motor commands for alternative dorsal or ventral turn behaviors following each and every reversal. We concluded from these results that the worm's action sequence is generated by motor command signals that are spread across many neurons. Thus the worm uses low-dimensional neuronal population dynamics that cycle in a lawful fashion in order to produce its cyclical action sequence. Because these patterns persist in immobilized animals in the absence of acute sensory stimuli, it is clear that specific time-varying sensory inputs are not required for the progression of motor commands along their lawful trajectory, unlike current models for the *Drosophila* grooming sequence (Seeds et al., 2014).

6.2 A revised understanding of pre-motor interneurons

As described in section 3.8, previous work has implicated a group of five pre-motor interneurons as the primary drivers of behavior in *C. elegans*. The best-studied of these interneurons is AVA, which is also the most highly connected neuron in the worm's nervous system. Three types of experiments together implicated AVA as a primary driver of reversal behaviors: (1) AVA was shown to be the most crucial pre-motor interneuron for reversal behavior by laser ablation experiments (Chalfie et al., 1985; Wicks et al., 1996); (2) Optogenetic stimulation of AVA effectively induces reversals at short latency (e.g. (Shipley et al., 2014)); and (3) AVA activity is increased during reversals (Article 1, Figure 2) (Kawano et al., 2011; Piggott et al., 2011). These three types of experiments, which test necessity, sufficiency, and activity during normal behavior, are typical not only for the interrogation of neurons in *C. elegans*, but also for functional studies of neuronal cell types in many genetic model organisms, including mammals (Clark et al., 2013). However, our results indicate that these experiments alone may result in a misleading picture of a neuron's role in behavior. We found that while AVA is indeed required to generate reversal behavior in moving animals, its inhibition only slightly affects the brain-wide reversal command generation in immobilized animals (Article 1, figure 5). In fact, the entire motor command sequence proceeds normally in the absence of AVA activity in immobilized animals. On the basis of these data, we concluded that AVA plays only a very minor role in generating spontaneous reversal commands, and that the term "command interneuron" is therefore a misnomer. Importantly, we can make this conclusion only for the spontaneous reversal behaviors (and reversal motor commands) we describe in Article 1 (which should correspond to the reversal behaviors described in, for example, (Gray et al., 2005)); in contrast, escape reversal behaviors, such as those induced by the nociceptive sensory neuron ASH, may still involve AVA in a command neuron role (Chalfie et al., 1985; Guo et al., 2009; Piggott et al., 2011). In moving animals, the

reversal phase of the action sequence is replaced by a prolonged pausing phase, during which time the brain is in the reversal command state despite the lack of reversal behavior (Article 1, figure 5F-H). Combined with our observation of decreased A-MN activity in AVA-inhibited immobilized animals, these data indicate that (1) AVA is required for proper communication of the reversal command to motor neurons, and therefore proper execution of the reversal behavior and (2) feedback from affected neurons (AVA, RIM, AVE, or A-MNs), or from the behavioral execution itself (e.g. via proprioceptive mechanisms), is required for proper reversal command state duration in moving animals. We therefore concluded that AVA's role is rather that of a crucial output node for communication of the brain's command state to the motor neurons. Our revision of AVA's role in reversal command generation benefited from two crucial approaches: (1) observing how reversal commands are generated at the brain-wide level, and (2) monitoring other neurons participating in behavior generation, both in the fictive state in immobilized animals and during altered behavior in moving animals. These findings provide an illustrative example of how standard necessity and sufficiency experiments that use behavioral readouts only may not suffice when it comes to understanding the function of individual components of a highly recurrent nervous system.

6.3 Low-dimensional population dynamics: consequences and generality

The work presented in Article 1 builds upon a growing body of research describing behavior generation as the result of a dynamical system, the evolution of which can be captured by quantifications of latent dimensions within neuronal population activity (Ahrens et al., 2012; Allen et al., 2019; Bouchard et al., 2013; Briggman, 2005; Bruno et al., 2015; Georgopoulos and Carpenter, 2015; Harvey et al., 2012; Shenoy et al., 2013; Stringer et al., 2019). These studies were undertaken in various invertebrates and vertebrates, including mice, monkeys, and humans, suggesting that low-dimensional population dynamics may be a highly conserved

mechanism by which nervous systems encode and generate behavior. What distinguishes the work presented in this thesis is that we recorded activity in a brain-wide manner; thus we were not limited by either small samples of large neuronal populations (suggested by (Stringer et al., 2019) to be an issue) nor by restriction to brain regions of interest. This depth and breadth of coverage is only so far possible in larval zebrafish, other than the worm. Further, both Articles 1 and 2 describe the organization of multiple behaviors, rather than a single behavior. Our ability to record in a brain-wide manner likely enabled success in understanding complex behavioral patterns that may not be possible from sparser sampling approaches. Thus we suspect that as neuronal recording technologies improve, researchers may uncover low-dimensional neuronal population representations behind more complex and more ethological behavioral repertoires.

6.4 Open questions in understanding *C. elegans* global brain dynamics

While the work presented in Article 1 represents a major step forward in understanding how the worm's brain generates motor commands and coordinates them into an action sequence, several open questions remain. First, how does sensory input modulate the motor command sequence, for example to cause increases or decreases in reversal frequency (Article 1 figures 6 and S7)? Both our whole-brain and freely moving animal recordings showed that several neurons just one synapse downstream of responsive sensory neurons faithfully encode instantaneous behavior, regardless of sensory environment and resulting changes in behavior. However, these and other first- and second-layer interneurons had previously been implicated in sensory input computations (Chalasani et al., 2007; 2010; Clark et al., 2006; Gabel et al., 2007; Gray et al., 2005; Guillermin et al., 2017; Iino and Yoshida, 2009; Larsch et al., 2015; Oda et al., 2011; Tsalik and Hobert, 2003). Either the conditions in which these studies were performed (immobilized worm, short pre-stimulus periods preventing analysis of ongoing

activity (Kaplan et al., 2018)) led to an incorrect or incomplete picture of these neurons' functions, or these neurons perform these computations on top of their instantaneous coding for behavior. For certain interneurons like AIY, the latter may be the case, because AIY signals are often recorded from the neuronal process (Chalasani et al., 2010; Li et al., 2014; Liu et al., 2018). Measuring compartmentalized dynamics was crucial for understanding the sensorimotor transformation performed by RIA. Whether this is the case for other interneurons, like AIY, remains unclear; likewise, the extent to which important compartmentalized signals are missed in brain-wide soma or nuclear recordings remains unknown. Several neurons do show clustering of synaptic input and output sites, similar to RIA, suggesting that localized processing may be commonplace (White et al., 1986). Future studies examining neuron-wide cytoplasmic responses to sensory inputs, perhaps using red-shifted calcium indicators (Dana et al., 2016) in conjunction with nuclear-localized pan-neuronal GCaMP, should distinguish these possibilities.

The whole-brain imaging results presented in Article 1 open up additional interesting avenues of investigation. How are these coordinated population dynamics produced? It remains possible that a small kernel of neurons generates the flip-flop forward-reverse command dynamics intrinsically, and sends efference copies to the other neurons that show these signals (though this possibility was excluded for the AVA interneuron). Alternatively, many or all neurons may show intrinsic bi-stable dynamics, which are then coordinated by the many synapses between them. Single- and multi-neuron inhibition experiments, for example using histamine-gated chloride channels, can address this question. Another question is how the functional connectome relates to the structural connectome. *C. elegans* is the only organism in which this question can currently be asked at the single-cell, brain-wide level. An important concern here is how each dataset is defined. First, the structural connectome has been reconstructed from just two individuals; it remains unclear how much the connectome varies

from animal to animal. Second, as discussed in Article 2, standard methods for quantifying functional connectivity in a pairwise manner are inadequate for the relatively sparse activity patterns in whole-brain recordings. The method presented in Article 2, figure 3 may be extended beyond the forward command periods examined there, and combined with more standard measures like cross-correlation, to obtain a metric for functional connectivity. These developments should allow a thorough investigation of the relationship between functional and structural connectivity in the worm, which could provide a roadmap for understanding this relationship in more complex brains as other connectomes become available. Another important question relates to the differences seen between moving and immobilized animals. The major difference we observed is a prolonged reversal command period. Our data show that both microfluidic device immobilization as well as tetramisole each individually can cause this effect. AVA inhibition also caused moving animals to show prolonged reversal commands (though animals remained paused rather than executing a reversal). A parsimonious explanation would be that the worm can sense whether or not its reversal command has been completed; this would allow it to continue its attempt at reversing in unsuccessful cases, which may be crucial for predator avoidance. Future work investigating this possibility could not only reveal an interesting proprioceptive mechanism, but could also enable the prevention of this effect in immobilized animals, so that immobilized worm motor command dynamics better resemble those in freely moving animals. This would greatly facilitate the study of sensorimotor transformations, because while these can be observed and therefore studied in immobilized animals (Article 1 figure 6), sensory effects on motor commands are less efficient compared to moving animals, perhaps due to the prolonged reversal.

6.5 The neuronal implementation of a multi-timescale behavioral hierarchy

The second aim of my thesis work was to test Tinbergen's long-standing hierarchy model for behavior (Dawkins, 1976; Tinbergen, 1951). Specifically, a non-overlapping hierarchical control of behavior should have the property that switches between fast timescale actions belonging to different behavioral programs require switching between the programs themselves, one level up in the hierarchy (Dawkins, 1976). In Article 2, my colleagues and I describe several instances of this type of control, within the context of three different timescale behaviors in *C. elegans*. First, we showed that the B-MNs, which drive mid-level propagated-bends, are toggled between oscillatory and inactive states depending on the state of the upper-level forward/reverse cycle. This enforces the rule that anterior-to-posterior propagated-bends only occur during forward periods. Second, we described a new *C. elegans* behavior, which we termed head-casts, and we showed that head-casts are likewise restricted to forward states. However, unlike the B-MNs, the head-cast-driving SMD neurons are not simply switched to an inactive state during reversals; rather, their activity becomes lower amplitude and less frequent. Inhibition experiments suggested that this switch in activity pattern is accompanied by a switch in functional role, such that the SMDs act more like interneurons rather than motor neurons during reversals. Thus, animals in a reversal state can only perform propagated-bends and head-casts by first switching the upper-level state to forward; this is instantiated by a strict control of B-MN and SMD activity patterns and functional role depending on upper-level state. Finally, we showed that two different SMD activity patterns are phase-nested, such that the two co-occurring behaviors are phase-nested as well. Again, for the worm to switch from ventral to dorsal head-casts (from SMDV to SMDD unilateral oscillations), it would have to switch first one level up, to the correct phase of the propagated-bend cycle (of the SMD alternation cycle). Altogether, these results show that these worm behaviors exhibit a strict, non-overlapping hierarchical organization, and that this organization is implemented by nested

neuronal interactions in which slow timescale dynamics maintain tight control over faster timescale ones. Importantly, at least for the SMD neurons, the circuit architecture underlying these nested dynamics is not obviously hierarchical (White et al., 1986); therefore several aspects of behavioral organization could not have been predicted from the connectome alone, but required neuronal activity data in addition. This work provides crucial mechanistic support for Tinbergen's hierarchy model; further, these mechanisms involve nested neuronal dynamics similar to those described in a wide variety of other species (Buzsáki et al., 2013; Fayyazuddin and Dickinson, 1999; Hyafil et al., 2015; Moore et al., 2013; Putney et al., 2019; Sponberg and Daniel, 2012), suggesting potentially broad generality.

6.6 Nested neuronal dynamics: consequences and generality

The important role for nested neuronal dynamics that my colleagues and I described in Article 2 may have broad implications for understanding neuronal activity patterns more generally. Especially in the mammalian brain, neuronal dynamics spanning a wide variety of timescales occur simultaneously, with significant interactions between different timescales (Buzsáki et al., 2013; Hyafil et al., 2015). However, the behavioral relevance of many of these different timescale patterns and interactions remains unclear (Hyafil et al., 2015). Our work suggests that neuronal dynamics can have considerable cross-timescale interactions, resulting in specific effects on behavioral output. The best example of this is the switch in SMD functional role. Without knowledge of the slow-timescale forward/reverse state, could an observer understand the function of SMD's faster timescale activity? While SMD activity patterns do show differences between forward and reverse states, there remains variability in SMD peak amplitude within each state, such that the behavioral impact of each SMD peak may be ambiguous without reference to the current forward/reverse command state. However, knowledge of this longer-timescale state allows an observer (or other neurons) to better

interpret the functional impact of each SMD activity peak. Therefore, especially with regard to faster-timescale activities, knowledge of activity in other neuronal classes, even (or especially) if they act on different timescales, is crucial to understanding how certain neurons affect behavior. Fast neuronal activity recordings of sufficient duration do capture multiple co-occurring timescales of dynamics; future researchers should take advantage of this to examine cross-timescale effects, especially top-down ones, in which slower modulations may impact faster-timescale activity patterns and functions (Clark et al., 2013) as we have observed.

The experiments in Article 2 reveal a non-overlapping hierarchical organization of behavior at the level of motor actions; the slower-timescale behavioral state switch between roaming and dwelling is not well-described by this model. Roaming and dwelling switches can rather be described as part of a less strict, overlapping hierarchy model, because each state makes use of the same behaviors (forward, reverse, propagated-bends, head-casts), only with different frequencies. Therefore, both forward and reverse states each have both roaming and dwelling as "hierarchs," resulting in an overlapping hierarchy (Dawkins, 1976). This is in line with recent work suggesting hierarchical organization in various species at the level of motor control (Berman et al., 2016; Berwick et al., 2011; Glaze and Troyer, 2007; Markowitz et al., 2018; Marques et al., 2018; Moore et al., 2013) rather than at the level of slower-timescale behavioral states (Dawkins, 1976; Tinbergen, 1951). Phase-nesting in particular resembles recent descriptions of motor control in both mammals and insects. Orofacial behaviors in mice such as breathing and whisking show a similar organization as the worm's phase-nested behaviors, and anatomy supports a hierarchical interaction between the respective CPG pools (Moore et al., 2013). Several orofacial behaviors target overlapping muscles on the face of the mouse; similarly, propagated-bends and head-casts target overlapping neck muscles. This suggests that one role of hierarchical organization is to coordinate motor actions that could otherwise be in conflict. Finally, the impact of motor neurons controlling flight in insects

depends crucially on the phase of the wing beat cycle (Fayyazuddin and Dickinson, 1999; Putney et al., 2019; Sponberg and Daniel, 2012). Altogether, these findings suggest that hierarchical interactions between motor commands on different timescales, such as those described in Article 2, might represent a highly conserved form of motor control across the animal kingdom.

6.7 Open questions in understanding *C. elegans* nested neuronal dynamics

While Article 2 establishes nested neuronal dynamics as a key component of *C. elegans* behavioral organization, several open questions remain. First, the ever-expanding genetic toolkit of *C. elegans* can be used to dissect the cellular and synaptic bases for specific nested interactions. For example, how does the forward/reverse cycle impinge upon SMD dynamics and function? Several interneurons that are active specifically during forward or reverse phases are well-positioned to impact SMD, either through chemical synapses (e.g. AIB), gap junctions (e.g. RIB), or neuromodulators (e.g. tyramine from RIM (Alkema et al., 2005)). Further, the SMD neurons are capable of signaling via both acetylcholine and GABA (Gendrel et al., 2016). Presumably their positive correlation with head-bend angle is a result of excitatory cholinergic signaling; in contrast, how the SMDs play a potent interneuron-like role in reversal termination is unclear. One possibility is that GABA is specifically released during reversals, or alternatively, only affects neurons that are active during reversals. However, SMD's postsynaptic partners do not consist of any reverse-active neurons, so the connectome does not provide any hints in this direction. A further question is how phase-nesting between SMDD and SMDV is maintained. The SMDs have reciprocal synapses between each other that could support reciprocal inhibition; however, RIA may also be involved (Hendricks et al., 2012; Liu et al., 2018). On another note, the data in Article 2 support the idea that the SMDs, perhaps along with the RMEs, form a CPG. However, whole-brain imaging does not capture signals in

neuronal processes, such as SMD-dependent RIA signals (Hendricks et al., 2012). Therefore, it remains possible that the SMDs are simply outputs of a CPG somewhere upstream, which our whole-brain imaging setup may not be sensitive to. One way to address this would be to record GCaMP signals from dissociated *C. elegans* neurons (Kobayashi et al., 2016), including SMDs, to try to capture oscillatory activity patterns in the absence of synaptic inputs. Alternatively, one could express histamine-gated chloride channels pan-neuronally except in SMDs and RMEs, to try to reconstitute oscillatory activity patterns in a silenced brain background.

Another major direction regards the functional roles of phase-nesting and head-casting. Our data suggest that head-casting can serve both local exploration and local exploitation, depending on behavioral context (Article 2 figure 7); however, head-casts could play a prominent role in chemotaxis navigation, as similar behaviors do in *Drosophila* larvae (Gomez-Marin et al., 2011). Phase-nesting between propagated-bends and head-casts could be important for coordinating behaviors that make use of overlapping muscles, to prevent conflicting motor output. To test this, one could find a way to desynchronize SMD alternations from propagated-bends, so that SMD head-cast activity occurs at random times with respect to the propagated-bend phase. One possibility is that SMD alternations are synchronized with propagated-bends by proprioception (Yeon et al., 2018); however, our preliminary results suggest that the channels proposed to confer proprioceptive properties to SMD neurons are not required for SMD's behavior synchronization, so other methods would have to be used, such as laser surgery to remove SMD's non-synaptic, putatively proprioceptive processes (White et al., 1986). Another tantalizing possibility is that because the SMDs maintain clear relationships with head-bend angle during both head-casts and propagated-bends, SMD phase information may be used for the animal to properly integrate sensory inputs with respect to head-bend phase, for example during weathervaning (Iino and Yoshida, 2009; Liu et al., 2018; Lockery,

2011). If this is the case, sensory information should be integrated differentially depending on SMD phase even in immobilized animals. Specific phase windows for sensory integration have been proposed for both insects (Gupta et al., 2016) and mammals (Buzsáki and Draguhn, 2004; Yuste et al., 2005). Future investigations into nested neuronal dynamics therefore hold promise for further generalizable findings.

6.8 An extension of the CPG concept to more complex behavioral organization

In section 3.4, I introduced the concept of the CPG. The crucial feature of a CPG is that in a reduced animal preparation (e.g. deafferented, or *ex vivo*) in which behavior is not executed, neuronal dynamics resembling behavioral patterns can be measured. The discovery of CPGs was powerful in two respects: (1) their existence proves that several features of behavioral output are intrinsic to the neuronal networks that produce the behavior, rather than requiring sensory input such as feedback from behavioral execution, and (2) they enable experiments in simplified settings (i.e. non-moving preparations without any need to control sensory input) to examine the production of intrinsic network dynamics alone (Marder and Bucher, 2001). Then, the reduced preparation can be compared to the intact one during behavior, to determine which components of the behavior are guided or modulated by sensory inputs. The results from both Articles 1 and 2 suggest that the worm's encoding of its action sequence, as well as certain aspects of its hierarchically organized behavior, exhibit CPG-like properties. The motor command sequence, phase-nested SMD dynamics, and forward/reverse command cycle modulation of B-MN and SMD neurons can all be captured in immobilized animals, with several key features retained from the freely moving case. As with CPGs, these discoveries have two major implications: (1) these features of higher-order behavioral organization are the product of intrinsic neuronal network interactions, modulated by but not requiring time-varying sensory inputs, and (2) therefore, these intrinsic circuit interactions may

be dissected in the immobilized worm preparation, and their interaction with sensory feedback can be examined by comparison to moving animals. Therefore, at least for the worm, the CPG concept can be extended beyond simple rhythmic behaviors to more complex, non-rhythmic, multi-action, and multi-timescale behavioral organizations like action sequences and hierarchies. The extent to which this result is generalizable beyond *C. elegans* awaits studies in other species, which may require novel reduced animal preparations that produce neuronal dynamics bearing some resemblance to intact neuronal activity patterns during behavior.

6.9 The immobilized animal preparation: strengths and weaknesses

In both Articles 1 and 2, my colleagues and I compared neuronal activity patterns in freely moving versus immobilized animals, and found numerous similarities and differences. This approach proved highly informative, especially for distinguishing aspects of behavioral organization that can be pinned down to specific neuronal circuit interactions, as opposed to resulting from sensory input during behavioral execution (see section 6.8). Immobilization was originally an unfortunate but necessary step for whole-brain imaging; now, however, we view immobilized worm imaging as an important component of our research. The worm has several potential sources of proprioceptive input (Li et al., 2006a; Wen et al., 2012; Yeon et al., 2018), which have even been observed in various motor neuron classes; thus recordings in moving animals cannot easily distinguish motor command signals from proprioceptive feedback signals. Still, many questions cannot be addressed in the immobilized worm only, and we indeed observed several differences between certain neurons' activities in immobilized versus moving conditions. One prominent example is the prolonged reversal state in immobilized animals (see section 6.4). We also observed that reversal-active neurons show little amplitude variation between reversal commands in immobilized animals, yet varied strongly in amplitude between reversals in moving animals (Article 1). Another difference was that the frequencies

of SMD and DB oscillations were about an order of magnitude slower in immobilized animals versus moving ones (Article 2); such a reduction in frequency has been observed for CPGs in other species (Fox, 2006; Goulding, 2009). Altogether, moving animals show additional proprioceptive signals, additional amplitude variations, and higher frequencies of activity. While we validated that these changes do not affect our conclusions in Articles 1 and 2, it remains likely that whole-brain imaging in moving animals will result in a markedly different, likely higher-dimensional picture of brain-wide as well as single-neuron activity. One study has reported exactly that (Scholz et al., 2018). However, my colleagues and I argue that this preprint (1) understates our expectation of differences between moving and immobilized animals, stated in Article 1, and (2) does not convincingly demonstrate that the GCaMP signals reported are sufficiently lacking in movement artifacts. This last point is underscored by the apparent lack of reproduction of several results obtained by multiple research groups including ours, such as RIB's relationship to the worm's instantaneous forward locomotion speed. It should be further emphasized that our comparison of individual neurons' activities in immobilized versus moving conditions not only confirms many of our interpretations from immobilized animal data, but also allows us to draw several conclusions that would not be possible otherwise, such as which neurons or interactions do and do not require proprioceptive input. Altogether, the work presented in Articles 1 and 2 illustrates how multiple approaches and experimental setups can be combined to produce insights in a highly synergistic manner.

6.10 Conclusions

In this thesis, I aimed to provide dynamical and mechanistic neuronal activity descriptions for two types of behavioral organization in *C. elegans*: an action sequence and a multi-timescale hierarchy. In Article 1, my colleagues and I showed that the worm's action sequence is embedded in low-dimensional, brain-wide population dynamics. Further, these

dynamics persist in the absence of behavioral execution as a motor command sequence, similar to how CPGs drive simpler rhythmic behaviors. In this context, we redefined the role of the worm's most connected neuron, AVA, showing that it is in fact dispensable for spontaneous reversal command generation and is rather required only for communicating this reversal command state to downstream motor neurons. We further showed that the worm's latent behavioral command generation is robust to a sensory input, even when that input modifies command frequencies. In Article 2, we described a previously unreported *C. elegans* behavior, head-casting, and showed that its execution depends crucially on the phase of the slower-timescale propagated-bend cycle; we termed this relationship phase-nesting. We further showed that both behaviors are restricted to forward locomotion periods. Altogether, these strict organizational rules of worm behavior form a three-level hierarchy. We went on to identify putative CPGs for both propagated-bends and head-casts, and showed how interactions between those CPGs, as well as with the brain-wide dynamics described in Article 1, implement the organizational rules that make up the behavioral hierarchy. Thus, we provided crucial support for Tinbergen's model of hierarchical behavioral organization, and in doing so, discovered that the nested neuronal oscillations that implement the behavioral hierarchy are a repeated dynamical motif of the *C. elegans* nervous system. We concluded Article 2 by showing how both a salient sensory input and an internal state change can act via these nested dynamics to cause ethologically relevant behavioral changes.

This work bears potential relevance to the neuroscience community beyond *C. elegans* in at least three ways. First, we expect that the results of Article 1 foreshadow widespread latent state behavior encoding in other animals (Ahrens et al., 2012; Musall et al., 2019; Stringer et al., 2019), as new technologies become available approaching the scope of what can be accomplished in the worm. Second, the nested neuronal dynamics in Article 2 resemble similar cross-timescale interactions in a wide variety of other species, many of which remain

functionally mysterious. We find clear behavioral correlates for multi-timescale interactions in the worm, opening up avenues of investigation for how and why they arise. Third, our unprecedented access to single-cell brain-wide neuronal activity recordings has led us to descriptions of behavioral organization. This is not because we set out to study behavioral organization specifically, but rather because we found clear, highly invariable relationships between neuronal activities that begged for functional explanations – and we found those explanations in the worm's action sequence and a multi-timescale behavioral hierarchy. This suggests that a primary function of the nervous system is to produce behavioral output that is strictly organized temporally. Early thinkers in ethology (Dawkins, 1976; Lashley, 1951; Moltz, 1961; Slater, 1973; Tinbergen, 1951) focused on these and other types of behavioral organization, and increasingly more attention has been paid to behavioral organization in recent years (Berman et al., 2016; Brown and de Bivort, 2018; Brown et al., 2013; Krakauer et al., 2017; Markowitz et al., 2018; Marques et al., 2018; McKellar et al., 2019; Moore et al., 2013; Seeds et al., 2014; Stephens et al., 2008; Wiltschko et al., 2015). The degree to which *C. elegans* brain activity is devoted to behavioral organization, as described in this thesis, is a testament to ongoing work in this direction.

7. References

Ahrens, M.B., Li, J.M., Orger, M.B., Robson, D.N., Schier, A.F., Engert, F., and Portugues, R. (2012). Brain-wide neuronal dynamics during motor adaptation in zebrafish. Nature *19*, 519–534.

Ahrens, M.B., Orger, M.B., Robson, D.N., Li, J.M., and Keller, P.J. (2013). Whole-brain functional imaging at cellular resolution using light-sheet microscopy. Nat Meth *10*, 413–420.

Alkema, M.J., Hunter-Ensor, M., Ringstad, N., and Horvitz, H.R. (2005). Tyramine Functions Independently of Octopamine in the Caenorhabditis elegans Nervous System. Neuron *46*, 247–260.

Allen, W.E., Chen, M.Z., Pichamoorthy, N., Tien, R.H., Pachitariu, M., Luo, L., and Deisseroth, K. (2019). Thirst regulates motivated behavior through modulation of brainwide neural population dynamics. Science *364*, eaav3932.

Ausborn, J., Stein, W., and Wolf, H. (2007). Frequency Control of Motor Patterning by Negative Sensory Feedback. Journal of Neuroscience *27*, 9319–9328.

Barclay, J.W., Morgan, A., and Burgoyne, R.D. (2012). Neurotransmitter release mechanisms studied in Caenorhabditis elegans. Cell Calcium *52*, 289–295.

Ben Arous, J., Laffont, S., and Chatenay, D. (2009). Molecular and Sensory Basis of a Food Related Two-State Behavior in C. elegans. PLoS ONE *4*, e7584–e7588.

Bentley, B., Branicky, R., Barnes, C.L., Chew, Y.L., Yemini, E., Bullmore, E.T., Vértes, P.E., and Schafer, W.R. (2016). The Multilayer Connectome of Caenorhabditis elegans. PLoS Comput Biol *12*, e1005283–31.

Berman, G.J., Bialek, W., and Shaevitz, J.W. (2016). Predictability and hierarchy in Drosophilabehavior. Proc Natl Acad Sci USA *113*, 11943–11948.

Berwick, R.C., Okanoya, K., Beckers, G.J.L., and Bolhuis, J.J. (2011). Songs to syntax: the linguistics of birdsong. Trends in Cognitive Sciences *15*, 113–121.

Bouchard, K.E., Mesgarani, N., Johnson, K., and Chang, E.F. (2013). Functional organization of human sensorimotor cortex for speech articulation. Nature 1–8.

Briggman, K.L. (2005). Optical Imaging of Neuronal Populations During Decision-Making. Science *307*, 896–901.

Broekmans, O.D., Rodgers, J.B., Ryu, W.S., and Stephens, G.J. (2016). Resolving coiled shapes reveals new reorientation behaviors in C. elegans. eLife *5*, e17227.

Brown, A.E., and de Bivort, B. (2018). Ethology as a physical science. Nature Physics 1–5.

Brown, A.E.X., Yemini, E.I., Grundy, L.J., Jucikas, T., and Schafer, W.R. (2013). A dictionary of behavioral motifs reveals clusters of genes affecting Caenorhabditis elegans locomotion. Proc Natl Acad Sci USA *110*, 791–796.

Bruno, A.M., Frost, W.N., and Humphries, M.D. (2015). Modular Deconstruction Reveals the Dynamical and Physical Building Blocks of a Locomotion Motor Program. Neuron *86*, 304–318.

Buzsáki, G., and Draguhn, A. (2004). Neuronal oscillations in cortical networks. Science *304*, 1926–1929.

Buzsáki, G., Logothetis, N., and Singer, W. (2013). Scaling Brain Size, Keeping Timing: Evolutionary Preservation of Brain Rhythms. Neuron *80*, 751–764.

Calhoun, A.J., Chalasani, S.H., and Sharpee, T.O. (2014). Maximally informative foraging by Caenorhabditis elegans. eLife *3*, 8616–13.

Chalasani, S.H., Chronis, N., Tsunozaki, M., Gray, J.M., Ramot, D., Goodman, M.B., and Bargmann, C.I. (2007). Dissecting a circuit for olfactory behaviour in Caenorhabditis elegans. Nature *450*, 63–70.

Chalasani, S.H., Kato, S., Albrecht, D.R., Nakagawa, T., Abbott, L.F., and Bargmann, C.I. (2010). Neuropeptide feedback modifies odor-evoked dynamics in Caenorhabditis elegans olfactory neurons. Nat Neurosci *13*, 615–621.

Chalfie, M., Sulston, J.E., White, J.G., Southgate, E., Thomson, J.N., and Brenner, S. (1985). The neural circuit for touch sensitivity in Caenorhabditis elegans. Journal of Neuroscience *5*, 956–964.

Chen, T.-W., Wardill, T.J., Sun, Y., Pulver, S.R., Renninger, S.L., Baohan, A., Schreiter, E.R., Kerr, R.A., Orger, M.B., Jayaraman, V., et al. (2013). Ultrasensitive fluorescent proteins for imaging neuronal activity. Nature *499*, 295–300.

Chronis, N., Zimmer, M., and Bargmann, C.I. (2007). Microfluidics for in vivo imaging of neuronal and behavioral activity in Caenorhabditis elegans. Nat Meth *4*, 727–731.

Churchland, M.M., Cunningham, J.P., Kaufman, M.T., Foster, J.D., Nuyujukian, P., Ryu, S.I., and Shenoy, K.V. (2012). Neural population dynamics during reaching. Nature *487*, 51–56.

Clark, D.A., Biron, D., Sengupta, P., and Samuel, A.D.T. (2006). The AFD Sensory Neurons Encode Multiple Functions Underlying Thermotactic Behavior in Caenorhabditis elegans. J. Neurosci. *26*, 7444–7451.

Clark, D.A., Gabel, C.V., Gabel, H., and Samuel, A.D.T. (2007). Temporal Activity Patterns in Thermosensory Neurons of Freely Moving Caenorhabditis elegans Encode Spatial Thermal Gradients. J. Neurosci. *27*, 6083–6090.

Clark, D.A., Freifeld, L., and Clandinin, T.R. (2013). Mapping and Cracking Sensorimotor Circuits in Genetic Model Organisms. Neuron *78*, 583–595.

Collins, K.M., and Koelle, M.R. (2013). Postsynaptic ERG Potassium Channels Limit Muscle Excitability to Allow Distinct Egg-Laying Behavior States in Caenorhabditis elegans. J. Neurosci. *33*, 761–775.

Dana, H., Mohar, B., Sun, Y., Narayan, S., Gordus, A., Hasseman, J.P., Tsegaye, G., Holt, G.T., Hu, A., Walpita, D., et al. (2016). Sensitive red protein calcium indicators for imaging neural activity. eLife *5*.

Dankert, H., Wang, L., Hoopfer, E.D., Anderson, D.J., and Perona, P. (2009). Automated monitoring and analysis of social behavior in Drosophila. Nat Meth *6*, 297–303.

Dawkins, R. (1976). Hierarchical organisation: A candidate principle for ethology. In Growing Points in Ethology, (Oxford, England: Cambridge U Press SN -).

de Bono, M., and Bargmann, C.I. (1998). Natural variation in a neuropeptide Y receptor homolog modifies social behavior and food response in C. elegans. Cell *94*, 679–689.

Dickson, B.J. (2008). Wired for sex: the neurobiology of Drosophila mating decisions. Science *322*, 904–909.

Donnelly, J.L., Clark, C.M., Leifer, A.M., Pirri, J.K., Haburcak, M., Francis, M.M., Samuel, A.D.T., and Alkema, M.J. (2013). Monoaminergic Orchestration of Motor Programs in a Complex C. elegans Behavior. PLoS Biol *11*, e1001529–17.

Faumont, S., Rondeau, G., Thiele, T.R., Lawton, K.J., McCormick, K.E., Sottile, M., Griesbeck, O., Heckscher, E.S., Roberts, W.M., Doe, C.Q., et al. (2011). An Image-Free Opto-Mechanical System for Creating Virtual Environments and Imaging Neuronal Activity in Freely Moving Caenorhabditis elegans. PLoS ONE *6*, e24666–12.

Fayyazuddin, A., and Dickinson, M.H. (1999). Convergent mechanosensory input structures the firing phase of a steering motor neuron in the blowfly, Calliphora. Journal of Neurophysiology *82*, 1916–1926.

Fouad, A.D., Teng, S., Mark, J.R., Liu, A., Alvarez-Illera, P., Ji, H., Du, A., Bhirgoo, P.D., Cornblath, E., Guan, S.A., et al. (2018). Distributed rhythm generators underlie Caenorhabditis elegans forward locomotion. eLife *7*, e29913.

Fox, L.E. (2006). Coordination and Modulation of Locomotion Pattern Generators in Drosophila Larvae: Effects of Altered Biogenic Amine Levels by the Tyramine beta Hydroxlyase Mutation. Journal of Neuroscience *26*, 1486–1498.

Franklin, D.W., and Wolpert, D.M. (2011). Computational Mechanisms of Sensorimotor Control. 1–18.

Gabel, C.V., Gabel, H., Pavlichin, D., Kao, A., Clark, D.A., and Samuel, A.D.T. (2007). Neural Circuits Mediate Electrosensory Behavior in Caenorhabditis elegans. J. Neurosci. *27*, 7586–7596.

Gao, S., Guan, S.A., Fouad, A.D., Meng, J., Kawano, T., Huang, Y.-C., Li, Y., Alcaire, S., Hung, W., Lu, Y., et al. (2018). Excitatory motor neurons are local oscillators for backward locomotion. eLife *7*, e29915.

Gendrel, M., Atlas, E.G., and Hobert, O. (2016). A cellular and regulatory map of the GABAergic nervous system of C. elegans. eLife *5*, e17686.

Georgopoulos, A.P., and Carpenter, A.F. (2015). ScienceDirect Coding of movements in the motor cortex. Current Opinion in Neurobiology *33*, 34–39.

Glaze, C.M., and Troyer, T.W. (2007). Behavioral Measurements of a Temporally Precise Motor Code for Birdsong. Journal of Neuroscience *27*, 7631–7639.

Gomez-Marin, A., Stephens, G.J., and Brown, A.E.X. (2016). Hierarchical compression of Caenorhabditis eleganslocomotion reveals phenotypic differences in the organization of behaviour. J. R. Soc. Interface *13*, 20160466–20160469.

Gomez-Marin, A., Stephens, G.J., and Louis, M. (2011). Active sampling and decision making in Drosophila chemotaxis. Nature Communications *2*, 441–10.

Gordus, A., Pokala, N., Levy, S., Flavell, S.W., and Bargmann, C.I. (2015). Feedback from Network States Generates Variability in a Probabilistic Olfactory Circuit. Cell 1–23.

Goulding, M. (2009). Circuits controlling vertebrate locomotion: moving in a new direction. 1–12.

Gray, J.M., Hill, J.J., and Bargmann, C.I. (2005). A circuit for navigation in Caenorhabditis elegans. Proc. Natl. Acad. Sci. U.S.a. *102*, 3184.

Gray, J.M., Karow, D.S., Lu, H., Chang, A.J., Chang, J.S., Ellis, R.E., Marletta, M.A., and Bargmann, C.I. (2004). Oxygen sensation and social feeding mediated by a C. elegans guanylate cyclase homologue. Nature *430*, 317–322.

Guillermin, M.L., Carrillo, M.A., and Hallem, E.A. (2017). A Single Set of Interneurons Drives Opposite Behaviors in C. elegans. Current Biology 1–23.

Guo, Z.V., Hart, A.C., and Ramanathan, S. (2009). Optical interrogation of neural circuits in Caenorhabditis elegans. Nat Meth *6*, 891–896.

Gupta, N., Singh, S.S., and Stopfer, M. (2016). Oscillatory integration windows in neurons. Nature Communications *7*, 13808.

Harvey, C.D., Coen, P., and Tank, D.W. (2012). Choice-specific sequences in parietal cortex during a virtual-navigation decision task. Nature *484*, 62–68.

Haspel, G., and O'Donovan, M.J. (2011). A Perimotor Framework Reveals Functional Segmentation in the Motoneuronal Network Controlling Locomotion in Caenorhabditis elegans. J. Neurosci. *31*, 14611–14623.

Hendricks, M., Ha, H., Maffey, N., and Zhang, Y. (2012). Compartmentalized calcium dynamics in a C. elegans interneuron encode head movement. Nature *487*, 99–103.

Hills, T.T., Todd, P.M., Lazer, D., Redish, A.D., Couzin, I.D., the Cognitive Search Research Group9 (2015). Exploration versus exploitation in space, mind, and society. Trends in Cognitive Sciences *19*, 46–54.

Hubel, D.H., and Wiesel, T.N. (1962). Receptive fields, binocular interaction and functional architecture in the cat's visual cortex. J Physiol *160*, 106–154.

Hums, I., Riedl, J., Mende, F., Kato, S., Kaplan, H.S., Latham, R., Sonntag, M., Traunmüller, L., and Zimmer, M. (2016). Regulation of two motor patterns enables the gradual adjustment of locomotion strategy in Caenorhabditis elegans. eLife *5*, e14116.

Hyafil, A., Giraud, A.-L., Fontolan, L., and Gutkin, B. (2015). Neural Cross-Frequency Coupling: Connecting Architectures, Mechanisms, and Functions. Trends in Neurosciences *38*, 725–740.

Iino, Y., and Yoshida, K. (2009). Parallel Use of Two Behavioral Mechanisms for Chemotaxis in Caenorhabditis elegans. J. Neurosci. *29*, 5370–5380.

Jin, X., and Costa, R.M. (2015). ScienceDirect Shaping action sequences in basal ganglia circuits. Current Opinion in Neurobiology *33*, 188–196.

Kaplan, H.S., Nichols, A.L.A., and Zimmer, M. (2018). Sensorimotor integration in Caenorhabditis elegans: a reappraisal towards dynamic and distributed computations. Philos. Trans. R. Soc. Lond., B, Biol. Sci. *373*, 20170371–12.

Kawano, T., Po, M.D., Gao, S., Leung, G., Ryu, W.S., and Zhen, M. (2011). An Imbalancing Act: Gap Junctions Reduce the Backward Motor Circuit Activity to Bias C. elegans for Forward Locomotion. Neuron *72*, 572–586.

Kobayashi, K., Nakano, S., Amano, M., Tsuboi, D., Nishioka, T., Ikeda, S., Yokoyama, G., Kaibuchi, K., and Mori, I. (2016). Single-Cell Memory Regulates a Neural Circuit for Sensory Behavior. CellReports *14*, 11–21.

Krakauer, J.W., Ghazanfar, A.A., Gomez-Marin, A., MacIver, M.A., and Poeppel, D. (2017). Neuroscience Needs Behavior: Correcting a Reductionist Bias. Neuron *93*, 480–490.

Kwon, N., Hwang, A.B., You, Y.-J., V Lee, S.-J., and Ho Je, J. Dissection of C. elegans behavioral genetics in 3-D environments. Sci Rep *5*, 9564EP–.

Kwon, N., Pyo, J., Lee, S.-J., and Je, J.H. (2013). 3-D Worm Tracker for Freely Moving C. elegans. PLoS ONE *8*, e57484–e57486.

Larsch, J., Ventimiglia, D., Bargmann, C.I., and Albrecht, D.R. (2013). High-throughput imaging of neuronal activity in Caenorhabditis elegans. Proc Natl Acad Sci USA *110*, E4266–E4273.

Larsch, J., Flavell, S.W., Liu, Q., Gordus, A., Albrecht, D.R., and Bargmann, C.I. (2015). A Circuit for Gradient Climbing in C. elegans Chemotaxis. CellReports 1–40.

Lashley, K.S. (1951). The problem of serial order in behavior. In Cerebral Mechanisms in Behavior; the Hixon Symposium, (Oxford, England: Wiley SN -), pp. 112–146.

Laurent, P., Soltesz, Z., Nelson, G.M., Chen, C., Arellano-Carbajal, F., Levy, E., and de Bono, M. (2015). Decoding a neural circuit controlling global animal state in C. elegans. eLife *4*.

Li, W., Feng, Z., Sternberg, P.W., and Shawn Xu, X.Z. (2006). A C. elegans stretch receptor neuron revealed by a mechanosensitive TRP channel homologue. Nature *440*, 684–687.

Li, Z., Liu, J., Zheng, M., and Xu, X.Z.S. (2014). Encoding of Both Analog- and Digital-like Behavioral Outputs by One C. elegans Interneuron. Cell *159*, 751–765.

Liu, H., Yang, W., Wu, T., Duan, F., Soucy, E., Jin, X., and Zhang, Y. (2018). Cholinergic Sensorimotor Integration Regulates Olfactory Steering. Neuron *97*, 390–405.e393.

Liu, P., Chen, B., Mailler, R., and Wang, Z.-W. (2017). Antidromic-rectifying gap junctions amplify chemical transmission at functionally mixed electrical-chemical synapses. Nature Communications *8*, 1–16.

Lockery, S.R. (2011). The computational worm: spatial orientation and its neuronal basis in C. elegans. Current Opinion in Neurobiology *21*, 782–790.

Long, M.A., Jin, D.Z., and Fee, M.S. (2010). Support for a synaptic chain model of neuronal sequence generation. Nature *468*, 394–399.

Luo, L., Wen, Q., Ren, J., Hendricks, M., Gershow, M., Qin, Y., Greenwood, J., Soucy, E.R., Klein, M., Smith-Parker, H.K., et al. (2014). Dynamic Encoding of Perception, Memory, and Movement in a C. elegans Chemotaxis Circuit. Neuron *82*, 1115–1128.

Marder, E., and Bucher, D. (2001). Central pattern generators and the control of rhythmic movements. 1–11.

Marder, E. (2009). Electrical Synapses: Rectification Demystified. Current Biology *19*, R34–R35.

Markowitz, J.E., Gillis, W.F., Beron, C.C., Neufeld, S.Q., Robertson, K., Bhagat, N.D., Peterson, R.E., Peterson, E., Hyun, M., Linderman, S.W., et al. (2018). The Striatum Organizes 3D Behavior via Moment-to- Moment Action Selection. Cell 1–33.

Marques, J.C., Lackner, S., Félix, R., and Orger, M.B. (2018). Structure of the Zebrafish Locomotor Repertoire Revealed with Unsupervised Behavioral Clustering. Current Biology 1–34.

McKellar, C.E., Lillvis, J.L., Bath, D.E., Fitzgerald, J.E., Cannon, J.G., Simpson, J.H., and Dickson, B.J. (2019). Threshold-Based Ordering of Sequential Actions during Drosophila Courtship. Current Biology *29*, 426–434.e426.

Moltz, H. (1961). The fixed action pattern: empirical properties and theoretical implications. Recent Adv Biol Psychiatry *4*, 69–85.

Moore, J.D., Deschênes, M., Furuta, T., Huber, D., Smear, M.C., Demers, M., and Kleinfeld, D. (2013). Hierarchy of orofacial rhythms revealed through whisking and breathing. Nature *497*, 205–210.

Murray, J.M., and Escola, G.S. (2017). Learning multiple variable-speed sequences in striatum via cortical tutoring. eLife *6*.

Musall, S., Kaufman, M.T., Juavinett, A.L., Gluf, S., and Churchland, A.K. (2019). Single-trial neural dynamics are dominated by richly varied movements. bioRxiv *94*, 866–32.

Nakai, J., Ohkura, M., and Imoto, K. (2001). A high signal-to-noise Ca(2+) probe composed of a single green fluorescent protein. Nat Biotechnol *19*, 137–141.

Nguyen, J.P., Shipley, F.B., Linder, A.N., Plummer, G.S., Liu, M., Setru, S.U., Shaevitz, J.W., and Leifer, A.M. (2016). Whole-brain calcium imaging with cellular resolution in freely behaving Caenorhabditis elegans. Proc Natl Acad Sci USA *113*, E1074–E1081.

Nichols, A.L.A., Eichler, T., Latham, R., and Zimmer, M. (2017). A global brain state underlies C. elegansslеep behavior. Science *356*, eaam6851–11.

O'Keefe, J. (1976). Place units in the hippocampus of the freely moving rat. Exp Neurol *51*, 78–109.

Oda, S., Tomioka, M., and Iino, Y. (2011). Neuronal plasticity regulated by the insulin-like signaling pathway underlies salt chemotaxis learning in Caenorhabditis elegans. Journal of Neurophysiology *106*, 301–308.

Pierce-Shimomura, J.T., Morse, T.M., and Lockery, S.R. (1999). The fundamental role of pirouettes in Caenorhabditis elegans chemotaxis. Journal of Neuroscience *19*, 9557–9569.

Piggott, B.J., Liu, J., Feng, Z., Wescott, S.A., and Xu, X.Z.S. (2011). The Neural Circuits and Synaptic Mechanisms Underlying Motor Initiation in C. elegans. Cell *147*, 922–933.

Pirri, J.K., McPherson, A.D., Donnelly, J.L., Francis, M.M., and Alkema, M.J. (2009). A Tyramine-Gated Chloride Channel Coordinates Distinct Motor Programs of a Caenorhabditis elegans Escape Response. Neuron *62*, 526–538.

Putney, J., Conn, R., and Sponberg, S. (2019). Timing is (almost) everything in a comprehensive, spike-resolved flight motor program. bioRxiv 602961.

Rakowski, F., Srinivasan, J., Sternberg, P.W., and Karbowski, J. (2013). Synaptic polarity of the interneuron circuit controlling C. elegans locomotion. Front. Comput. Neurosci. *7*, 128.

Roberts, W.M., Augustine, S.B., Lawton, K.J., Lindsay, T.H., Thiele, T.R., Izquierdo, E.J., Faumont, S., Lindsay, R.A., Britton, M.C., Pokala, N., et al. (2016). A stochastic neuronal model predicts random search behaviors at multiple spatial scales in C. elegans. eLife *5*, e12572.

Scholz, M., Linder, A.N., Randi, F., Sharma, A.K., Yu, X., Shaevitz, J.W., and Leifer, A.M. (2018). Predicting natural behavior from whole-brain neural dynamics. bioRxiv 445643.

Schrödel, T., Prevedel, R., Aumayr, K., Zimmer, M., and Vaziri, A. (2013). Brain-wide 3D imaging of neuronal activity in Caenorhabditis elegans with sculpted light. Nat Meth *10*, 1013–1020.

Seeds, A.M., Ravbar, P., Chung, P., Hampel, S., Midgley, F.M., Jr, Mensh, B.D., and Simpson, J.H. (2014). A suppression hierarchy among competing motor programs drives sequential grooming in Drosophila. eLife *3*, 3–23.

Shaw, M., Zhan, H., Elmi, M., Pawar, V., Essmann, C., and Srinivasan, M.A. (2018). Three-dimensional behavioural phenotyping of freely moving C. elegans using quantitative light field microscopy. PLoS ONE *13*, e0200108.

Shenoy, K.V., Sahani, M., and Churchland, M.M. (2013). Cortical Control of Arm Movements: A Dynamical Systems Perspective. Annu. Rev. Neurosci. *36*, 337–359.

Shipley, F.B., Clark, C.M., Alkema, M.J., and Leifer, A.M. (2014). Simultaneous optogenetic manipulation and calcium imaging in freely moving C. elegans. Front. Neural Circuits *8*, 28.

Skora, S., Mende, F., and Zimmer, M. (2018). Energy Scarcity Promotes a Brain-wide Sleep State Modulated by Insulin Signaling in C. elegans. CellReports *22*, 953–966.

Slater, P.J.B. (1973). Describing Sequences of Behavior. In Perspectives in Ethology, P.P.G. Bateson, and P.H. Klopfer, eds. (Boston, MA: Springer US), pp. 131–153.

Sponberg, S., and Daniel, T.L. (2012). Abdicating power for control: a precision timing strategy to modulate function of flight power muscles. Proceedings of the Royal Society B: Biological Sciences *279*, 3958–3966.

Stephens, G.J., Johnson-Kerner, B., Bialek, W., and Ryu, W.S. (2008). Dimensionality and Dynamics in the Behavior of C. elegans. PLoS Comput Biol *4*, e1000028–10.

Stringer, C., Pachitariu, M., Steinmetz, N., Reddy, C.B., Carandini, M., and Harris, K.D. (2019). Spontaneous behaviors drive multidimensional, brainwide activity. Science *364*, 255–13.

Sulston, J.E., and Horvitz, H.R. (1977). Post-embryonic cell lineages of the nematode, Caenorhabditis elegans. Developmental Biology *56*, 110–156.

Tinbergen, N. (1951). The study of instinct. (New York, NY, US: Clarendon Press/Oxford University Press SN -).

Tsalik, E.L., and Hobert, O. (2003). Functional mapping of neurons that control locomotory behavior inCaenorhabditis elegans. J. Neurobiol. *56*, 178–197.

Varshney, L.R., Chen, B.L., Paniagua, E., Hall, D.H., and Chklovskii, D.B. (2011). Structural Properties of the Caenorhabditis elegans Neuronal Network. PLoS Comput Biol *7*, e1001066–21.

Venkatachalam, V., Ji, N., Wang, X., Clark, C., Mitchell, J.K., Klein, M., Tabone, C.J., Florman, J., Ji, H., Greenwood, J., et al. (2016). Pan-neuronal imaging in roaming Caenorhabditis elegans. Proc Natl Acad Sci USA *113*, E1082–E1088.

Wen, Q., Po, M.D., Hulme, E., Chen, S., Liu, X., Wai Kwok, Sen, Gershow, M., Leifer, A.M., Butler, V., Fang-Yen, C., et al. (2012). Proprioceptive Coupling within Motor Neurons Drives C. elegans Forward Locomotion. Neuron *76*, 750–761.

White, J.G., Southgate, E., Thomson, J.N., and Brenner, S. (1986). The structure of the nervous system of the nematode Caenorhabditis elegans. Philosophical Transactions of the Royal Society B: Biological Sciences *314*, 1–340.

Wicks, S.R., Roehrig, C.J., and Rankin, C.H. (1996). A dynamic network simulation of the nematode tap withdrawal circuit: predictions concerning synaptic function using behavioral criteria. Journal of Neuroscience *16*, 4017–4031.

Wiltschko, A.B., Johnson, M.J., Iurilli, G., Peterson, R.E., Katon, J.M., Pashkovski, S.L., Abraira, V.E., Adams, R.P., and Datta, S.R. (2015). Mapping Sub-Second Structure in Mouse Behavior. Neuron *88*, 1121–1135.

Wood, W.B., and researchers, C.O.C.E. (1988). The nematode Caenorhabdtis elegans (Cold Spring Harbor: Cold Spring Harbor laboratory Press).

Yang, S.C.-H., Wolpert, D.M., and Lengyel, M. (2016). ScienceDirect Theoretical perspectives on active sensing. Current Opinion in Behavioral Sciences *11*, 100–108.

Yemini, E., Jucikas, T., Grundy, L.J., Brown, A.E.X., and Schafer, W.R. (2013). A database of Caenorhabditis elegans behavioral phenotypes. Nat Meth *10*, 877–879.

Yeon, J., Kim, J., Kim, D.-Y., Kim, H., Kim, J., Du, E.J., Kang, K., Lim, H.-H., Moon, D., and Kim, K. (2018). A sensory-motor neuron type mediates proprioceptive coordination of steering in C. elegans via two TRPC channels. PLoS Biol *16*, e2004929–26.

Yuste, R., MacLean, J.N., Smith, J., and Lansner, A. (2005). The cortex as a central pattern generator. Nat Rev Neurosci *6*, 477–483.

Zimmer, M., Gray, J.M., Pokala, N., Chang, A.J., Karow, D.S., Marletta, M.A., Hudson, M.L., Morton, D.B., Chronis, N., and Bargmann, C.I. (2009). Neurons Detect Increases and Decreases in Oxygen Levels Using Distinct Guanylate Cyclases. Neuron *61*, 865–879.